SOLID ROCKET BOOSTER STING INTERFERENCE WIND TUNNEL TEST ANALYSIS

Submitted To:

NATIONAL AERONAUTICS AND SPACE ADMINISTRATION
GEORGE C. MARSHALL SPACE FLIGHT CENTER
Science and Engineering Directorate

Under Contract NAS8--33816

Submitted By:

NORTHROP SERVICES, INC.

P. O. BOX 1484 Huntsville, Alabama 35807 (205) 837-0580

SPACE SHUTTLE SOLID ROCKET BOOSTER STING INTERFERENCE WIND TUNNEL TEST DATA ANALYSIS

15 SEPTEMBER 1981

by

B. Conine
W. Boyle

Prepared for:

NATIONAL AERONAUTICS AND SPACE ADMINISTRATION
GEORGE C. MARSHALL SPACE FLIGHT CENTER
SCIENCE AND ENGINEERING DIRECTORATE

Under Contract NAS8-33816

Reviewed and Approved by:

M N Burroughs
M. H. Burroughs, Manager

NORTHROP SERVICES, INC.
P.O. BOX 1484
HUNTSVILLE, ALABAMA 35807
(205)837-0580

FOREWORD

This report presents the results of work performed by Northrop Services, Inc., Engineering Technology Group for the Marshall Space Flight Center under Contract NAS8-33816. Portions of the analysis were performed by Lockheed Missiles and Space Co., Huntsville Research and Development Center. The NASA Technical Monitor for this contract was Mr. D. L. Bacchus. The authors wish to acknowledge the assistance and contributions provided by Mr. Bacchus toward the successful completion of this study. The authors also wish to thank Mr. Paul Ramsey (ED32) who provided access to the data, his test log, and took time to discuss the data and results with the authors.

TABLE OF CONTENTS

LIST OF ILLUSTRATIONS

LIST OF ILLUSTRATIONS (Continued)

LIST OF ILLUSTRATIONS (Continued)

LIST OF ILLUSTRATIONS (Continued)

LIST OF ILLUSTRATIONS (Continued)

LIST OF ILLUSTRATIONS (Continued)

LIST OF ILLUSTRATIONS (Continued)

LIST OF ILLUSTRATIONS (Continued)

LIST OF ILLUSTRATIONS (Concluded)

LIST OF TABLES

NOMENCLATURE (MISSILE AXIS SYSTEM*)

Symbol	Definition	Units
C_D	Crossflow drag coefficient, F_Z/qSp	
C_N	Normal force coefficient, F_Z/qS	
C_M	Pitching moment coefficient, M_Y/qSL_R	
C_Y	Side force coefficient, F_Y/qS	
C_n	Yawing moment coefficient, M_Z/qSL_R	
C_ℓ	Rolling moment coefficient, M_X/qSL_R	
C_A	Total axial force coefficient, F_X/qS	
F_Z	Normal force	lbs.
M_Y	Pitching moment	in.-lbs.
F_Y	Side force	lbs.
M_Z	Yawing moment	in.-lbs.
M_X	Rolling moment	in.-lbs.
F_X	Total axial force	lbs.
q	Free stream dynamic pressure	$lbs./in.^2$
S	Reference area (SRB body cross sectional area)	$in.^2$
S_p	Model planform area	$in.^2$
L_B	Body length (SRB total length including nozzle extension)	in.
L_R	Reference length (SRB body diameter)	in.
M_∞	Free stream Mach number	
RN	Free stream Reynolds number per foot	1/ft
RN_d	Free stream Reynolds number based on model cylinder diameter	
α	Total angle of attack, angle between the X-axis and the free stream vector (see Figure 2-5)	degrees

*The missile axis system is shown in Figure 2-5.

Symbol	Definition	Units
ϕ	Model roll angle (see Figure 2-5)	degrees
SRB	Abbreviation for solid rocket booster	
X_{cp}/L_B	Longitudinal center of pressure location in percent of body length from nose, $X_{cp}/L_B = \frac{X_{MRP}}{L_B} - \frac{C_M}{C_N}\frac{L_R}{L_B}$	
X_{cg}	Longitudinal center of gravity location measured from the nose	in.
X_M, Y_M, Z_M	Missile axes	
X_{MRP}, Y_{MRP}, Z_{MRP}	Abbreviations for the location of the moment reference point in the missile axis system (note that $X_{MRP} \neq X_{cg}$)	in.

Section I

INTRODUCTION

The analysis of the wind tunnel test results from SRB sting interference test TWT 660 and HRWT 042 was undertaken to evaluate the sting interference that may be present in the Space Shuttle SRB reentry aerodynamic math model. The wind tunnel test program was designed to obtain six-component static stability data on a model of the Space Shuttle 146-inch diameter right Solid Rocket Booster (SRB) model mounted on various sting arrangements and combinations to determine the sting effects. The test program is a result of recommendations made in Reference 1. The technique of developing the sting interference data is to mount the SRB model on a nose-mounted sting and obtain data with and without dummy side-mounted stings. The dummy side mounted stings are configured to simulate stings used at ARC, MSFC 14-inch TWT, MSFC High Reynolds number stings, and AEDC. The test program thus provided a data base that can be used to develop delta coefficients which may be used to develop corrections to the side-mounted sting SRB data base. An additional portion of the test program consisted of mounting the SRB model on various side-mounted stings to obtain data with and without a dummy nose sting. This procedure provided a check of the mutual sting interference, since the corrected data for both nose and side-mounted stings should agree if the total sting interference is removed from the data and no mutual sting interference exists.

The total test program consisted of tests in the MSFC 14-inch Trisonic wind tunnel and the MSFC High Reynolds number facility. The test program conducted in the MSFC 14-inch Trisonic wind tunnel developed data at Mach numbers of 0.6, 0.8, 1.05, 1.1, 1.2, and 1.46, angles of attack from 100 to 140 degrees, and roll angles of 0, 45, and 90 degrees. The test program conducted in the MSFC High Reynolds number facility developed data at Mach numbers of 0.4, 0.6, and 0.8, angles of attack from 100 to 120 degrees, and roll angles of 0 and 90 degrees. The Reynolds number range was from 1.5×10^6 to 9.5×10^6, based on the model diameter.

This report documents the procedure developed to determine the sting interference, the development of the corrected aerodynamic data, the results of the analysis of the sting interference data and the corrected aerodynamic data, and the development of a new SRB aerodynamic math model.

Section II

WIND TUNNEL TEST PROGRAMS

Two wind tunnel test programs were conducted to develop the required sting interference data. The wind tunnel tests consisted of a transonic test, in the MSFC 14-inch Trisonic Wind Tunnel (TWT 660) and a High Reynolds number test in the MSFC High Reynolds Number Wind Tunnel (HRWT 042). Combinations of single and dummy sting arrangements were used during both tests to obtain the necessary data for the evaluation of the sting interference. A brief discussion of each test program is presented below. A brief discussion of the test programs and sting configurations used to develop the current SRB reentry aerodynamic data base and data tapes is also presented for reference.

TWT 660 TEST PROGRAM

The TWT 660 test program was designed to obtain six-component static stability data on a model of the 146-inch diameter SRB model mounted on various sting arrangements and combinations to determine the sting effects. The technique of developing the sting interference data is to mount the SRB model on a nose-mounted sting and obtain data with and without dummy side-mounted stings. The dummy side mounted stings are configured to simulate stings used at ARC, MSFC 14-inch TWT, MSFC High Reynolds number stings and AEDC. The test program thus provided a data base that can be used to develop Δ coefficients which may be used to develop corrections to the side-mounted sting SRB data base. An additional portion of the test program consists of mounting the SRB model on various side-mounted stings to obtain data with and without a dummy nose sting. This procedure provided a check of the mutual sting interference, since the corrected data for both nose and side-mounted stings should agree if the total sting interference is removed from the data and no mutual sting interference exists.

The test program conducted in the MSFC 14-inch Trisonic wind tunnel provided data at Mach numbers of 0.6, 0.8, 1.05, 1.1, 1.2, and 1.46, for angles of attack from 100 to 140 degrees, and roll angles of 0, 45, and 90 degrees.

The model used during the test program was MSFC model 486, a 0.5478 percent scale model of the 146-inch diameter right-hand SRB reentry configuration. The SRB reentry configuration is the configuration of the SRB after staging of the nozzle extension and prior to deployment of the nose cap that initiates deployment of the drogue chute (see Figure 2-1). Details of the wind tunnel model are given in Figure 2-2. Figure 2-3 shows the location of the right hand SRB on the Space Shuttle launch configuration. The SRB consists of a spherically blunt 18 degree half angle cone, a cylindrical body, engine shroud, protuberances, and truncated engine nozzle. The SRB model did not have the engine shroud thermal shield simulated. Figure 2-4 shows the SRB nozzle extension that is separated at apogee and the thermal shield. The SRB aerodynamic data are developed in the missile axis system. The missile axis system is shown in Figure 2-5.

STING HARDWARE

The various sting configurations used are shown in Figures 2-6 through 2-21 and described in Table 2-1. The symbols used in the six character sting configuration identifiers are defined as follows:

Character	Symbol	Definition
1	M	TWT sting
	A	ARC sting
	H	HRWT sting
2,3	SS	Side-mounted sting
	SD	Side-mounted dummy sting
	OO	No side sting used
4,5	NS	Nose-mounted sting
	ND	Nose-mounted dummy sting
	OO	No nose sting used
6	A	Configuration for angle-of-attack range A (100°-120°)
	B	Configuration for angle-of-attack range B (120°-140°)

The Mach numbers for which data was obtained are 0.6, 0.8, 0.9, 1.05, 1.1, 1.2 and 1.46. The angle of attack range was from 100 to 140 degrees. Six component force and moment data were taken at angle-of-attack increments of 2.0 degrees. The model was tested at roll angles of 0, 45, and 90 degrees. A

series of different sting configurations were used during the program. Three basic single sting configurations were tested. The single sting configurations included MSFC side mount (MSSOOA/B), Ames side mount (ASSOOA/B), and the MSFC nose mount configuration (MOONSA/B). Five dual sting configurations were tested with various combinations of active and dummy nose and side mounts. The dummy side mount configurations used with the active nose mount included the MSFC (MSDNSA/B), Ames (ASDNSA/B) and MSFC High Reynolds number (HSDNSA/B) sting configuration. The dummy nose mount configurations used with the active side mount stings were the MSFC (MSSNDA/B), and Ames (ASSNDA/B) sting configurations. It is noted that each basic sting has two configurations. Each configuration is designed for a particular angle of attack sweep range. Sting configurations with a letter designation ending in A are used for the A angle of attack range (α = 100 to 120 degrees). Sting configurations with a letter designation ending in B are used for the B angle of attack range (α = 120 to 140 degrees). Additional details concerning the test and test hardware can be obtained from Reference 2.

STING INTERFERENCE ANALYSIS PROCEDURE - TWT 660

The procedure for determining the sting interference is the following. The sting interference for the side mount sting configurations is determined by

$$\Delta C_{x_{\substack{\text{Side Mount}\\ \text{Sting Interference}}}} = C_{x_{\substack{\text{Dummy Side Mount}\\ \text{With Active Nose}\\ \text{Mount}\\ \text{(MSDNSA/B),}\\ \text{(ASDNSA/B)}\\ \text{or (HSDNSA/B)}}}} - C_{x_{\substack{\text{Nose Mount}\\ \text{Only}\\ \text{(MOONSA/B)}}}}$$

The corrected side mount sting data is thus

$$C_{x_{\substack{\text{Corrected}\\ \text{Side Mount}}}} = C_{x_{\substack{\text{Active Side}\\ \text{Mount}\\ \text{(MSSOOA/B),}\\ \text{(ASSOOA/B)}}}} - \Delta C_{x_{\substack{\text{Side Mount}\\ \text{Sting Interference}}}}$$

The sting interference for the nose mount configuration is determined by

$$\Delta C_{x_{\text{Nose Mount Sting Interference}}} = C_{x_{\text{Dummy Nose Mount With Active Side Mount}}} - C_{x_{\text{Side Mount Only}}}$$

(MSSNDA/B) (ASSNDA/B) or (MSSOOA/B) (ASSOOA/B)

The corrected nose mount sting data is thus

$$C_{x_{\text{Corrected Nose Mount}}} = C_{x_{\text{Nose Mount (MOONSA/B)}}} - \Delta C_{x_{\text{Nose Mount Sting Interference}}}$$

It is noted that the nose mount sting interference could be obtained with two different side mount configurations (MSSNDA and ASSNDA). The nose sting was identical in both cases. Then the difference in the procedure is only in the use of different side mount stings. The nose mount sting interference has been labled differently to distinguish what side mount sting was used to develop the sting interference data.

HRWT 042 TEST PROGRAM

The HRWT 042 test program was a three part program that consisted of testing one configuration from the TWT 660 test program, testing a basic cylinder to verify basic cylinder data trends and the sting interference portion of the test program.

The model configuration used for the TWT 660 verification was configuration ASSOOA/B. The model and sting configuration used for the HRWT 042 test is presented in Figure 2-22. The test configuration used for this hardware during the TWT 660 test is shown in Figure 2-15. The TWT sting and SRB model hardware for this configuration was tested in the High Reynolds number tunnel.

The cylinder test used a symmetric and asymmetric cylinder with a side mount sting (see Figures 2-23 through 2-25). The cylinder test allowed a check with previously published high Reynolds number cylinder data and allowed the evaluation of basic cylinder moment interference due to the sting.

The sting interference portion of the test consisted of using a series of sting configurations utilized in earlier SRB testing (HRWT 039) along with

new configuration that allowed the evaluation of the sting interference. The SRB model configuration used for the test is presented in Figure 2-26. The single and dual sting configurations used are presented in Figures 2-27 through 2-34. The single sting configurations used are the side mount sting (HSSOOA/B) shown in Figures 2-27 and 2-28 and the nose mount sting (HOONSA/B) shown in Figures 2-29 and 2-30. The dual sting configurations include the side mount with dummy nose mount (HSSNDA/B) shown in Figures 2-31 and 2-32 and the nose mount with the Dummy side mount (HSDNSA/B) shown in Figures 2-33 and 2-34. Additional details concerning the test program and model hardware can be obtained from Reference 3.

STING INTERFERENCE ANALYSIS PROCEDURE - HRWT 042

The procedure for determining the sting interference is the following. The sting interference for the side mount sting configurations is determined by

$$\Delta C_{x_{\text{Side Mount Sting Interference}}} = C_{x_{\text{Dummy Side Mount With Active Nose Mount (HSDNSA/B)}}} - C_{x_{\text{Nose Mount Only (HOONSA)}}}$$

The corrected side mount sting data is thus

$$C_{x_{\text{Corrected Side Mount}}} = C_{x_{\text{Active Side Mount (HSSOOA/B)}}} - \Delta C_{x_{\text{Side Mount Sting Interference}}}$$

The sting interference for the nose mount configuration is determined by

$$\Delta C_{x_{\text{Nose Mount Sting Interference}}} = C_{x_{\text{Dummy Nose Mount With Active Side Mount (HSSNDA/B)}}} - C_{x_{\text{Side Mount Only (HSSOOA/B)}}}$$

The corrected nose mount sting data is thus

$$C_{x_{\text{Corrected Nose Mount}}} = C_{x_{\text{Nose Mount (HOONSA/B)}}} - \Delta C_{x_{\text{Nose Mount Sting Interference}}}$$

OTHER TEST PROGRAMS

The reentry aerodynamic static stability data base for the 146-inch diameter right side Space Shuttle SRB was developed from a series of wind tunnel test programs. These wind tunnel test programs are defined below.

- TWT 640 (SA14Fb); conducted in the NASA/MSFC 14-inch Trisonic Wind Tunnel, Reference 4.
- Project P41C-E3A (SA16F); conducted in the 4T Arnold Engineering Development Wind Tunnel, Reference 5.
- ARC 11-74-1 (SA11F); conducted in the Ames Research Centers Unitary Tunnels, References 6 and 7.
- HRWT 034 (SA30F); conducted in the NASA/MSFC High Reynolds Number Wind Tunnel Facility, Reference 8.
- HRWT 039 (SA31F); conducted in the NASA/MSFC High Reynolds Number Wind Tunnel Facility, Reference 9.
- TWT 596 (SA21F); conducted in the NASA/MSFC 14-inch Trisonic Wind Tunnel, Reference 10.

The range of test conditions for the major test programs are presented in Table 2-2. These test programs were used to develop two aerodynamic math models of the SRB reentry aerodynamic characteristics. The Math models were put on magnetic tape for use in SRB reentry dynamics studies and are identified as SRB Aero data Tape #1 and #2. SRB data Tape #1 was developed using results from tests HRWT 034, TWT 640, and SA16F. Test TWT 640 provides the data basis for both data tapes. Test TWT 640 was the only test that covered the complete angle of attack range (α = 0 to 180 degrees) and roll angle range (θ = 0 to 315 degrees) as shown in Table 2-2. All other tests provided only partial attitude coverage. Test TWT 640 used the sting configurations shown in Figures 2-35 and 2-36. Test SA16F used the sting configuration shown in Figure 2-37. This sting configuration was also used in portions of test TWT 640 for the angle of attack range from 130 to 150 degrees.

Data Tape #2 was developed using the results from three supplemental test programs. These test programs were SA11F, SA21F, and SA31F. Test SA11F used a larger model (2.8 percent scale) and thus the model had improvements in the number and fidelity of protuberances. The model was tested over a limited range of attitude and roll angles however (see Table 2-2). The Ames test (SA11F) used the sting configuration shown in Figures 2-38 and 2-39. Test SA21F was a test to develop rolling moment data for every 22 1/2 degrees of roll angle. The integral of the rolling moment coefficient at a constant angle of attack should be near zero. Test SA21F provided the required data to improve the rolling moment coefficient math model for data Tape #2. Test SA31F was used to provide high Reynolds number data trends for the SRB model with protuberances for use in the development of Tape #2. The sting configuration used for test SA31F (HRWT 039) are presented in Figures 2-40 and 2-41. Thus the SRB reentry aerodynamic data base was developed using the sting configuration presented in Figures 2-37 through 2-41 for the angle of attack range from 60 to 180 degrees. The sting configuration presented in Figures 2-6 through 2-34 provide the means of evaluating the sting interference for the data base stings over the critical angle of attack range from 100 to 140 degrees.

TABLE 2-1. TWT 660 STING CONFIGURATIONS

Identifier	Description	Figure
MSSOOA	TWT side-mount sting 138, $100° \leq \alpha \leq 120°$	2-6
MSSOOB	TWT side-mount sting 137, $120° \leq \alpha \leq 140°$	2-7
MOONSA	Nose-mount sting 140, $100° \leq \alpha \leq 120°$	2-8
MOONSB	Nose-mount sting 141, $120° \leq \alpha \leq 140°$	2-9
MSSNDA	TWT side-mount sting 138, nose dummy 140-D $100° \leq \alpha \leq 120°$	2-10
MSSNDB	TWT side-mount sting 137, nose dummy 141-D, $120° \leq \alpha \leq 140°$	2-11
MSDNSA	TWT side dummy 138-D, nose-mount sting 140, $100° \leq \alpha \leq 120°$	2-12
MSDNSB	TWT side dummy 137-D, nose-mount sting 141, $120° \leq \alpha \leq 140°$	2-13
ASSOOA	ARC side-mount sting 142, $100° \leq \alpha \leq 120°$	2-14
ASSOOB	ARC side-mount sting 142, $120° \leq \alpha \leq 140°$	2-15
ASSNDA	ARC side-mount sting 142, nose dummy 140-D, $100° \leq \alpha \leq 120°$	2-16
ASSNDB	ARC side-mount sting 142, nose dummy 141-D, $120° \leq \alpha \leq 140°$	2-17
ASDNSA	ARC side dummy sting 142 (W/O balance adapt.), nose-mount sting 140, $100° \leq \alpha \leq 120°$	2-18
ASDNSB	ARC side dummy sting 142 (W/O balance adapter), nose-mount sting 141, $120° \leq \alpha \leq 140°$	2-19
HSDNSA	HRWT side dummy HRWT1-D, nose-mount sting 140, $100° \leq \alpha \leq 120°$	2-20
HSDNSB	HRWT side dummy HRWT2-D, nose-mount sting 141, $120° \leq \alpha \leq 140°$	2-21

TABLE 2-2. SRB DATA BASE TEST PROGRAMS

FACILITY NO. AND TEST SERIES	MACH NUMBER	ANGLES OF ATTACK (DEGREES)	ROLL ANGLES (DEGREES)	REYNOLDS NO. (RN_d x 10^{-6})
HRWT 039 (SA31F)	0.4, 0.5, 0.6, 0.7, 0.8, & 0.9	101°, 105°, 110°, 115°, 120°, 125°, 135°, & 140°	0°, 45°, 90°, 135°, 180°, 225°, 270°, & 315°	2.45 to 12.46
TWT 640 (SA14Fb)	0.4, 0.5, 0.6, 0.7, 0.8, 0.9, 1.0, 1.2, 1.46, 1.96, 2.74 3.48, & 4.45	-10° to 190° in 2.° increments	0°, 45°, 90°, 135°, 180°, 225°, 270°, & 315°	0.233 to 0.5
P41C-E3A (SA16F)	0.4, 0.5, 0.6, 0.7, 0.8, 0.9, 1.0, & 1.2	113° to 187° in 2° increments	0°, 90°, & 270°	0.233 to 0.273
TST-074 (SA11F)	0.4, 0.5, 0.6, 0.7, 0.8, 0.9, 1.1, 1.2, 1.4, 1.96, 2.50, 3.00, & 3.48	60° to 195° in 5° increments	0°, 45°, 90° & 225°	0.341 to 2.044

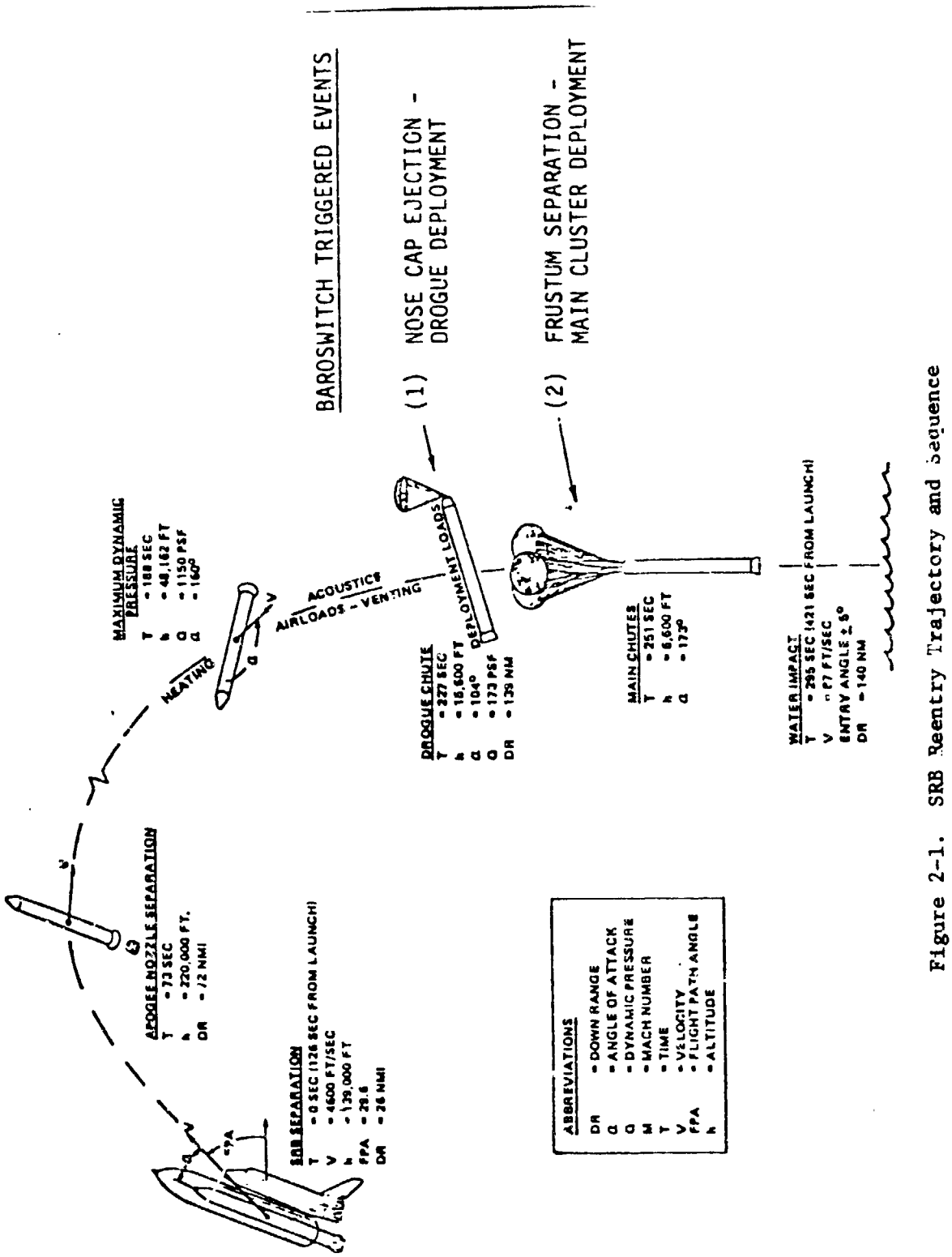

Figure 2-1. SRB Reentry Trajectory and Sequence

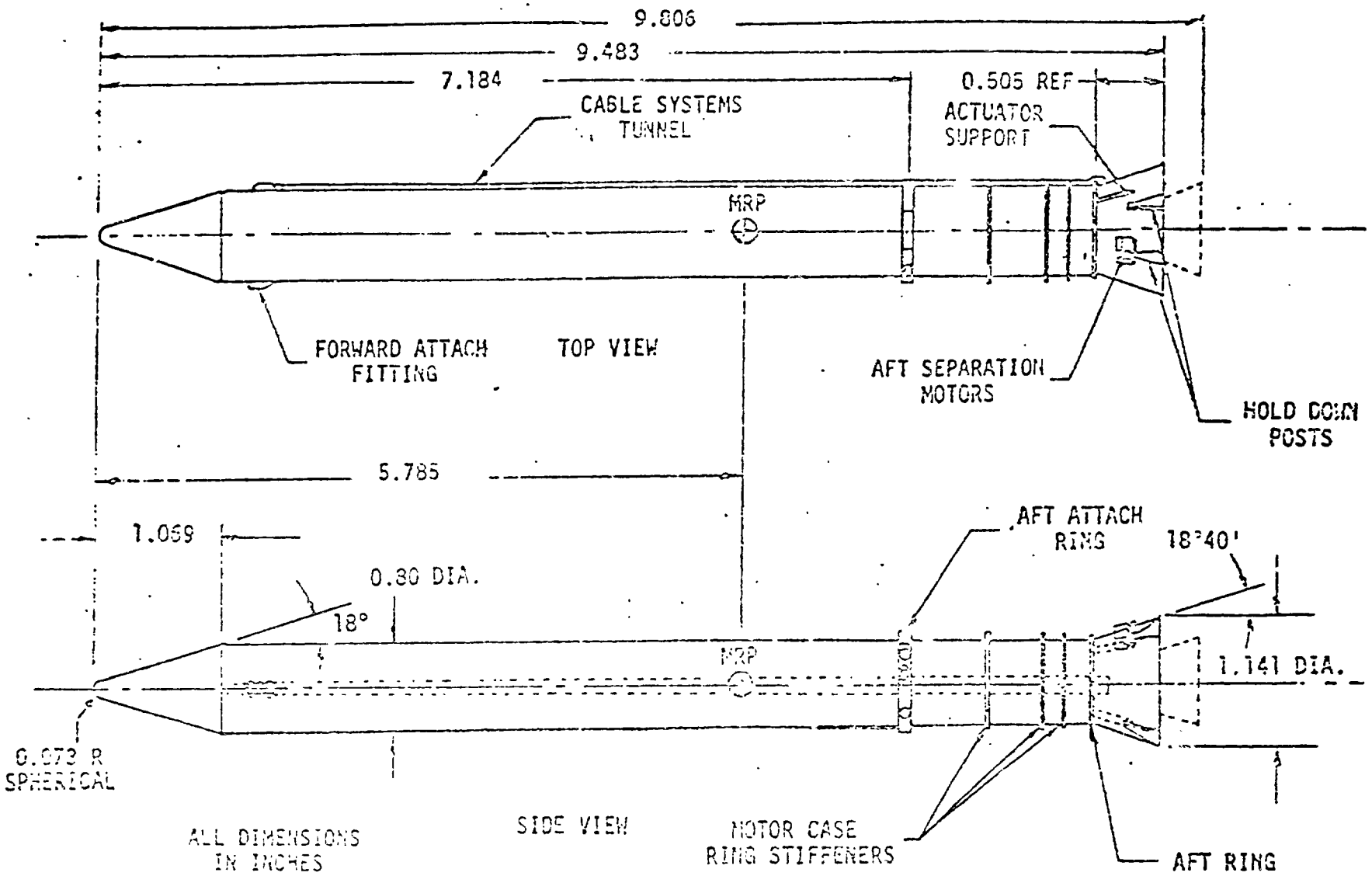

Figure 2-2. General SRB Model Arrangement

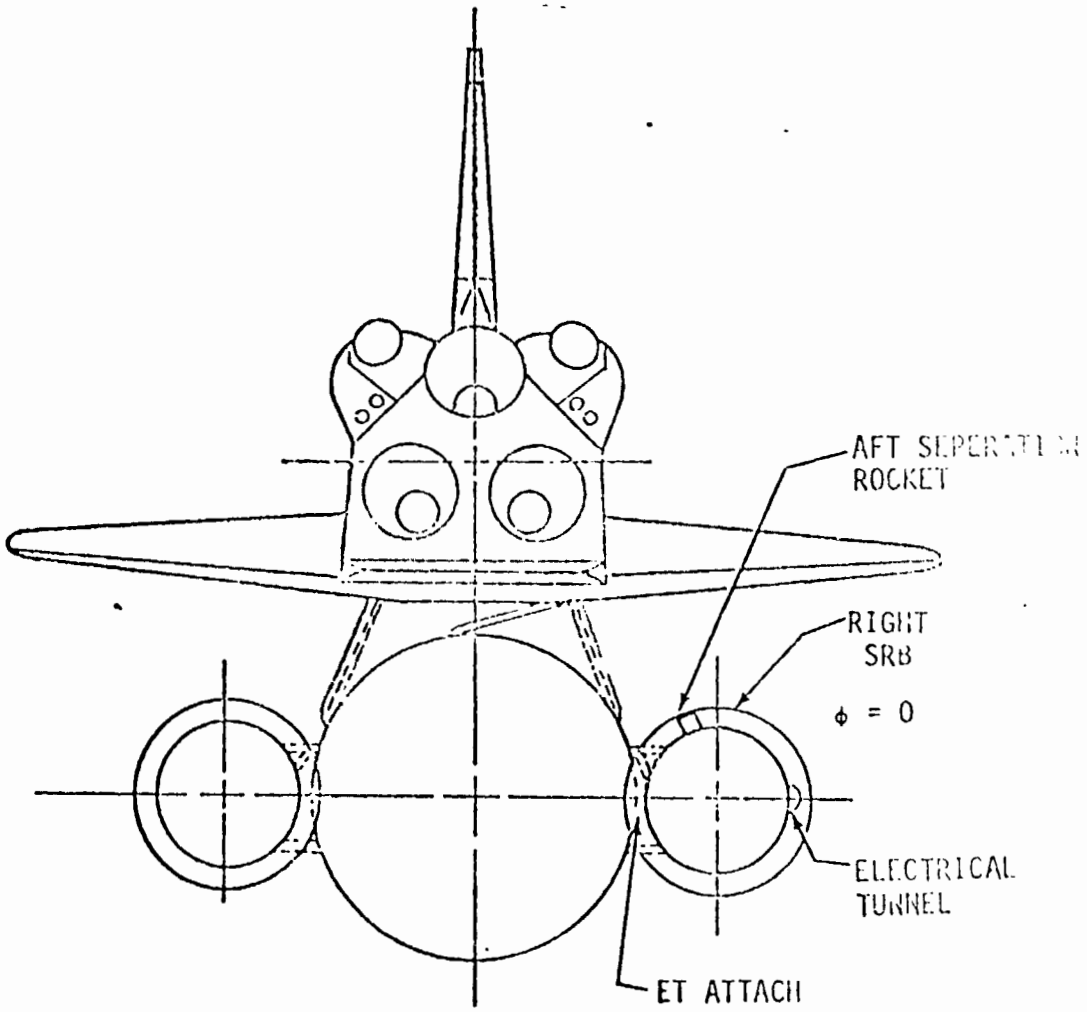

REAR VIEW

Figure 2-3. Space Shuttle Launch Configuration

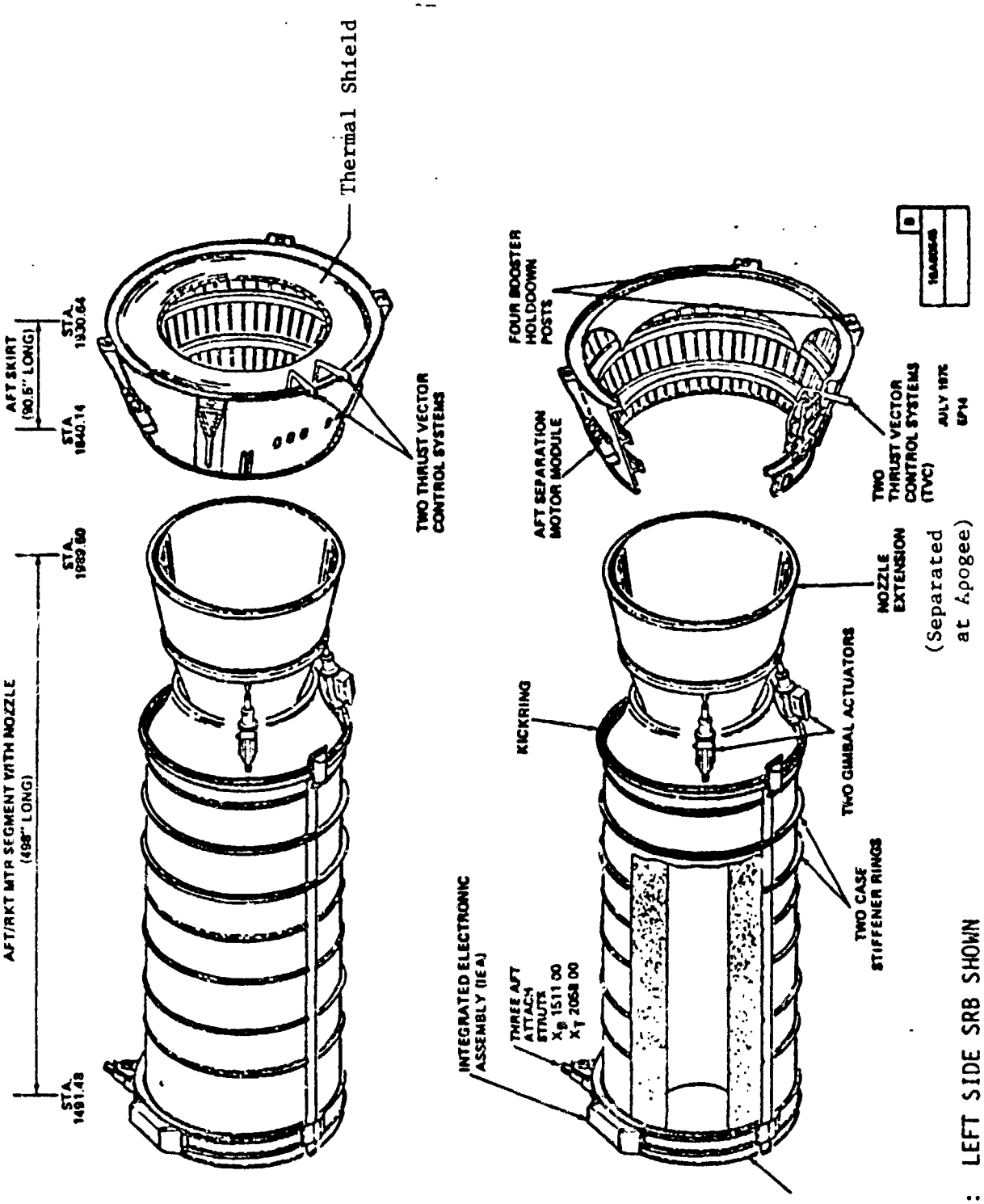

NOTE: LEFT SIDE SRB SHOWN

Figure 2-4. SRB Aft Components

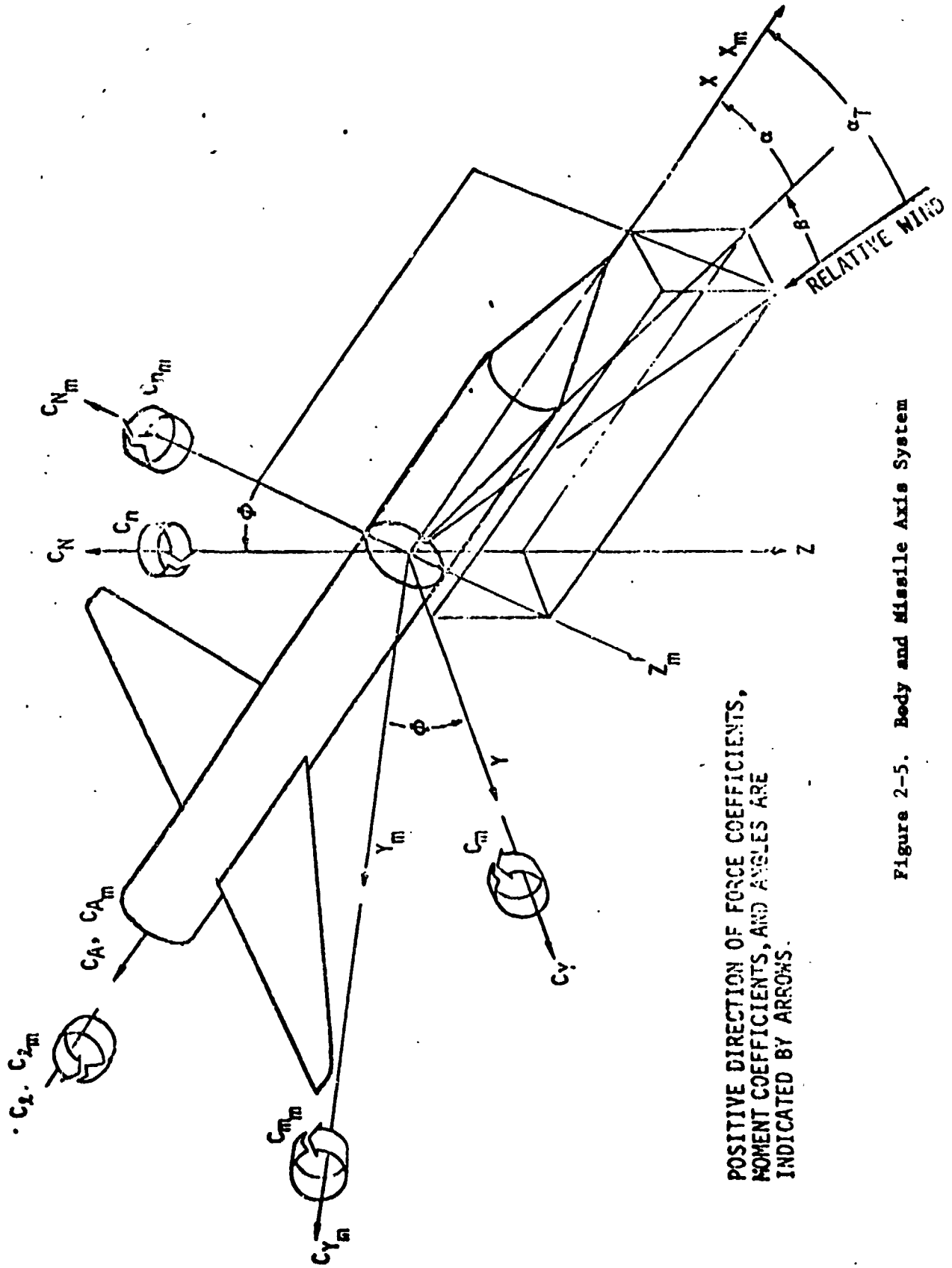

POSITIVE DIRECTION OF FORCE COEFFICIENTS, MOMENT COEFFICIENTS, AND ANGLES ARE INDICATED BY ARROWS.

Figure 2-5. Body and Missile Axis System

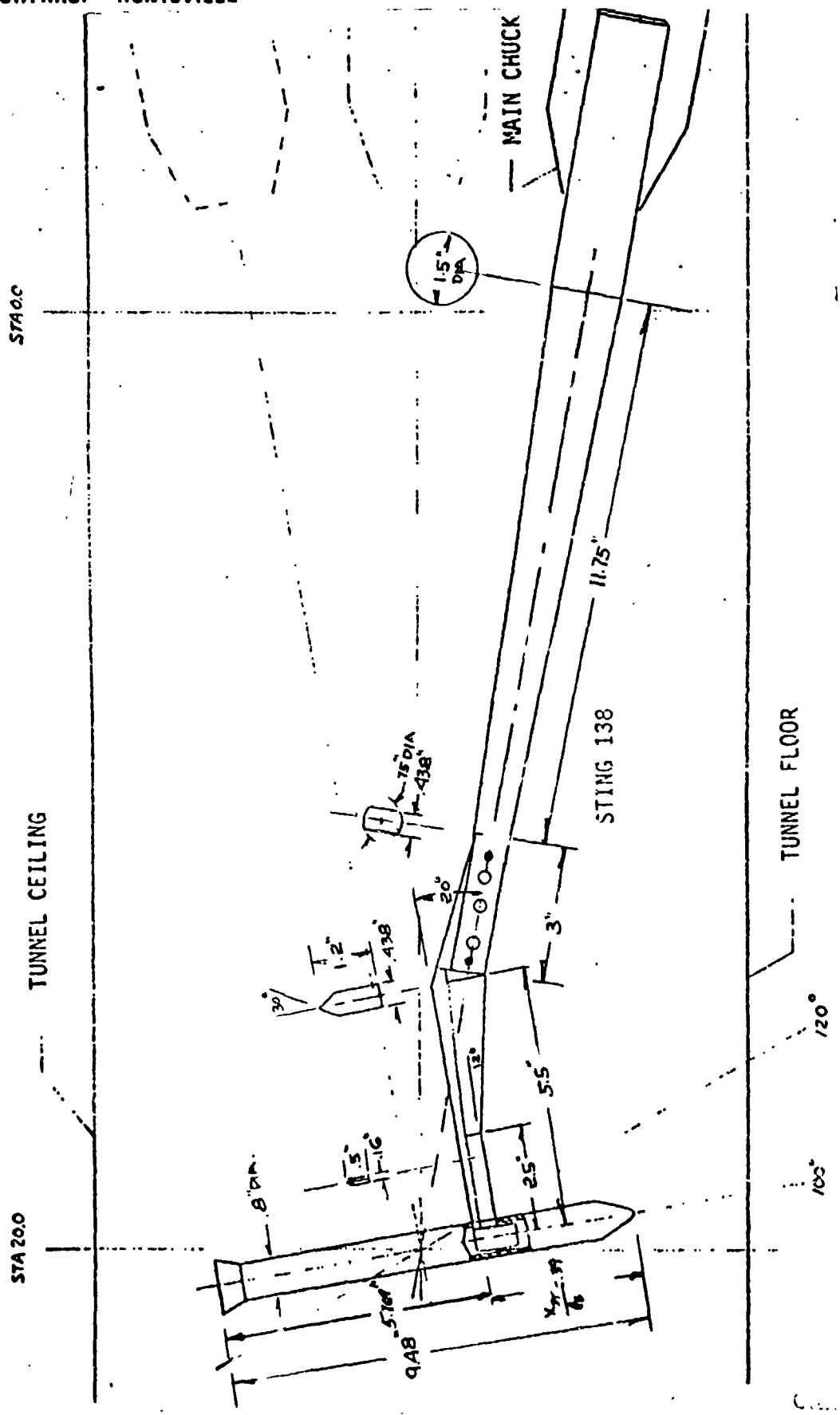

Figure 2-6. Sting Configuration MS00A, $100° \leq \alpha \leq 120°$

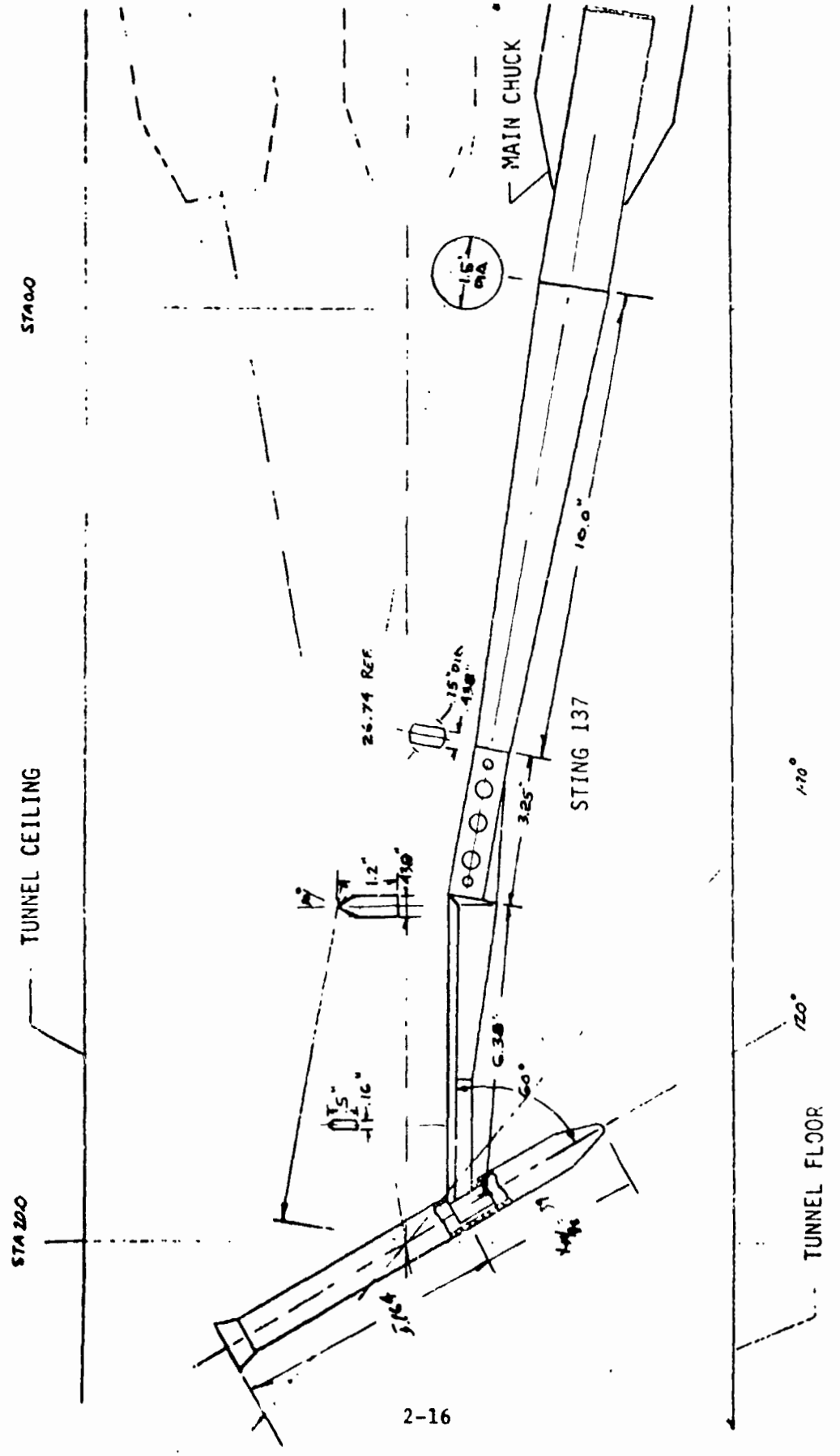

Figure 2-7. Sting Configuration MSS00B, $120° \leq \alpha \leq 140°$

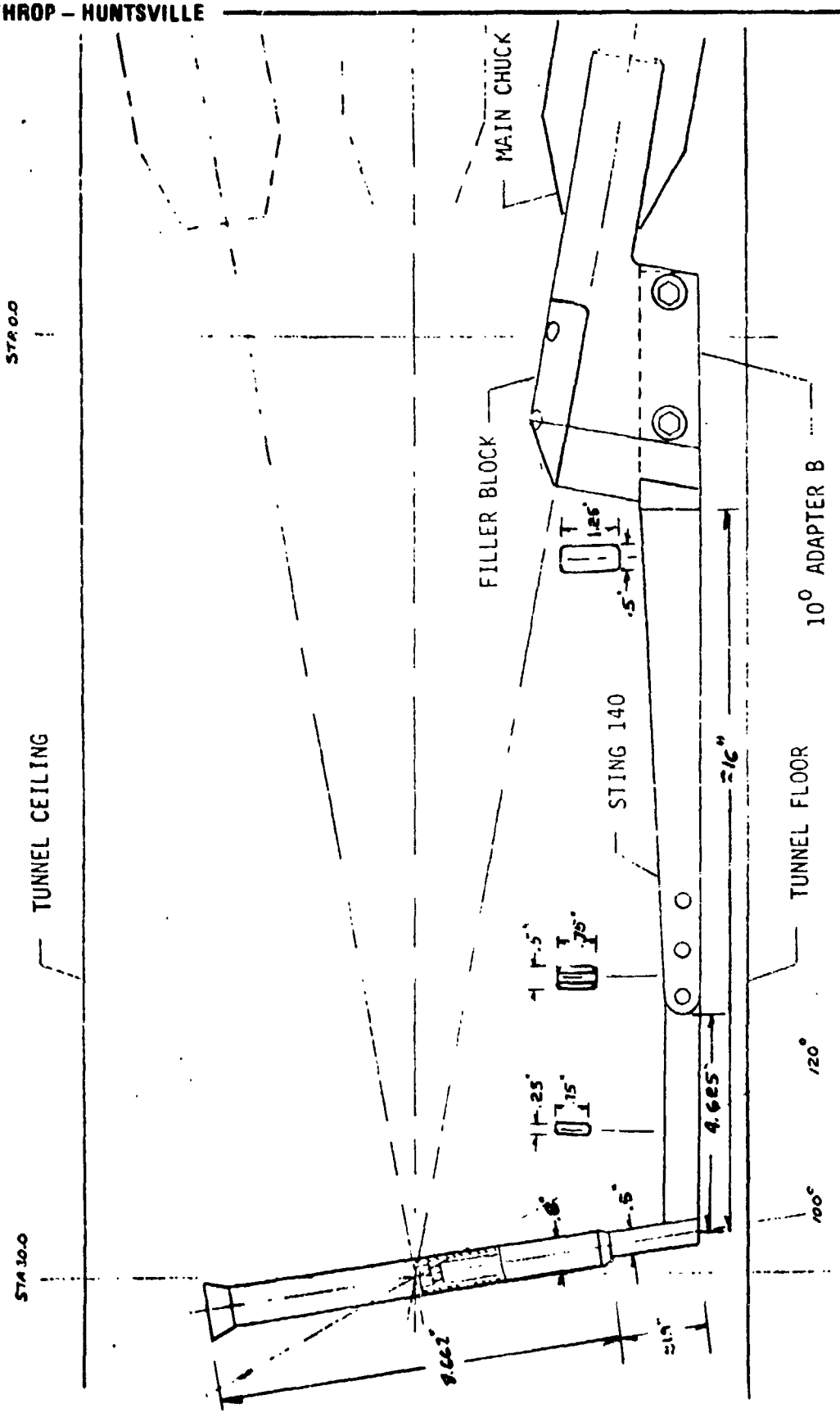

Figure 2-8. Sting Configuration MOONSA, $100° \leq \alpha \leq 120°$

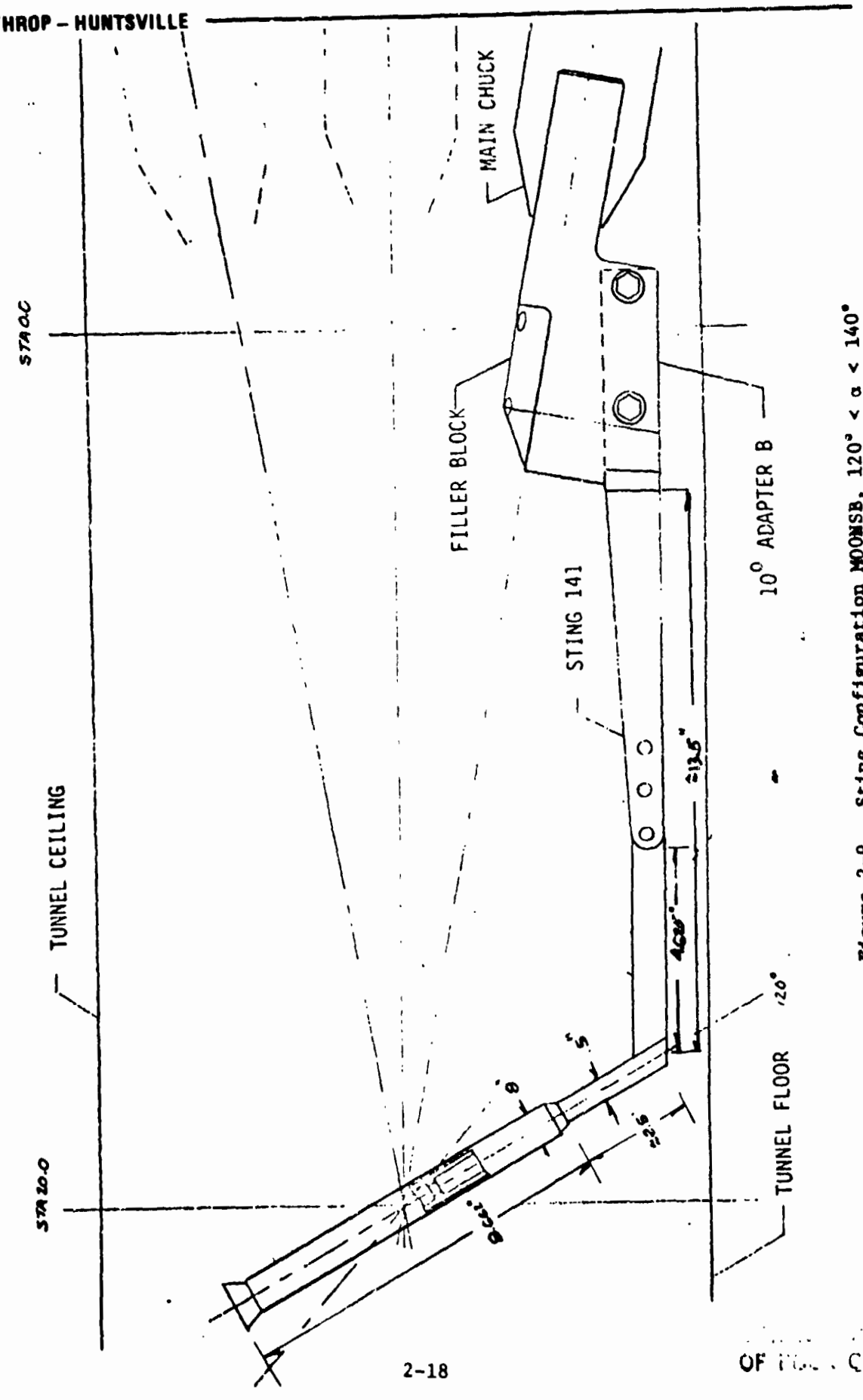

Figure 2-9. Sting Configuration MOONSB, $120^{\circ} \leq \alpha \leq 140^{\circ}$

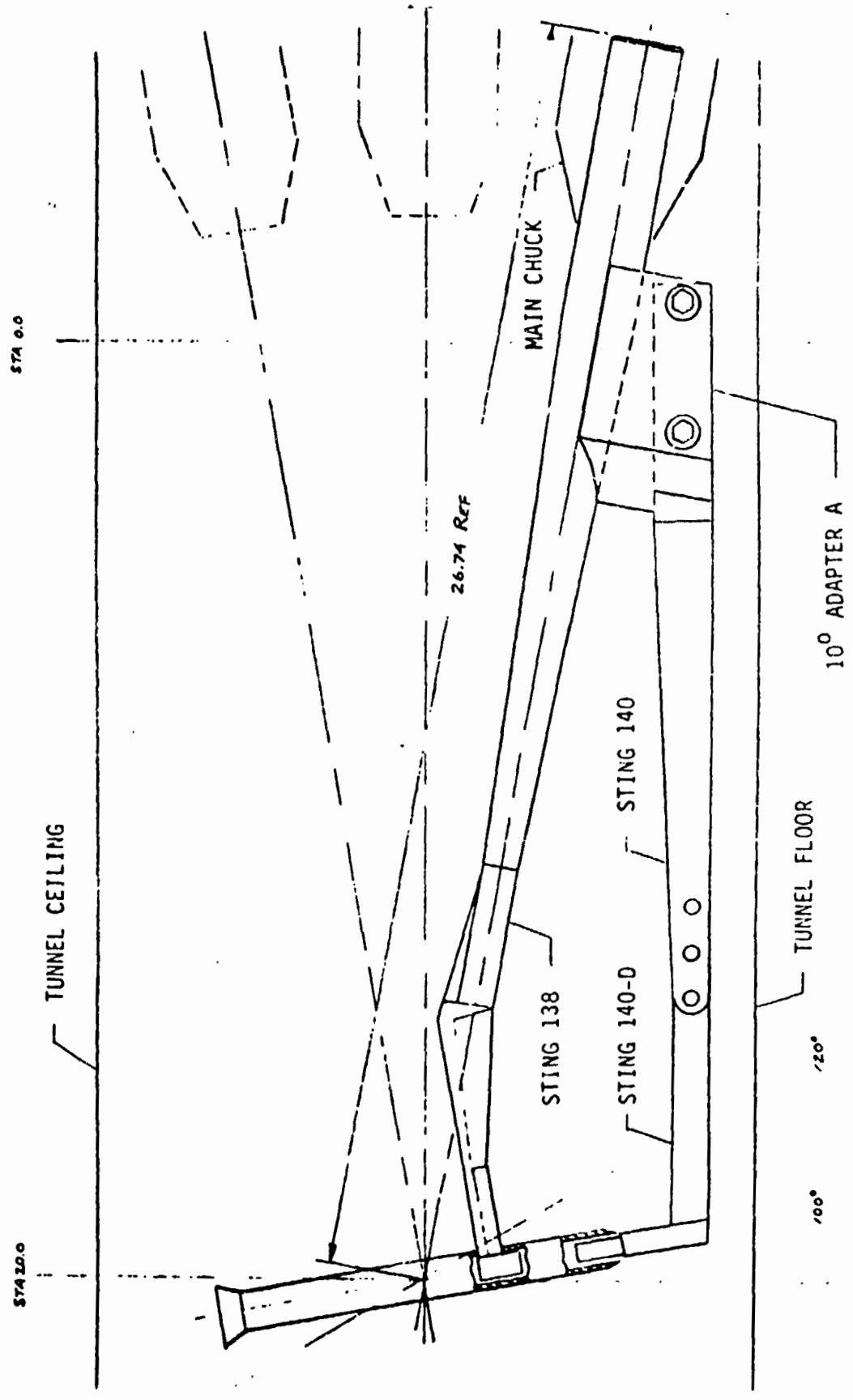

Figure 2-10. Sting Configuration MSSNDA, $100° \leq \alpha \leq 120°$

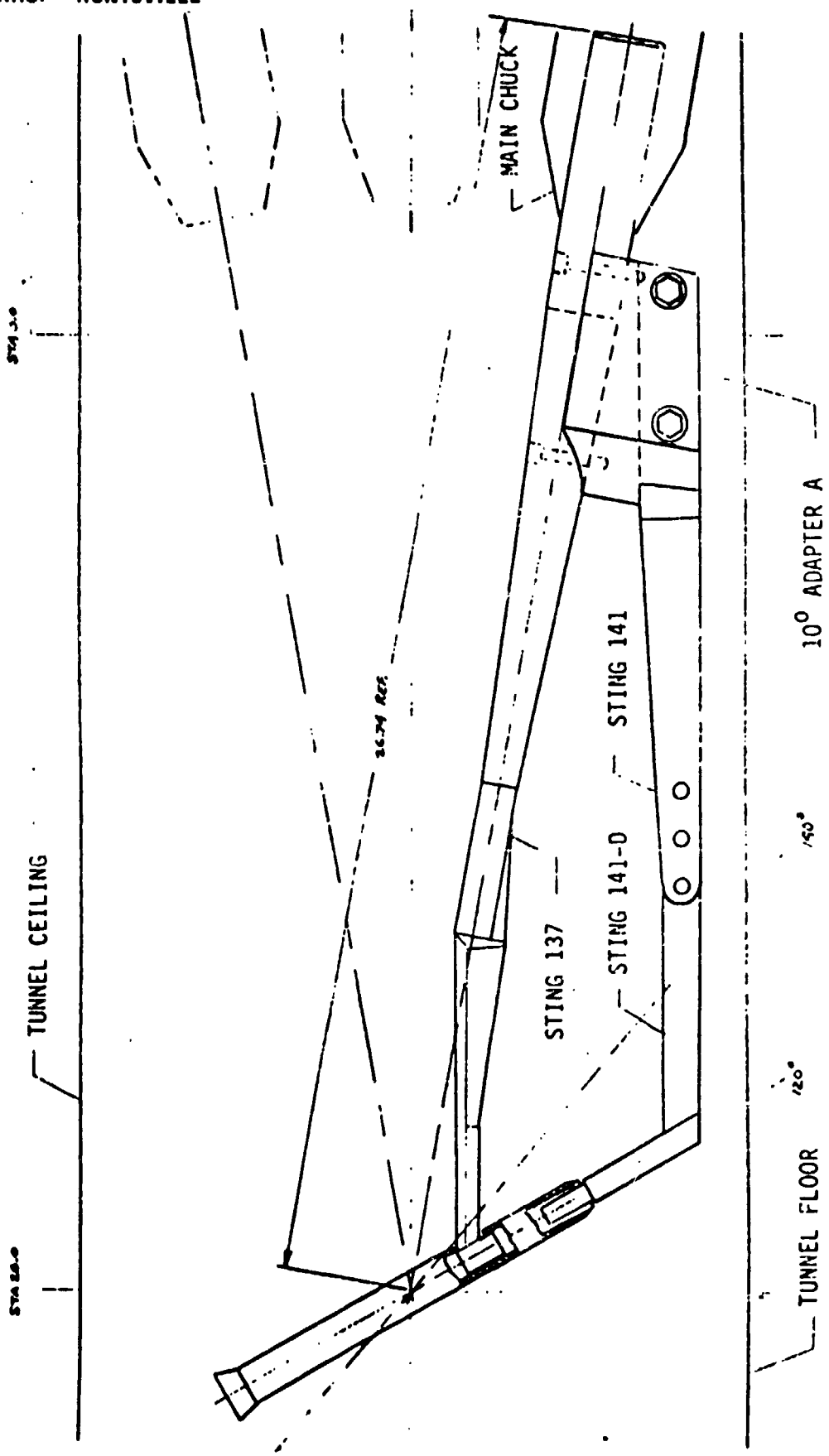

Figure 2-11. Sting Configuration MSSNDB, $120° \leq \alpha \leq 140°$

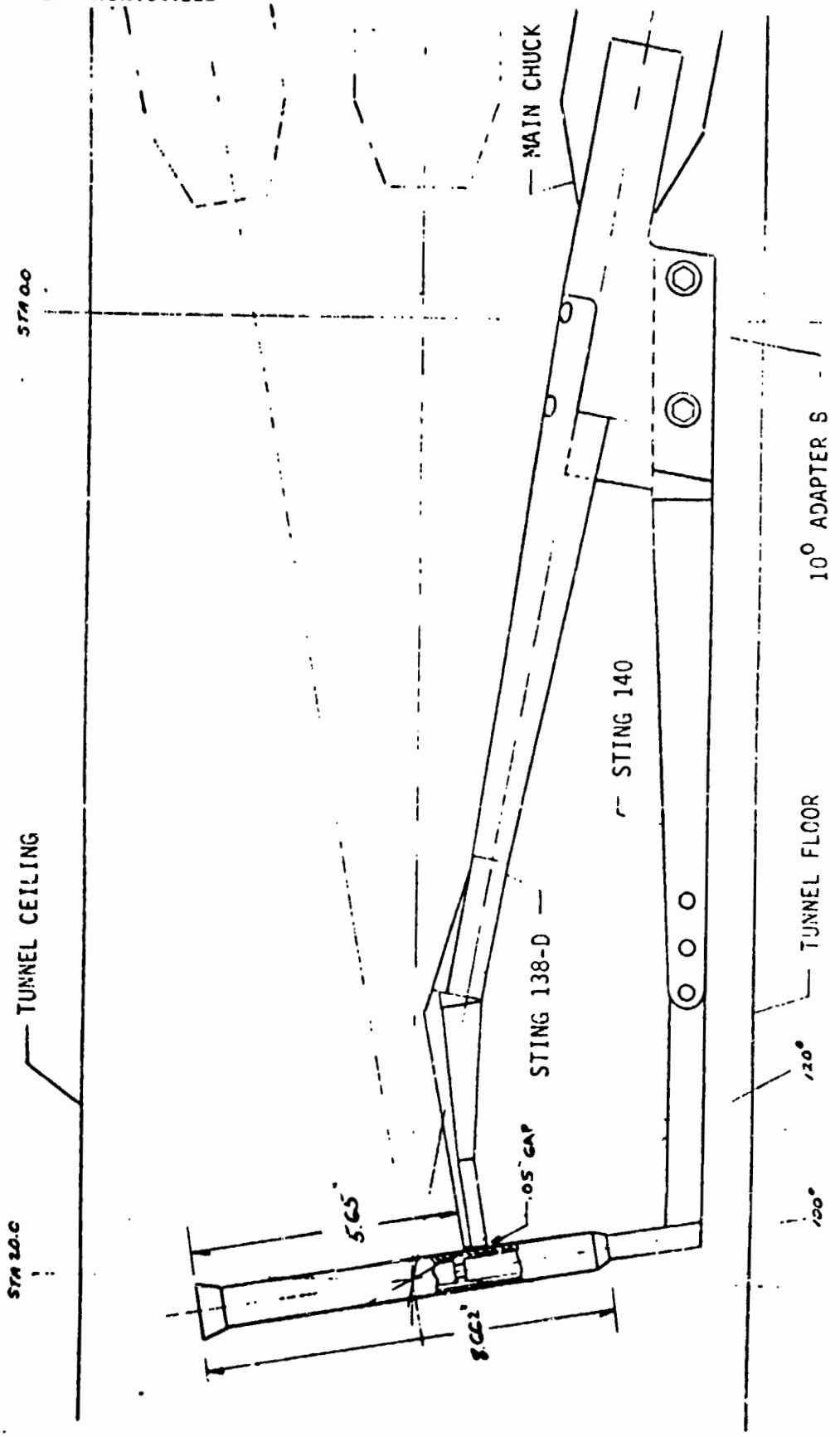

Figure 2-12. Sting Configuration MSDNSA, 100° ≤ α ≤ 120°

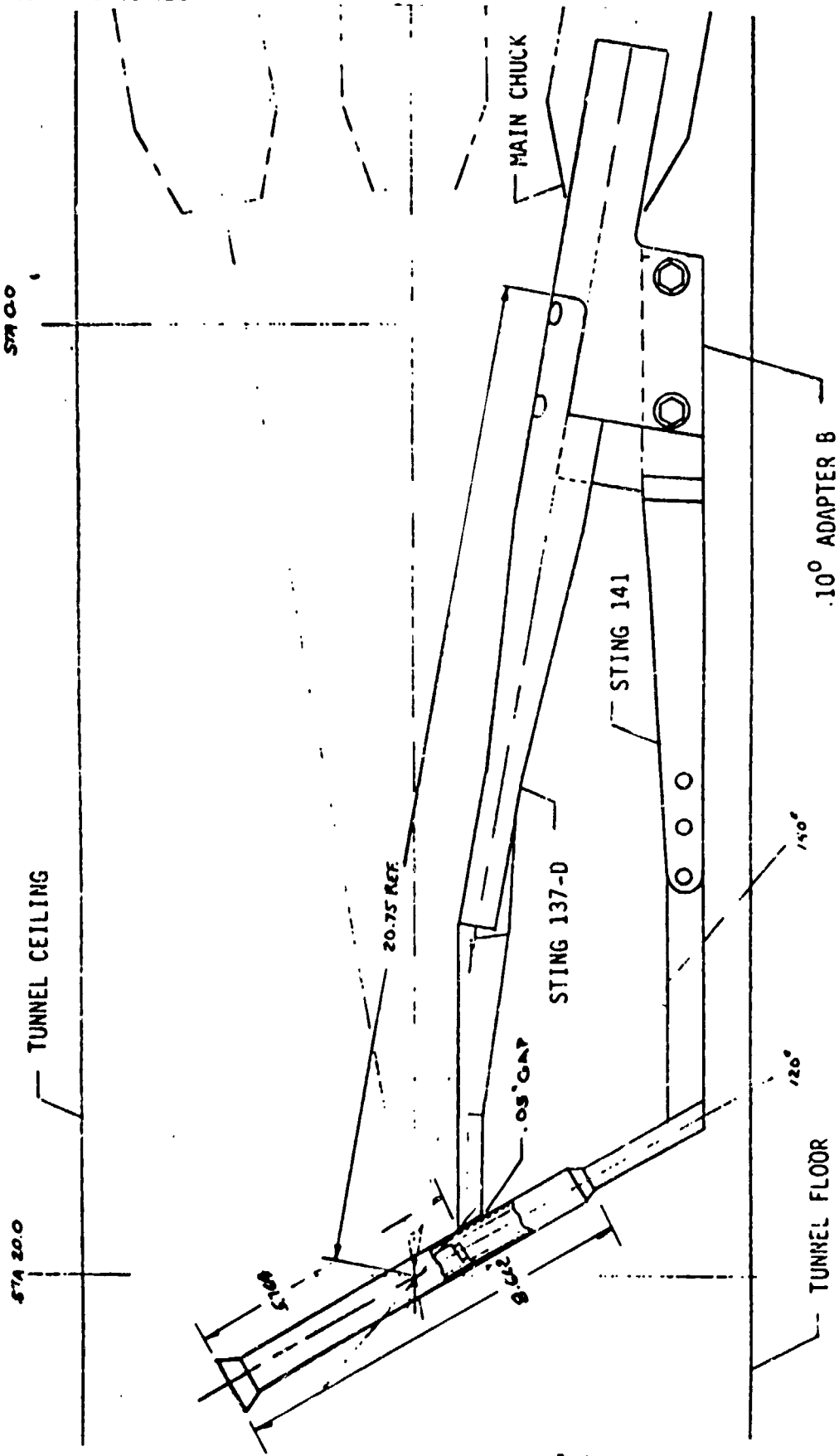

Figure 2-13. Sting Configuration MSDNSB, $120° \leq \alpha \leq 140°$

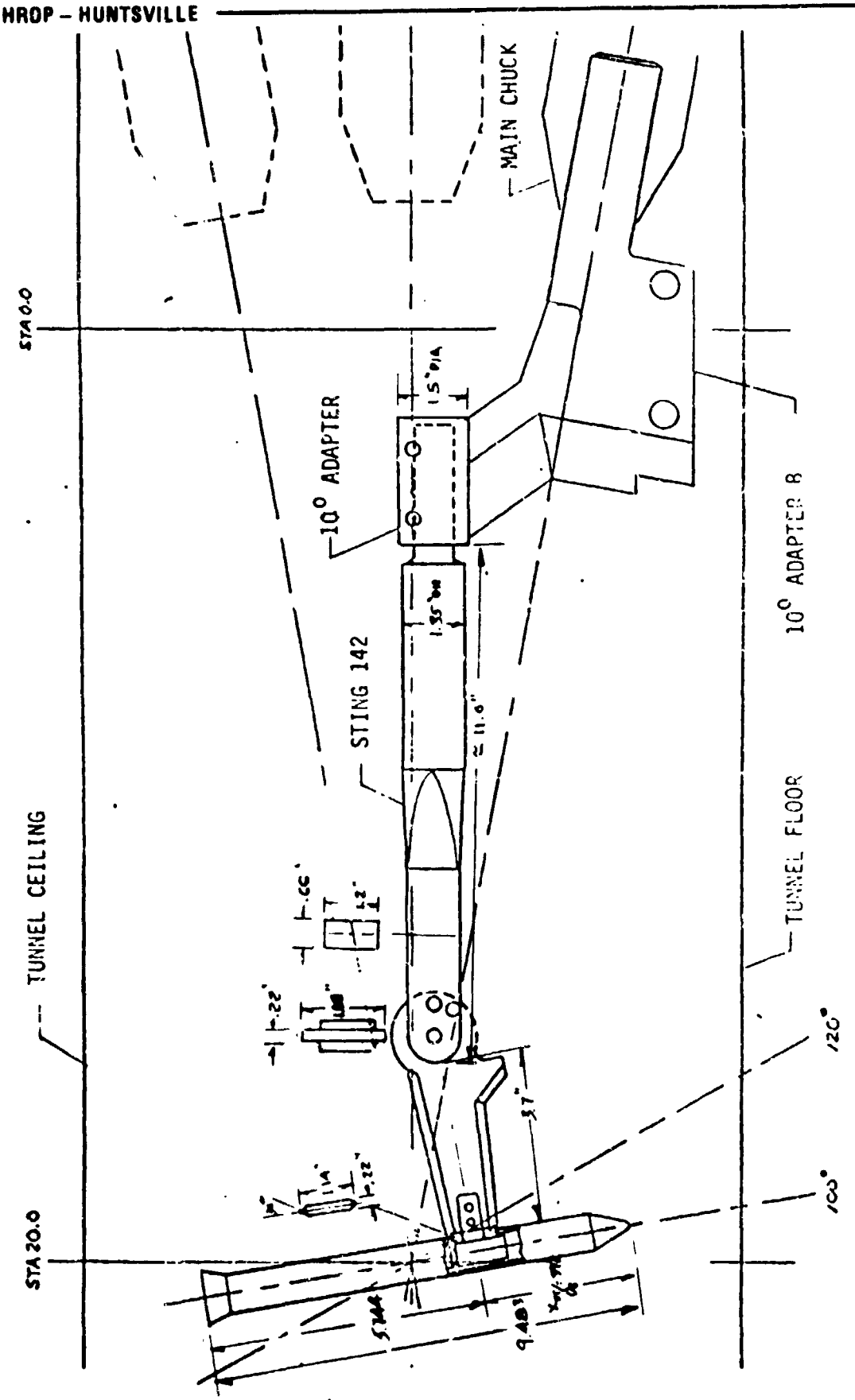

Figure 2-14. Sting Configuration ASS00A, $100° \leq \alpha \leq 120°$

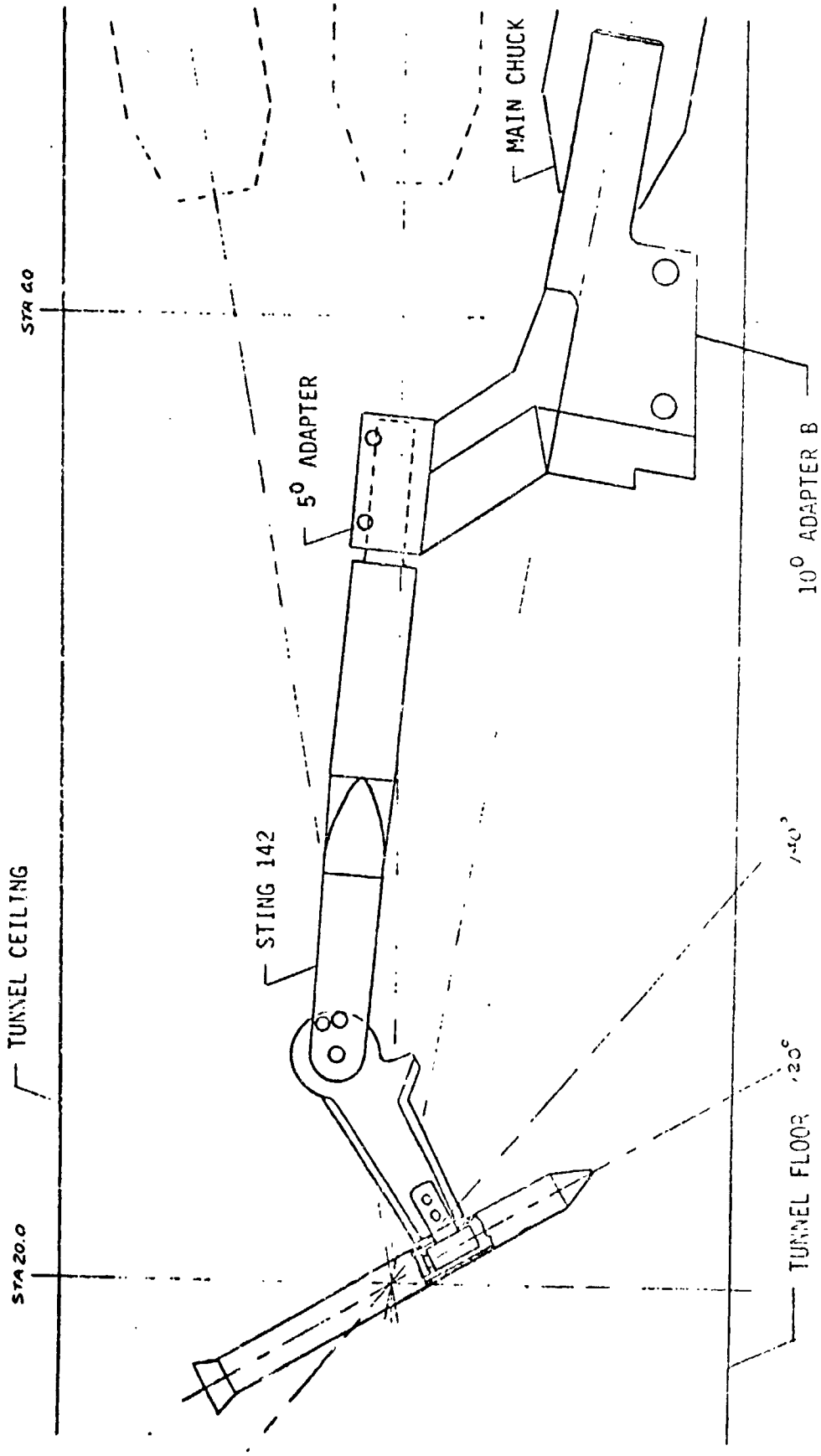

Figure 2-15. Sting Configuration ASSOOB, $120° \leq \alpha \leq 140°$

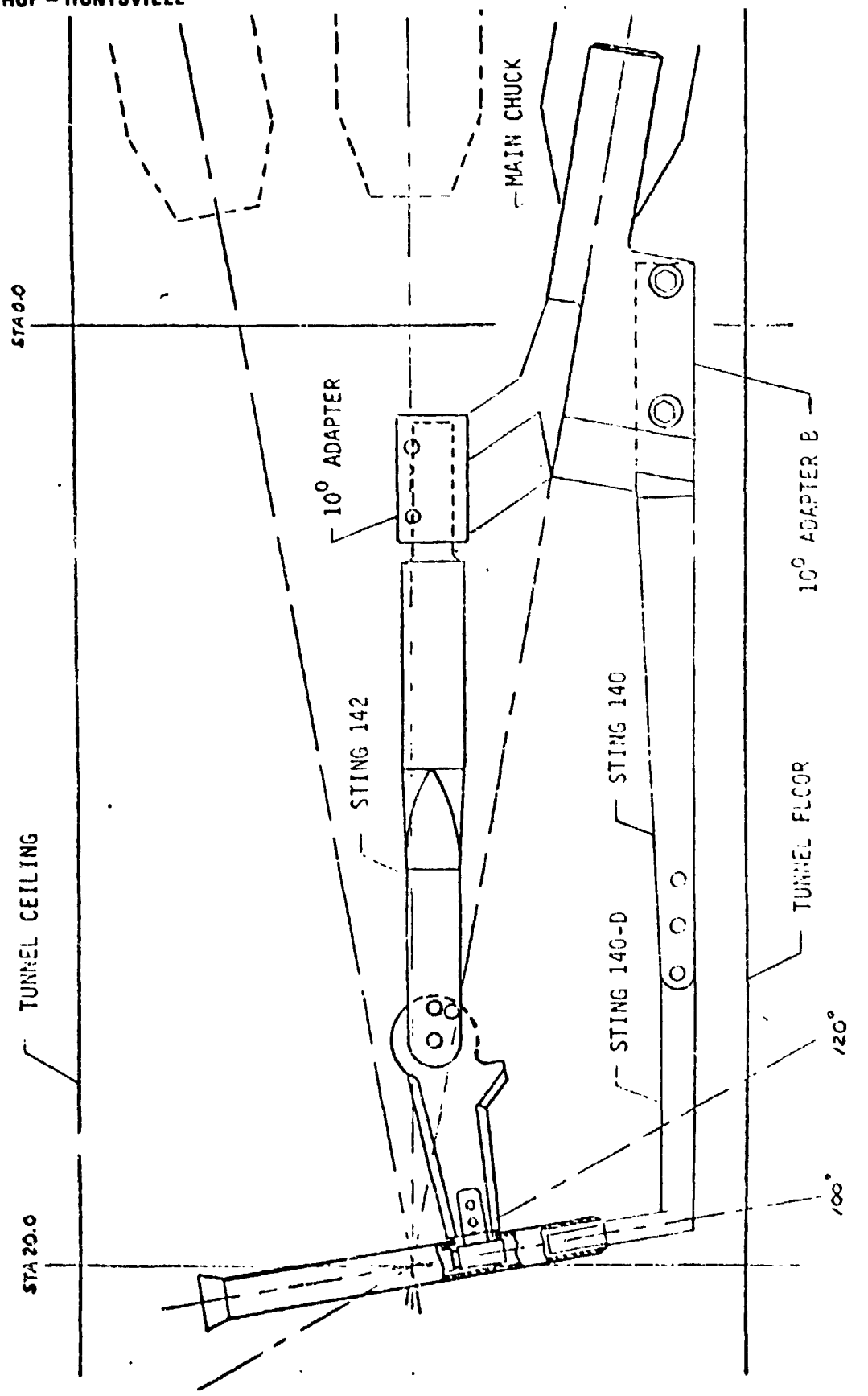

Figure 2-16. Sting Configuration ASSNDA, $100° \leq \alpha \leq 120°$

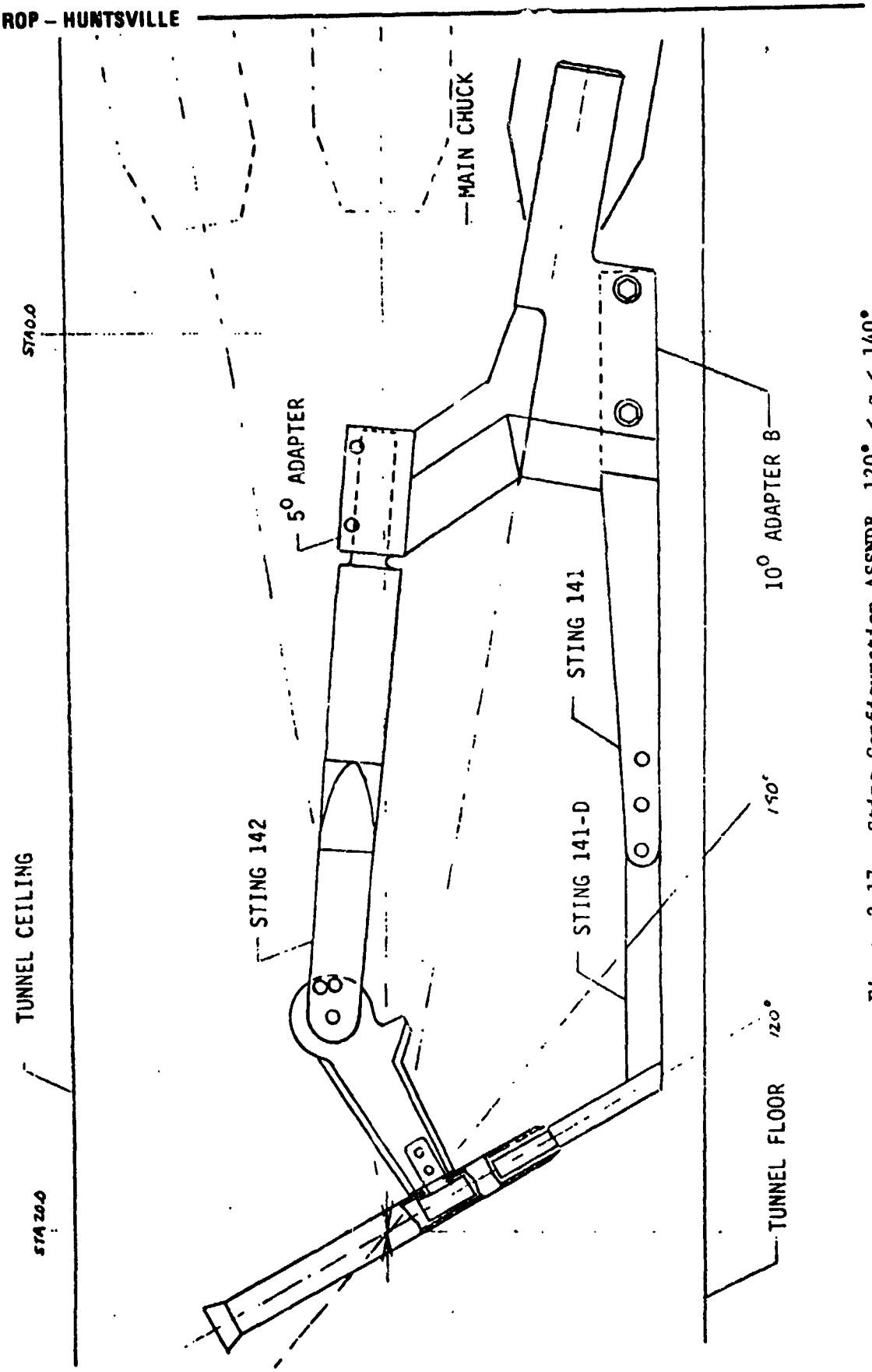

Figure 2-17. Sting Configuration ASSNDB, $120° \leq \alpha \leq 140°$

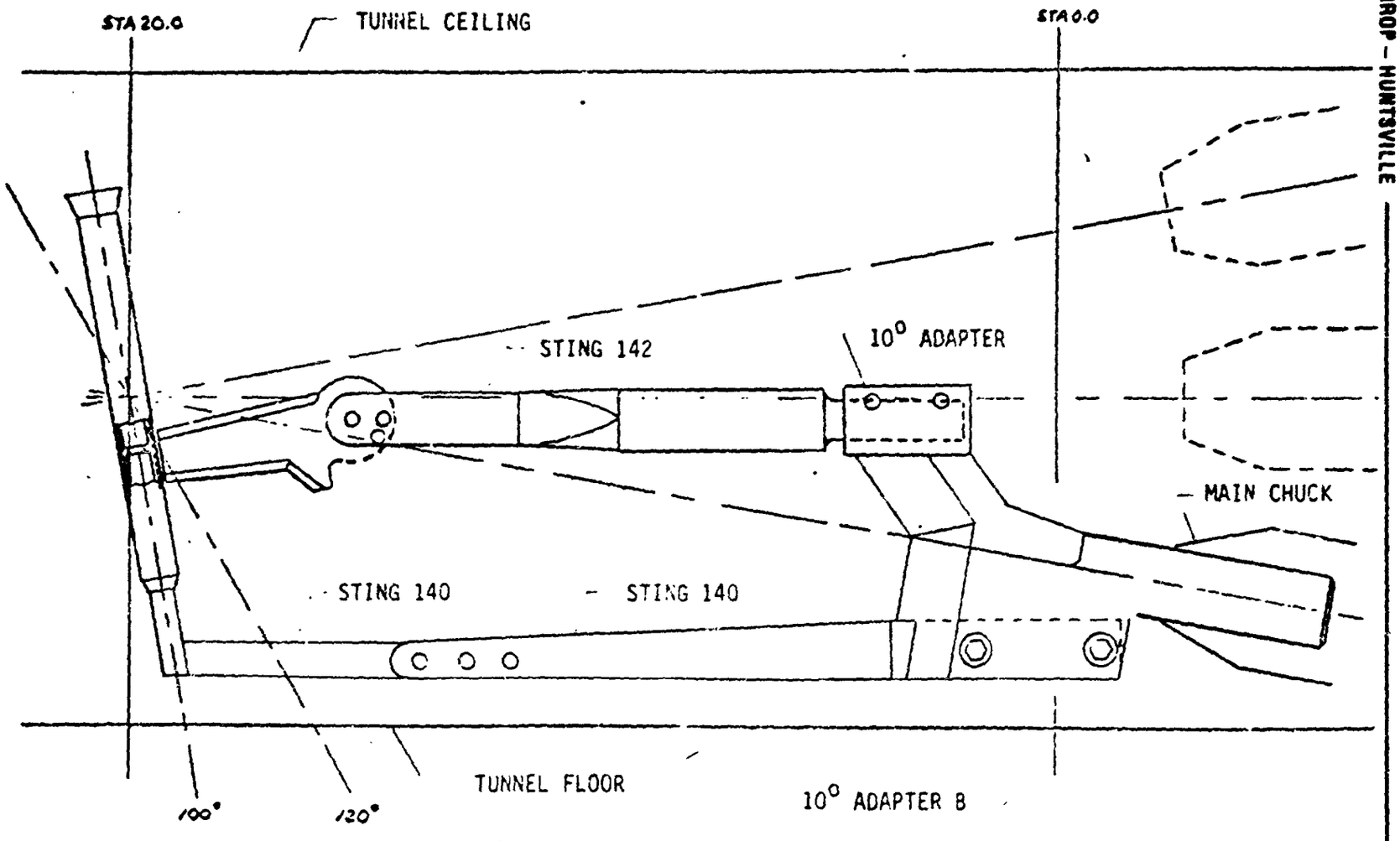

Figure 2-18. Sting Configuration ASDN6A, 100° ≤ α ≤ 120°

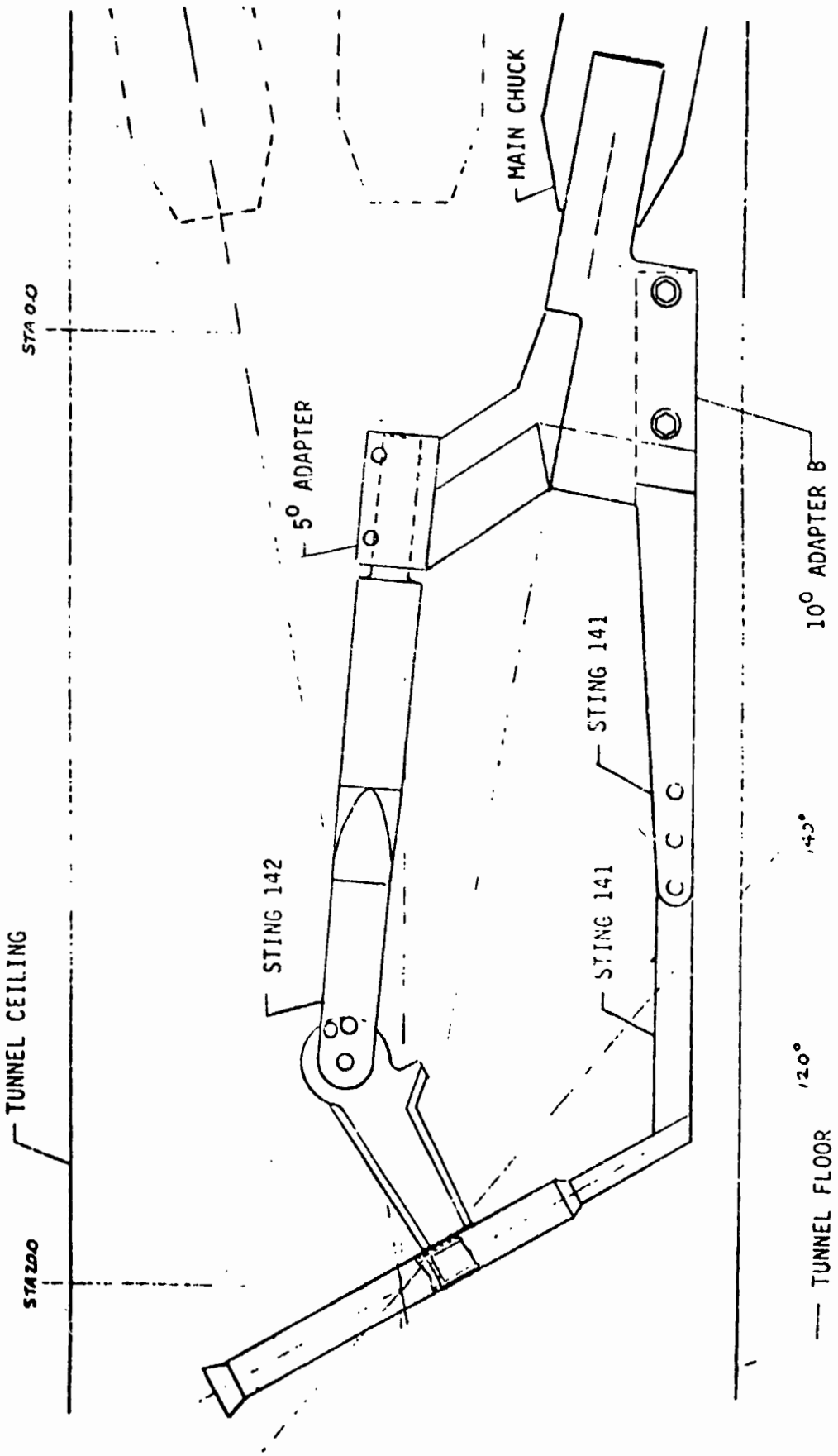

Figure 2-19. Sting Configuration ASDNSB, 120° ≤ α ≤ 140°

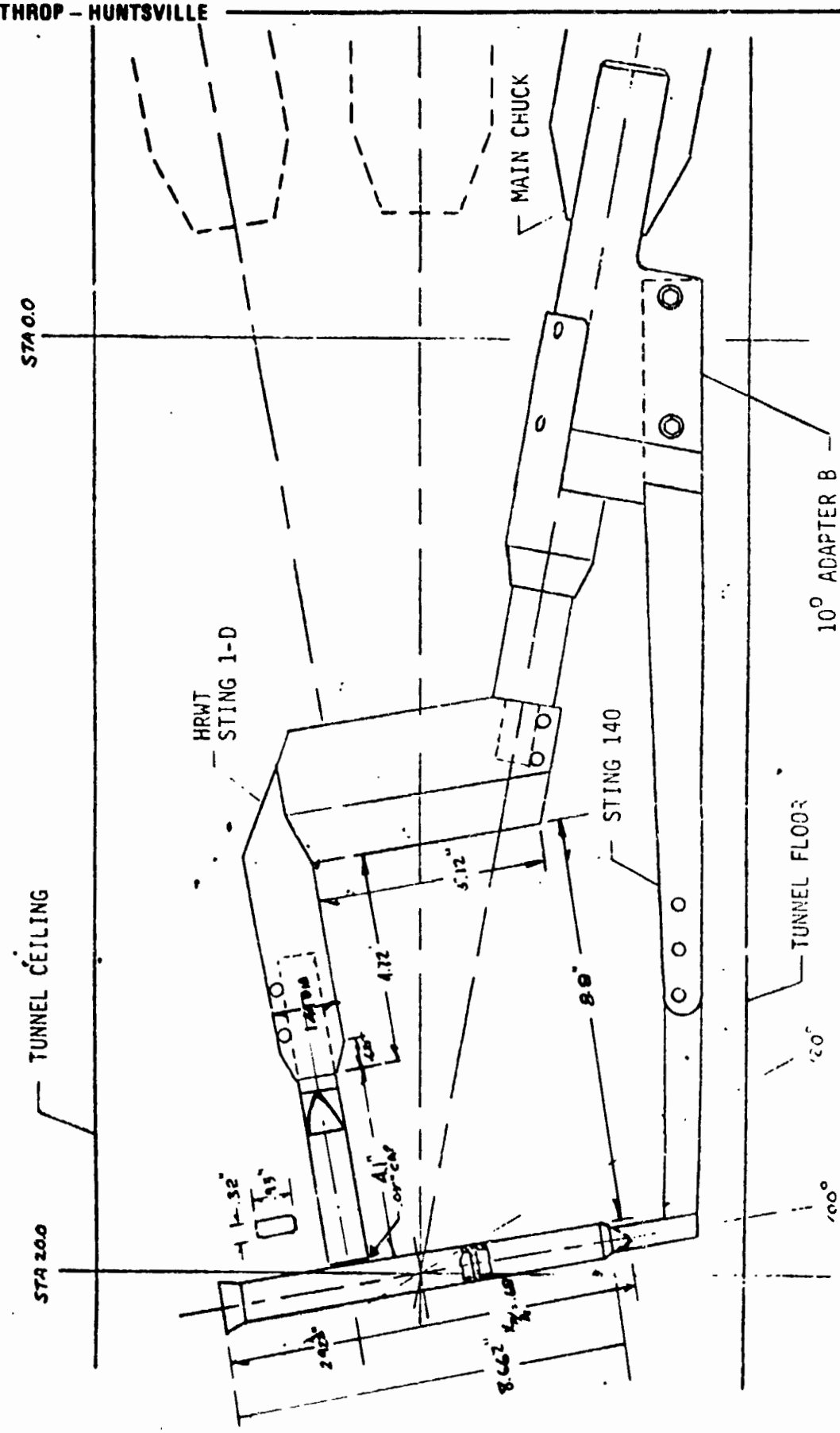

Figure 2-20. Sting Configuration HSDNSA, 100° ≤ α ≤ 120°

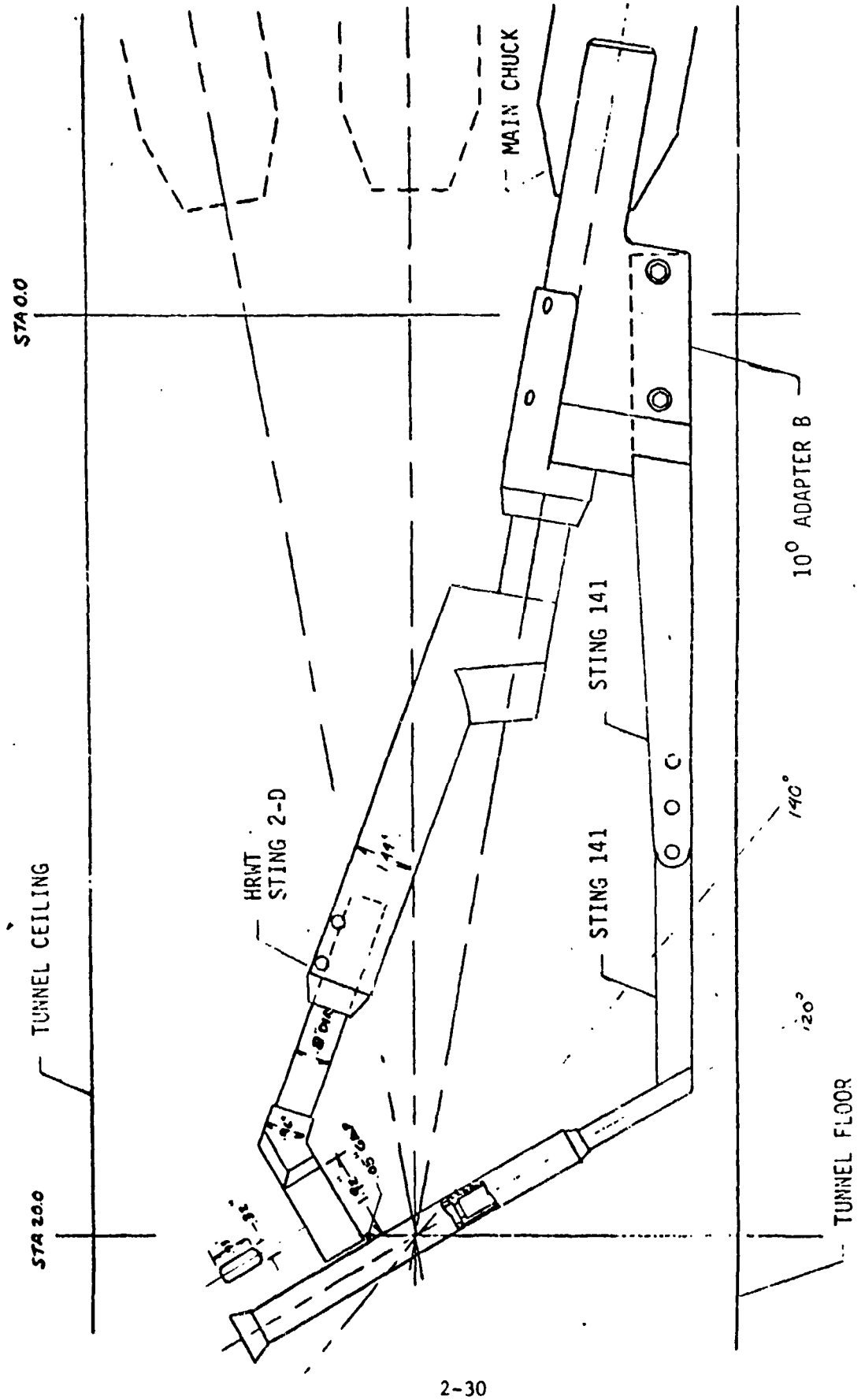

Figure 2-21. Sting Configuration HSDNSB, $120° \leq \alpha \leq 140°$

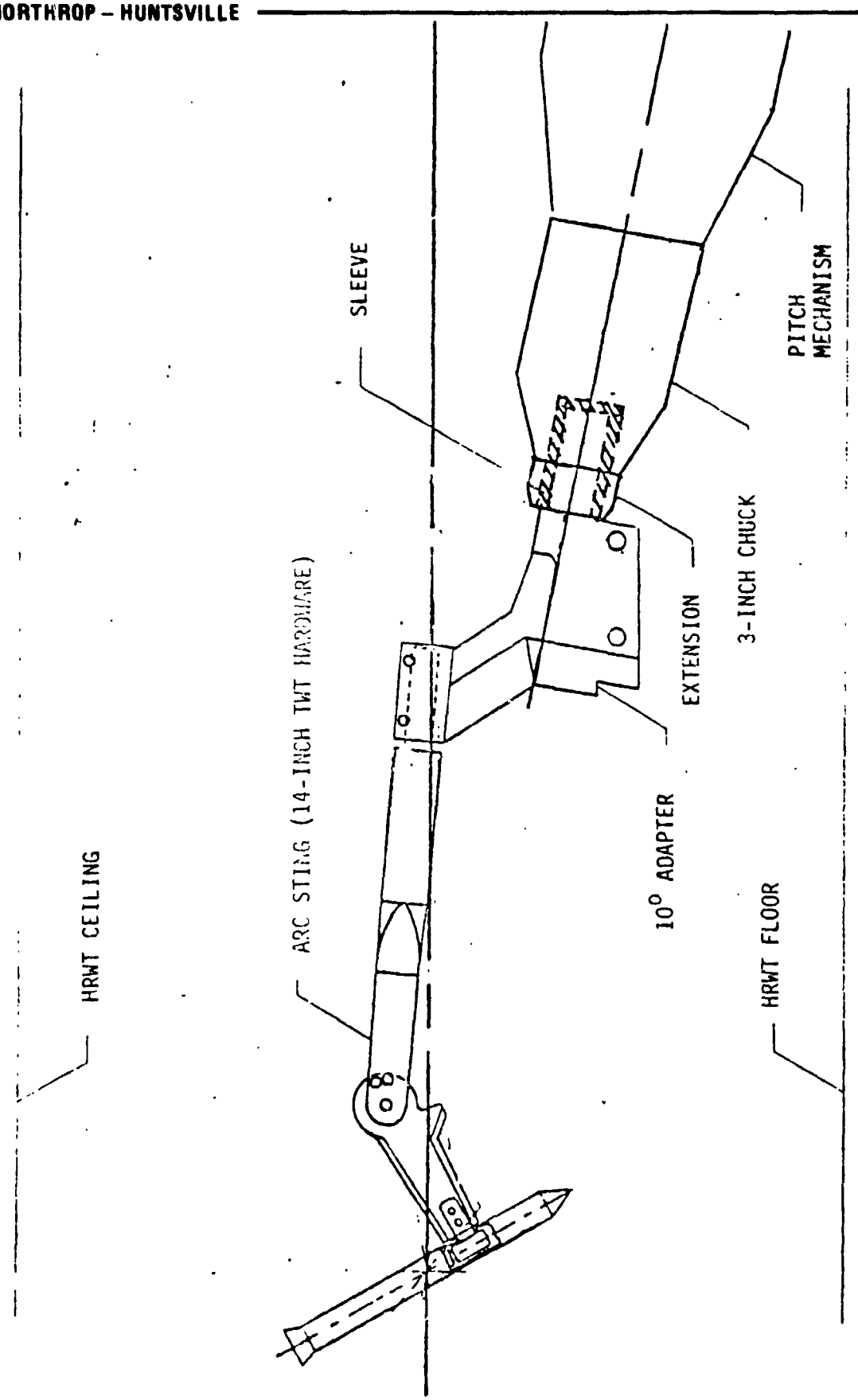

Figure 2-22. Sting Configuration ASS00B HRWT 042

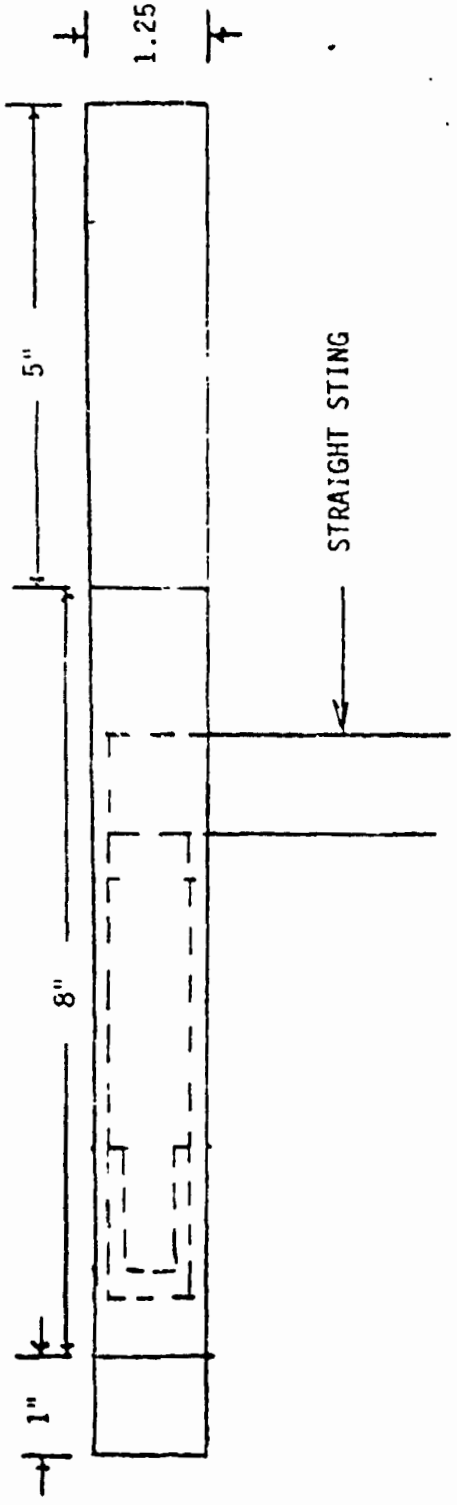

(a) SYMMETRIC CYLINDER CONFIGURATION

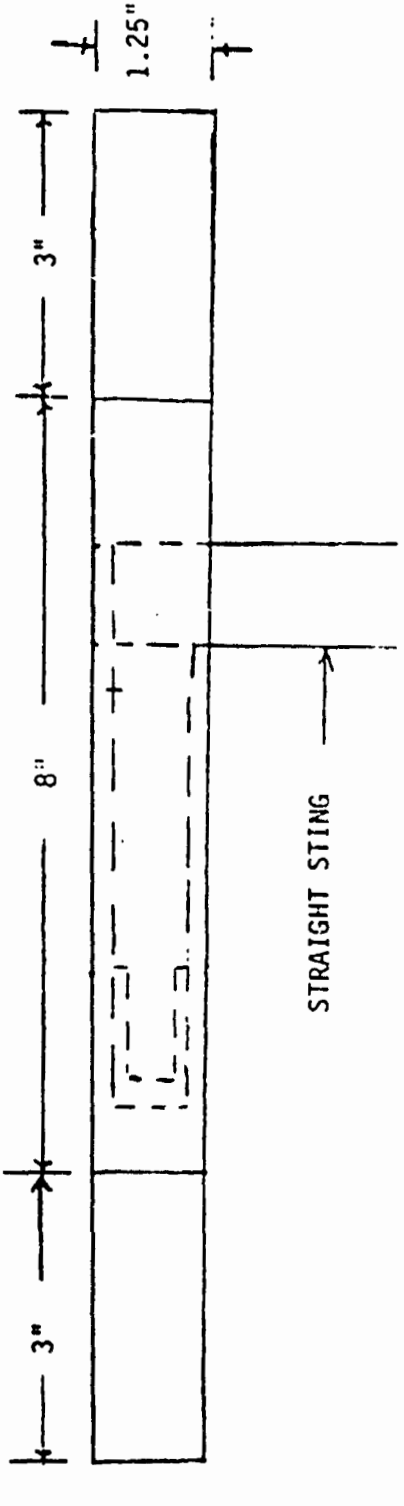

(b) ASYMMETRIC CYLINDER CONFIGURATION

Figure 2-23. Cylinder Model HRWT 042

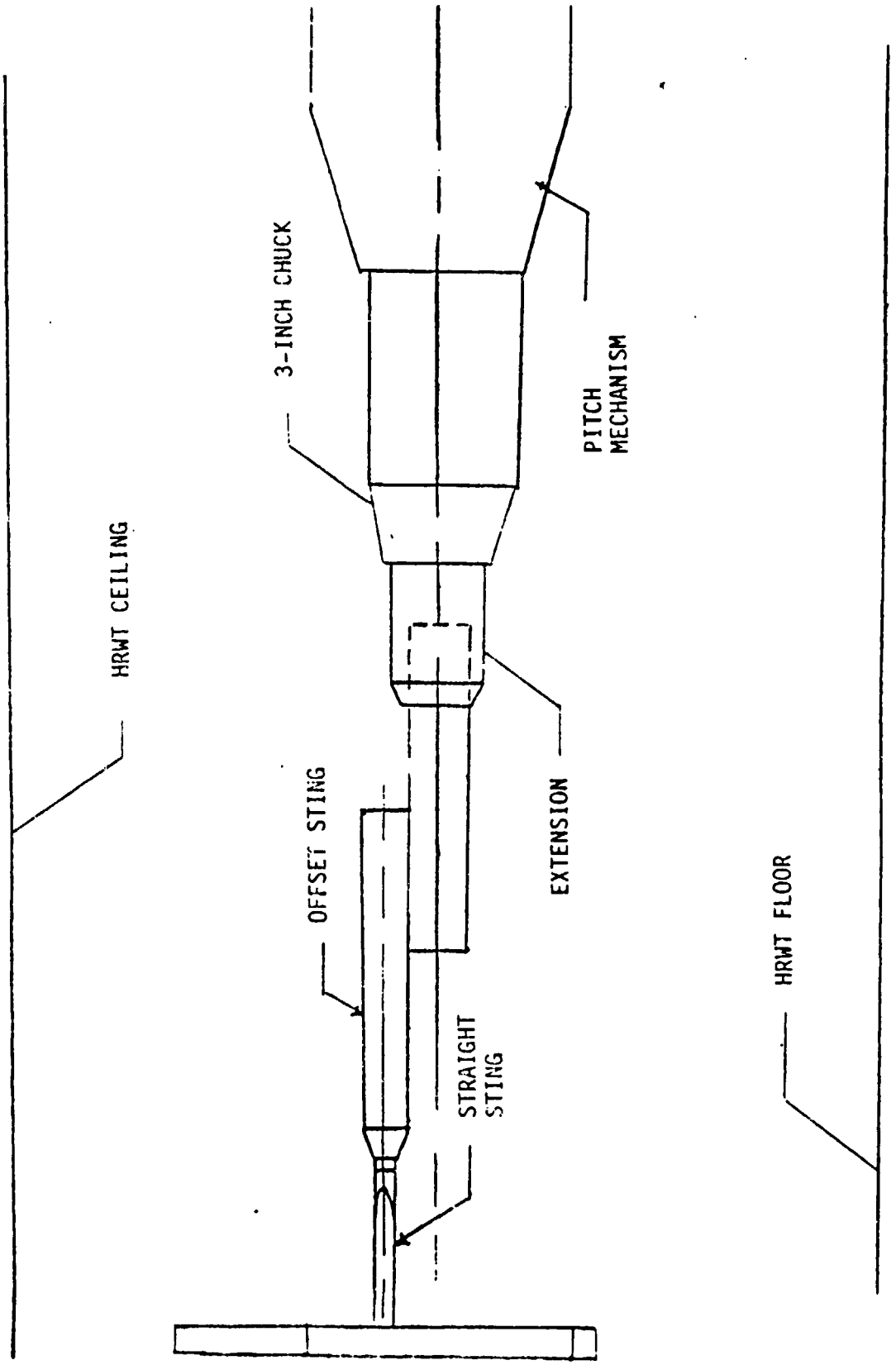

Figure 2-24. Sting Configuration for Symmetric Cylinder

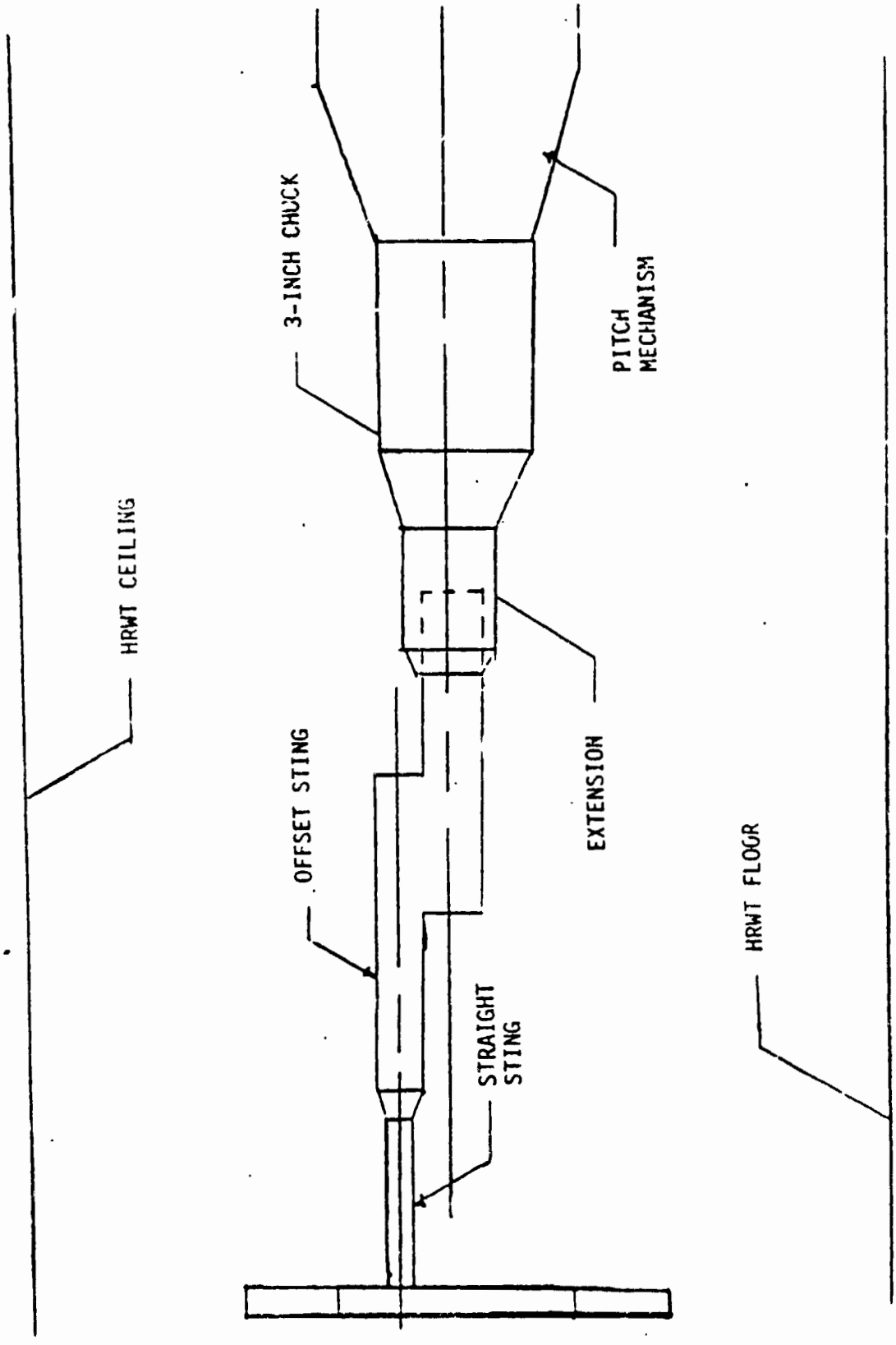

Figure 2-25. Sting Configuration for Assymmetric Cylinder

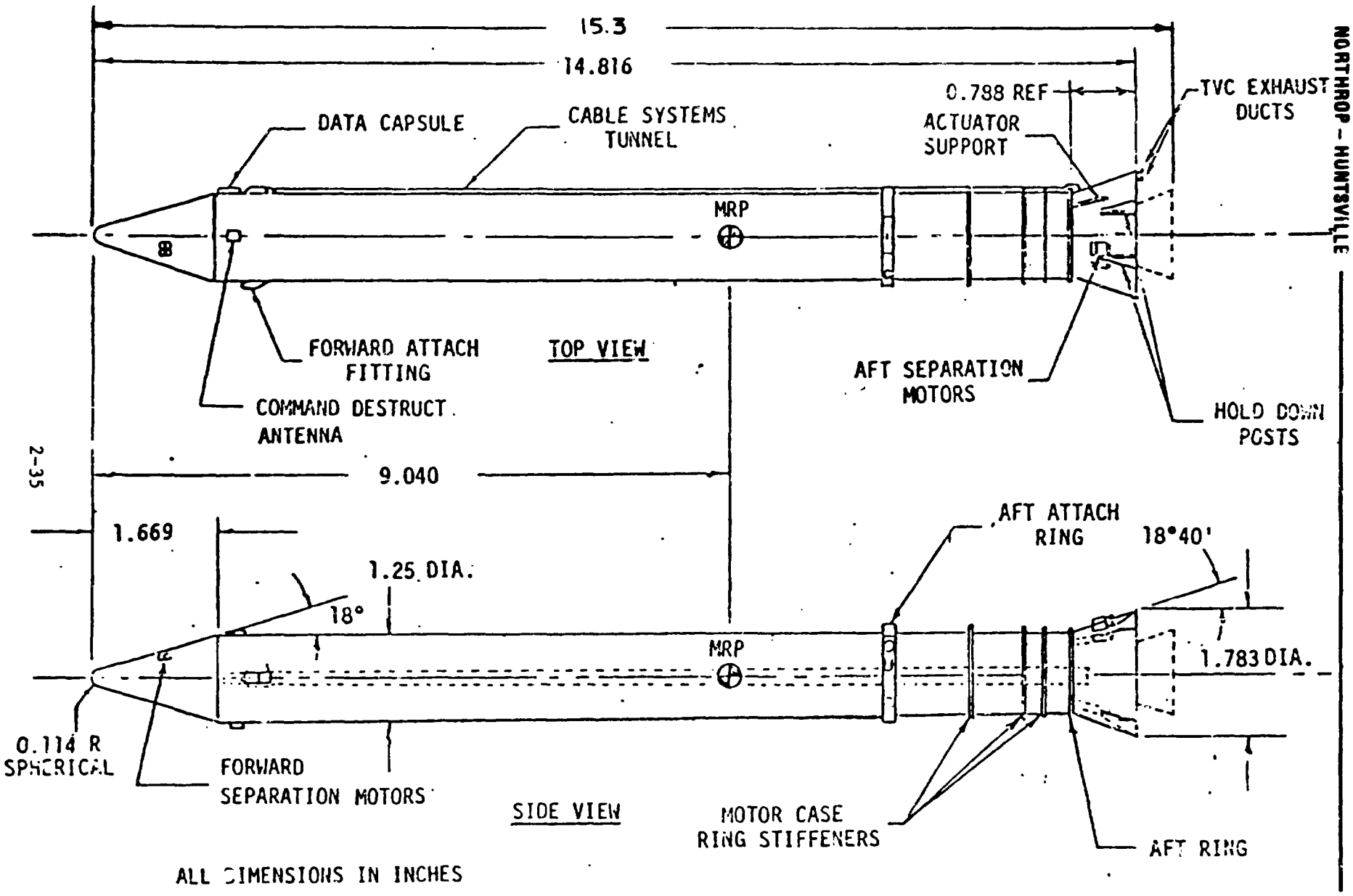

Figure 2-26. General SRB Model Arrangement HRWT 042

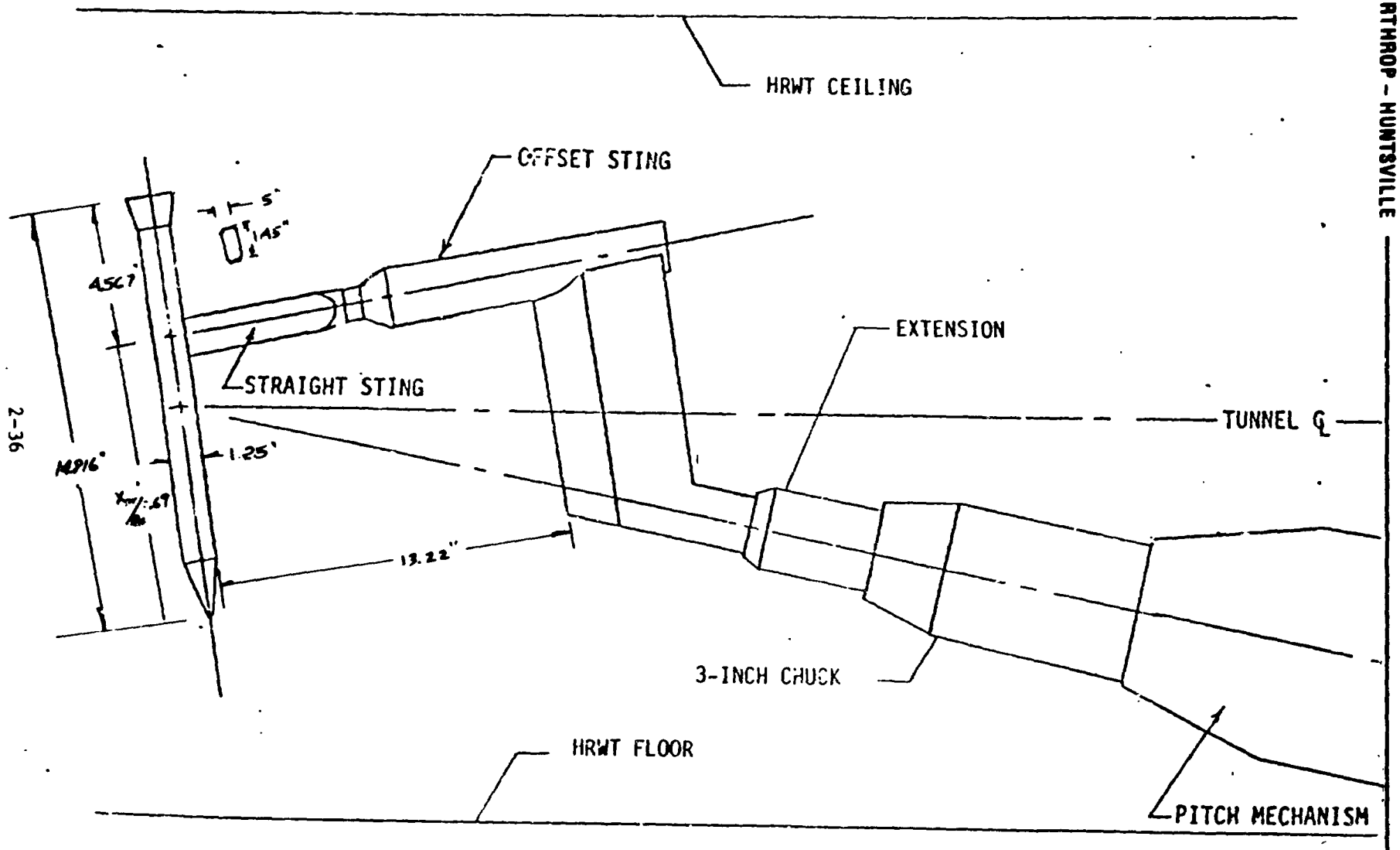

Figure 2-27. Sting Configuration HSS00A, 100° ≤ 120° HRWT 042

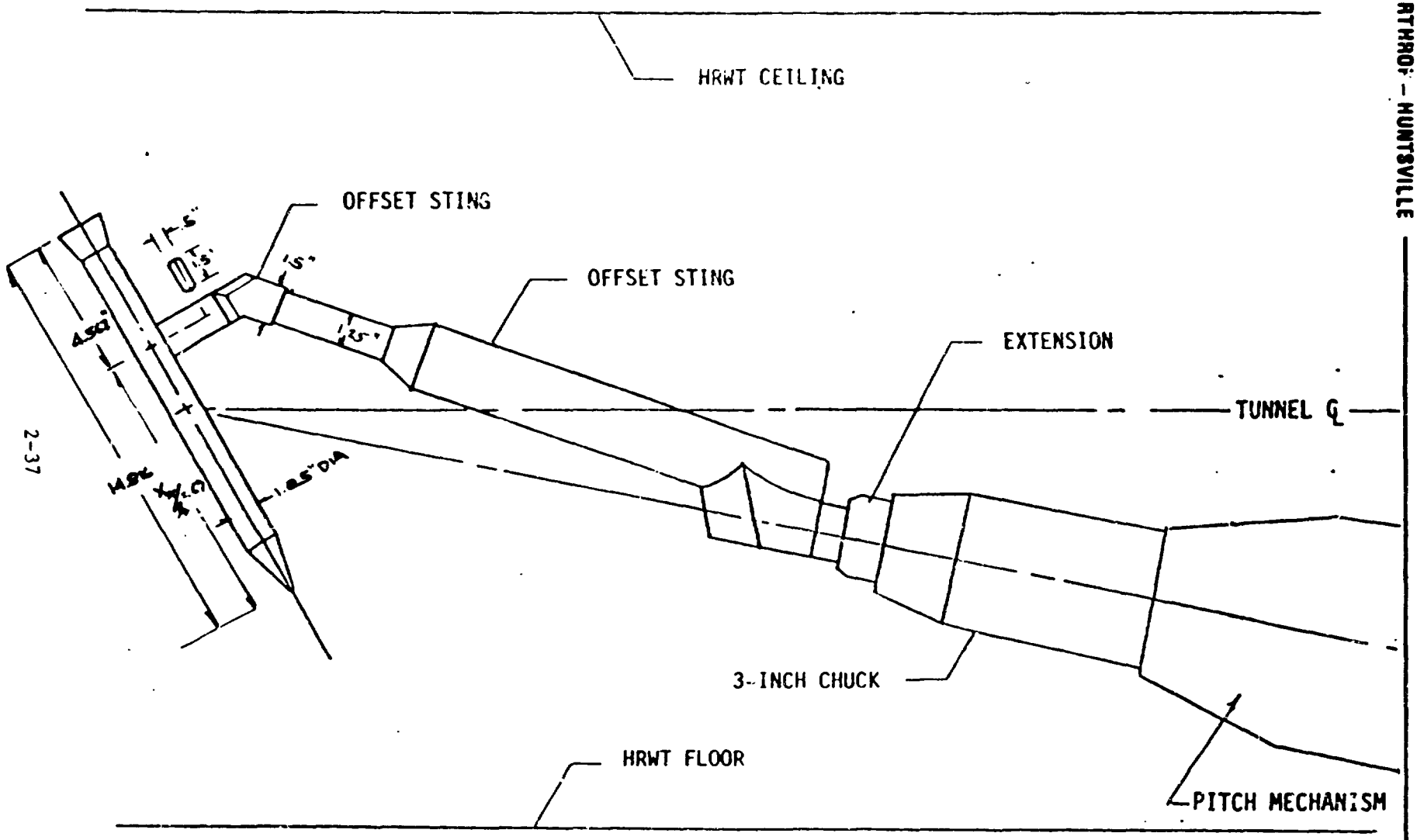

Figure 2-28. Sting Configuration HSS00B, 120° ≤ 140° HRWT

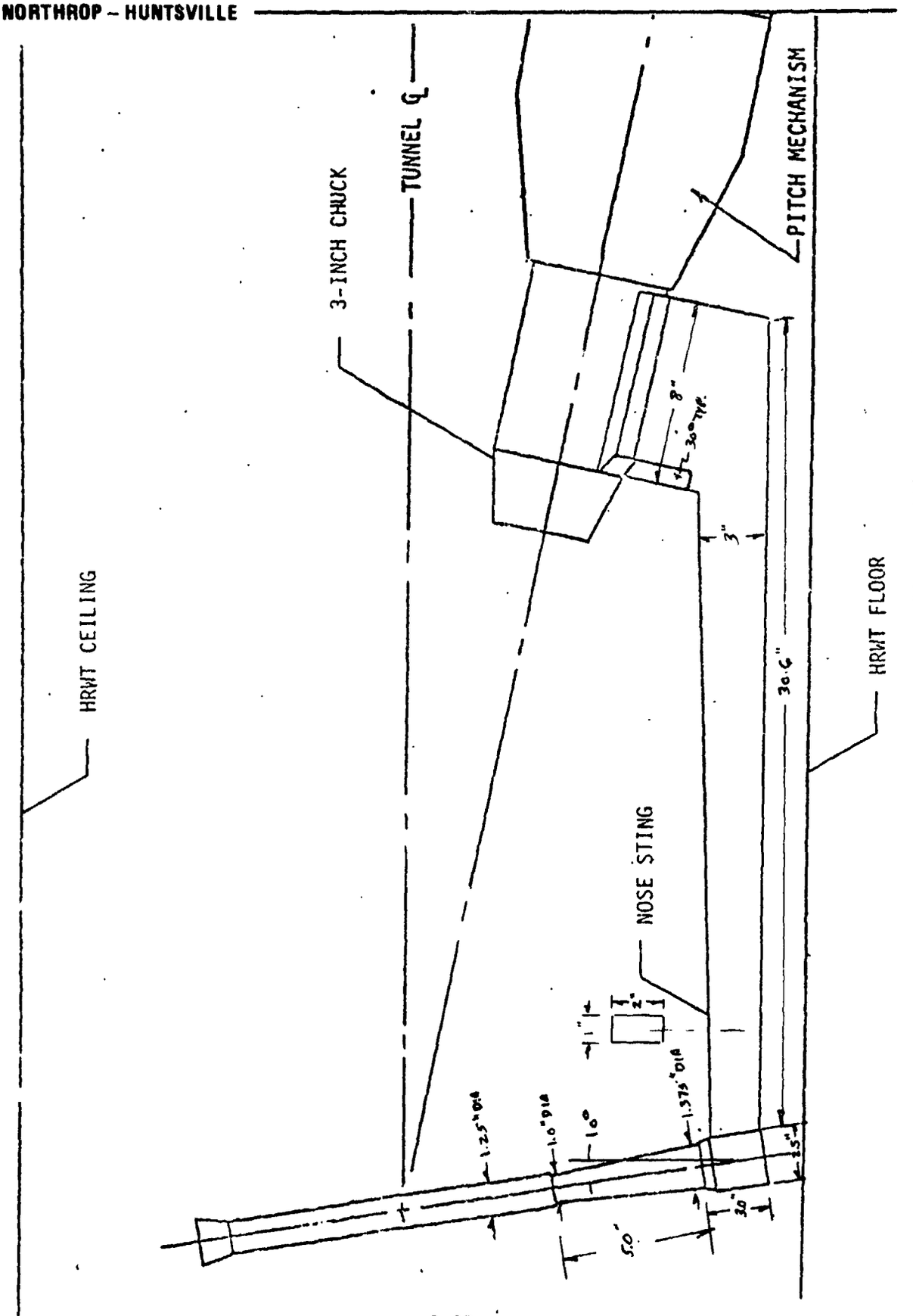

Figure 2-29. Sting Configuration HOONSA, $100° \leq \alpha \leq 120°$

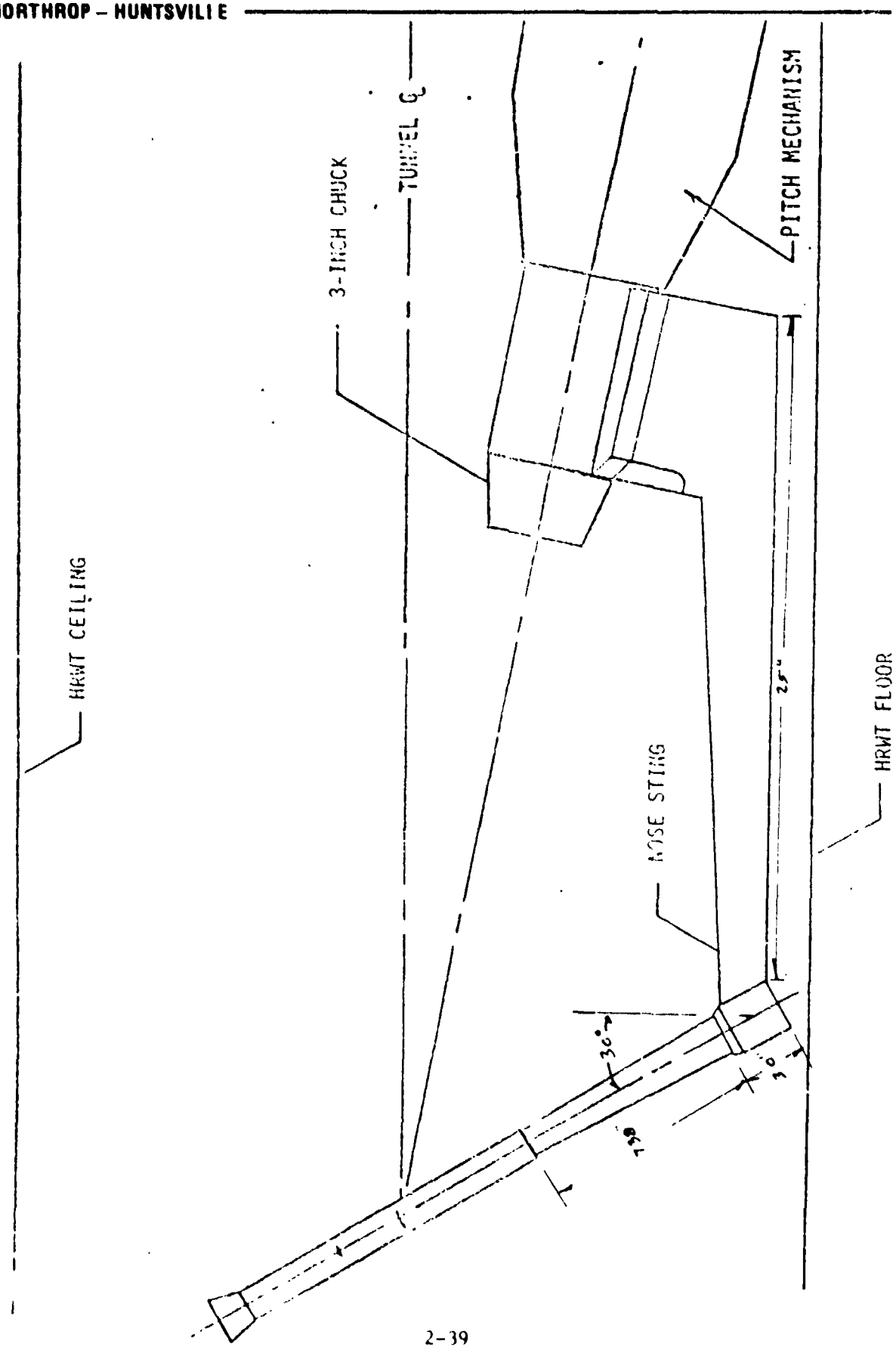

Figure 2-30. Sting Configuration HOONSB, 120° ≤ α ≤ 140°

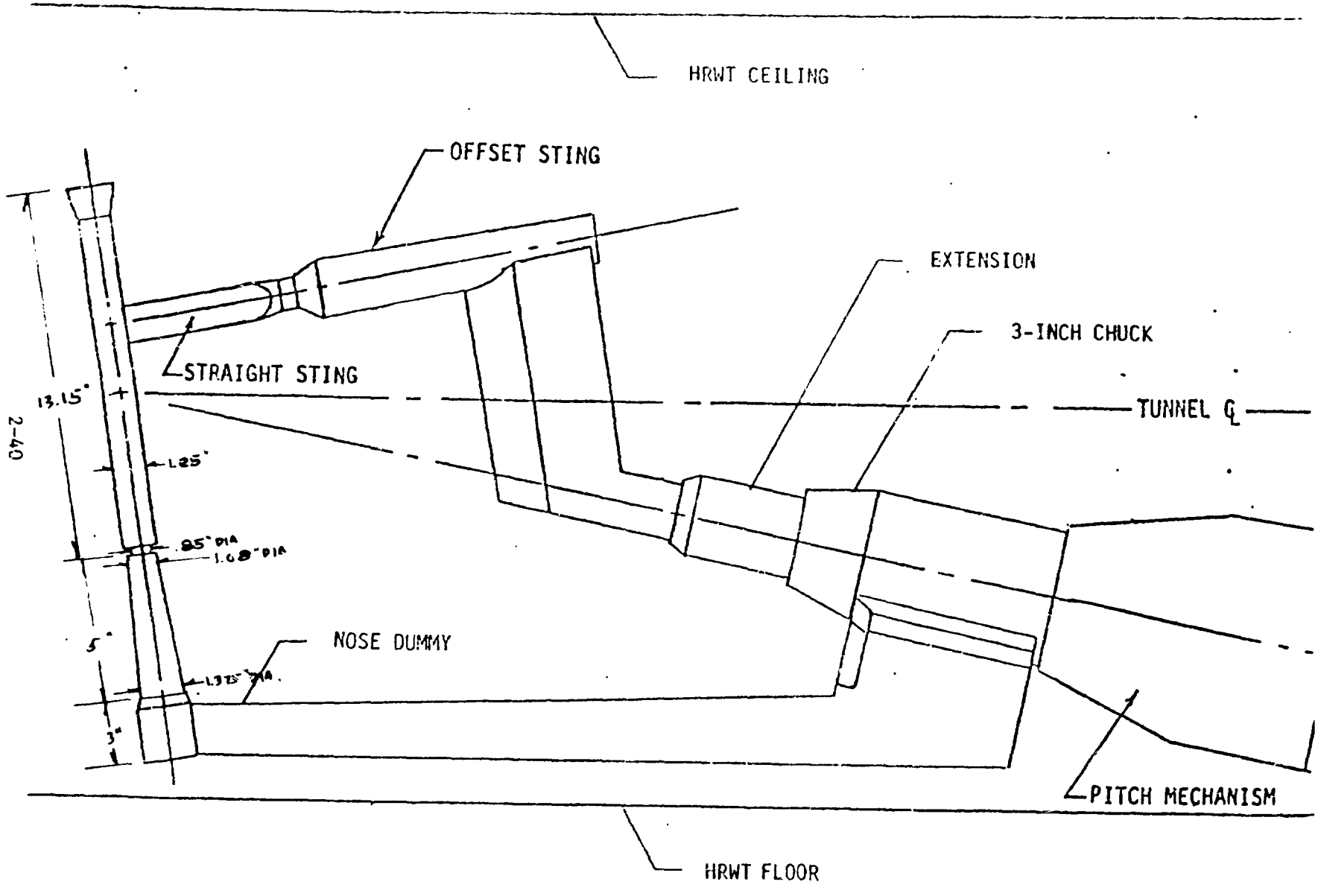

Figure 2-31. Sting Configuration HSSNDA, 100° $\leq \alpha \leq$ 120°

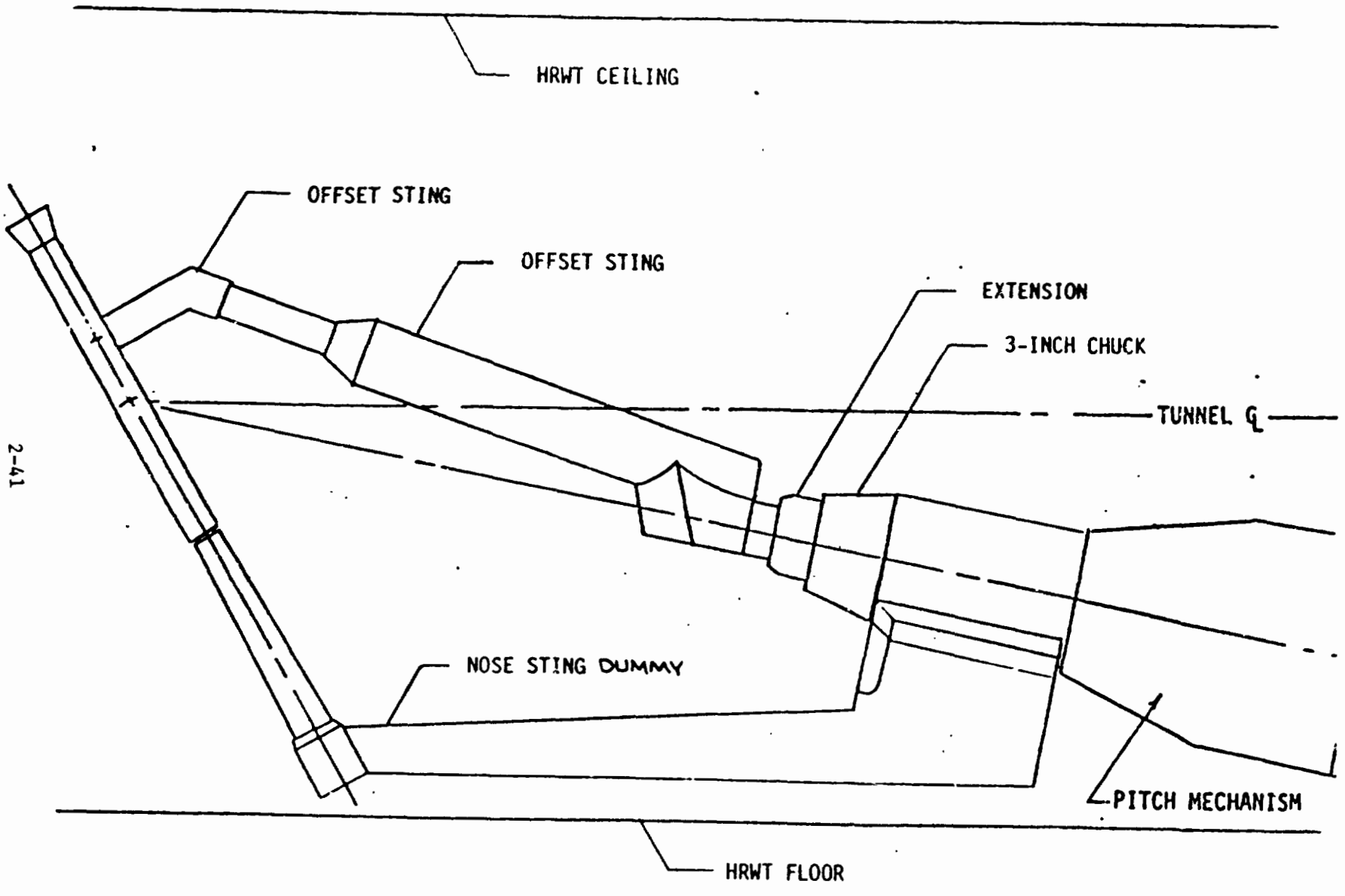

Figure 2-32. Sting Configuration HSSNDB, 120° $\leq \alpha \leq$ 140°

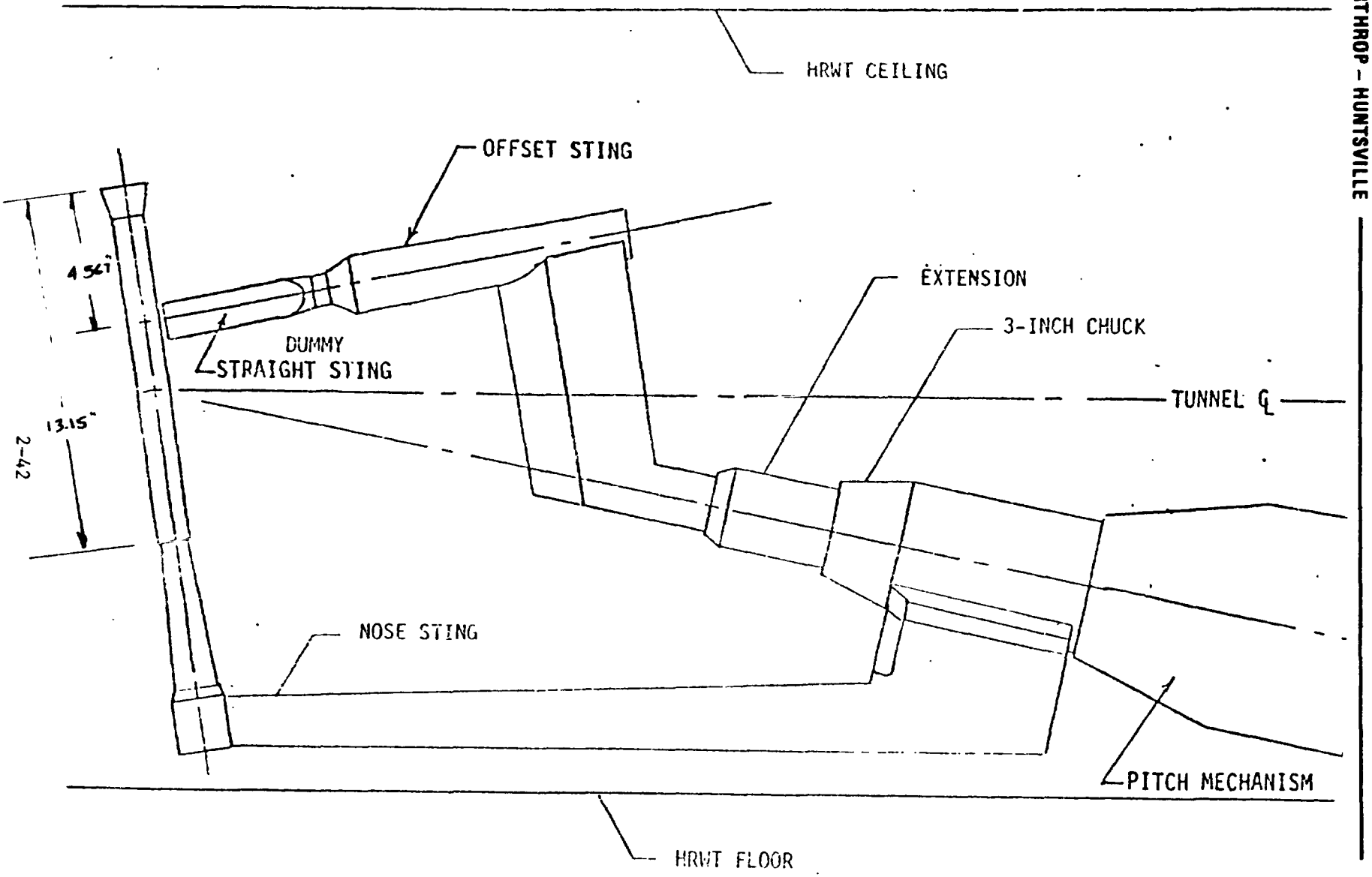

Figure 2-33. Sting Configuration HSDNSA, $100° \leq \alpha \leq 120°$

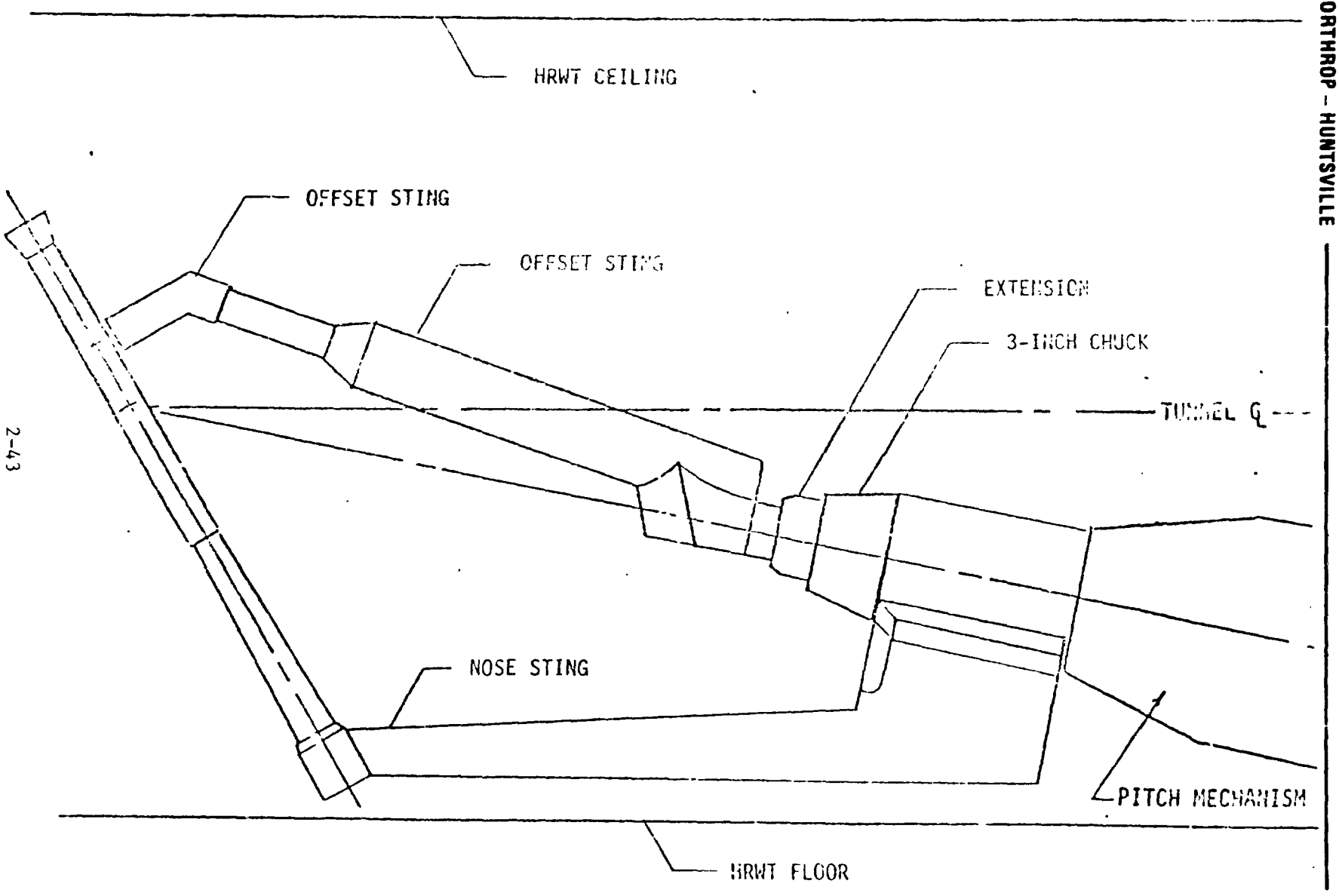

Figure 2-34. Sting Configuration HSDNSB, 120° $\leq \alpha \leq$ 140°

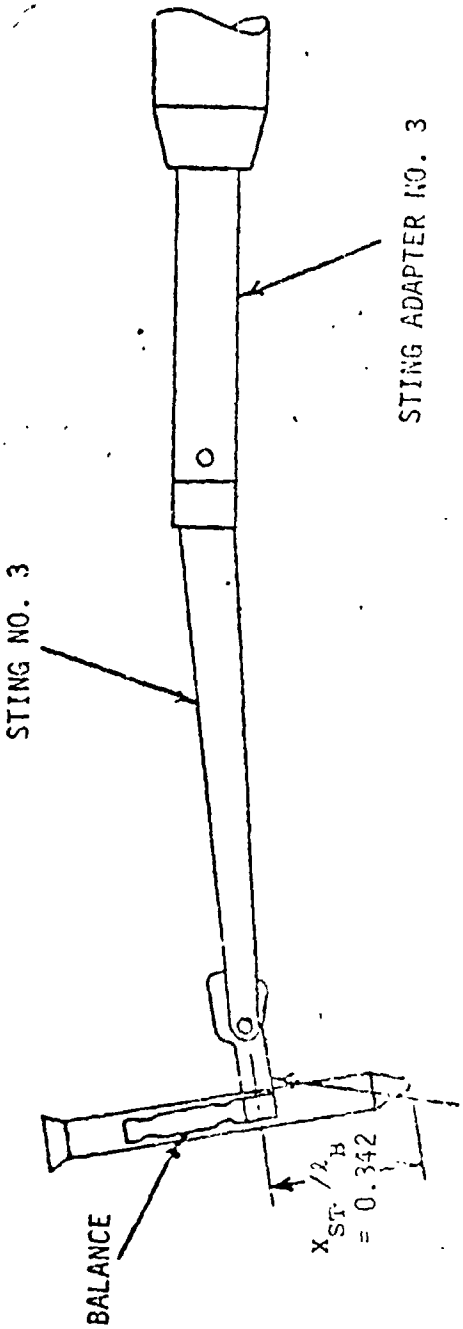

Figure 2-35. Side Mount Support Setup for Test SA14Fb

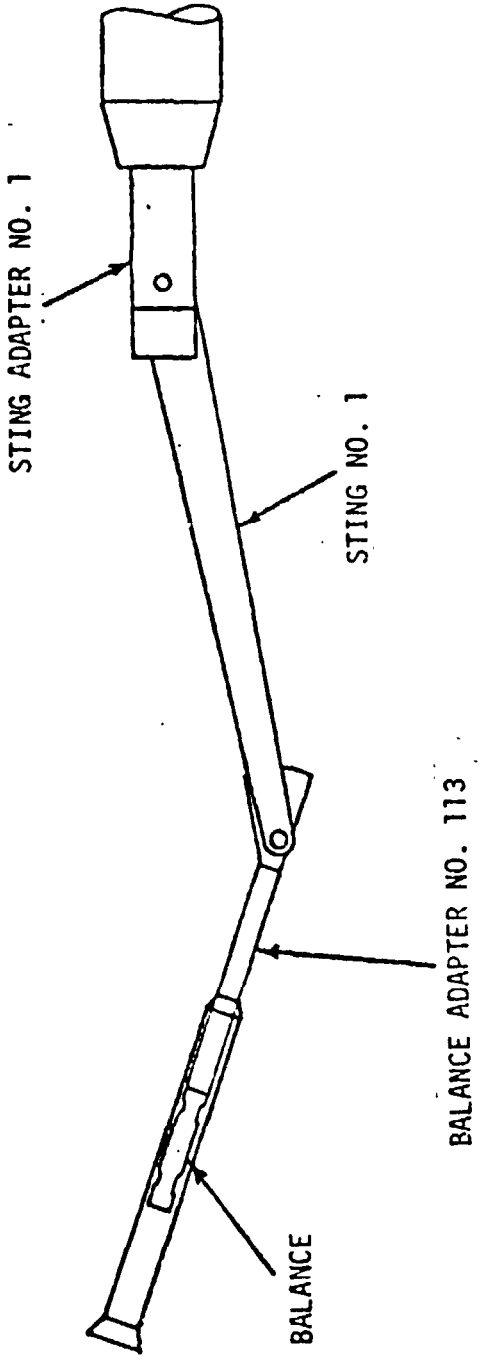

Figure 2-36. Nose Mount Support Setup for Test SA14Fb

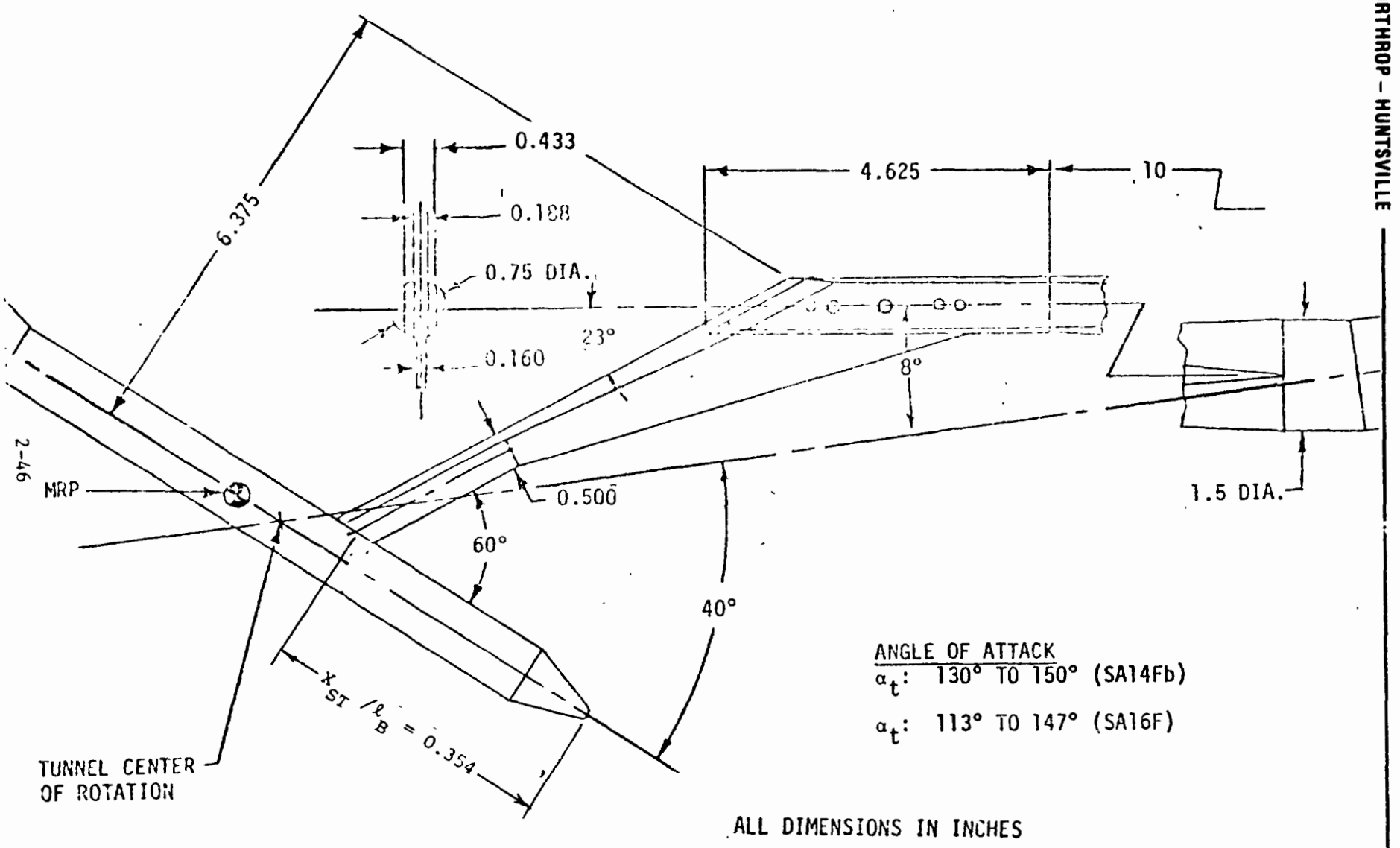

Figure 2-37. Side Mount Sting Support Setup for SA14Fb and SA16F

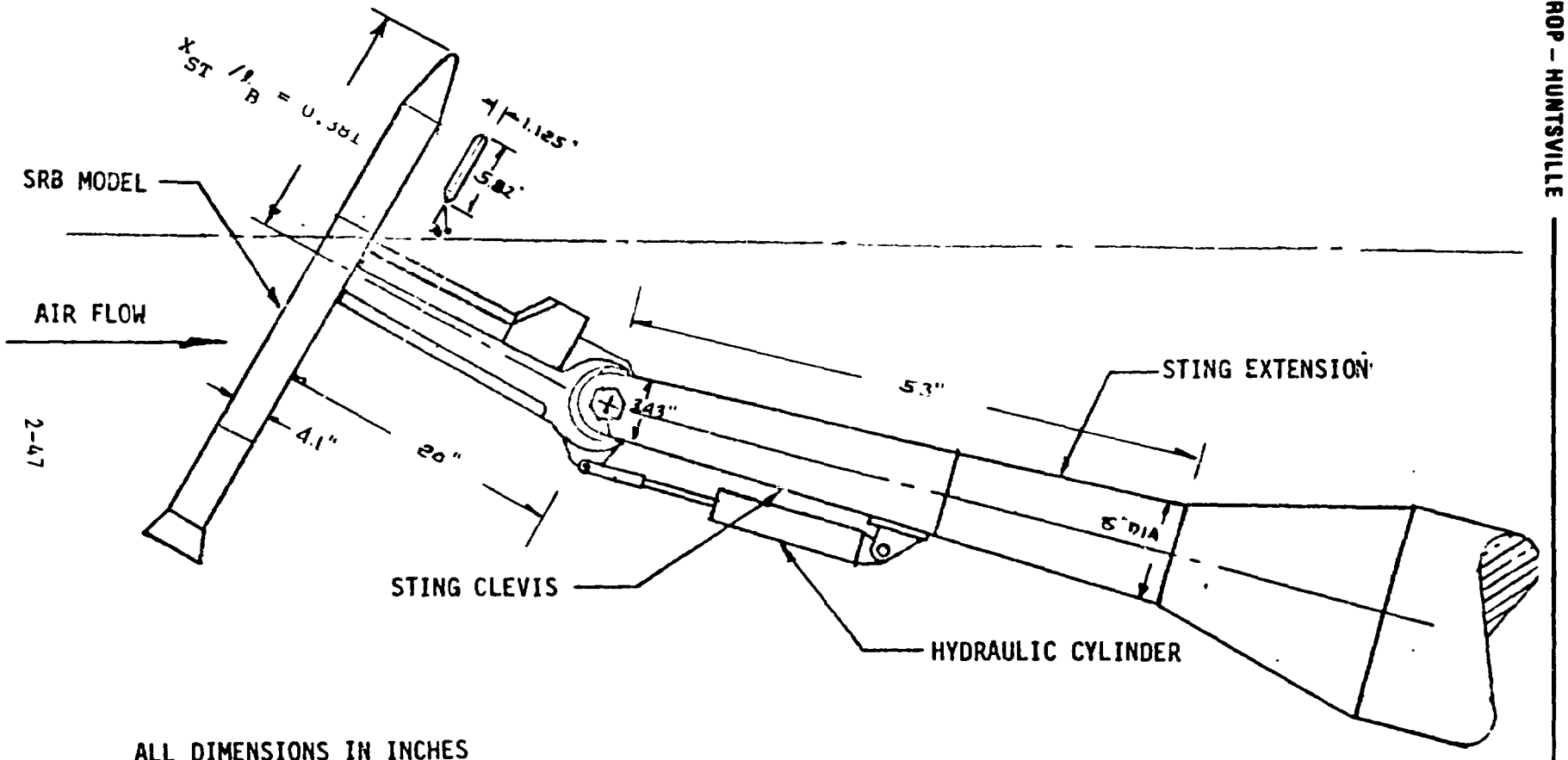

Figure 2-38. Side Mount Support Setup for SA11F

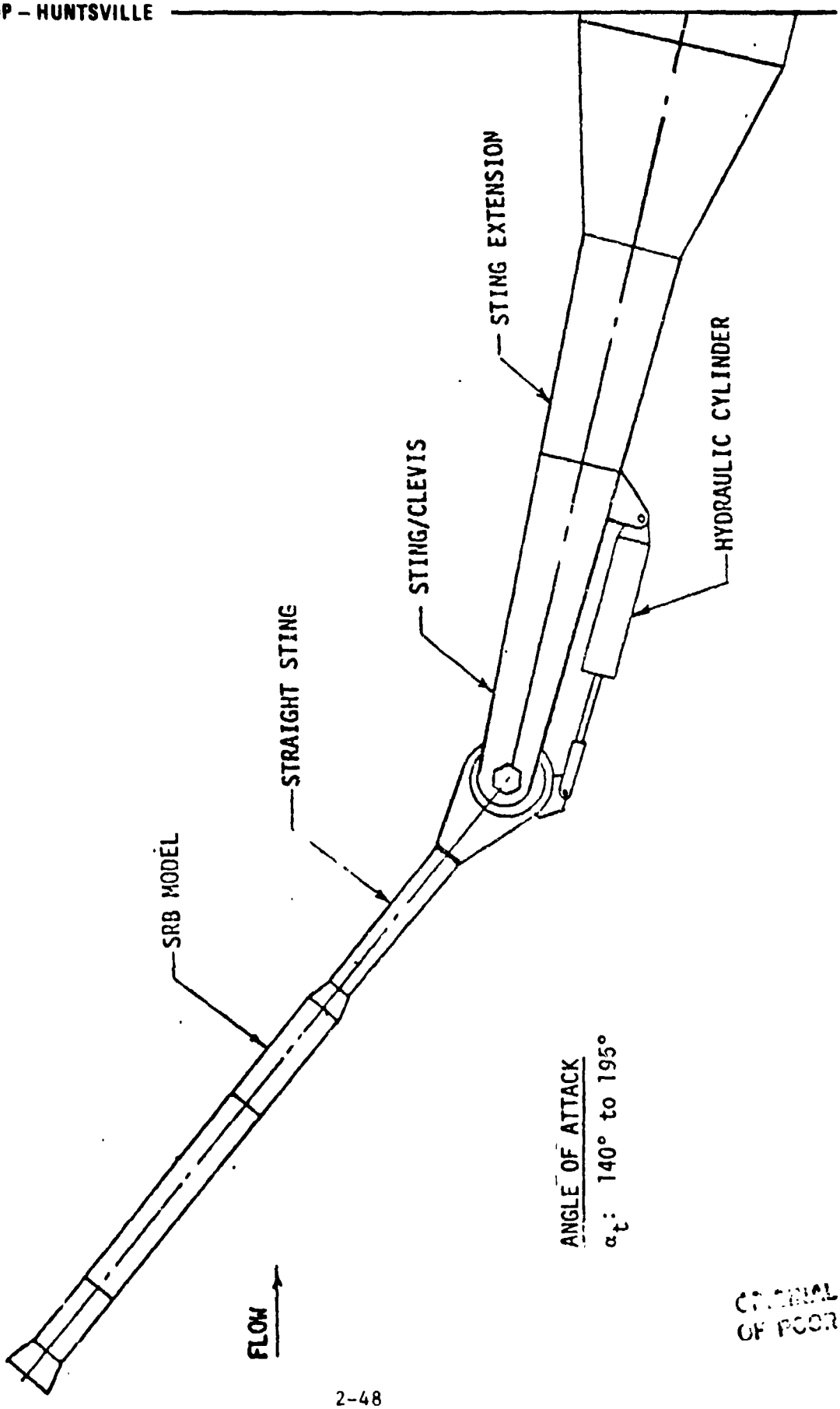

Figure 2-39. Nose Mount Support Setup for SA11F

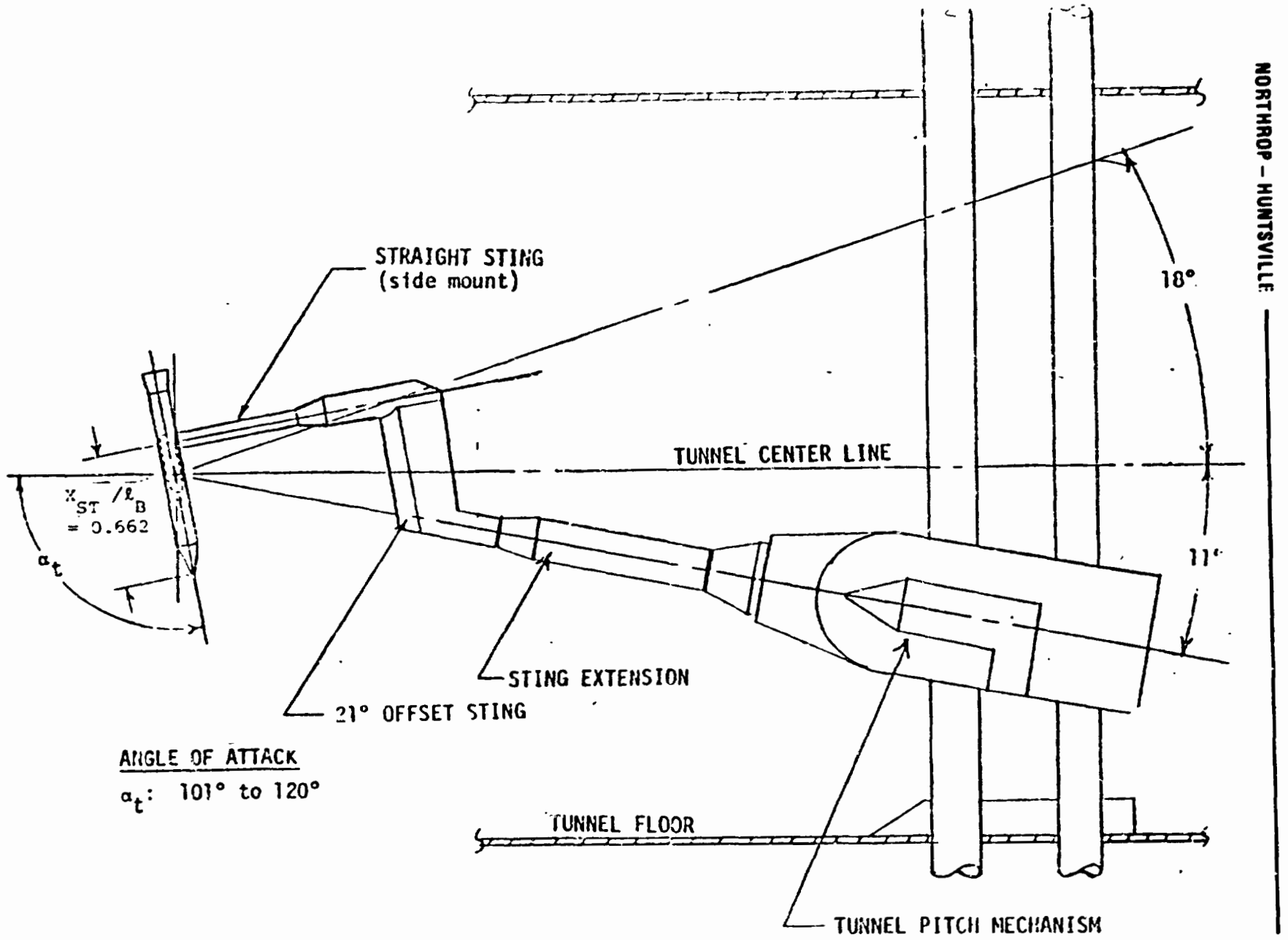

Figure 2-40. Side Mount Support Setup for SA31F (α = 100 to 120)

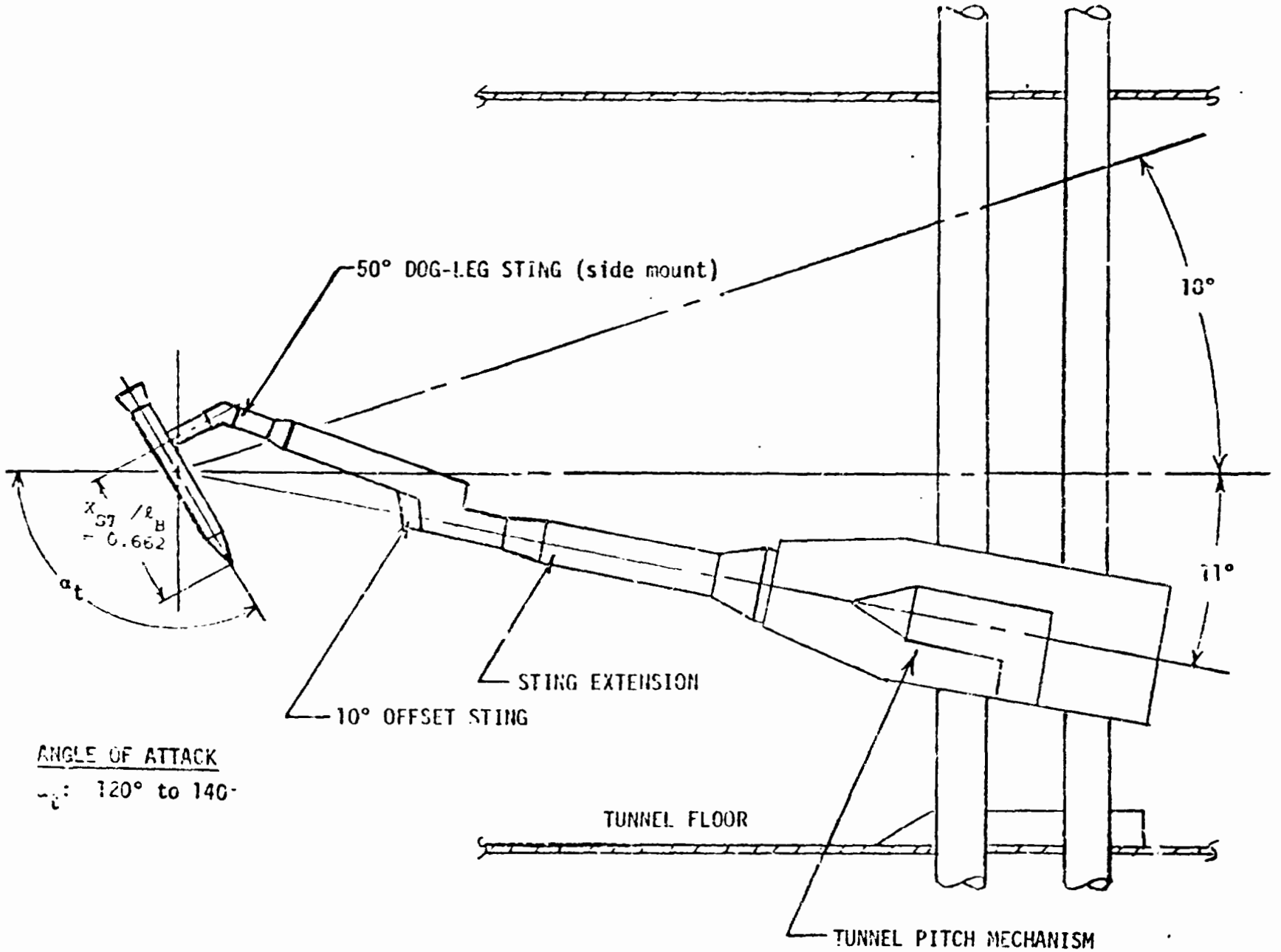

Figure 2-41. Side Mount Support Setup for SA31F (α = 120 to 140)

Section III

TWT TEST RESULTS

The procedure used to develop the sting interference data required that the wind tunnel test data for all configurations be interpolated to identical angles of attack since data had to be subtracted and added at the same value of angle of attack. A computer code was developed to perform the calculations identified in Section II to determine the amount of sting interference and calculate the sting interference free value of the aerodynamic coefficients. An example of the listing of the output of the code is presented in Tables 3-1 through 3-4. Summary tables of the value of the sting interference and the corrected data were also developed to assist in the analysis of the data. An example summary table is presented in Table 3-5. Tables of each coefficient are presented in Appendix A for each Mach number and roll angle tested and for each sting configuration. Table 3-1 shows an example of the data listing for the Ames nose mount configuration. A column listing of data for each configuration is presented corresponding to the equation required to determine the sting interference (see Section II). The value of the sting interference is listed as $\Delta C_{N_{ANM}}$ and the corrected nose mount data is listed in the last column as $C_{N_{ANM}}$. Tables 3-2 through 3-4 present similar data listings for the Marshall nose mount sting and the Ames and Marshall side mount sting configurations. It is noted that the Ames and Marshall nose mount stings are the identical nose sting configuration. The difference in the sting interference data is identified by the procedure used to obtain the sting interference data as identified in Section II. Table 3-5 presents a summary table of the sting interference for each configuration and the corrected data for each configuration. The summary table of sting interference is useful in that it allowed the identification of the largest and smallest level of sting interference. The summary of corrected data on the rightside of the table also includes the average of the data. This column allowed the evaluation of extremes in the corrected data base. The sting interference and the corrected data presented in Appendix A have been analyzed and the results of the analysis discussed below.

LONGITUDINAL DATA RESULTS

Values of the normal force sting interference are presented in Figures 3-1 through 3-5 versus angle of attack. The figures show that the side mounted stings have the largest interference with the AMES type sting having the largest normal force interference. The side mounted stings show a negative sting Δ which is a reduction in the aerodynamic normal force due to the presence of the sting. The nose mounted sting shows some positive and some negative sting interference at the lower Mach numbers. This could occur due to the method of mounting the nose sting. A portion of the nose of the SRB has to be removed to mount the nose sting. The nose sting has a cylindrical length that adds to the overall fineness ratio of the cylinder. The net nose sting interference is thus a trade between the reduction in nose airload due to removal of a portion of the nose and the additional airload due to the increased effective cylinder length. The questionable data trends are those that show a different sign for the nose mount sting (ANM and MNM) (see Figure 3-1, α = 100 to 120 degrees). This trend is believed to identify a difference in mutual sting interference due to the multiple stings. This trend occurred at Mach 0.6, 0.8, and 0.9 at ϕ = 0 degrees. The mutual interference is evident in the pitching moment sting interference discussed below. Figures 3-1 through 3-5 show that generally the nose mount sting has the smallest normal force interference, especially at the higher angles of attack.

The pitching moment sting interference is presented in Figures 3-6 through 3-10 for selected Mach numbers and roll angles. The figures show that the Marshall side mount sting configuration develops the smallest moment interference about the reference position of 59 percent of the body length. The side mount sting moment interference generally increases with angle of attack and can become very large at angles of attack near 140 degrees. The nose mount sting interference is generally largest at angles of attack near 100 degrees and decreases with angle of attack.

The variation of the normal force and pitching moment sting interference with Mach number is presented in Figures 3-11 through 3-16. Figures 3-11 and 3-12 show that the interference from the nose mount sting is smaller except

at Mach 1.46 at an angle of attack of 110 degrees. Figure 3-12 shows that the sting interference is small for the nose mount sting over a wide Mach number range. Figure 3-13 shows that the side mount sting creates a 6% error in the SRB normal force coefficient over a wide range of Mach numbers while the nose mount sting only has an error of 2 percent or less.

The center of pressure of the sting interference is presented in Figure 3-14. The center of pressure of the nose mount sting interference is noted to be located near the forward cylinder nose junction. The center of pressure of the side mount sting (located at X/ℓ_b of .39) is aft of the sting location, but in general forward of the moment reference point ($X/\ell_b = .59$). Thus the side and nose mount stings will shift the SRB X_{cp}/ℓ_b aft due to the sting interference reducing the airload forward of the MRP.

The pitching moment sting interference is presented in Figures 3-15 and 3-16 versus Mach number. The figures show that the side mount sting produces the lower pitching moment interference at angles of attack near 110 degrees while Figure 3-16 shows that the nose mount sting produces the lowest pitching moment interference at angles of attack near 130 degrees.

Corrected normal force and pitching moment coefficient data are presented in Figures 3-17 through 3-27. These figures present data at Mach numbers where the TWT results would not be appreciably influenced by Reynolds number. The figures present the working plots used to develop SRB aero data Tape #2. The figures contain the SA11F data, the SRB aero data Tape #1 data and the corrected data band from TWT 660.

The normal force data is presented in Figures 3-17 through 3-20. The figures show that the TWT 660 corrected data falls in a relatively narrow data band which is different from the SA11F results. Figures 3-18 and 3-20 show that if the TWT 660 Ames sting interference is applied directly to the SA11F data that a unrealistic curve shape results compared to the corrected data band.

The pitching moment data is presented in Figures 3-21 through 3-27. These figures show that the corrected data follows the Tape #1 (TWT 640) results closer than the Tape 2 (SA11F) data. This is to be expected since the sting interference results showed that the MSFC sting had the lower interference than the Ames sting configuration. The pitching moment comparison at Mach 1.1, 1.2 and 1.4 at $\phi = 0$ show that the corrected data approaches the high angle of attack nose mounted sting data. The high angle of attack trim conditions indicated by the nose mounted sting data from the TWT 640 and SA11F tests were not used to develop the aerodynamic data tapes. The corrected sting interference data shows that the nose mount data is the more correct data and should have been used to develop the two data tapes. This is confirmed by the plot of the magnitude of the sting interference data (Figures 3-9 and 3-10) which show that at the higher angles of attack the nose mount sting pitching moment interference is very small.

The corrected axial force coefficient is presented in Figure 3-28 versus Mach number. The axial force coefficient from Tape #1 and Tape #2 are presented for comparison. The figure shows that the corrected axial coefficient is lower than the Tape #1 or Tape #2 values over the majority of the Mach number range. This trend was generally consistent over the angle of attack range as shown in Figures 3-29 and 3-30. This reduction in axial force coefficient may be due to the models that were used during the TWT 660 test program. These models did not have the thermal shield that was present during the SA11F test (see Figure 2-4).

LATERAL DIRECTIONAL DATA RESULTS

The side force and yawing moment sting interference is presented in Figures 3-31 and 3-32 versus Mach number. Figure 3-31 shows that the side force sting interference is small except for the HRWT sting configuration. The HRWT sting interference is noted to be approximately 100 percent of the corrected side force in the Mach 1.1 range. The side force sting interference is reduced to about 17 percent at Mach 0.6.

The yawing moment sting interference is presented in Figure 3-32. The figure shows that the yawing moment sting interference is small except for the side mount sting configurations at Mach 0.6 and 0.8. It is noted that the Ames side mount sting interference is the largest in this Mach number range.

The HRWT sting interference is large over the total Mach number range and approaches 100 percent of the corrected value of side force at Mach 1.2. From Figure 3-32 it is evident that the side mount configurations have substantial yawing moment sting interference at Mach 0.6 and 0.8 while Figure 3-31 shows little side force interference at these Mach numbers. This condition is an indication of mutual sting interference causing a redistribution of the airload with no substantial change in level of the airload.

The corrected TWT 660 side force and yawing moment data have been overlayed over the SA11F and the SRB data Tape #1 results. The comparison data are presented in Figures 3-33 through 3-41. The figures show that the corrected TWT 660 data fall in a band that covers both the data Tape #1 results and the SA11F data. Thus no obvious data improvement could be identified. The rolling moment data would have to show a large difference to require a change since the rolling moment data for Tape #2 used the results of TWT 596 (SA21F). Test TWT 596 was a special rolling moment test that developed rolling moment data at roll angle at 22 1/2 degree increments. This test allowed the definition of the rolling moment data versus roll angle and was used to identify the value of the integral of the rolling m. . coefficient over all roll angles. This test showed that the integral should be approximately zero. The math model for SRB Tape #2 was thus adjusted such that the integral of the rolling moment coefficient was approximately zero when linearly interpolating the math model that defined rolling moment data at 45 degree increments.

The analysis of the TWT 660 test results at subsonic Mach number generally followed the transonic test results. The comparison of corrected data trends at subsonic Mach numbers required the additional consideration of the influence of Reynolds number and thus the subsonic trends are discussed in Section IV (HRWT Test Result) and Section V (Sting Interference Conclusions).

TABLE 3-1. SRB STING INTERFERENCE INTERPOLATED DATA - AMES NOSE MOUNT STING

ANM - AMES NOSE MOUNT

MACH= .601
ROLL= .000
ALPP= 110.0

CN AMES STING 'A' RANGE

ALPHA	CN ASSOOA	CN ASSNDA	CN MOONSA	ΔCN ANM	CN ANM
100.00	11.6892	11.5129	12.5278	-.1763	12.7041
102.00	11.6509	11.4781	12.6063	-.1728	12.7790
104.00	11.6482	11.4581	12.7060	-.1902	12.8962
106.00	11.7236	11.5045	12.6646	-.2191	12.8837
108.00	11.6720	11.4500	12.5142	-.2220	12.7363
110.00	11.5272	11.3580	12.4029	-.1692	12.5721
112.00	11.4336	11.2581	12.2825	-.1755	12.4580
114.00	11.3745	11.1891	12.1764	-.1854	12.3618
116.00	11.3360	11.1266	12.0723	-.2094	12.2817
118.00	11.2170	11.0546	11.9956	-.1624	12.1581

MACH= .601
ROLL= .000
ALPP= 130.0

CN AMES STING 'B' RANGE

ALPHA	CN ASSOOB	CN ASSNDB	CN MOONSB	ΔCN ANM	CN ANM
120.00	11.1040	10.9777	12.1395	-.1263	12.2658
122.00	10.8282	10.7095	11.7697	-.1187	11.8884
124.00	10.4393	10.3217	11.3322	-.1177	11.4499
126.00	9.8820	9.8244	10.8662	-.0576	10.9238
128.00	9.2684	9.3097	10.3357	.0413	10.2944
130.00	8.7481	8.7270	9.7453	-.0211	9.7665
132.00	8.1853	8.1495	9.1268	-.0358	9.1626
134.00	7.5532	7.5364	8.3360	-.0167	8.3527
136.00	6.8465	6.8026	7.4312	-.0439	7.4751
138.00	6.2373	6.2156	6.8372	-.0217	6.8589

TABLE 3-2. SRB STING INTERFERENCE INTERPOLATED DATA - MARSHALL NOSE MOUNT STING

MNM - MARSHALL NOSE MOUNT

MACH= .601
ROLL= .000
ALPP= 110.1

CN MARSHALL STING "A" RANGE

ALPHA	CN MSS00A	CN MSSNOA	CN MOONSA	ΔCN MNM	CN MNM
100.00	11.4431	11.8447	12.5278	.4016	12.1262
102.00	11.4717	11.8669	12.6063	.3952	12.2111
104.00	11.7091	11.9235	12.7060	.2144	12.4916
106.00	11.7104	11.9896	12.6646	.2792	12.3854
108.00	11.5083	11.8727	12.5142	.3644	12.1498
110.00	11.2147	11.6811	12.4029	.4664	11.9365
112.00	11.1108	11.5592	12.2825	.4485	11.8340
114.00	11.0501	11.5268	12.1764	.4767	11.6997
116.00	11.0773	11.4667	12.0723	.3894	11.6829
118.00	10.9399	11.3597	11.9956	.4198	11.5759

MACH= .601
ROLL= .000
ALPP= 130.0

CN MARSHALL STING "B" RANGE

ALPHA	CN MSS00B	CN MSSNOB	CN MOONSB	ΔCN MNM	CN MNM
120.00	11.2933	11.2540	12.1395	-.0393	12.1788
122.00	10.9298	10.7832	11.7697	-.1465	11.9162
124.00	10.3987	10.1960	11.3322	-.1926	11.5248
126.00	9.7405	9.6222	10.8662	-.1183	10.9845
128.00	9.1370	9.0841	10.3357	-.0529	10.3886
130.00	8.5213	8.5284	9.7453	.0071	9.7383
132.00	7.8757	7.9363	9.1268	.0606	9.0662
134.00	7.2260	7.3322	8.3360	.1062	8.2298
136.00	6.5985	6.7103	7.4312	.1118	7.3194
138.00	6.0595	6.1960	6.8372	.1365	6.7007

TABLE 3-3. SRB STING INTERFERENCE INTERPOLATION DATA - AMES SIDE MOUNT STING

ASM - AMES SIDE MOUNT

MACH= .601
ROLL= .000
ALPP= 110.0

CN AMES STING 'A' RANGE

ALPHA	CN MOONSA	CN ASONSA	CN ASSOOA	ΔCN ASM	CN ASM
100.00	12.5278	11.9698	11.6892	-.5581	12.2473
102.00	12.6063	11.9354	11.6509	-.6709	12.3218
104.00	12.7060	11.8865	11.6482	-.8194	12.4677
105.00	12.6646	11.8802	11.7236	-.7845	12.5081
106.00	12.5142	11.8601	11.6720	-.6542	12.3262
110.00	12.4029	11.8078	11.5272	-.5951	12.1223
112.00	12.2825	11.7758	11.4336	-.5067	11.9403
114.00	12.1764	11.6986	11.3745	-.4778	11.8523
116.00	12.0723	11.6243	11.3360	-.4480	11.7840
118.00	11.9956	11.5228	11.2170	-.4728	11.6898

MACH= .601
ROLL= .000
ALPP= 130.0

CN AMES STING 'B' RANGE

ALPHA	CN MOONSB	CN ASONSB	CN ASSOOB	ΔCN ASM	CN ASM
120.00	12.1395	11.4832	11.1040	-.6563	11.7603
122.00	11.7697	11.1473	10.8282	-.6224	11.4506
124.00	11.3372	10.7409	10.4393	-.5913	11.0306
126.00	10.8662	10.2662	9.8820	-.5800	10.4620
128.00	10.3357	9.7492	9.2684	-.5875	9.8559
130.00	9.7453	9.2083	8.7481	-.5370	9.2851
132.00	9.1268	8.6409	8.1853	-.4859	8.6712
134.00	8.3360	7.8595	7.5532	-.4765	8.0296
136.00	7.4312	6.9974	6.8465	-.4338	7.2803
138.00	6.8372	6.3915	6.2373	-.4458	6.6830

TABLE 3-4. SRB STING INTERFERENCE INTERPOLATED DATA - MARSHALL SIDE MOUNT STING

MSM - MARSHALL SIDE MOUNT

MACH= .601
ROLL= .000
ALPP= 110.0

CN MARSHALL STING "A" RANGE

ALPHA	CN MOONSA	CN MSONSA	CN MSSOOA	ΔCN MSM	CN MSM
100.00	12.5278	12.0799	11.4431	-.4480	11.8911
102.00	12.6063	12.1724	11.4717	-.4339	11.9056
104.00	12.7060	12.1263	11.7091	-.5797	12.2887
106.00	12.6646	12.1214	11.7104	-.5432	12.2536
108.00	12.5142	12.0695	11.5083	-.4447	11.9530
110.00	12.4029	11.8970	11.2147	-.5058	11.7205
112.00	12.2825	11.8134	11.1108	-.4691	11.5799
114.00	12.1764	11.8560	11.0501	-.3204	11.3705
116.00	12.0723	11.8681	11.0773	-.2042	11.2815
118.00	11.9956	11.7766	10.9399	-.2190	11.1590

MACH= .601
ROLL= .000
ALPP= 130.0

CN MARSHALL STING "B" RANGE

ALPHA	CN MOONSB	CN MSONSB	CN MSSOOB	ΔCN MSM	CN MSM
120.00	12.1395	11.3640	11.2933	-.7755	12.0687
122.00	11.7697	11.1290	10.9298	-.6407	11.5704
124.00	11.3322	10.7171	10.3887	-.6151	11.0039
126.00	10.8662	10.0642	9.7405	-.8021	10.5426
128.00	10.3357	9.3968	9.1370	-.9389	10.0759
130.00	9.7453	8.8111	8.5213	-.9343	9.4556
132.00	9.1266	8.2265	7.8757	-.9003	8.7760
134.00	8.3360	7.6173	7.2260	-.7187	7.9447
136.00	7.4312	6.9876	6.5985	-.4436	7.0421
138.00	6.8372	6.4036	6.0595	-.4336	6.4931

TABLE 3-5. SRB STING INTERFERENCE INTERPOLATED DATA - SUMMARY CORRECTED DATA

SUMMARY CORRECTED DATA

MACH= .601
ROLL= .000

ALPHA	ΔCN ASM	ΔCN MSM	ΔCN ANM	ΔCN MNM	ΔCN MSM	CN ASM	CN MSM	CN ANM	CN MNM	CN AVG
	ΔCN STING INTERFERENCE DELTAS					CN CORRECTED FOR STING INTERFERENCE				
100.00	-.5581	-.4480	-.1763	.4016	-.3802	12.2423	11.8911	12.7041	12.1262	12.2422
102.00	-.6705	-.4339	-.1728	.3952	-.5637	12.3218	11.9056	12.7790	12.2111	12.3044
104.00	-.8194	-.5797	-.1902	.2144	-.7473	12.4677	12.2887	12.8962	12.4916	12.5360
106.00	-.7845	-.5432	-.2191	.2792	-.6953	12.5081	12.2536	12.8837	12.3859	12.5077
108.00	-.6542	-.4447	-.2220	.3644	-.5185	12.3262	11.9530	12.7363	12.1498	12.2913
110.00	-.5951	-.5058	-.1692	.4664	-.4705	12.1223	11.7205	12.5721	11.9365	12.0878
112.00	-.5067	-.4691	-.1755	.4485	-.4395	11.9403	11.5799	12.4580	11.8340	11.9530
114.00	-.4778	-.3204	-.1854	.4767	-.4307	11.8523	11.3705	12.3618	11.6997	11.8211
116.00	-.4480	-.2042	-.2094	.3894	-.4229	11.7840	11.2815	12.2817	11.6829	11.7575
118.00	-.4728	-.2190	-.1624	.4198	-.4138	11.6899	11.1590	12.1581	11.5759	11.6457
120.00	-.6563	-.7755	-.1263	-.0353	-1.0537	11.7603	12.0687	12.2658	12.1788	12.0684
122.00	-.6224	-.6407	-.1187	-.1465	-1.0490	11.4506	11.5704	11.8884	11.9162	11.7064
124.00	-.5913	-.6151	-.1177	-.1926	-1.1155	11.0306	11.0038	11.4499	11.5248	11.2523
126.00	-.5800	-.8021	-.0576	-.1183	-1.2816	10.4620	10.5426	10.9236	10.9845	10.7282
128.00	-.5875	-.9389	.0413	-.0529	-1.3768	9.8559	10.0759	10.2948	10.3886	10.1537
130.00	-.5370	-.9343	-.0211	.0071	-1.3149	9.2851	9.4556	9.7665	9.7383	9.5614
132.00	-.4859	-.9003	-.0358	.0606	-1.2937	8.6712	8.7760	9.1626	9.0662	8.9190
134.00	-.4765	-.7187	-.0167	.1062	-1.2349	8.0296	7.9447	8.3527	8.2298	8.1392
136.00	-.4338	-.4436	-.0439	.1118	-.9651	7.2803	7.0421	7.4751	7.3194	7.2752
138.00	-.4456	-.4336	-.0217	.1365	-.7759	6.6830	6.4931	6.8589	6.7007	6.6839

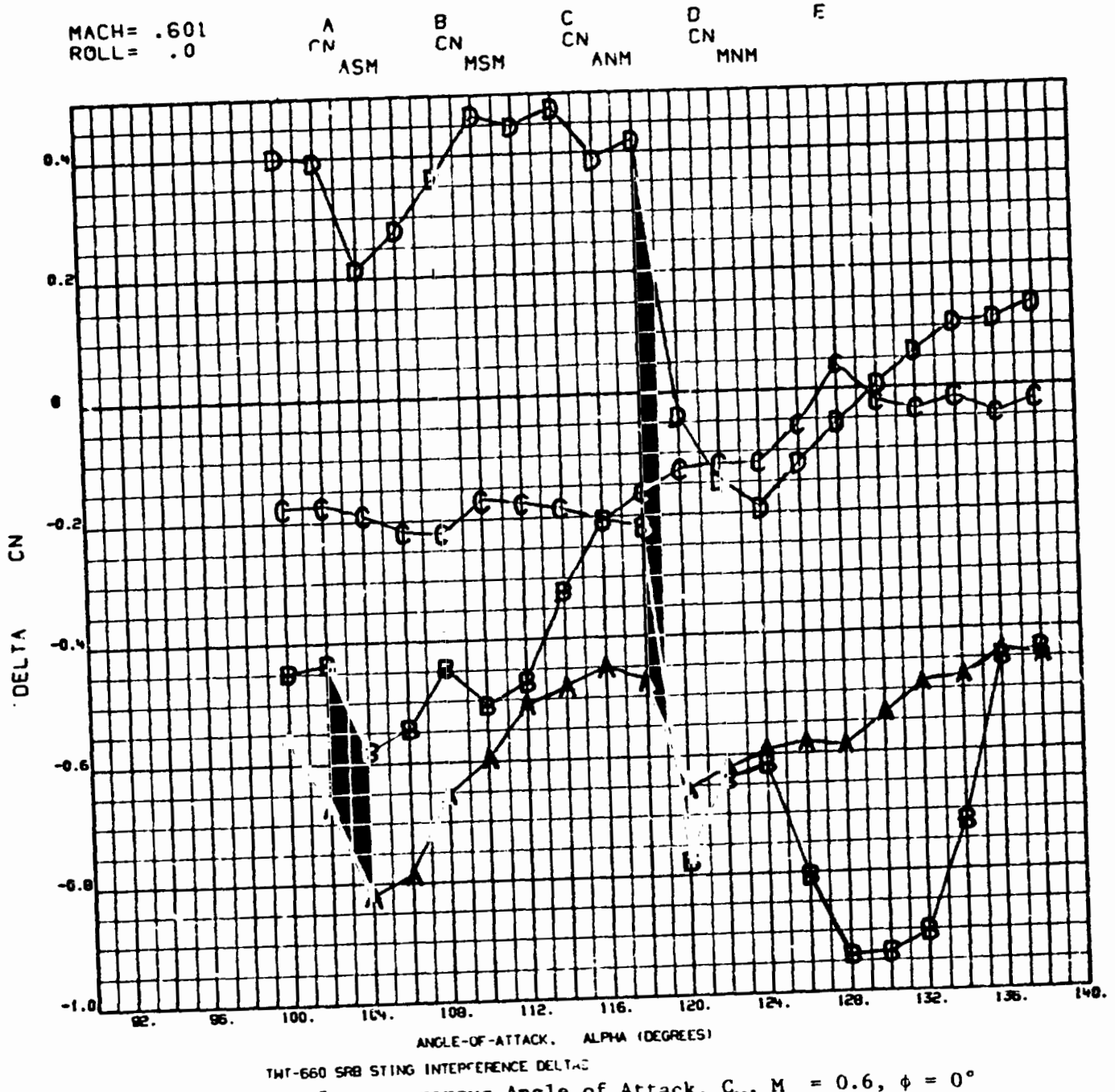

Figure 3-1. Sting Interference versus Angle of Attack, C_N, $M_\infty = 0.6$, $\phi = 0°$

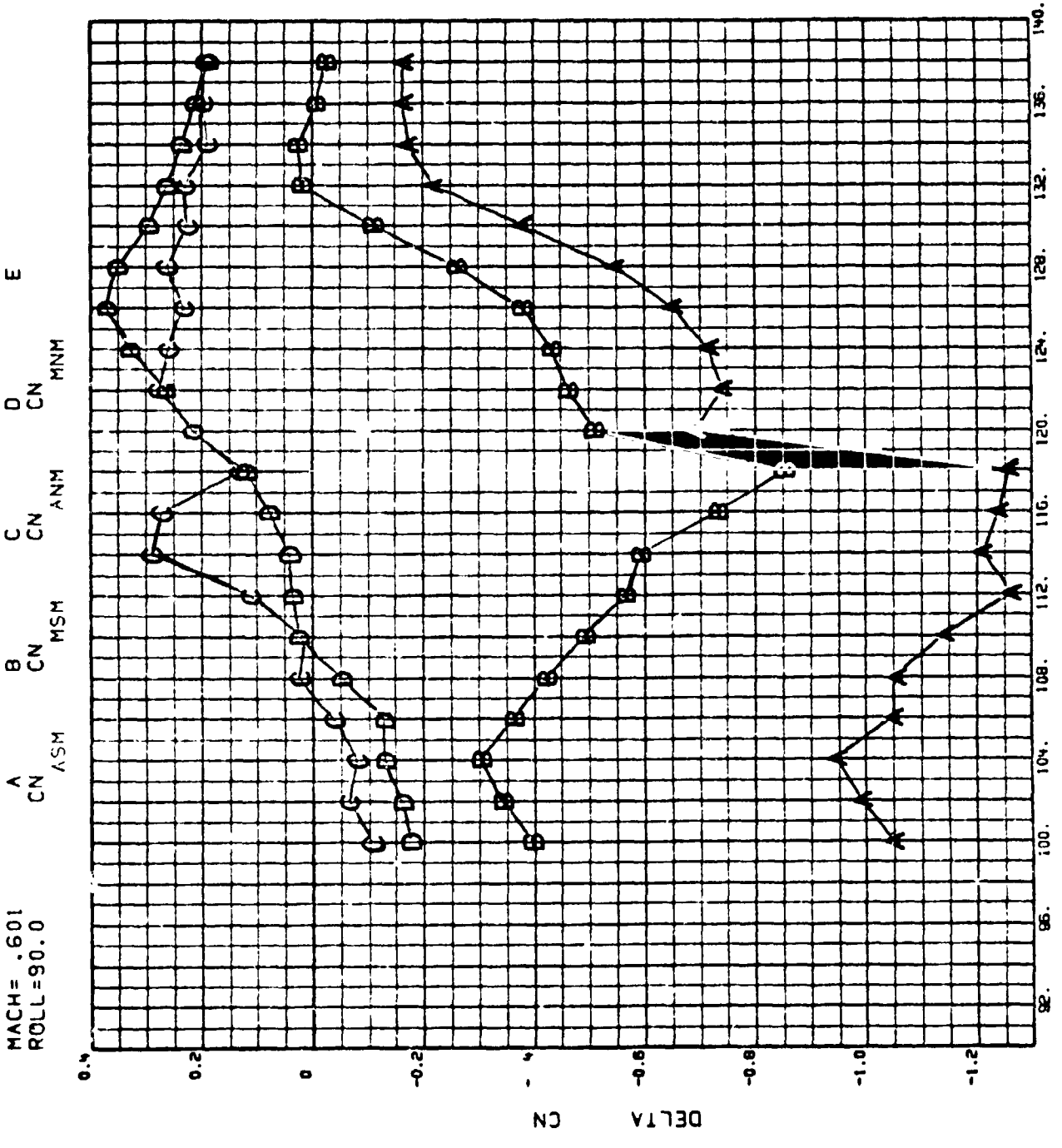

Figure 3-2. Sting Interference versus Angle of Attack, $C_{N'}$, $M_\infty = 0.6$, $\phi = 90°$

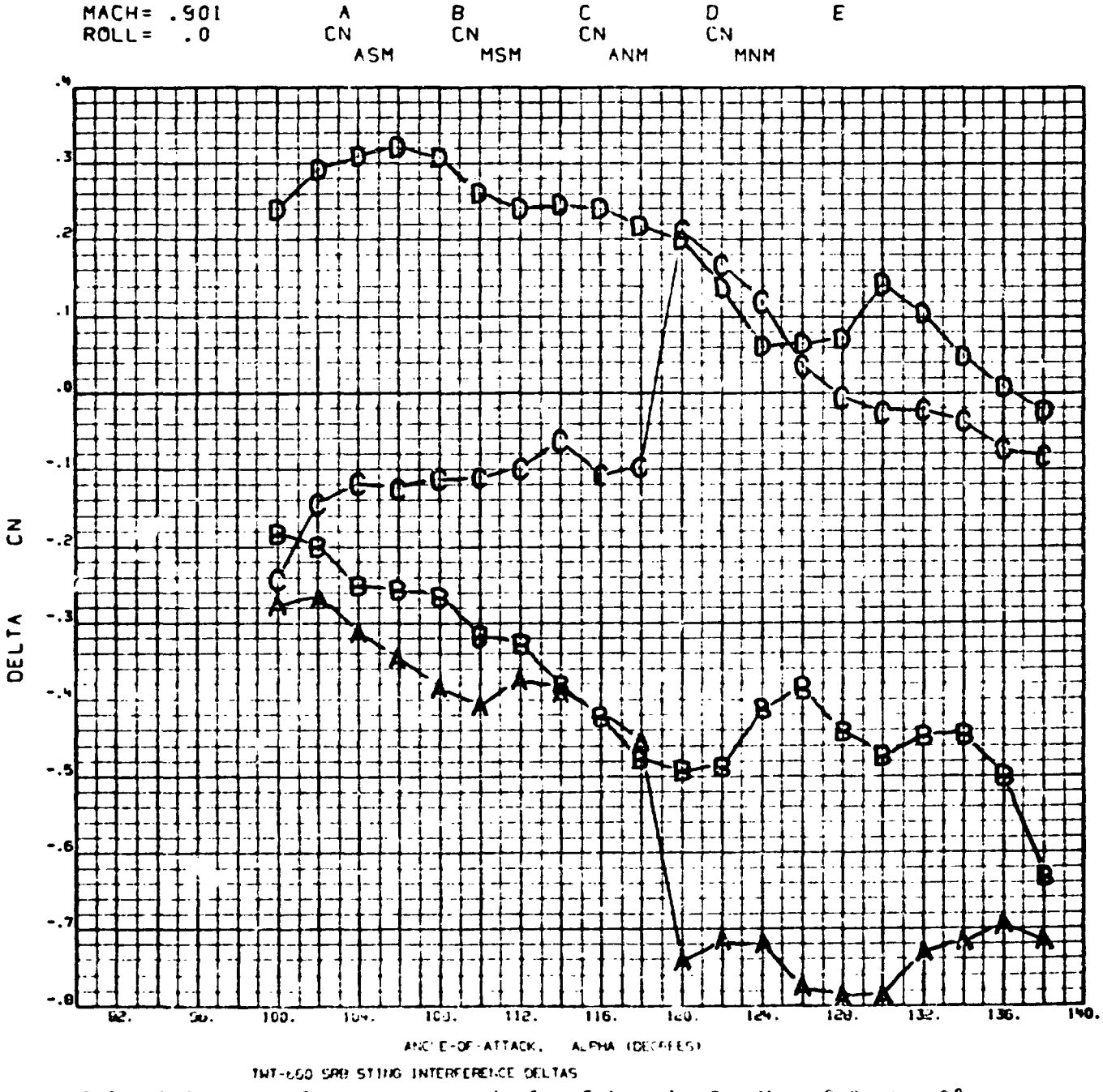

Figure 3-3. Sting Interference versus Angle of Attack, C_N, $M_\infty = 0.9$, $\phi = 0°$

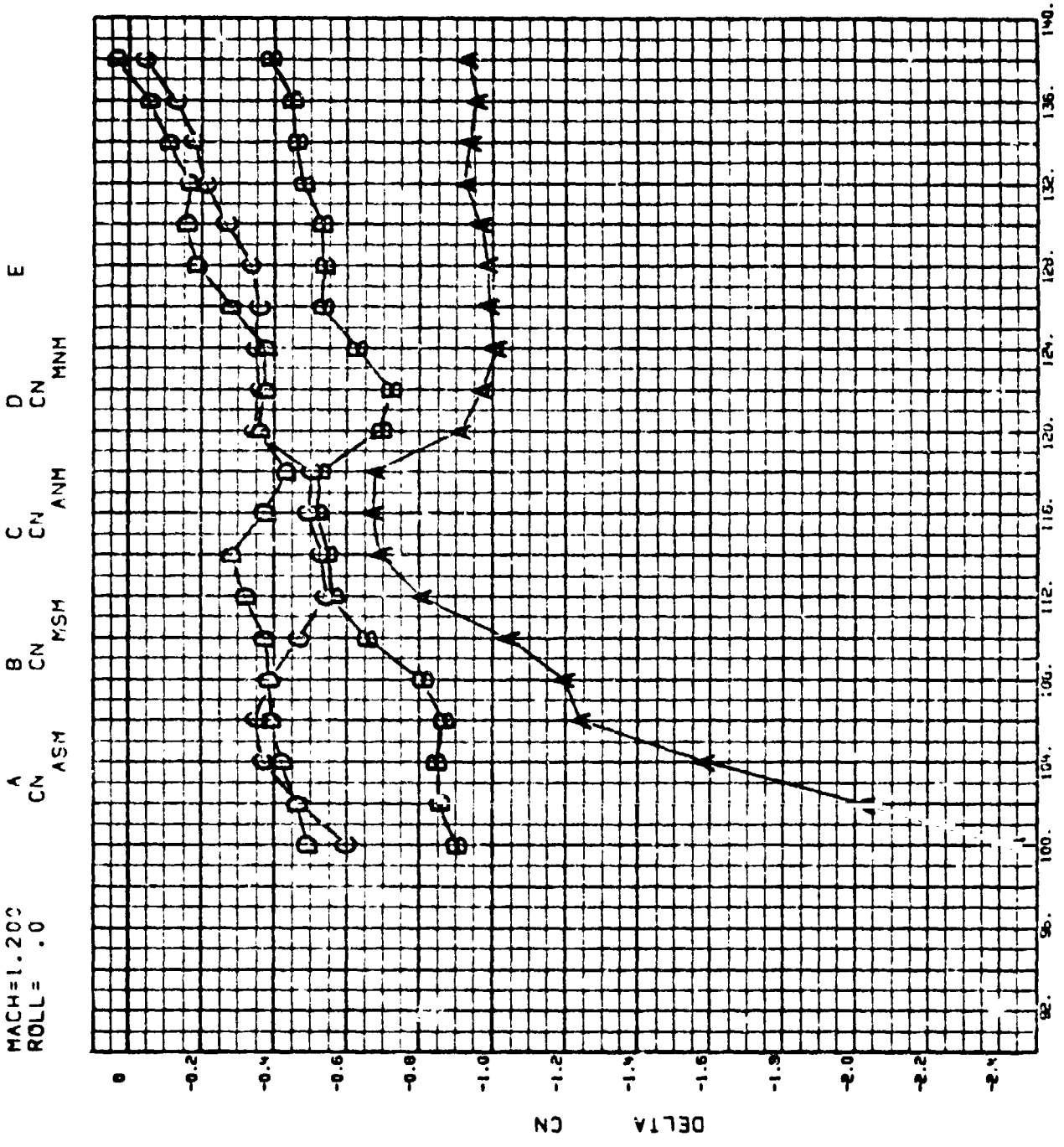

Figure 3-4. Sting Interference versus Angle of Attack, C_N, $M_\infty = 1.2$, $\phi = 0°$

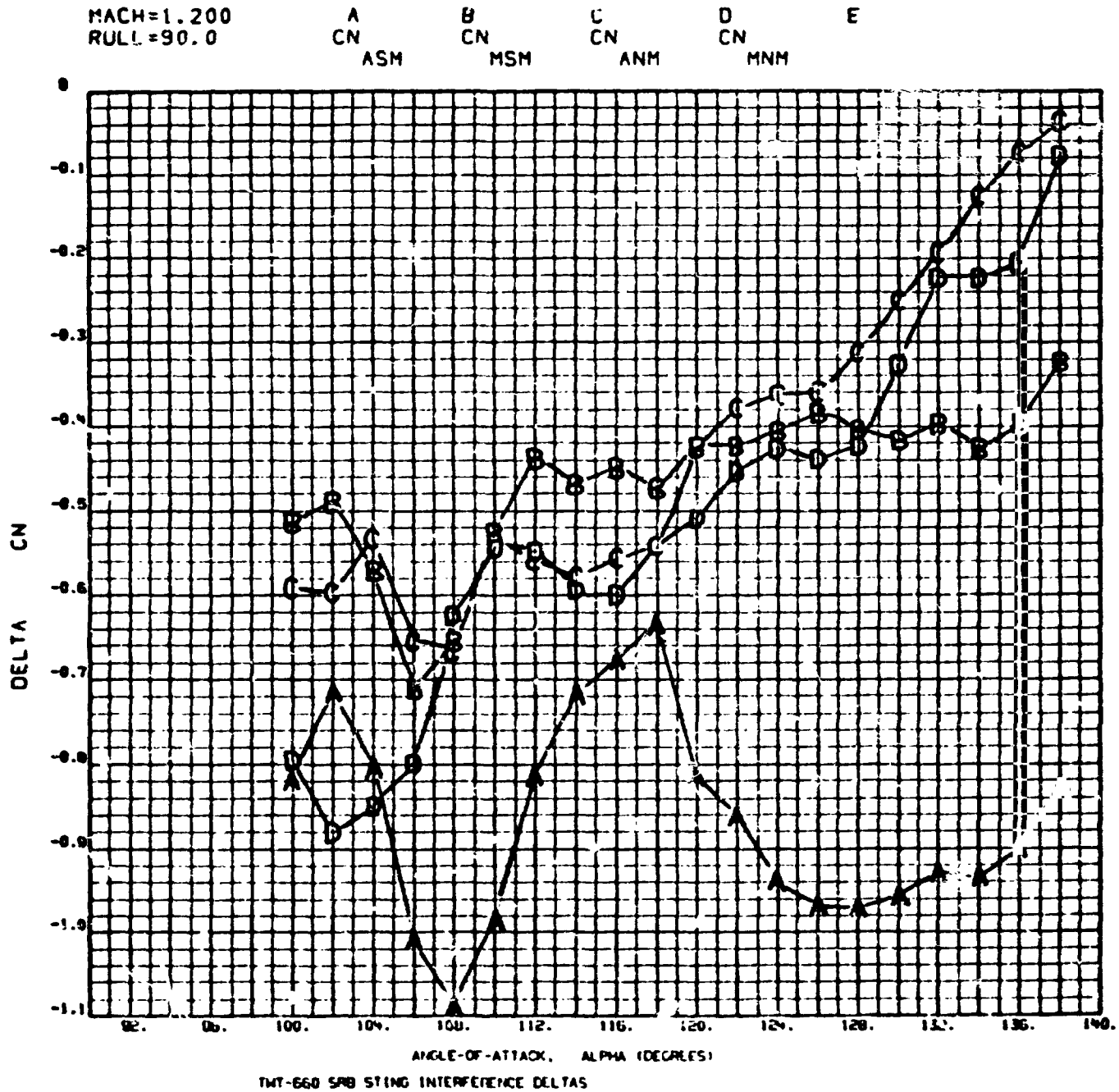

Figure 3-5. Sting Interference versus Angle of Attack, C_N, $M_\infty = 1.2$, $\phi = 90°$

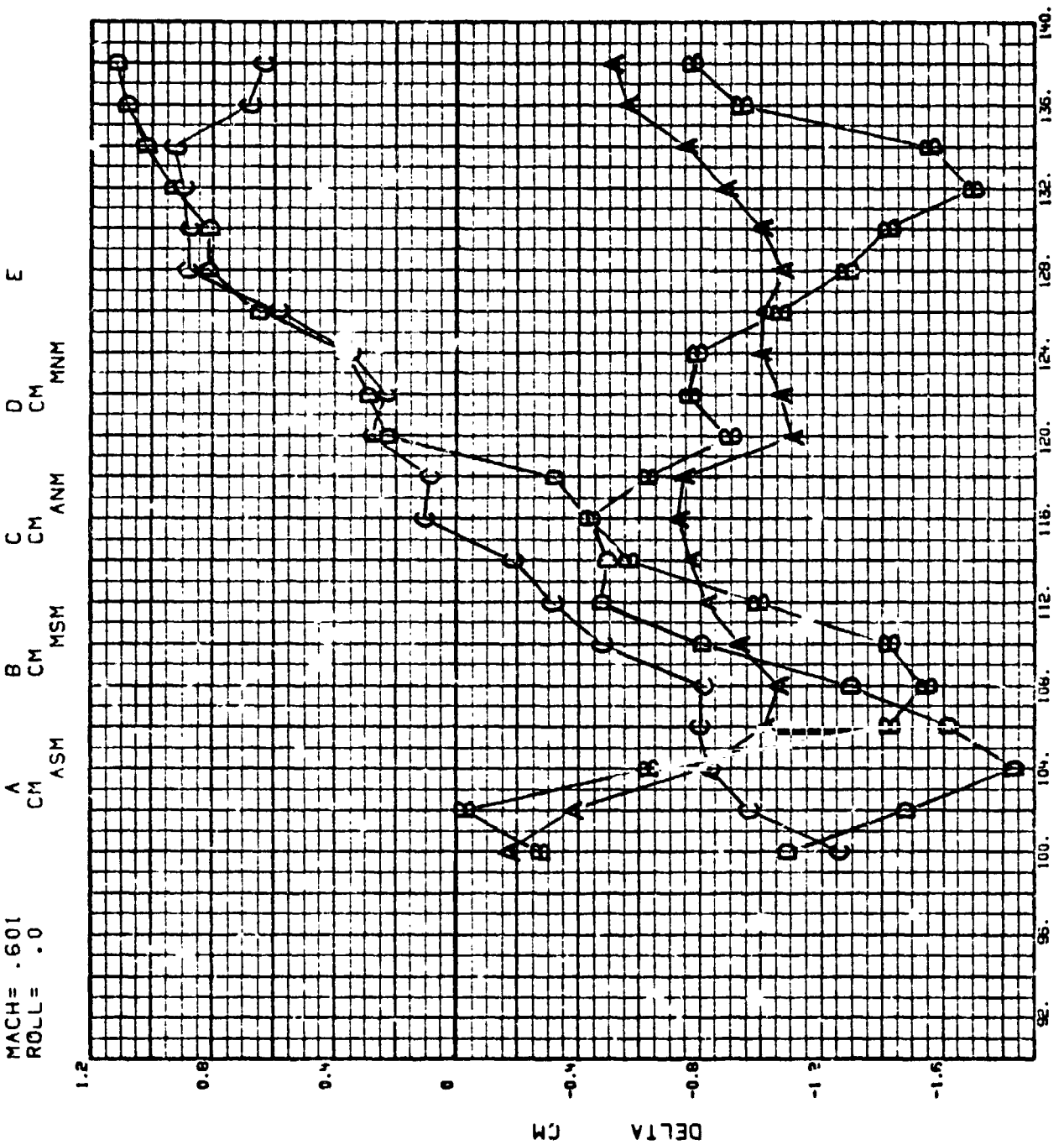

Figure 3-6. Sting Interference versus Angle of Attack, C_M, $M_\infty = 0.6$, $\phi = 0°$

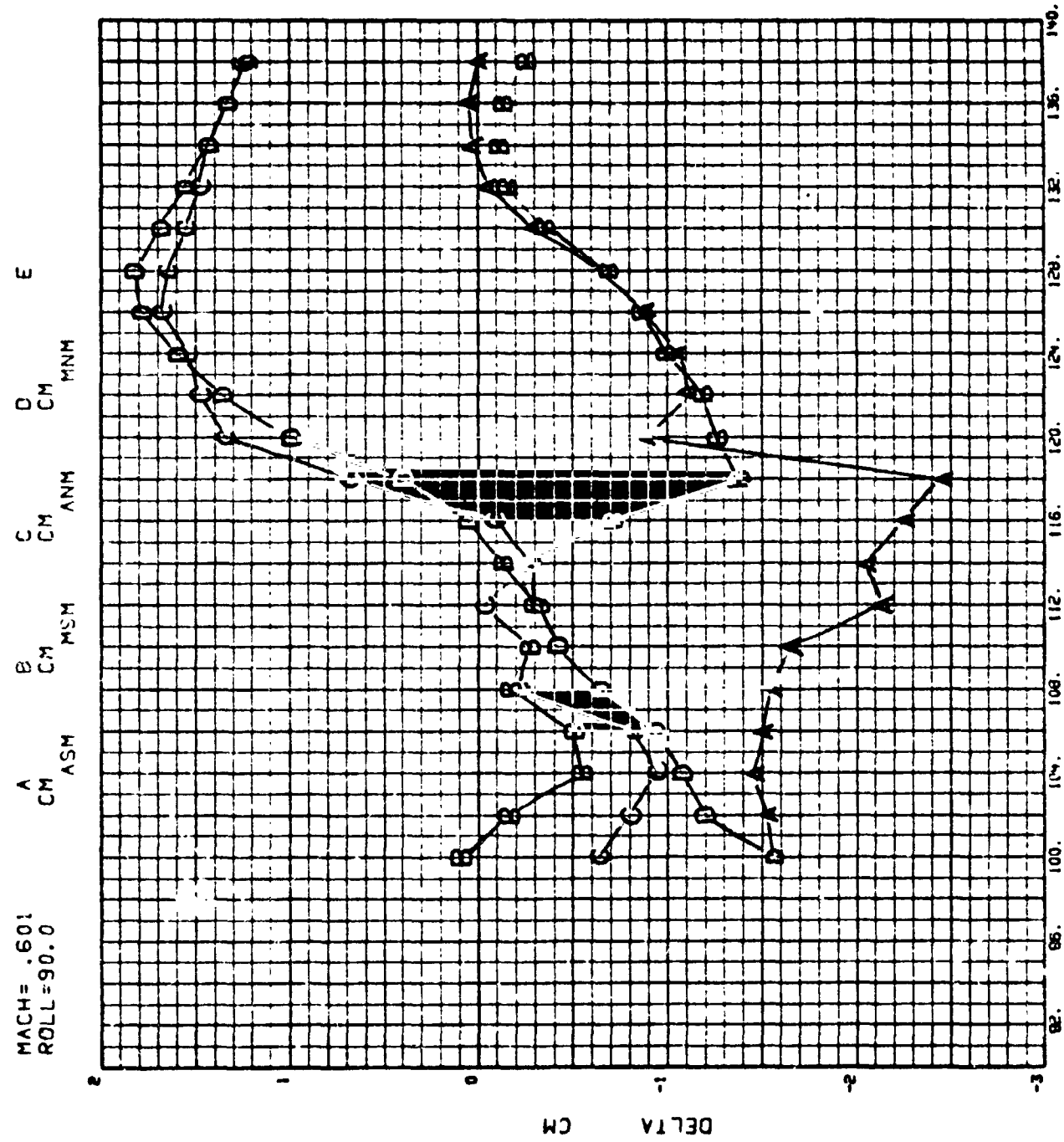

Figure 3-7. Sting Interference versus Angle of Attack, C_M, $M_\infty = 0.6$, $\phi = 90°$

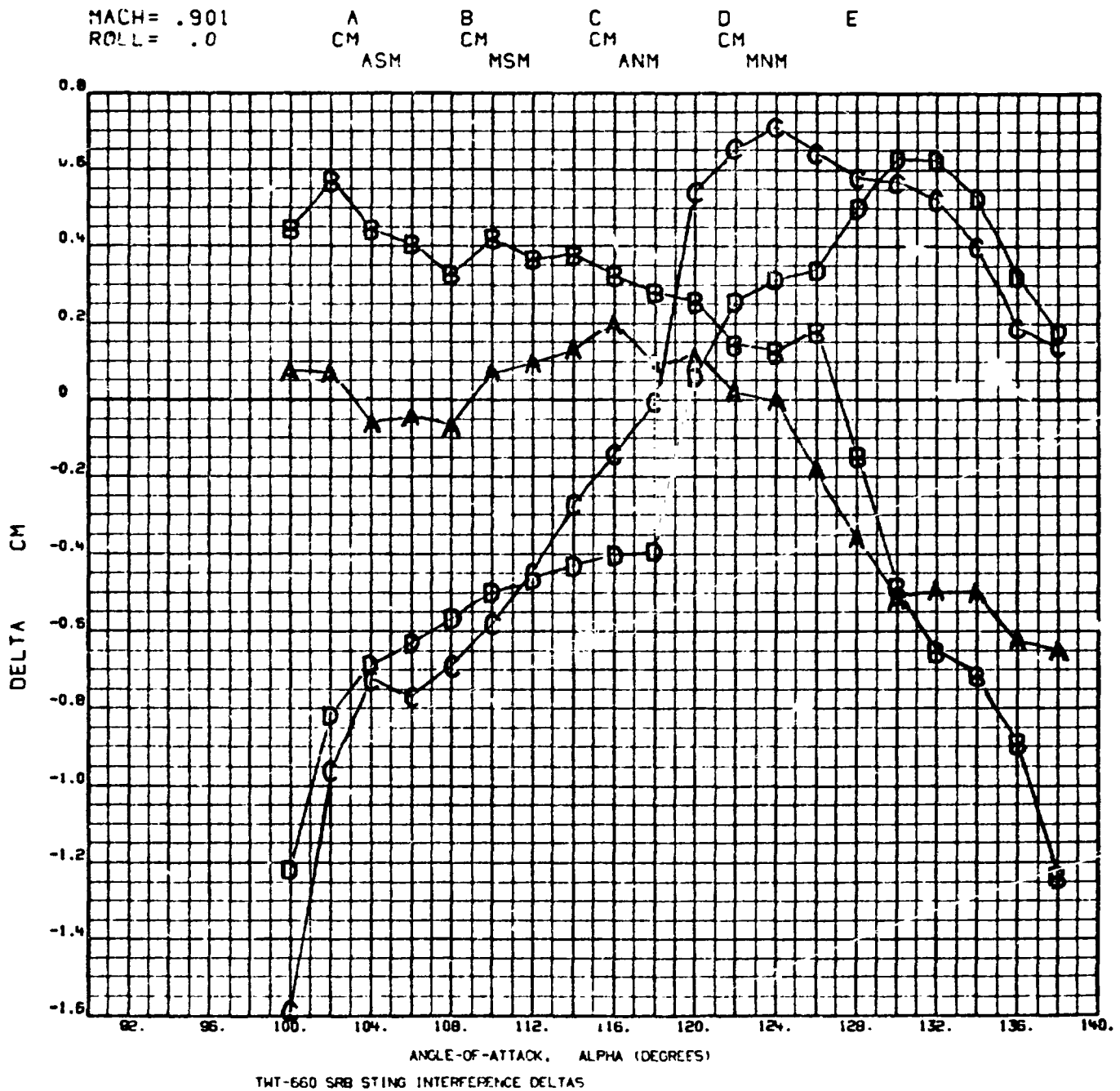

Figure 3-8. Sting Interference versus Angle of Attack, C_M, $M_\infty = 0.9$, $\phi = 0°$

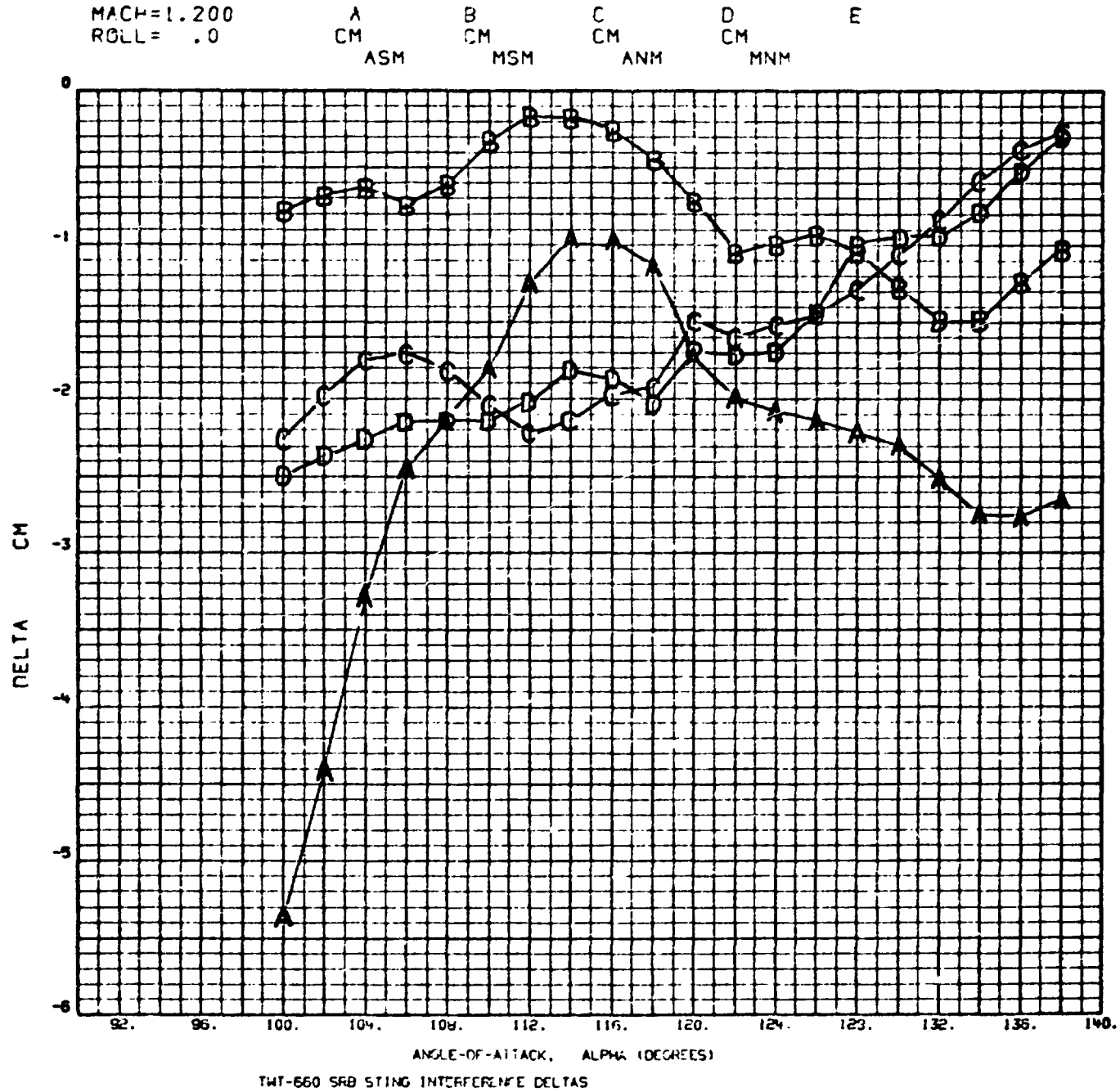

Figure 3-9. Sting Interference versus Angle of Attack, C_M, $M_\infty = 1.2$, $\phi = 0°$

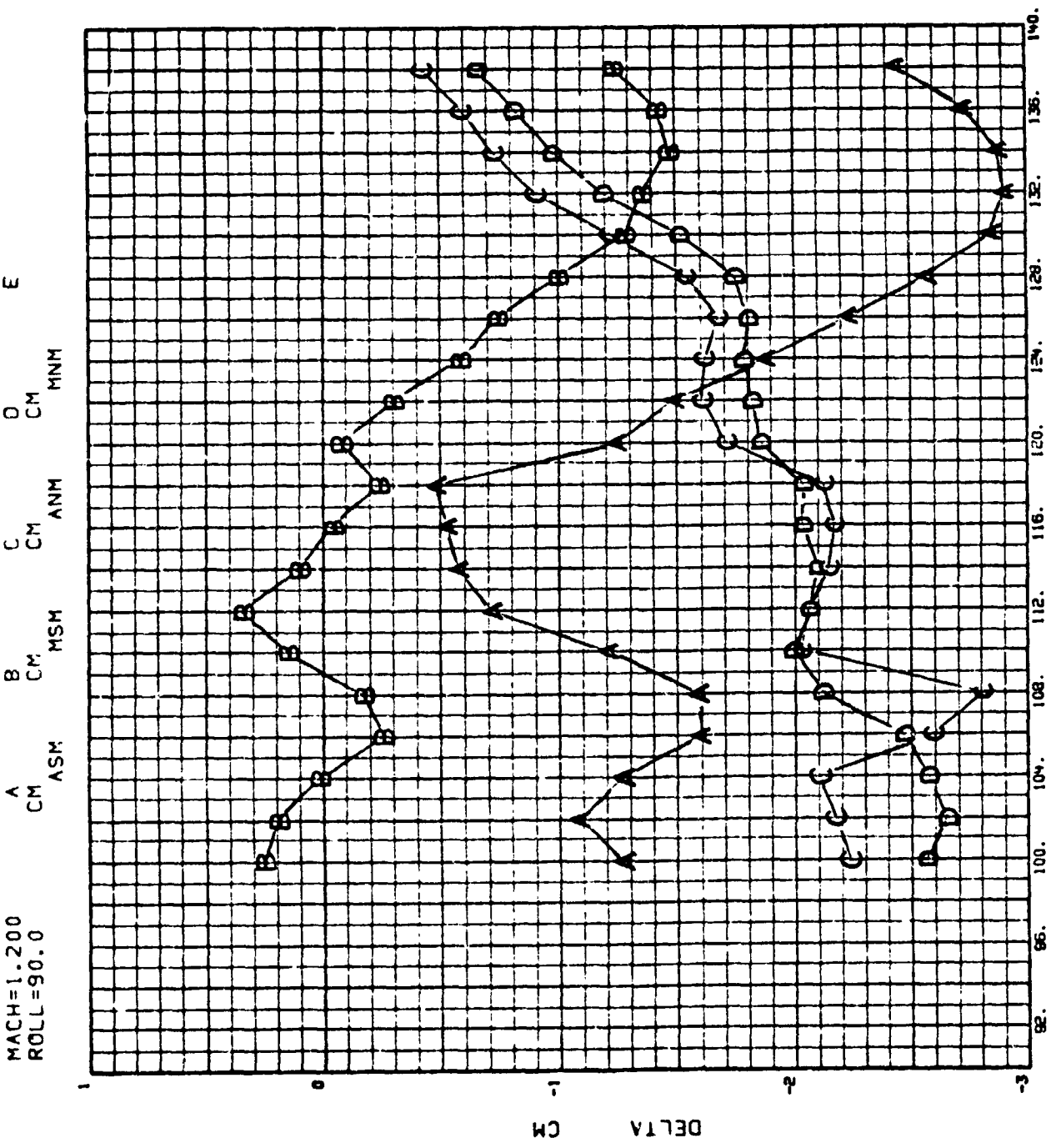

Figure 3-10. Sting Interference versus Angle of Attack, C_M, $M_\infty = 1.2$, $\phi = 90°$

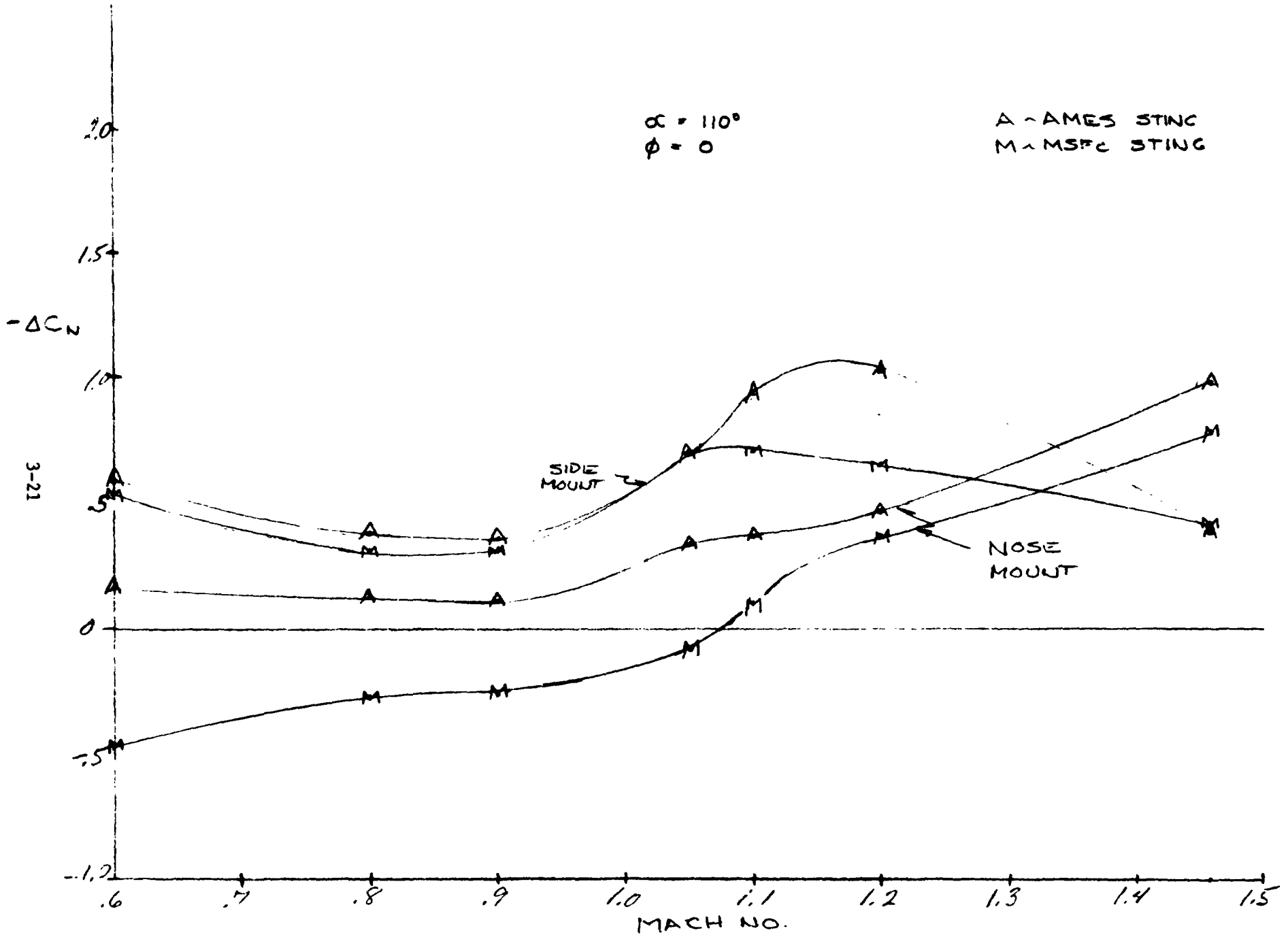

Figure 3-11. String Interference versus Mach Number, C_N, α = 110°

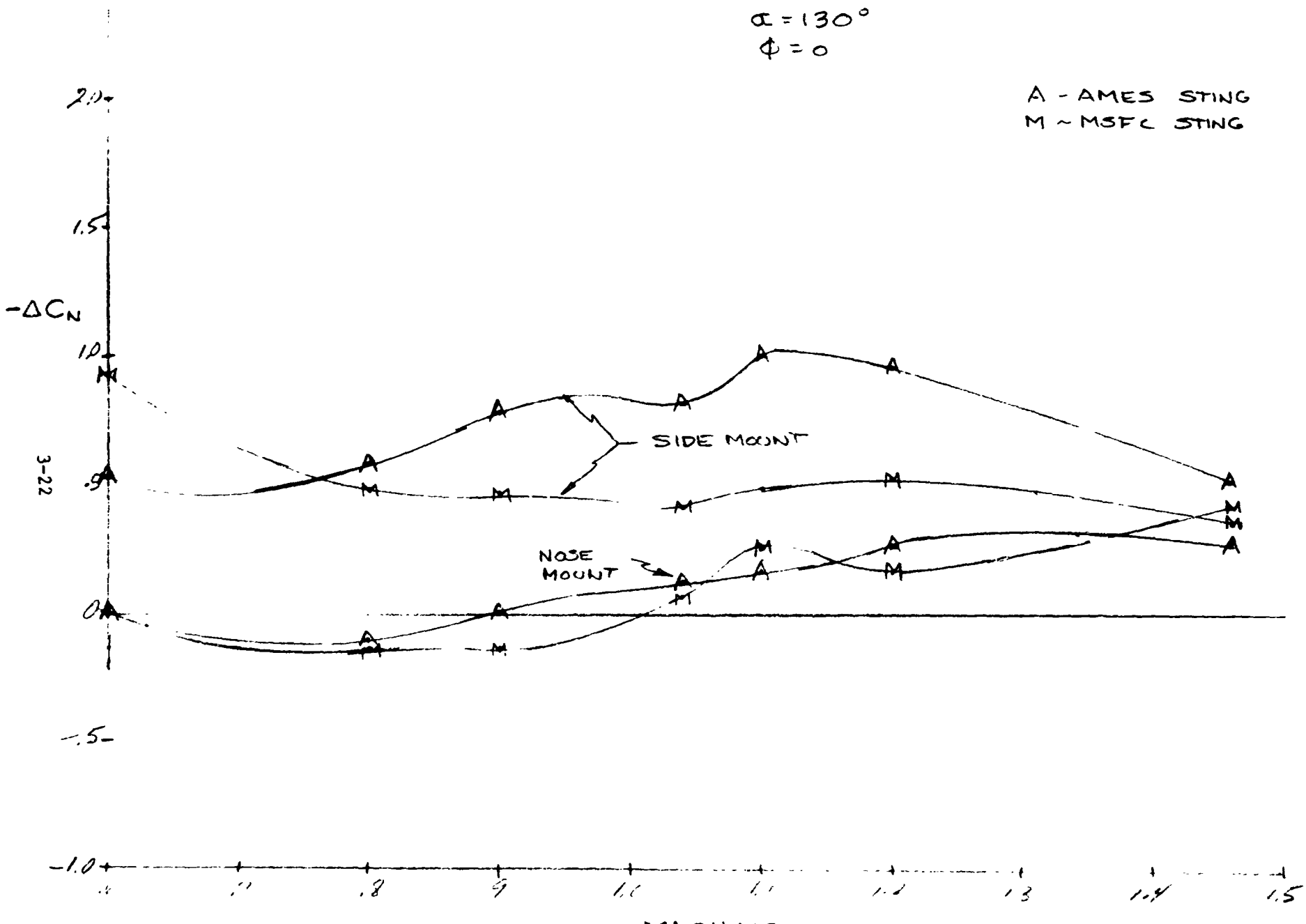

Figure 3-12. Sting Interference versus Mach Number, C_N, α = 130°

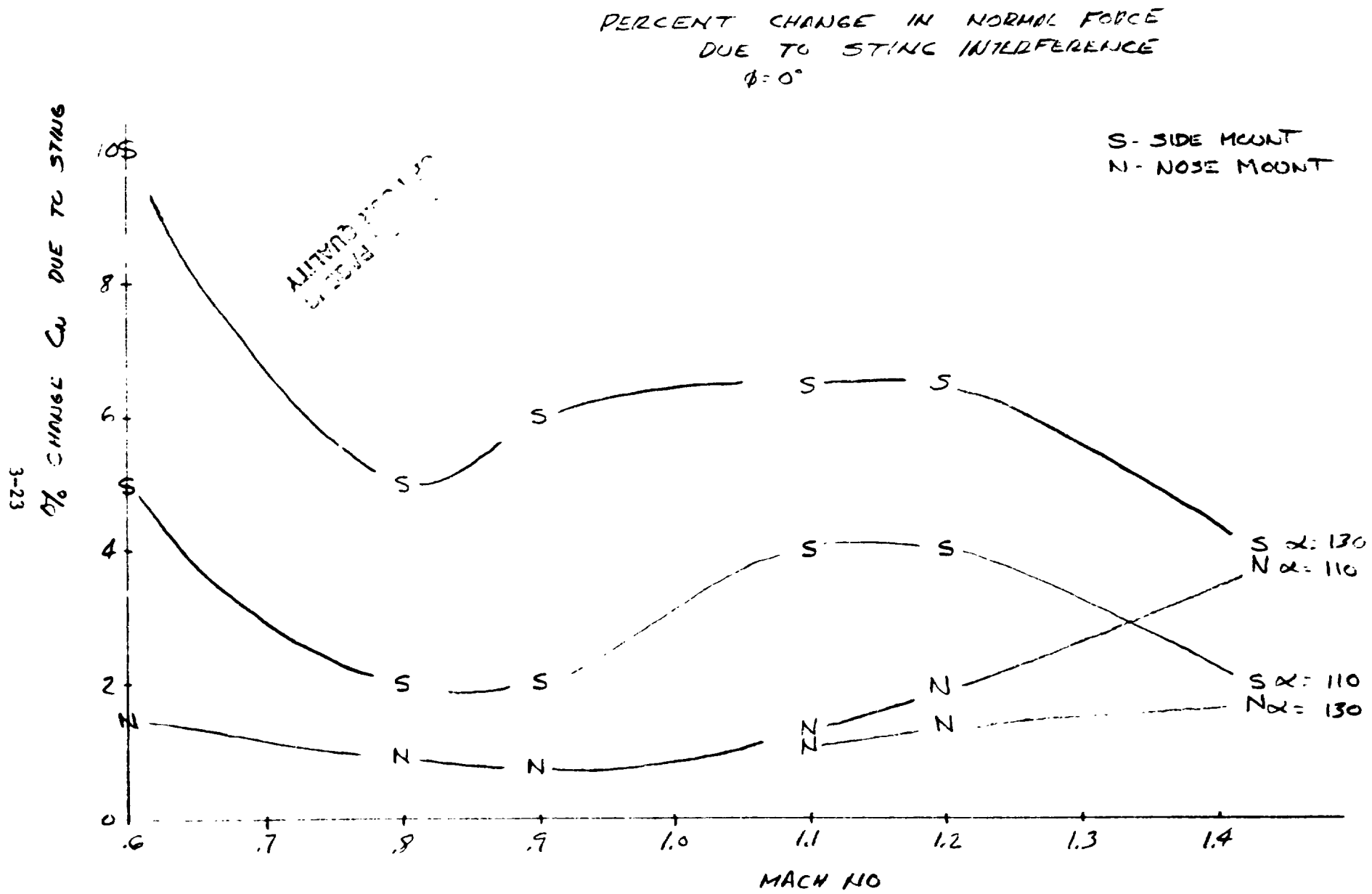

Figure 3-13. Sting Interference C_N Percent of Total

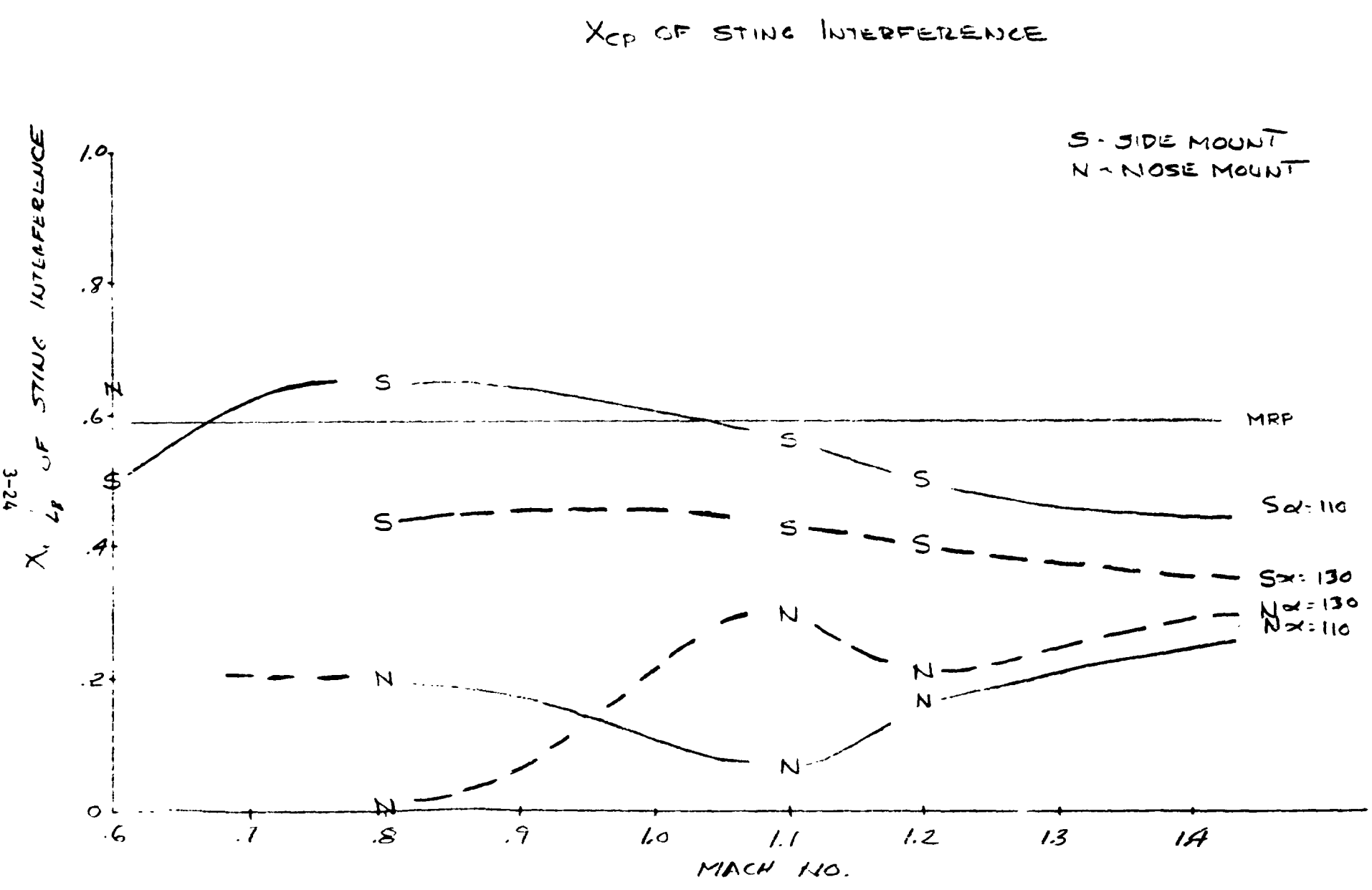

Figure 3-14. Sting Interference Center of Pressure

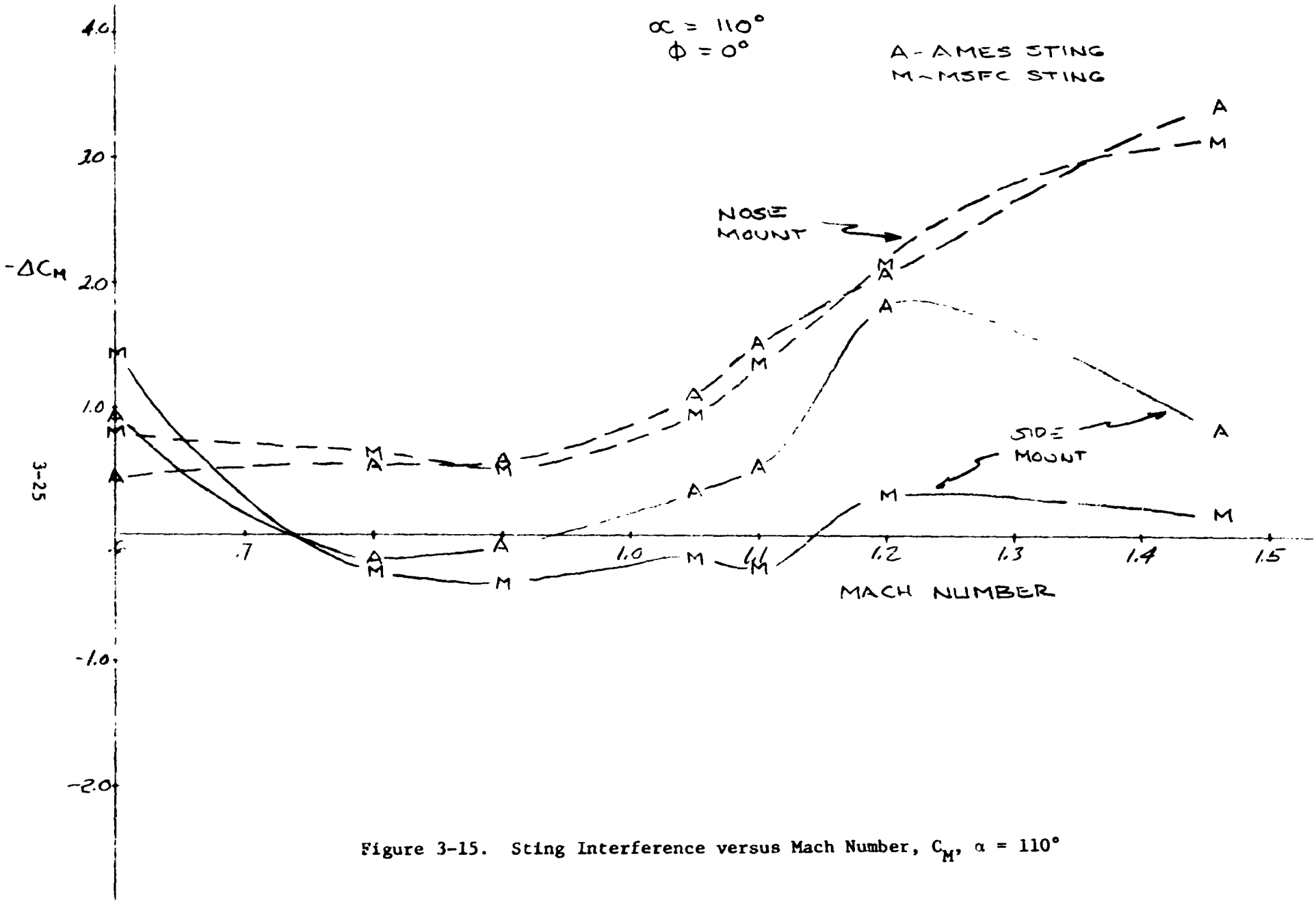

Figure 3-15. Sting Interference versus Mach Number, C_M, α = 110°

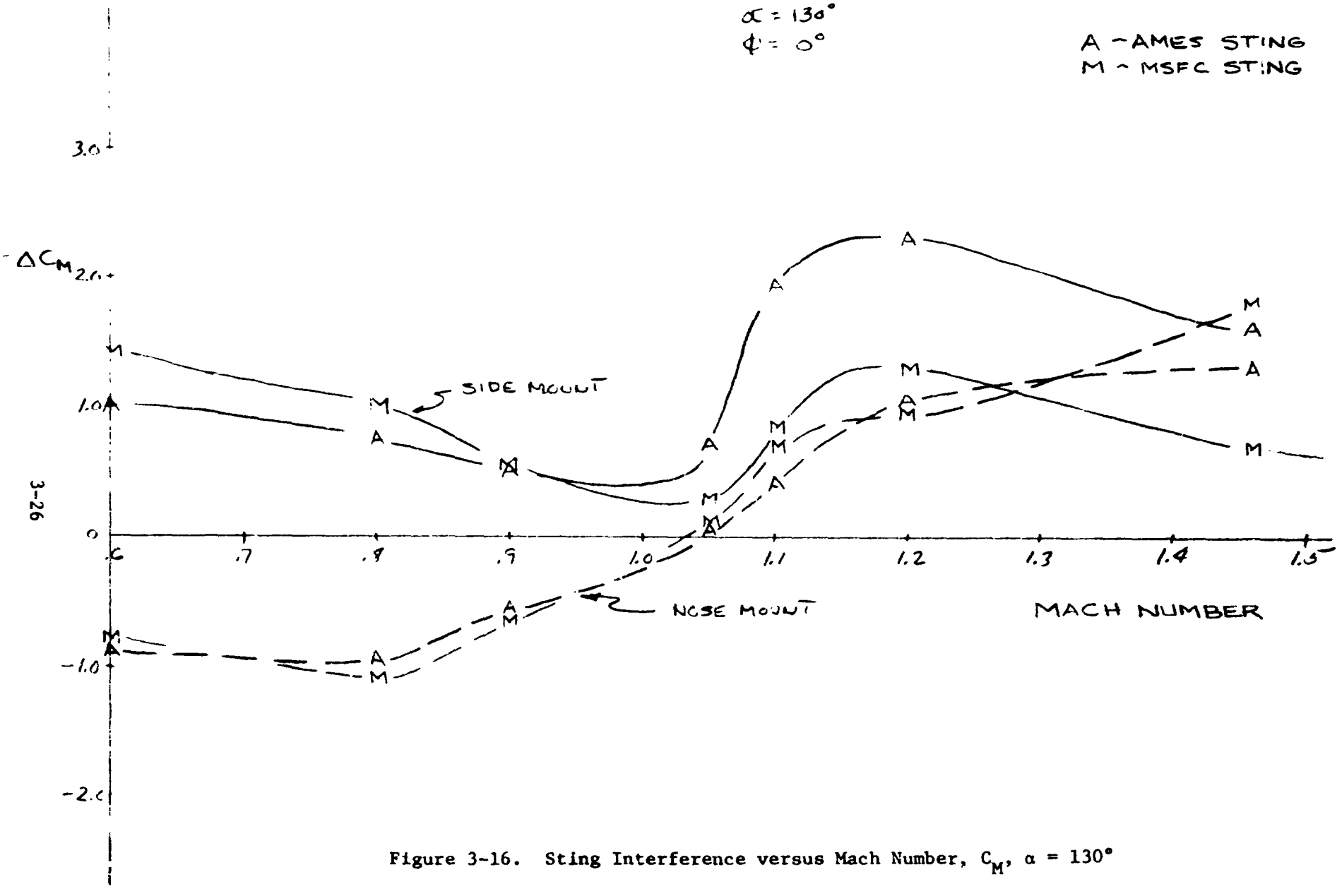

Figure 3-16. Sting Interference versus Mach Number, C_M, α = 130°

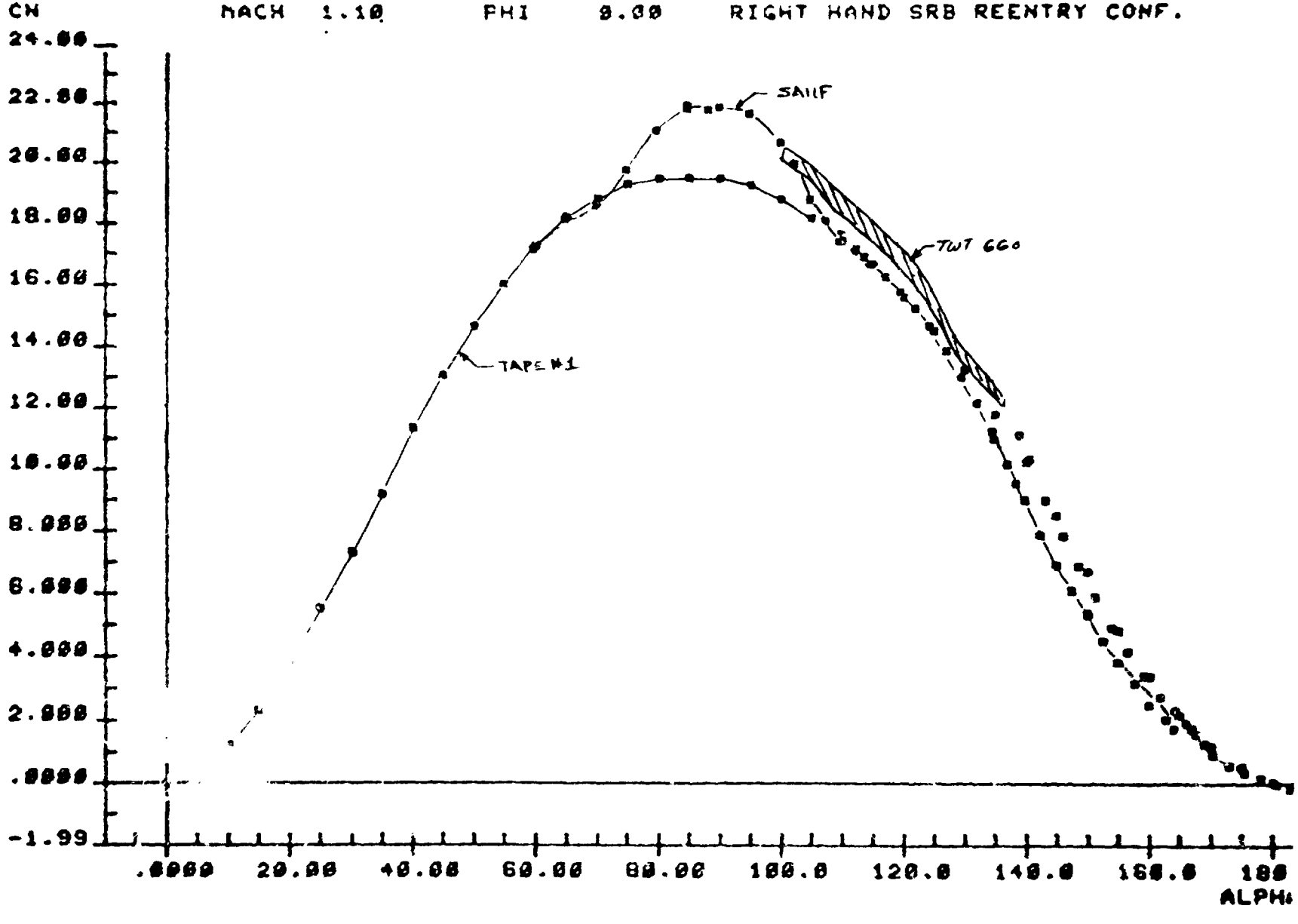

Figure 3-17. Normal Force Coefficient Versus α, M_∞ = 1.1, ϕ = 0

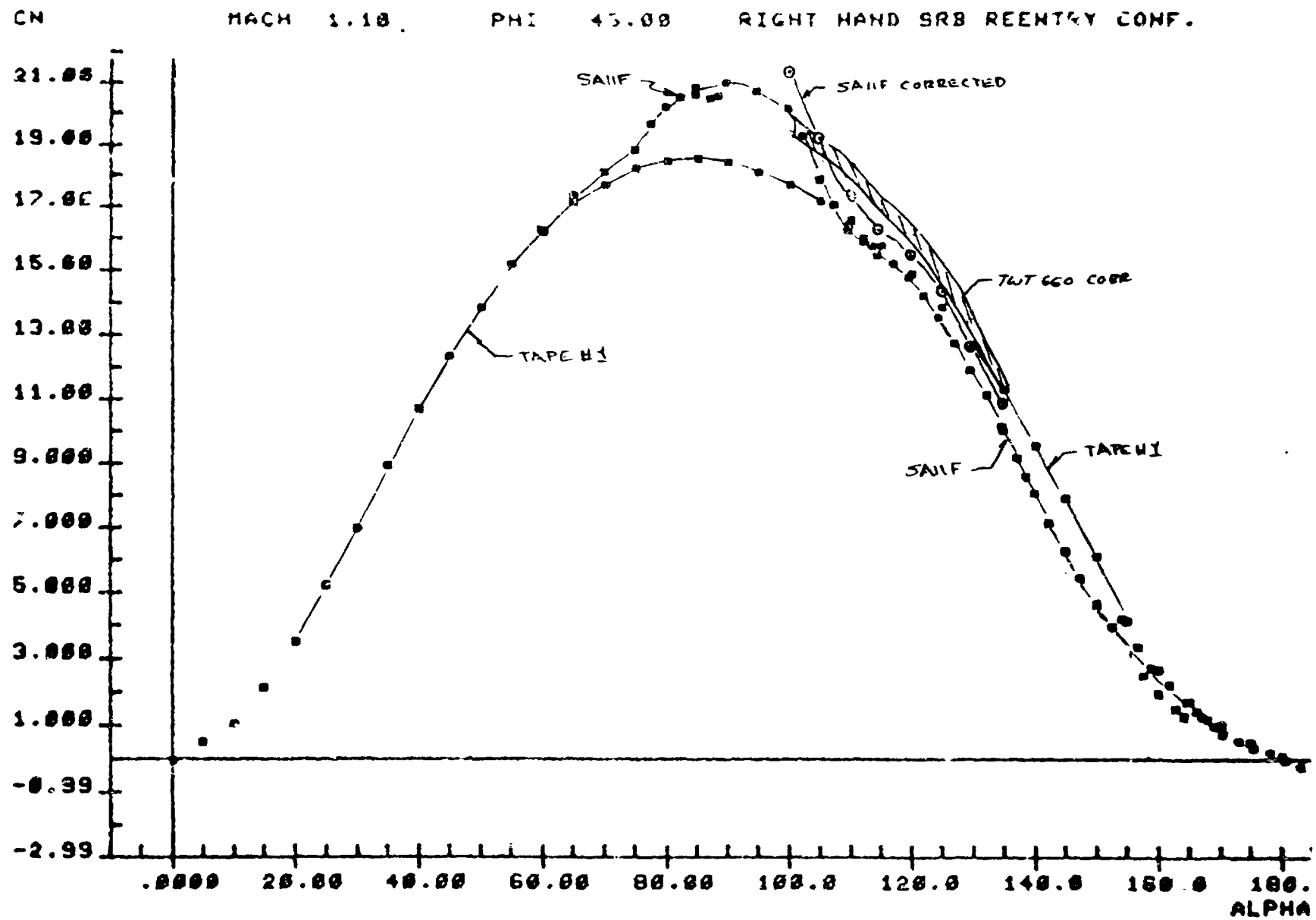

Figure 3-18. Normal Force Coefficient Versus α, M_∞ = 1.1, ϕ = 45

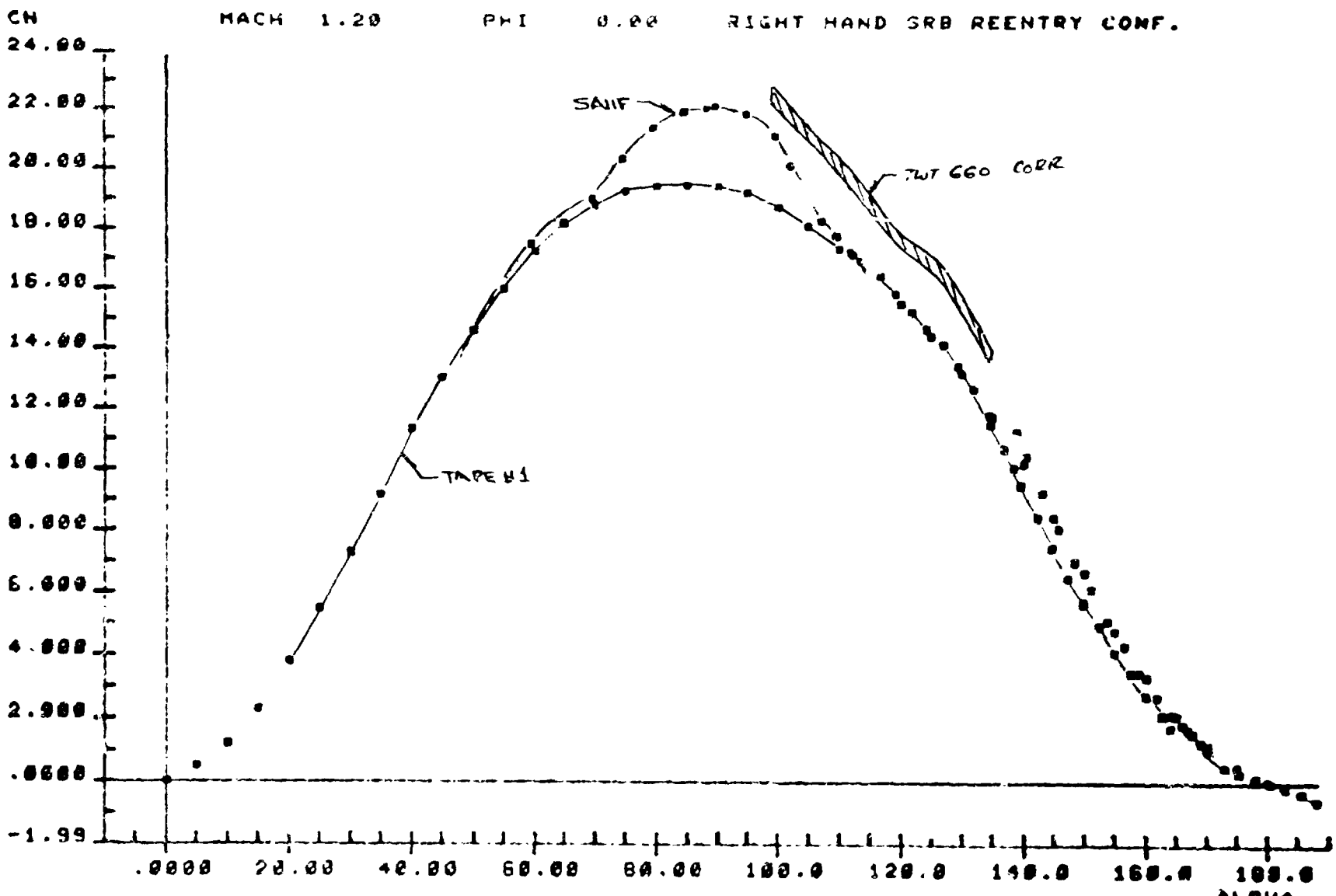

Figure 3-19. Normal Force Coefficient Versus α, $M_\infty = 1.2$, $\phi = 0$

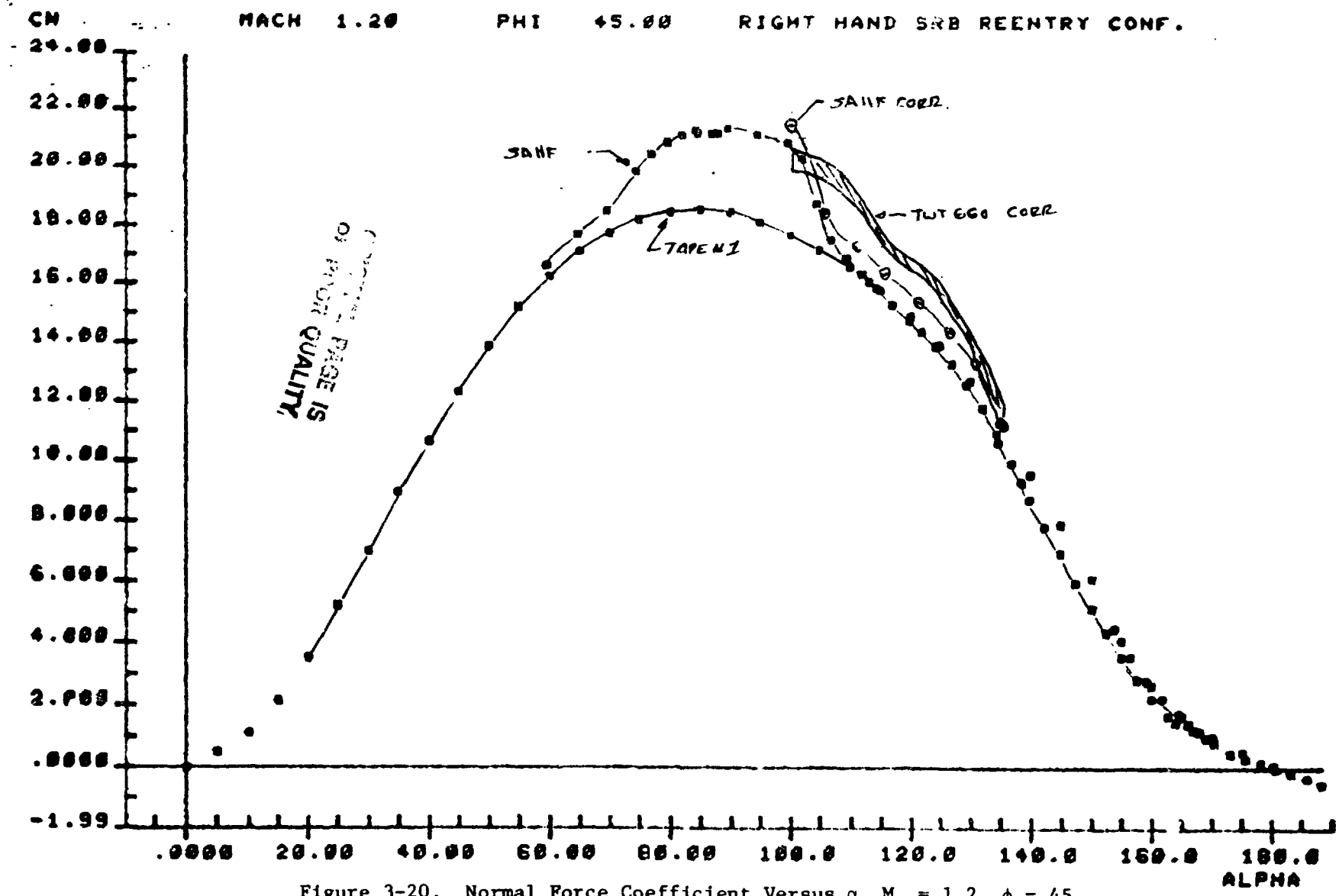

Figure 3-20. Normal Force Coefficient Versus α, $M_\infty = 1.2$, $\phi = 45$

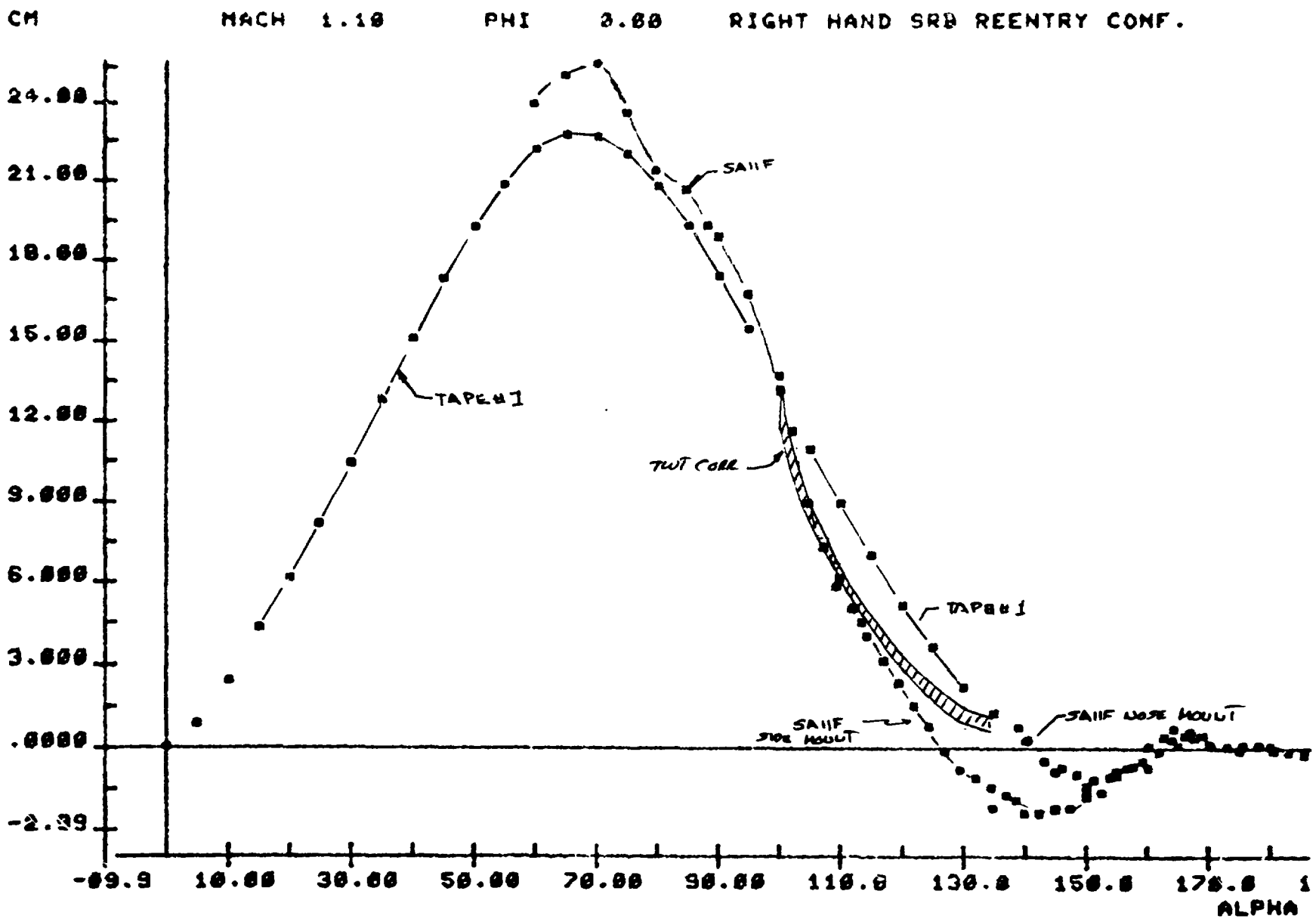

Figure 3-21. Pitching Moment Coefficient Versus α, $M_\infty = 1.1$, $\phi = 0$

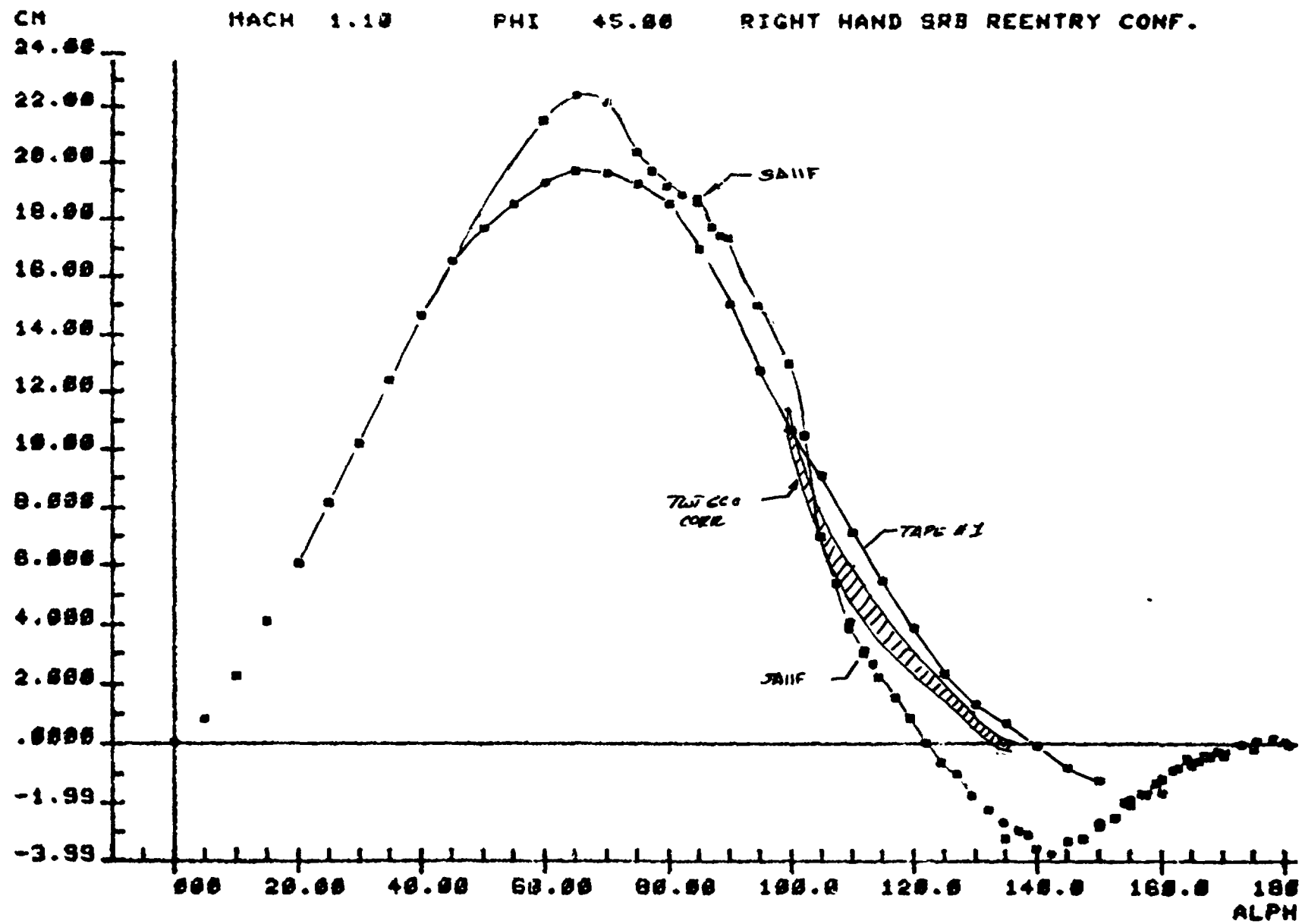

Figure 3-22. Pitching Moment Coefficient Versus α, $M_\infty = 1.1$, $\phi = 45$

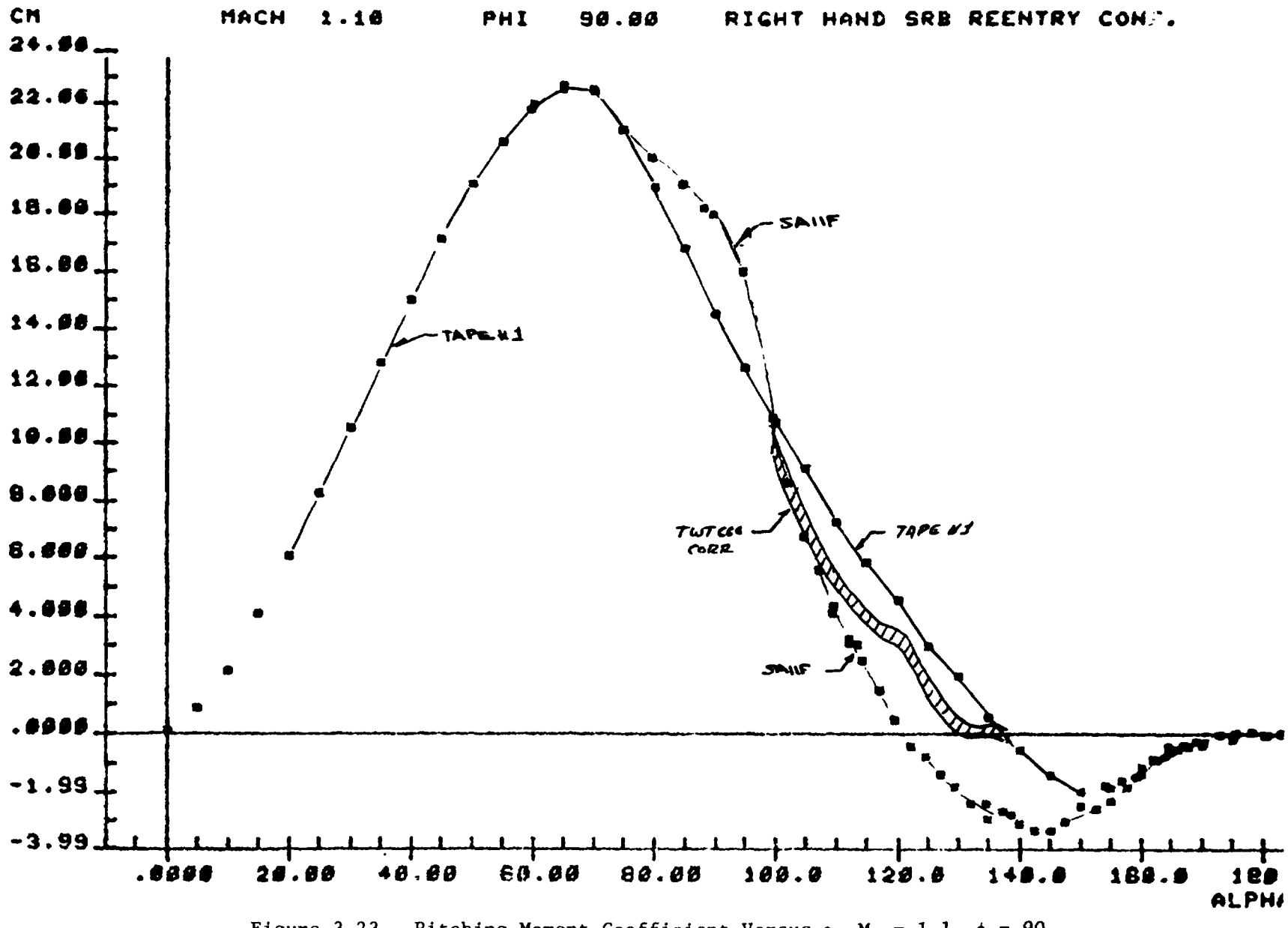

Figure 3-23. Pitching Moment Coefficient Versus α, $M_\infty = 1.1$, $\phi = 90$

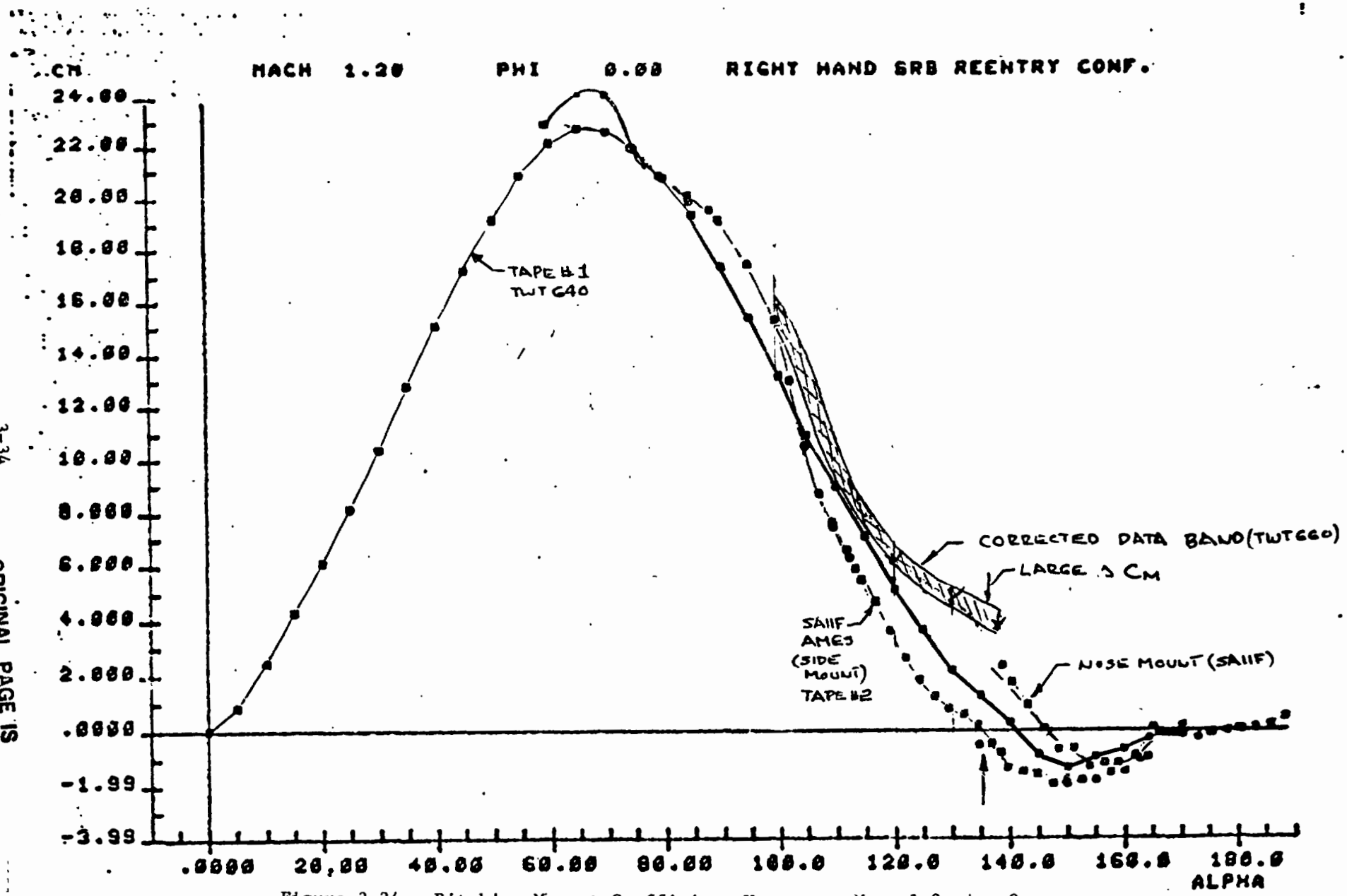

Figure 3-24. Pitching Moment Coefficient Versus α, $M_\infty = 1.2$, $\phi = 0$

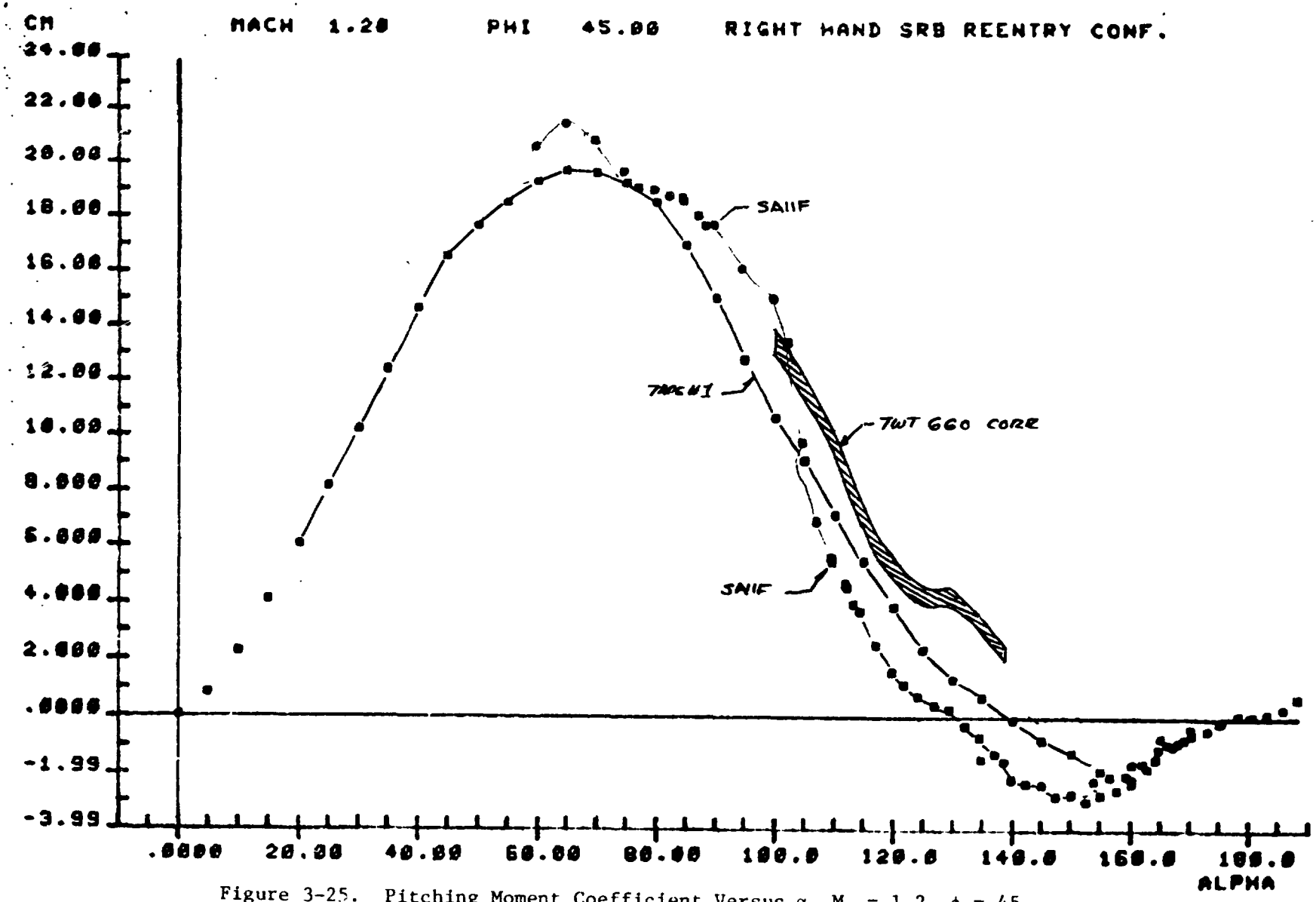

Figure 3-25. Pitching Moment Coefficient Versus α, $M_\infty = 1.2$, $\phi = 45$

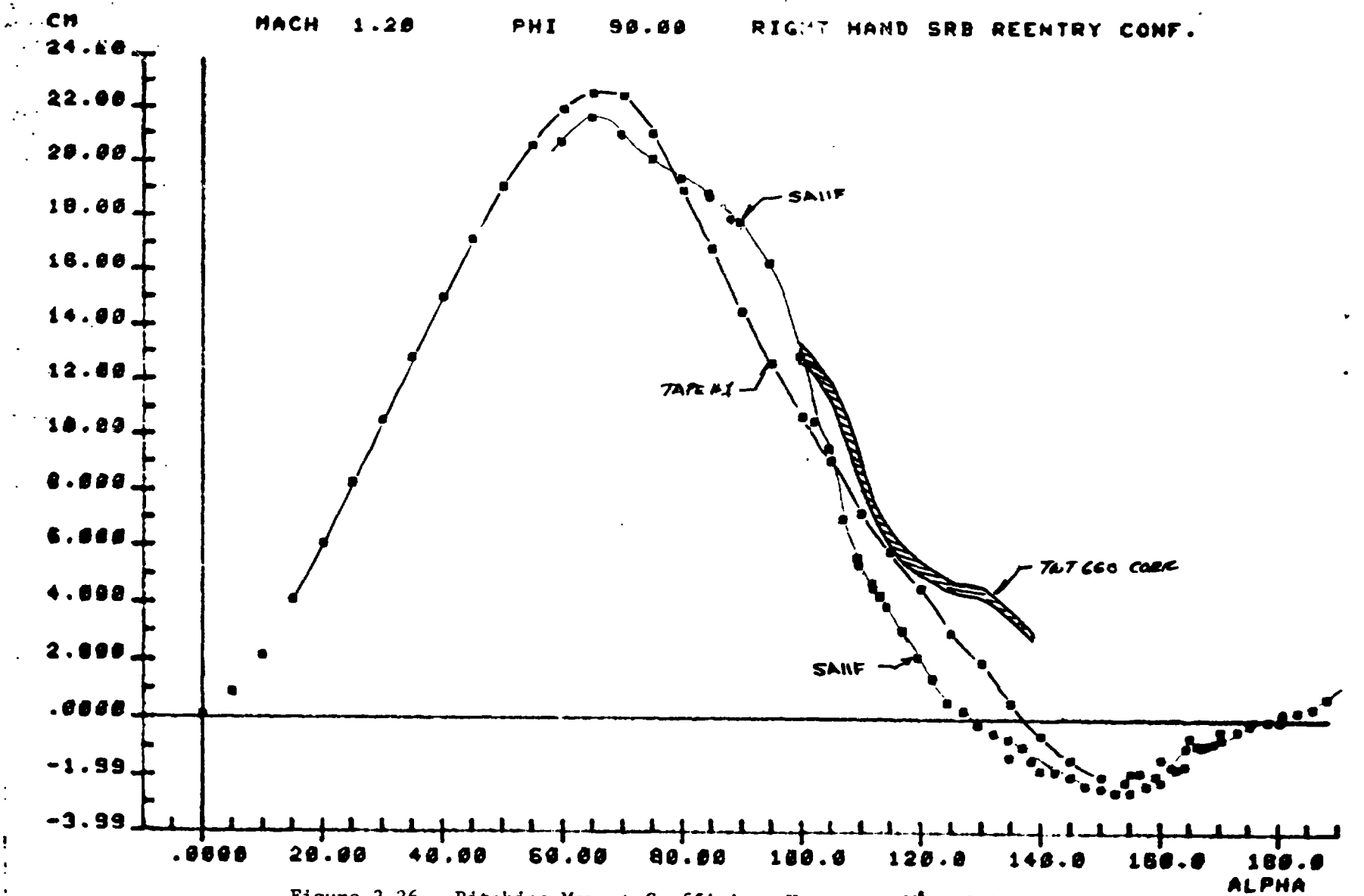

Figure 3-26. Pitching Moment Coefficient Versus α, $M_\infty^* = 1.2$, $\phi = 90$

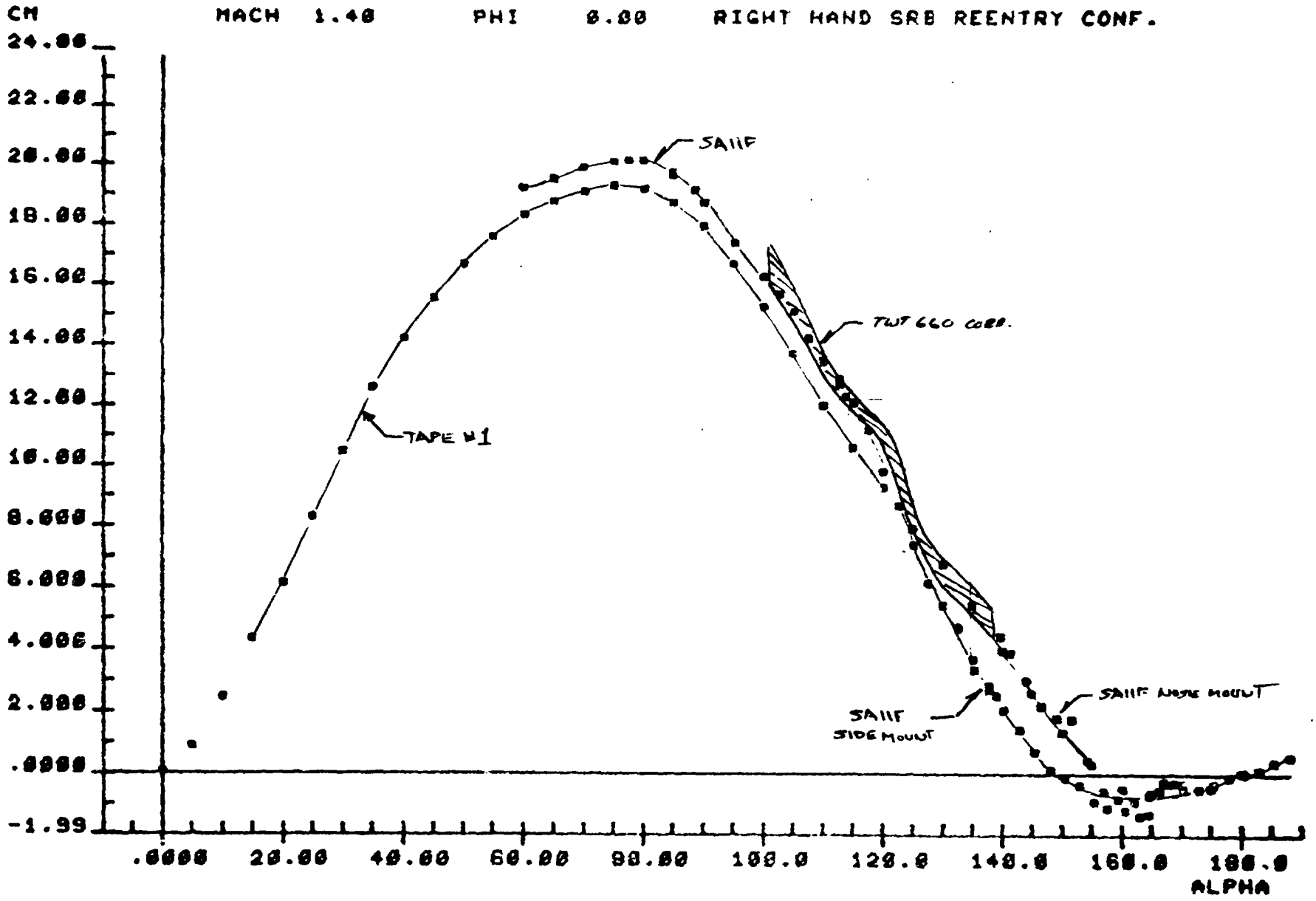

Figure 3-27. Pitching Moment Coefficient Versus α, $M_\infty = 1.4$, $\phi = 0$

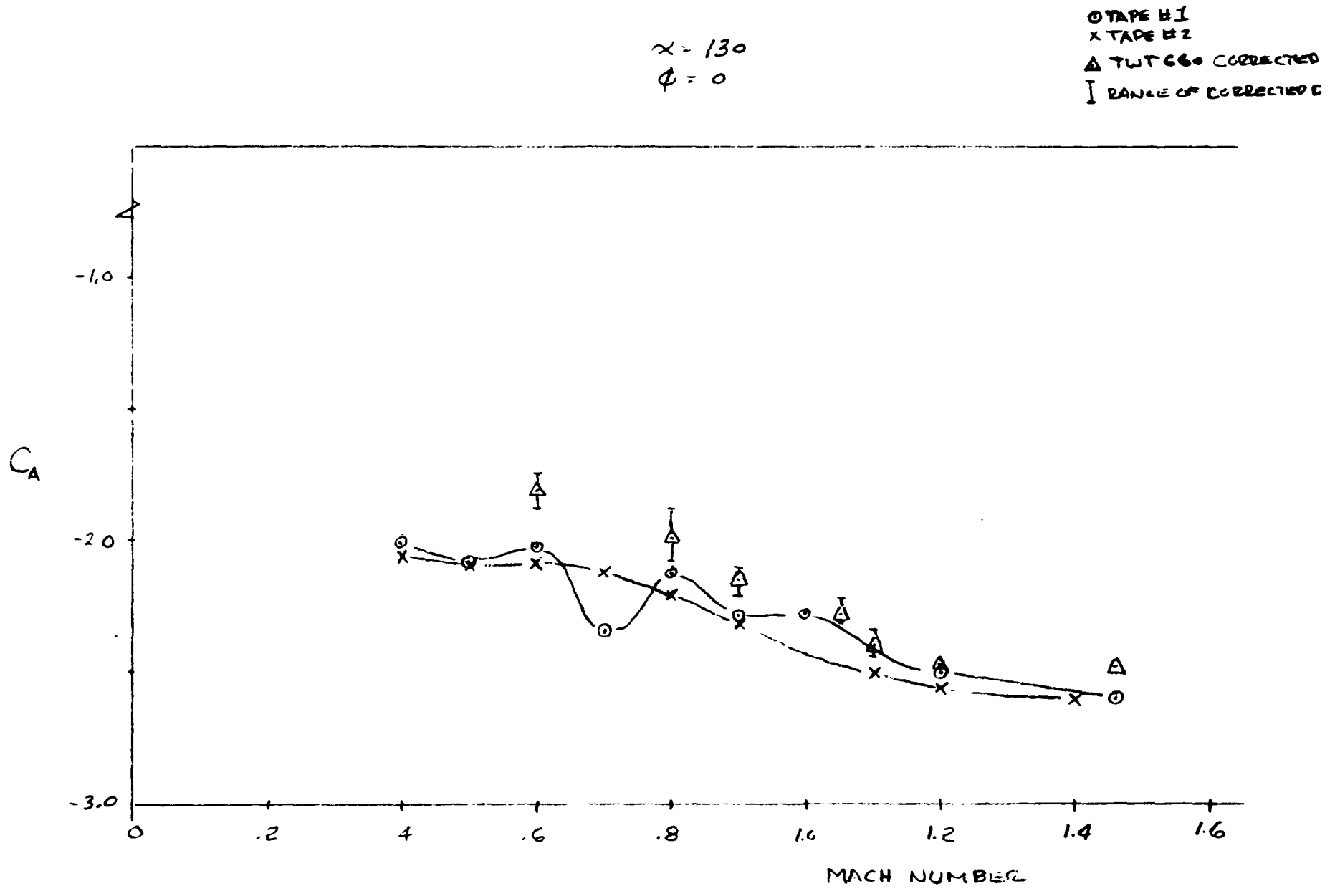

Figure 3-28. Axial Force Coefficient Versus Mach Number

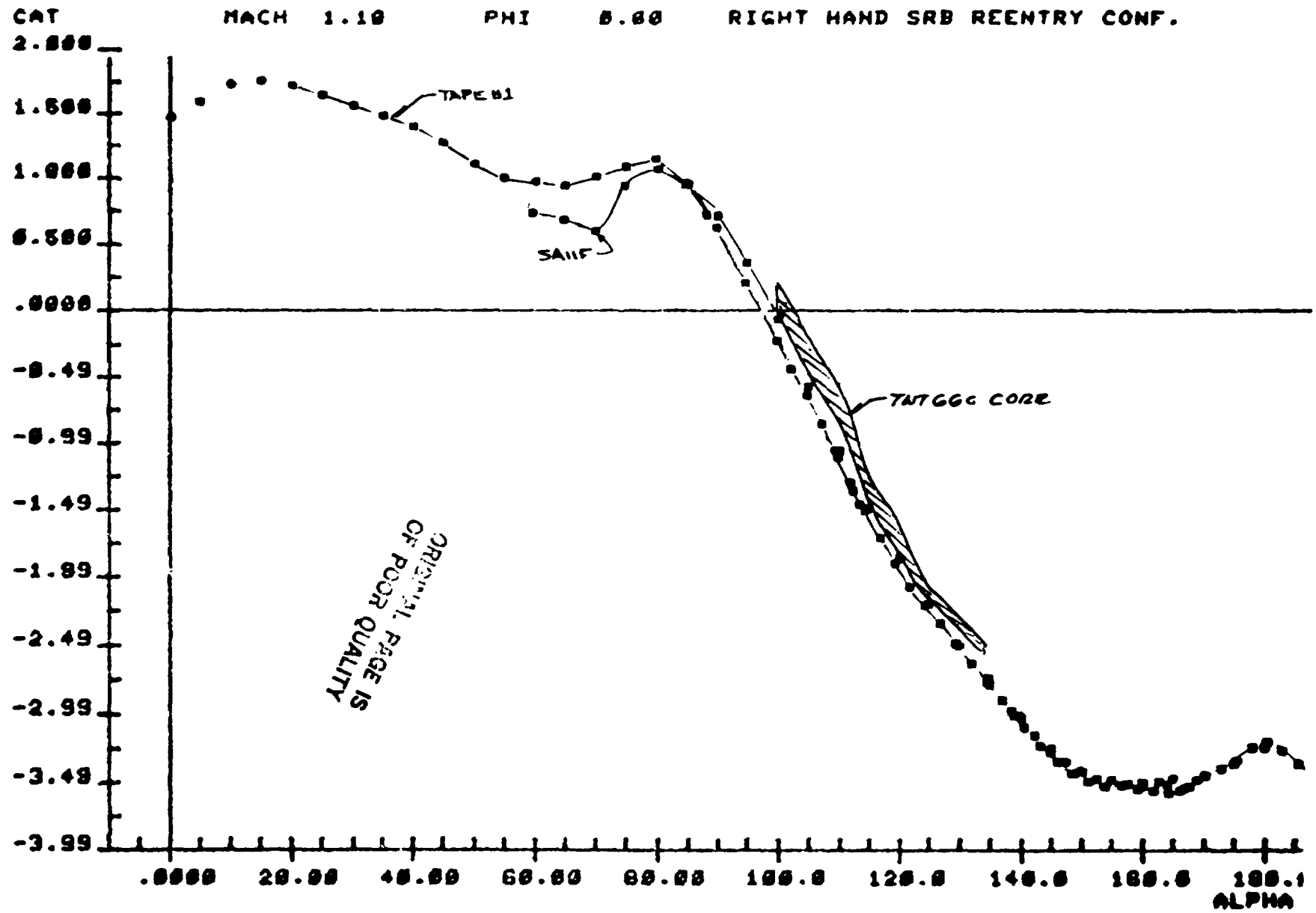

Figure 3-29. Axial Force Coefficient Versus α, $M_\infty = 1.1$, $\phi = 0$

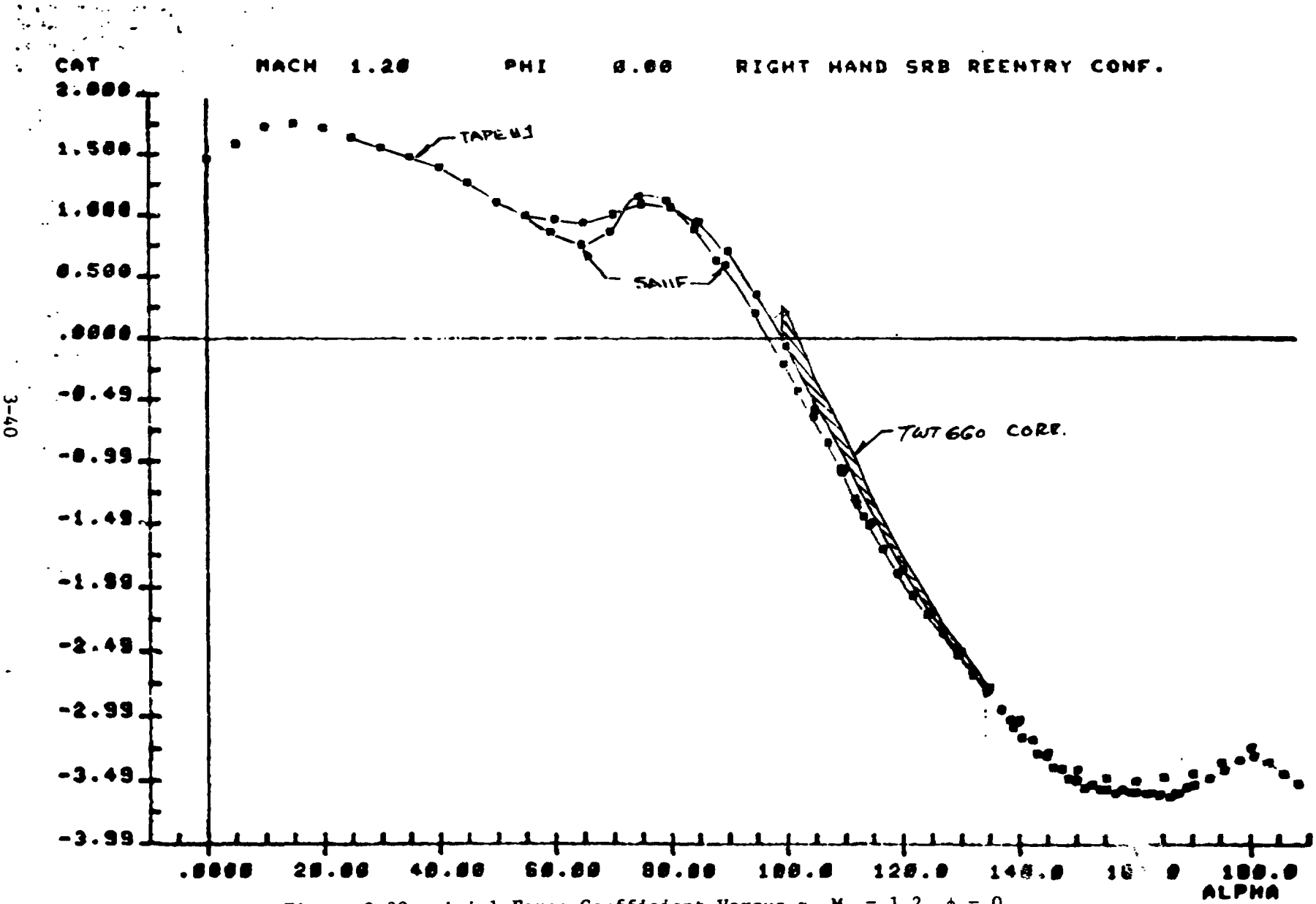

Figure 3-30. Axial Force Coefficient Versus α, $M_\infty = 1.2$, $\phi = 0$

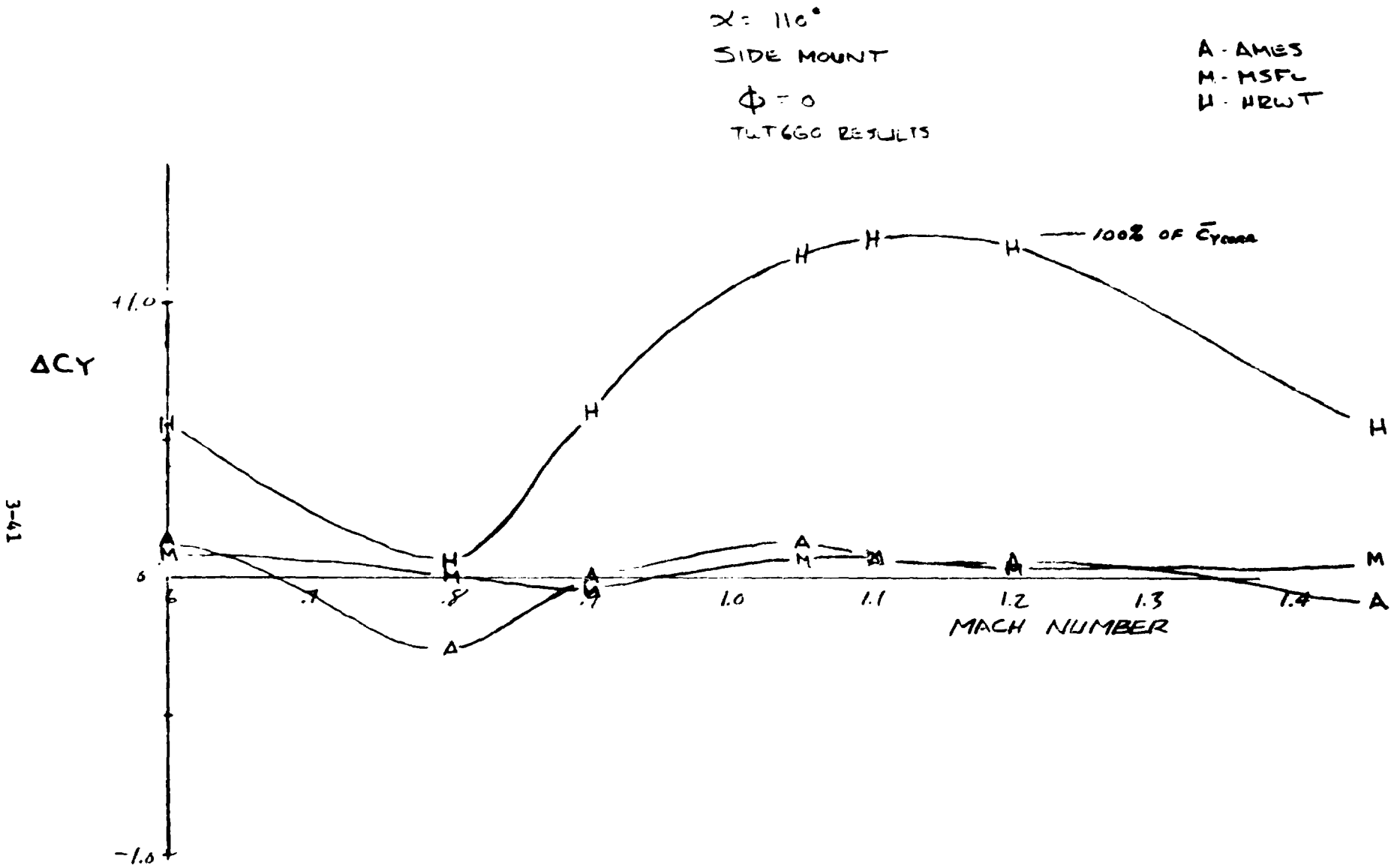

Figure 3-31. Side Force Sting Interference Versus Mach Number α = 110°

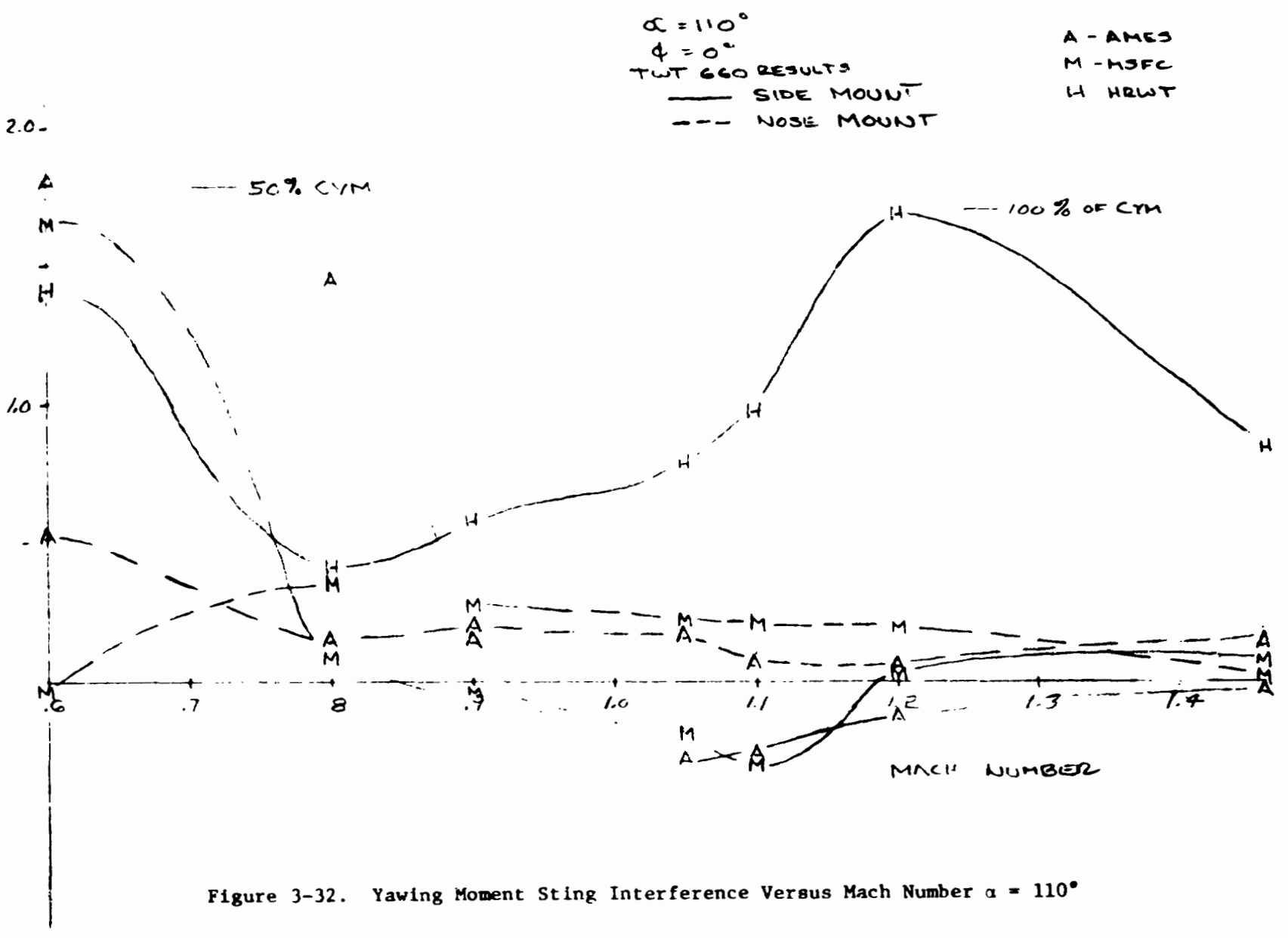

Figure 3-32. Yawing Moment Sting Interference Versus Mach Number α = 110°

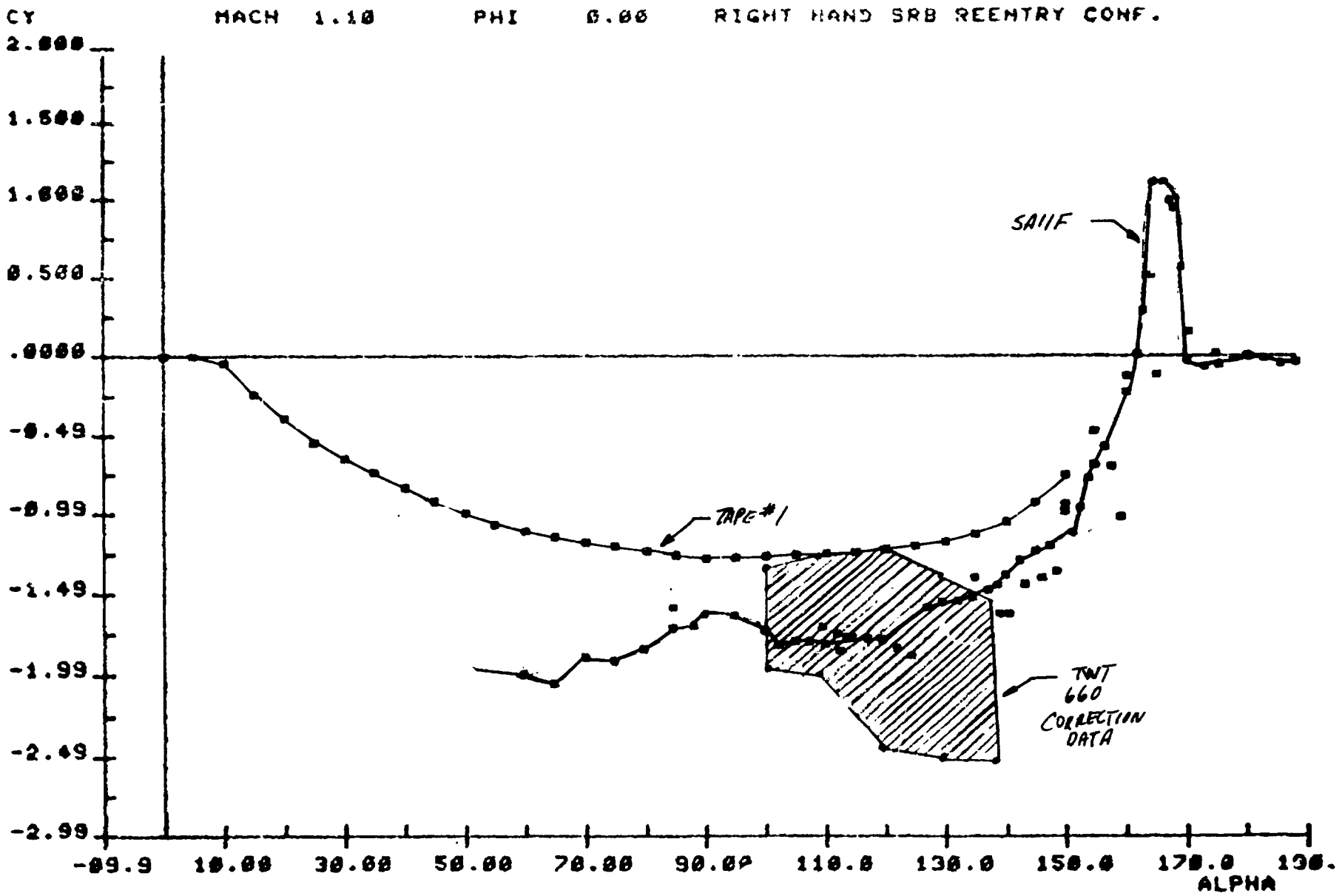

Figure 3-33. Side Force Coefficient Versus α, $M_\infty = 1.1$, $\phi = 0$

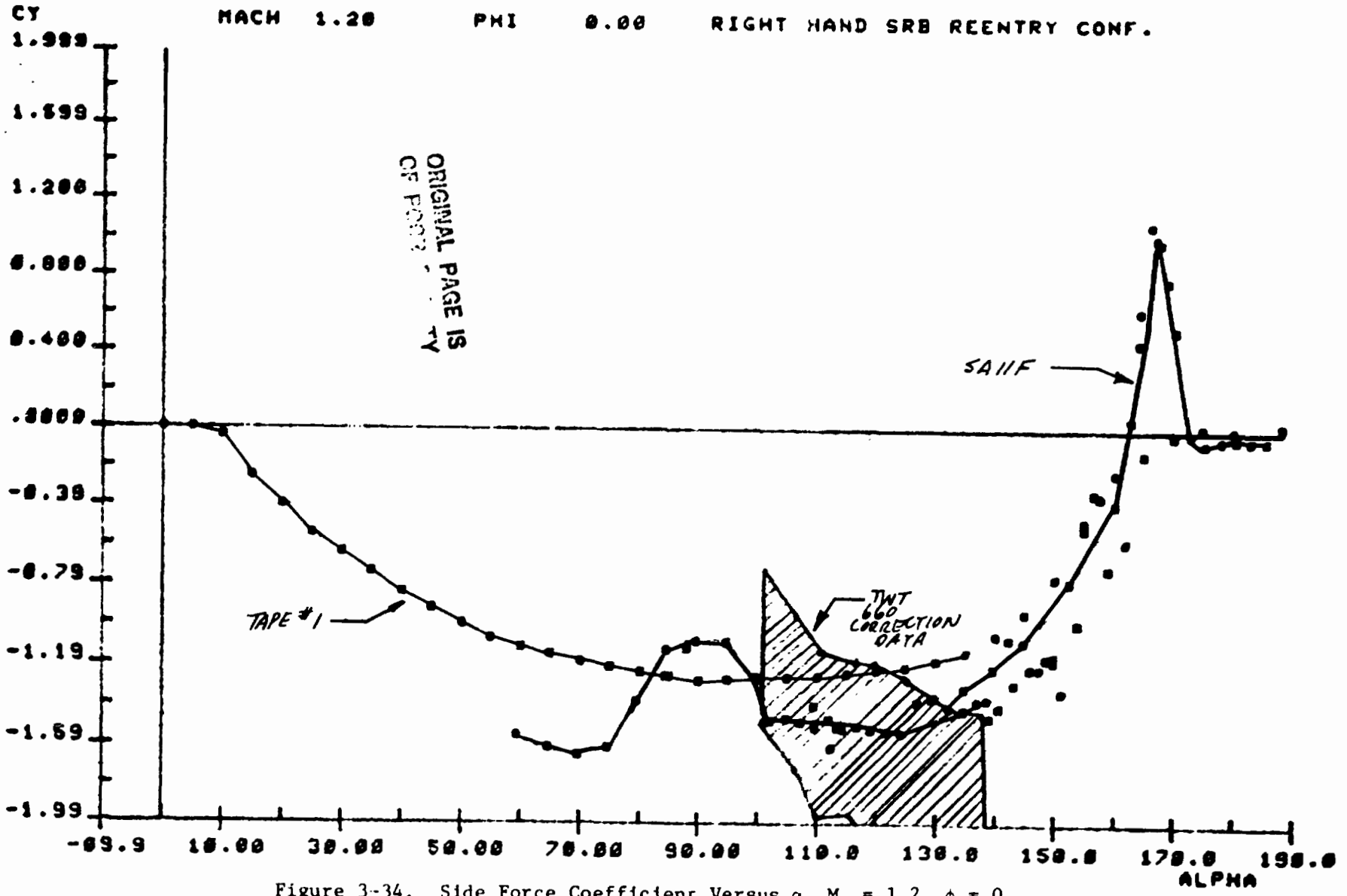

Figure 3-34. Side Force Coefficient Versus α, $M_\infty = 1.2$, $\phi = 0$

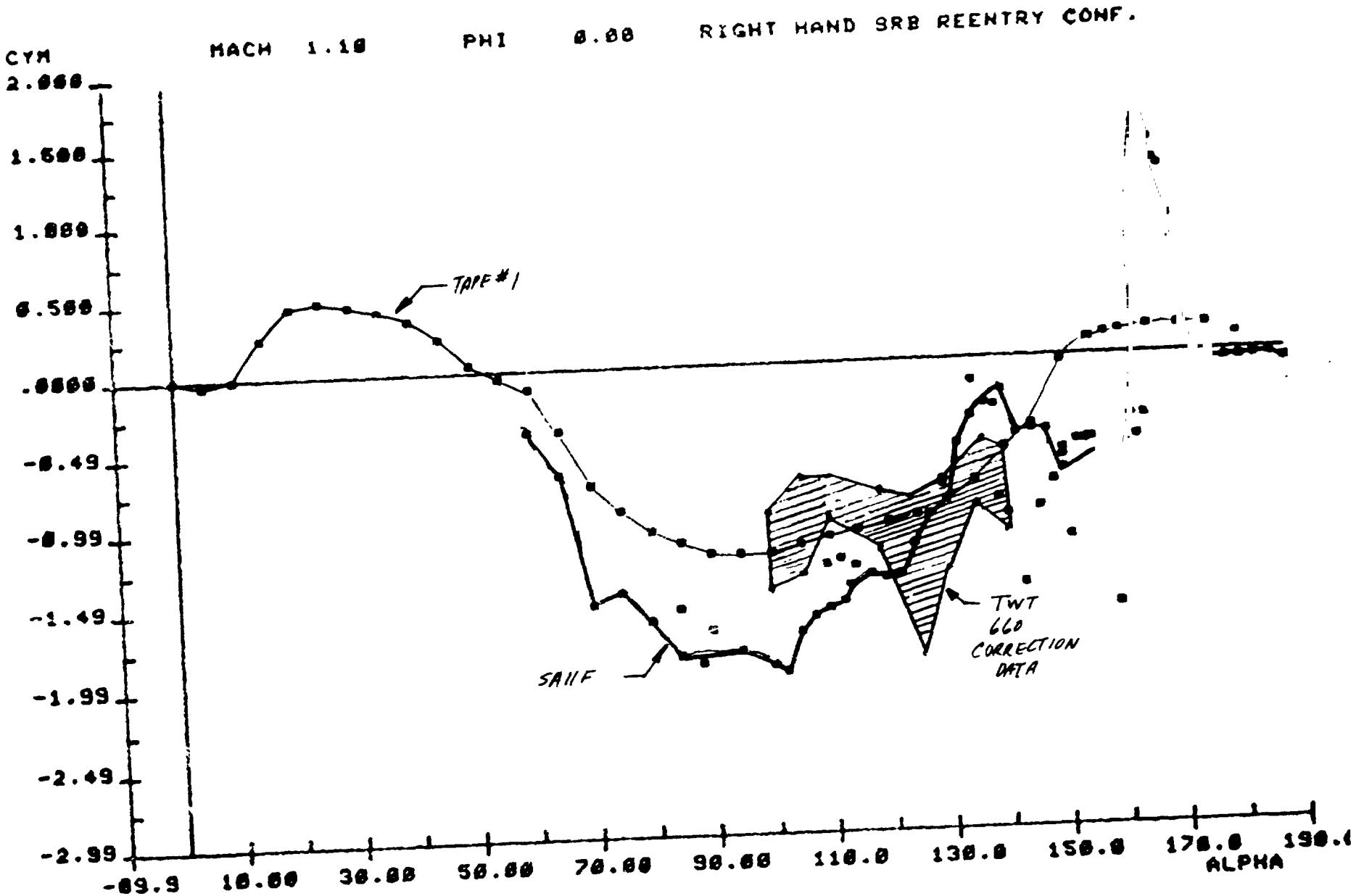

Figure 3-35. Yawing Moment Coefficient Versus α, $M_\infty = 1.1$, $\phi = 0$

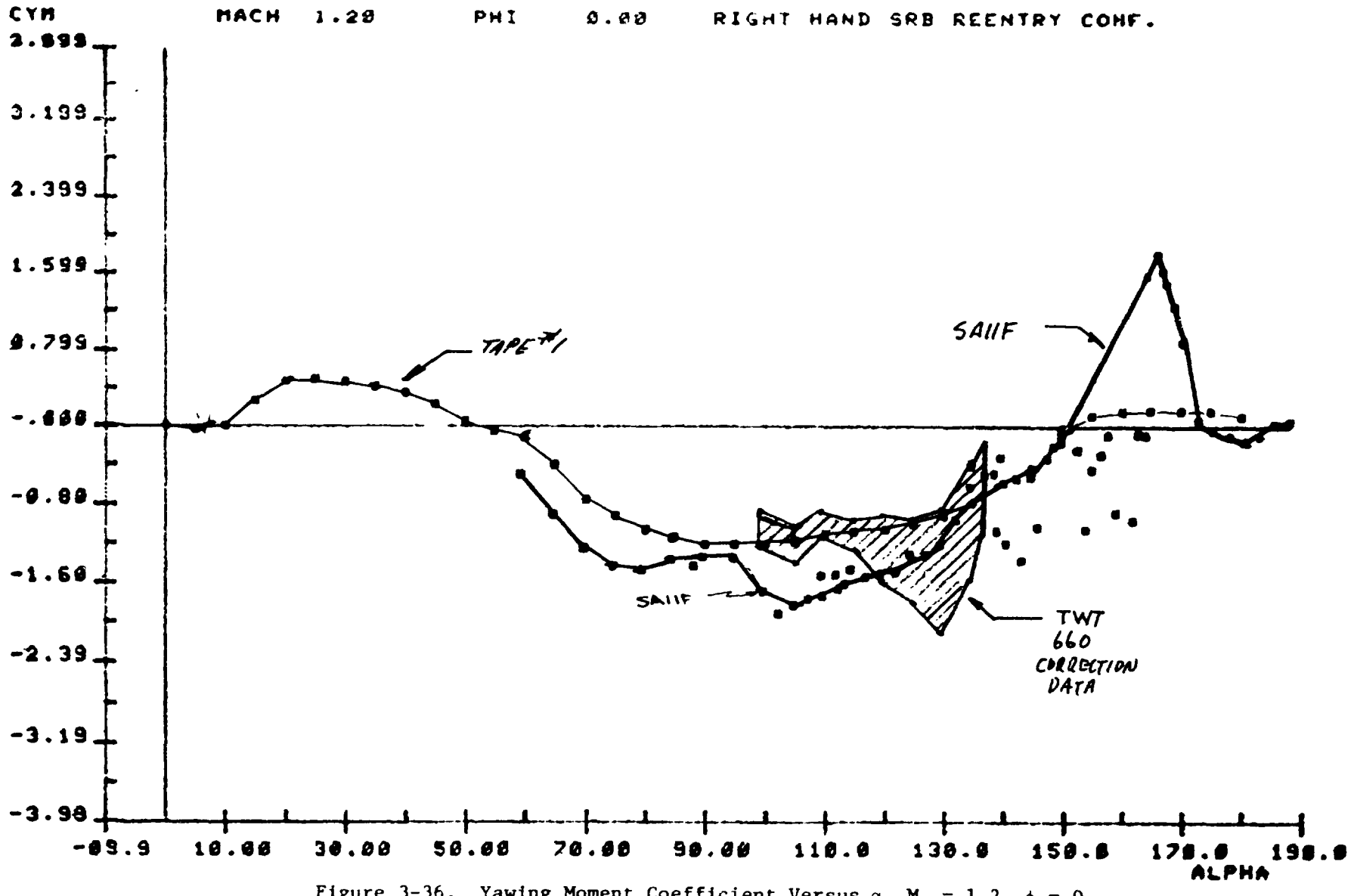

Figure 3-36. Yawing Moment Coefficient Versus α, $M_\infty = 1.2$, $\phi = 0$

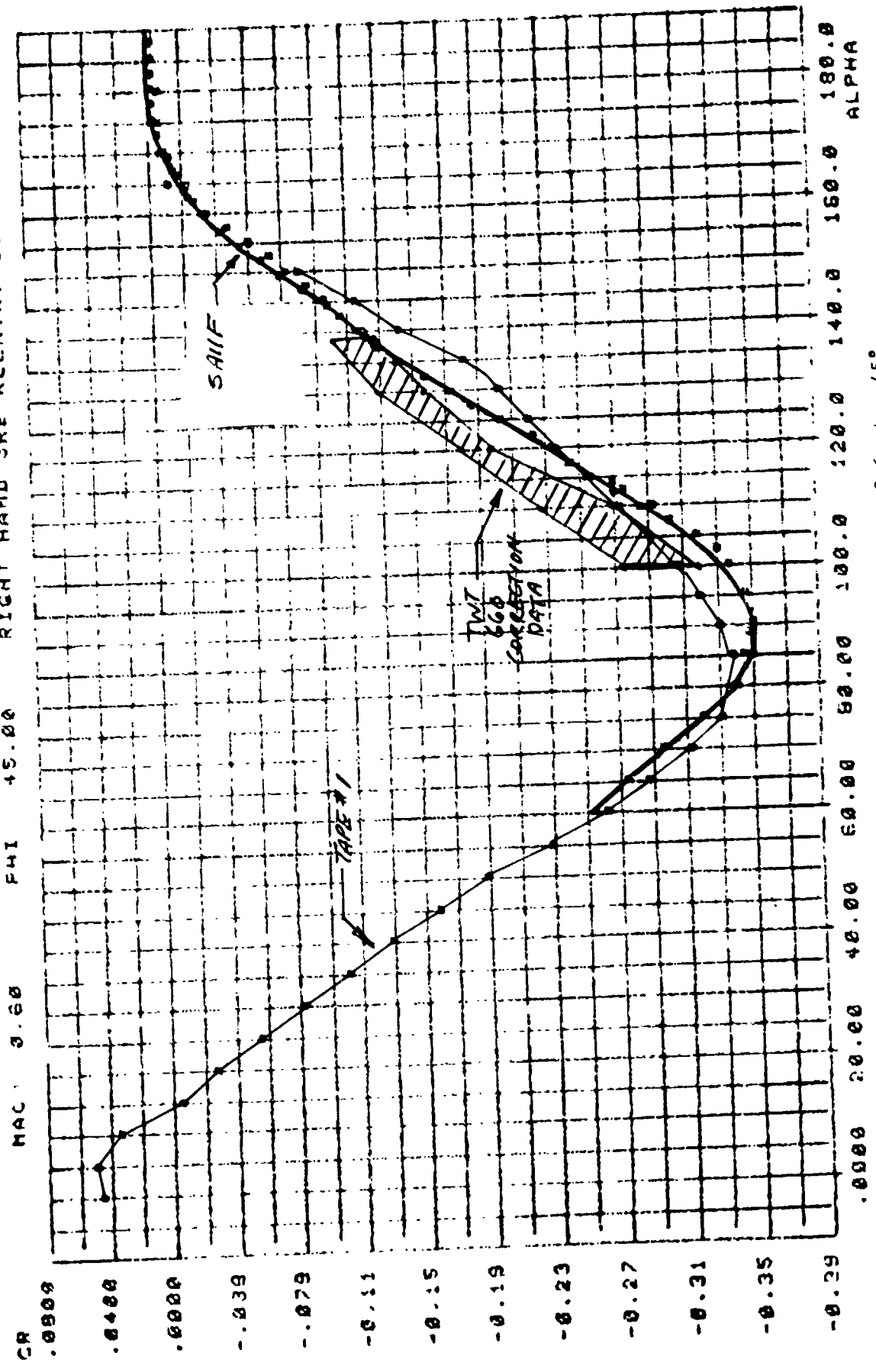

Figure 3-37. Rolling Moment Coefficient Versus α, $M_\infty = 0.6$, $\phi = 45°$

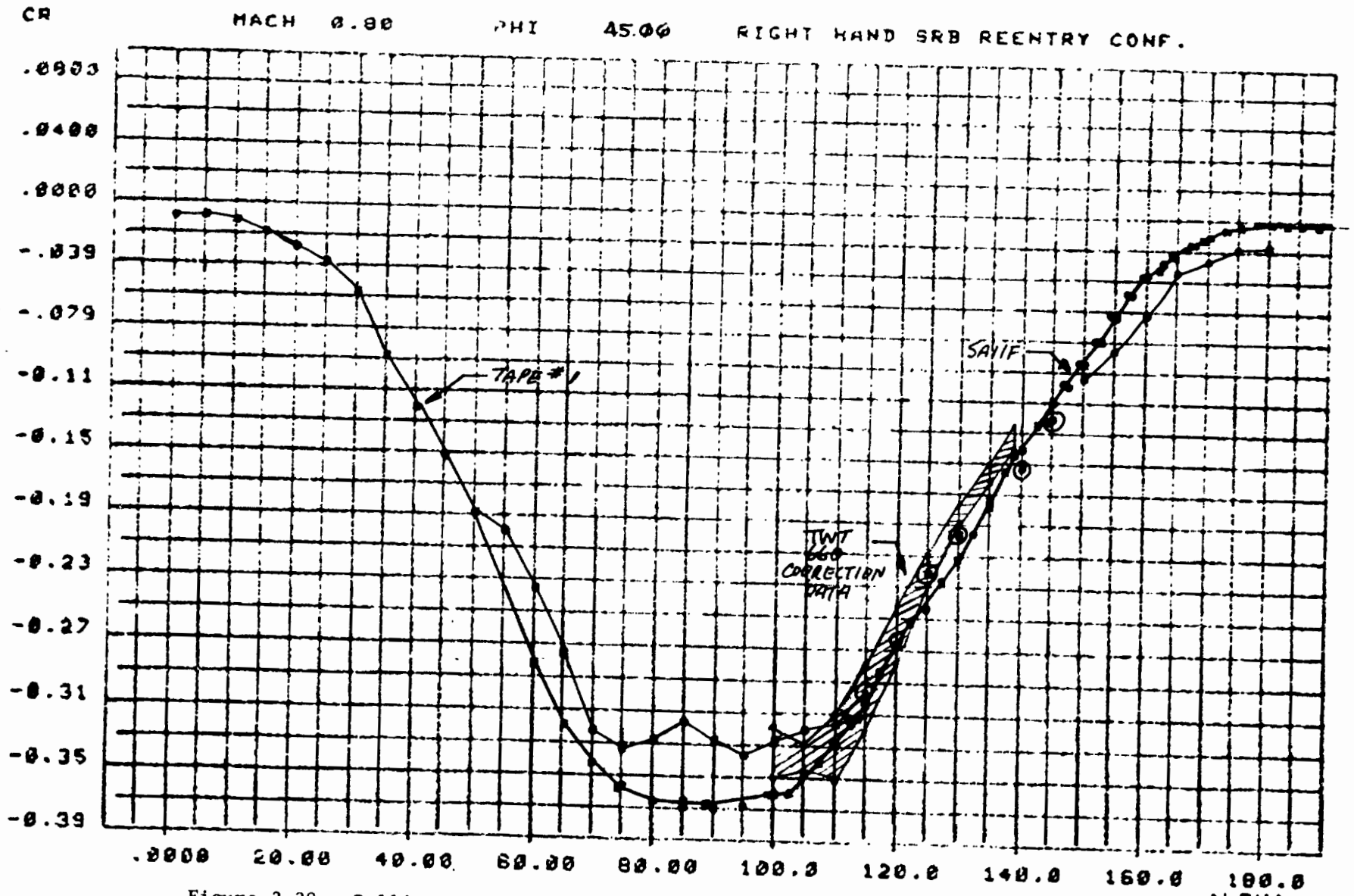

Figure 3-38. Rolling Moment Coefficient Versus α, $M_\infty = 0.8$, $\phi = 45°$

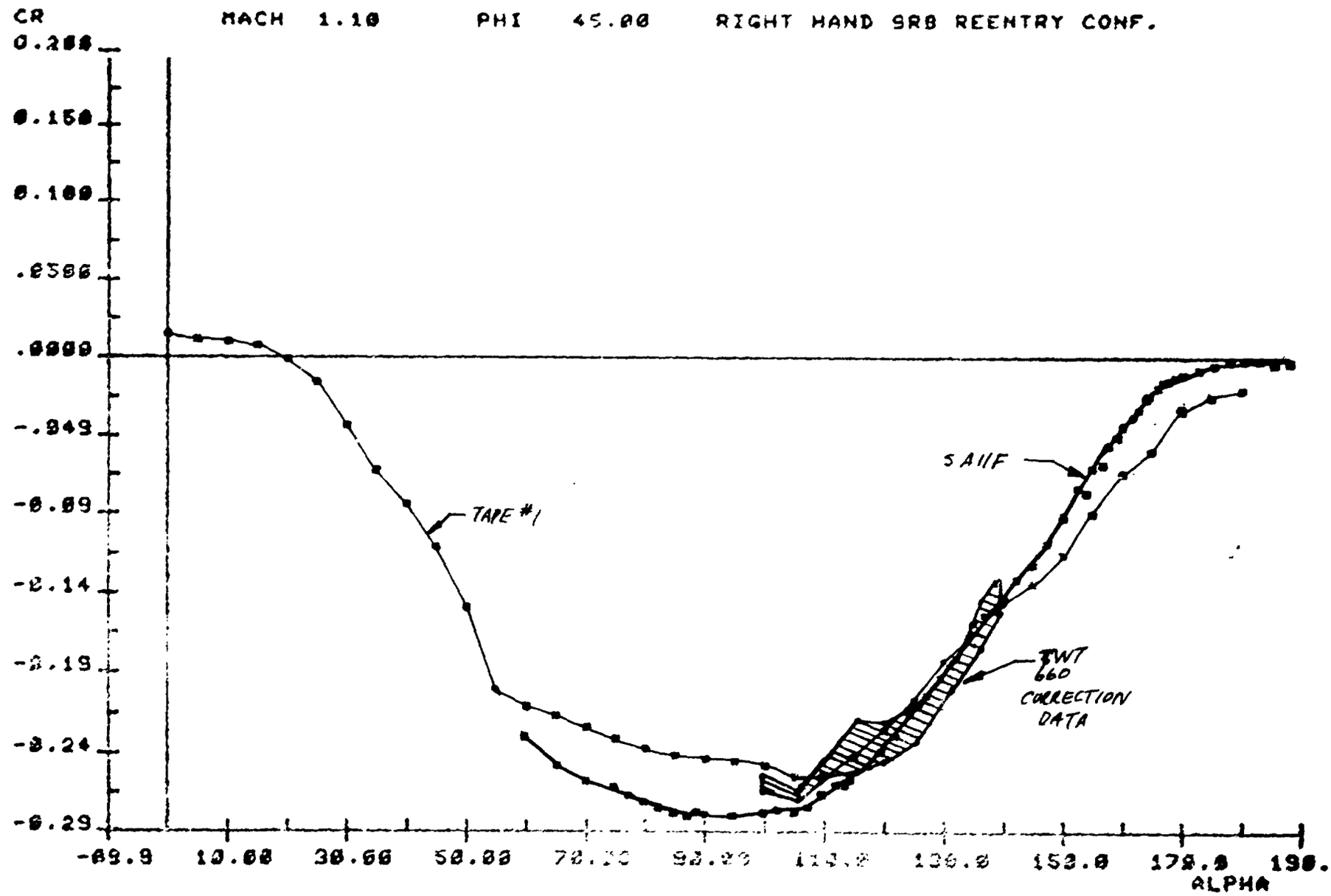

Figure 3-39. Rolling Moment Coefficient Versus α, $M_\infty = 1.1$, $\phi = 45°$

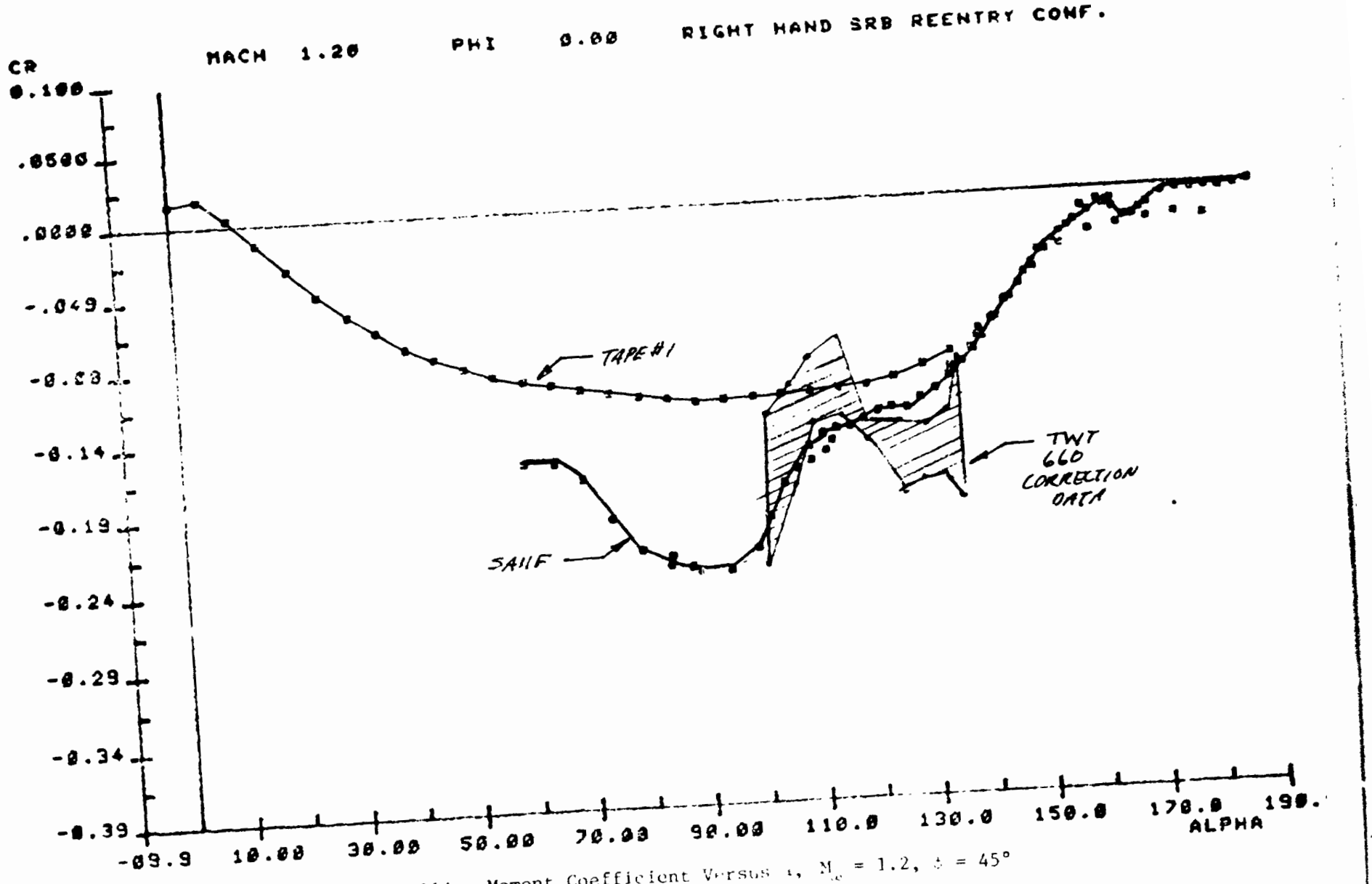

Figure 3-40. Rolling Moment Coefficient Versus α, $M_\infty = 1.2$, $\phi = 45°$

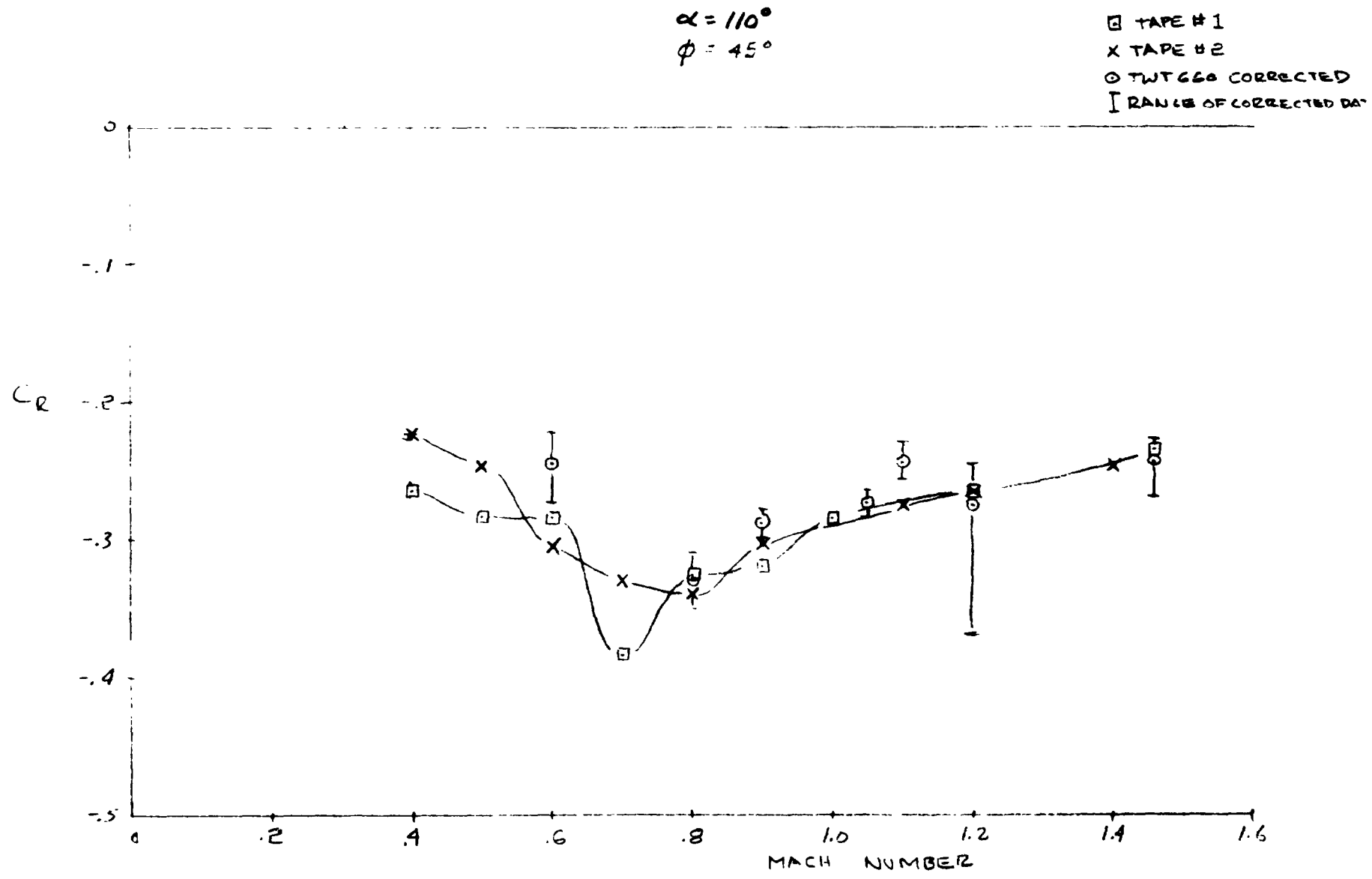

Figure 3-41. Rolling Moment Coefficient Versus Mach Number, α = 110°

Section IV

HIGH REYNOLDS NUMBER TEST RESULTS

The HRWT 042 test program was a three part program that consisted of testing one configuration from the TWT 660 test program, testing a basic cylinder to verify basic cylinder data trends and the sting interference portion of the test program. The test program, models and sting configurations are described in Section II (Wind Tunnel Test Programs). A listing of the data from each phase of the test program is presented in Appendix B.

The model configuration used for the TWT 660 verification phase was configuration ASSOOA/B. The model and sting configuration used for the HRWT 042 test is presented in Figure 2-22. The test configuration used for this hardware during the TWT 660 test is shown in Figure 2-15. The TWT sting and SRB model hardware for this configuration was tested in the High Reynolds Number Tunnel.

Comparison plots of the normal force and pitching moment coefficient for the Ames sting configuration are presented in Figures 4-1 through 4-4. Figures 4-1 and 4-2 show good agreement in the normal force coefficient comparisons. The pitching moment comparison at Mach 0.6, shown in Figure 4-3, shows poor agreement with a negative shift in the pitching moment over most of the angle of attack range tested. The pitching moment comparison at Mach 0.8 (Figure 4-4) shows much closer agreement. The comparisons show that good agreement exist except for the pitching moment coefficient at Mach 0.6.

The cylinder test used a symmetric and asymmetric cylinder with a side mount sting (see Figures 2-23 through 2-25). The cylinder test allowed a check with previously published high Reynolds number cylinder data and allowed the evaluation of basic cylinder moment interference due to the sting.

The cylinder test results are presented in Figures 4-5 through 4-8. The cylinder data was converted to cross flow drag coefficient form for comparison with other published cylinder data.

The cylinder crossflow drag coefficient data is presented in Figures 4-5, 4-6, and 4-7. Figure 4-5 shows the crossflow drag coefficient for the symmetric and asymmetric cylinder from the test HRWT 042. These data are compared with the 2-D cylinder data from Reference 11 and the 3-D cylinder data from Reference 12. The figure shows that the HRWT data is lower than the Reference 11 data at the higher Reynolds numbers and higher at the lower Reynolds numbers. It was anticipated that the HRWT crossflow drag data would be lower than the 2-D data since the cylinder had a finite length with a fineness ratio of 11.2 (see Fig. 2-23). The higher Reynolds number data shows a reduction in crossflow drag coefficient of approximately 20 percent due to the finite length cylinder. This compares favorably with the general data trends presented in Reference 12. It is noted that the 3-D cylinder data from Reference 12 is higher than the 2-D cylinder data from Reference 11 at a Reynolds number of 1.5×10^6. The HRWT 042 cylinder data is very close to the 3-D cylinder data from Reference 12 at a Reynolds number of 1.5×10^6. At a Reynolds number of 6×10^5 the HRWT data is higher than the Reference 12 data.

The crossflow drag coefficient data in the lower Reynolds number range of 10^6 are higher than the 2-D results from Reference 11. The reason for this type of result is unknown. It may be due to a combination of model roughness and/or tunnel turbulence. Reference 13 shows that the crossflow drag coefficient in the Reynolds number range of 10^6 can vary from 0.2 to 0.4 depending on the RMS cylinder roughness.

The high crossflow drag trend in the Reynolds number range of 10^6 has been a problem with several HRWT test programs. The HRWT test program was adjusted to provide data at Mach 0.3 to avoid the high Mach number gradient in crossflow drag at Mach 0.4. This high Mach number gradient is presented in Figure 4-6. The figure (from Reference 14) shows a crossflow drag coefficient bucket between Mach 0.2 and 0.4 that is strongly influenced by Reynolds number. The HRWT data at Mach 0.3 and 0.4 are shown for comparison. Thus the high HRWT data at Mach 0.3 in the Reynolds number range of 1.0×10^6 is not due to a Mach number gradient.

The results of the HRWT cylinder test conducted at Mach 0.4 are presented in Figure 4-7. The data band of the results at Mach 0.3 are also presented in the figure. The test at Mach 0.4 was conducted to allow comparisons with the results from Reference 11 and to evaluate the unusual peak in the data at a Reynolds number of 7.5×10^6. The HRWT results are noted to have a different trend in this Reynolds number range. The results from test HRWT 034 are noted to be considerably higher than the current HRWT results. Test HRWT 034 was a high Reynolds number test of a clean (no protuberances) SRB model. The results presented in Figure 4-7 show that the current test results (HRWT 042) compare more favorably with other published experimental data trends.

Comparison of the center of pressure from the symmetric and asymmetric cylinder is presented in Figure 4-8. No significant trend in the center of pressure shift could be identified with the asymmetric cylinder. The symmetric cylinder itself has a center of pressure that is generally within one percent of the center of the cylinder. The asymmetric cylinder center of pressure was expected to shift to the opposite side of the sting but no consistant trend could be identified.

The High Reynolds Number sting interference portion of the test program was an evaluation of the sting configurations used during test HRWT 039. Test 039 provided the high Reynolds number data base for the development of SRB data Tape #2. The SRB model configuration used for the test is presented in Figure 2-26. The single and dual sting configurations used are presented in Figures 2-27 through 2-34. The single sting configurations used are the side mount sting (HSS00A/B) shown in Figures 2-27 and 2-28 and the nose mount sting (H00NSA/B) shown in Figures 2-29 and 2-30. The dual sting configurations include the side mount with dummy nose mount (HSSNDA/B) shown in Figures 2-31 and 2-32 and the nose mount with the dummy side mount (HSDNSA/B) shown in Figures 2-33 and 2-34. The equations used to determine the sting interference are presented in Section II (Wind Tunnel Test Programs). The HRWT 042 test plan (Ref. 2) identified an "A" alpha range and a "B" alpha range test program. Scheduling problems created a conflict with the data analysis, however, and only limited data was obtained for the "B" alpha range.

LONGITUDINAL DATA

The normal force and pitching moment sting interference is presented in Figures 4-9 through 4-20. Figures 4-9 through 4-14 show that the sting normal force interference is not a strong function of Reynolds number, Mach number or roll angle. The side mount sting interference is considerably larger than the Ames or MSFC side mount sting interference. Compare Figures 4-11 and 4-12 with Figures 3-1 and 3-2. Detail comparisons of the sting interference from both test programs are presented in Section V (Sting Interference Conclusions).

The pitching moment sting interference is presented in Figures 4-15 through 4-20. It is noted that the pitching moment sting interference is large and of opposite sign for the side mount configuration than the TWT 660 data. Compare Figure 4-17 with Figure 3-6. The pitching moment sting interference also appears to be a function of roll angle.

Data plots used to develop the sting interference data are presented in Figures 4-21 through 4-28 for Mach 0.4, Figures 4-29 through 4-36 for Mach 0.6, and Figures 4-37 through 4-44 for Mach 0.8. Data for three Reynolds numbers are presented in each figure. This provided a method of identifying questionable data. Also superimposed on each data plot are the values of the coefficient from SRB data tape #1 and #2. This provides a general comparison for the corrected data with both current data tapes.

The normal force data for Mach 0.4 presented in Figures 4-21 through 4-24 show the general data trends for each Mach number. The nose mount sting developed the largest normal force coefficient as shown in Figure 4-21. The addition of the dummy side mount sting reduced the normal force load by unloading the model at the sting location (compare HOONSA with HSDNSA). Thus the side mounted dummy sting creates a negative normal force interference that must be added back to the side mount sting data (HSSOOA). The correction for sting interference thus increases the side mount data level as shown in the figure. It is noted in the figure that the side mount data (HSSOOA) at the low Reynolds number does not develop a representative curve versus angle of attack. This trend is consistant for the majority of the data and is believed due to the

relatively low loads developed on the model compared to the high loading environment at the high Reynolds number flow condition. The nose mount data presented in Figure 4-22 shows a problem with the side mount configuration (HSDNSA). It is noted in Figure 4-21 that configuration HSDNSA develops a larger normal force coefficient than configuration HSSNDA. This large a difference in data did not occur during the TWT 660 test program. This difference developed a significant difference in side mount and nose mount corrected data.

Summary plots of the corrected normal force and pitching moment data are presented in Figures 4-43 through 4-56. The Tape #1 and Tape #2 values are also presented for reference along with the data band of the TWT 660 corrected data at certain Mach numbers. The figures show that there is a substantial difference in level between the corrected HRWT nose mount and side mount data. The difference in data between configuration HSSNDA and HSDNSA is the major cause of this difference in corrected data. It is not known which data is the more correct. The average of the corrected HRWT data may be representative of the corrected trend. Using the average HRWT data trends it is evident from the figures that the corrected normal force data is close to data Tape #2 while the pitching moment data falls between Tape #1 and Tape #2 values.

Figures 4-47 through 4-50 show that the corrected TWT 660 data is close to the HRWT corrected data for zero roll angles. This trend is not surprising since the electrical conduit is at a critical position to influence the cylinder flow field Reynolds number trends at zero roll angle. The TWT 660 corrected data is noted to be higher than the HRWT data at a roll angle of 90 degrees (see Figure 4-48). Figure 4-48 indicates a Reynolds number influence at Mach 0.6. The corrected data at Mach 0.8 presented in Figure 4-50 shows that most of the data is higher than the data at zero roll angle presented in Figure 4-49. This trend occurred in the angle of attack range of 110 to 120 degrees. The TWT 660 data trend in this angle of attack range shows a large bump in the curve that matches the HRWT data. This data trend seemed unreasonable and has been ignored.

Comparison of the corrected pitching moment data presented in Figures 4-53 through 4-56 shows that the TWT 660 corrected data is significantly displaced from the HRWT corrected data. The limited amount of HRWT corrected data in the B alpha ($120 < \alpha < 140$) range presented in Figure 4-53 shows that the data trend versus angle of attack may follow the TWT trend resulting in a pitching moment coefficient data that is outside the range of both the Tape #1 and Tape #2 data base. Insufficient data was available to confirm this trend however.

The analysis of the corrected HRWT 042 and the corrected TWT 660 data showed the influence of Reynolds number on the corrected data trends. Specific quantitative estimates of the data trends with Reynolds numbers are difficult to assess due to the large HRWT data band considering the nose mount and side mount data. This large data band prevented any quantitative extrapolation of data bands to full scale Reynolds numbers.

LATERAL DIRECTIONAL DATA

The HRWT 042 nose mount and side mount lateral-directional data are presented in Figures 4-57 through 4-68. The data for the single sting configuration, dual sting configurations, and the corrected data are presented in each figure. The side force coefficient is presented in Figures 4-57 through 4-62. These figures show that at zero roll angle, where the side force is maximum, the side force sting interference is positive for the side mount sting and reduces the magnitude of the negative side force. It was expected that the nose mount lateral directional sting interference would be small, similar to the TWT 660 data trend, but Figure 4-57 shows a large side force sting interference for the nose mount sting. This may be due to a mutual sting interference problem that is due to a difference in data characteristics for sting configuration HSSNDA and HSDNSA. These two sting configurations are shown in Figures 2-31 and 2-33. It is noted in these figures that both configurations are dual sting arrangements. Configuration HSSNDA (Figure 2-31) has an active side mount with a dummy nose mount and configuration HSDNSA has an active nose mount with a dummy side mount. Figures 4-57

and 4-63 show that there is a substantial difference in data level for these two configurations. The reason for this difference is unknown. This difference in data level caused concern as to which data was the more accurate since there was a difference in level of the corrected data for a large portion of the data base.

The lateral directional subsonic corrected data from both tests were overlayed with the Tape #1 and SA11F (Tape #2) results to evaluate what change, if any, was required to data Tape #2. These results are presented in Figures 4-69 through 4-76. Appropriate test results are overlayed where available. The data are presented for the roll angle where the coefficient is a maximum. The side force and yawing moment is thus presented at a roll angle $\varphi = 0$ degrees.

The side force coefficient comparisons are presented in Figures 4-69 through 4-72. Figure 4-69 shows the side force comparison at Mach 0.4. The figure shows that the majority of the corrected high Reynolds number data follows the HRWT 039 test data trends. The side force coefficient at Mach 0.6 and 0.8 is presented in Figures 4-70 and 4-71 respectively. These figures show that the corrected TWT 660 data follows the TWT 640 data trends and the HRWT corrected data brackets the HRWT 039 data. The side force coefficient at an angle of attack of 110 degrees is presented versus Mach number in Figure 4-72. The figure shows that the corrected HRWT 042 data follows the data Tape #2 data trends and the TWT 660 corrected data at the higher Mach number is close to the Tape #2 data.

The yawing moment comparisons are presented in Figures 4-73 through 4-76. The comparison at Mach 0.4 is presented in Figure 4-73. The figure shows that the corrected HRWT 042 data covers the HRWT 039 data trends. The HRWT 042 data does not have the same slope as the SA11F or the 039 data. Data comparisons at Mach 0.6 and 0.8 are presented in Figures 4-74 and 4-75. The figures show that the corrected TWT 660 data band follows the Tape #1 data trends while the majority of the HRWT 042 data follows the HRWT 039 and SA11F data trends. It is noted that at Mach 0.8 the nose mount corrected HRWT 042

data has a different sign than the corrected side mount data. The SA11F data also has a different sign compared to the TWT 640 and Tape #1 results.

A comparison of the yawing moment at α = 110 degrees is presented versus Mach number in Figure 4-76. The figure shows that the corrected TWT 660 data is considerably different from the Tape #1 result at Mach 0.6. This is due to the large sting interference at Mach 0.6 identified in Figure 3-39. The HRWT 042 test results generally confirm the SA11F and Tape #2 trends. The Tape #2 yawing moment coefficient at Mach 0.6 and 0.5 probably has the wrong sign in the angle of attack range of 110 degrees.

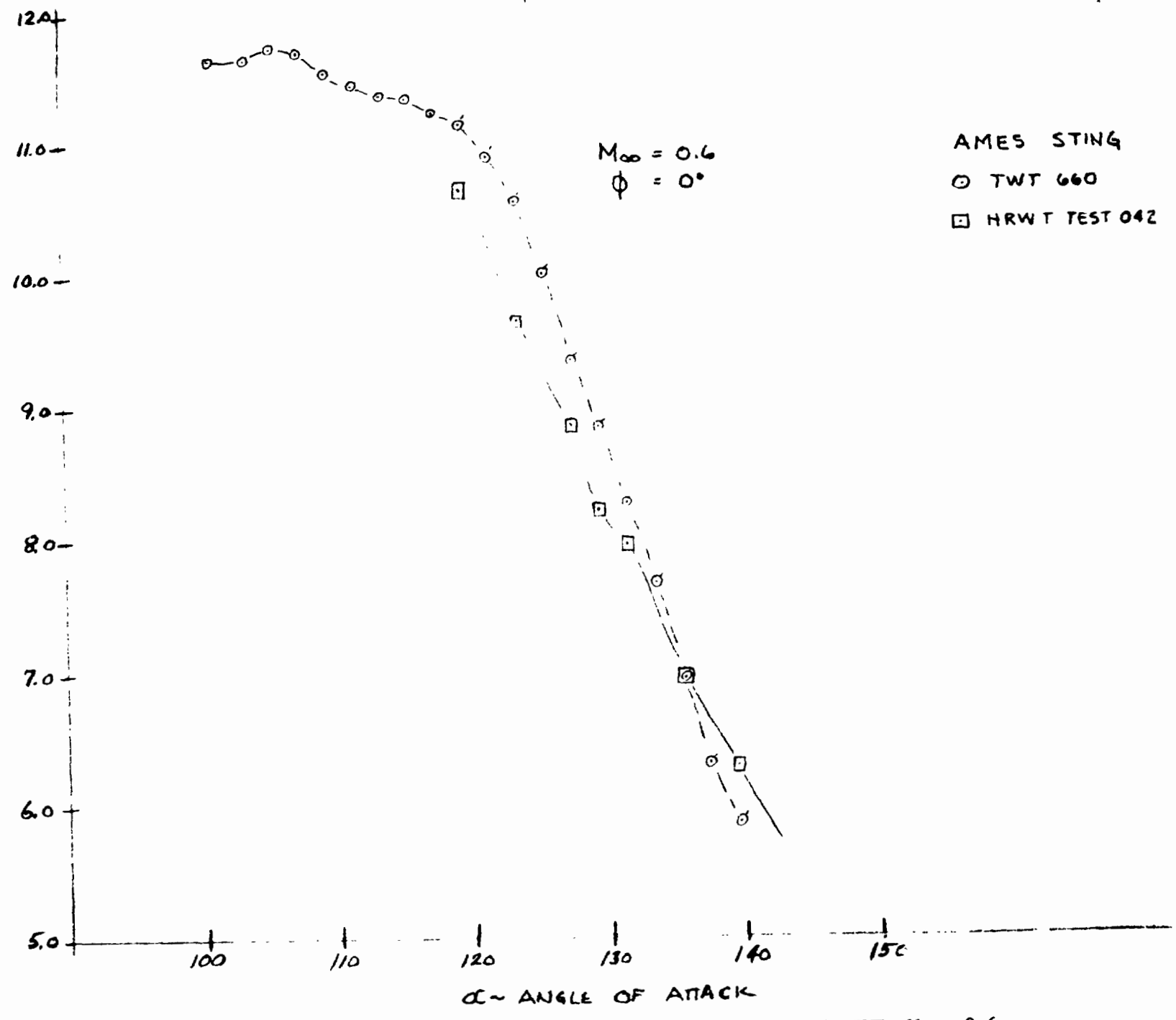

Figure 4-1. Normal Force Coefficient Versus α, TWT and HRWT, M_∞ = 0.6

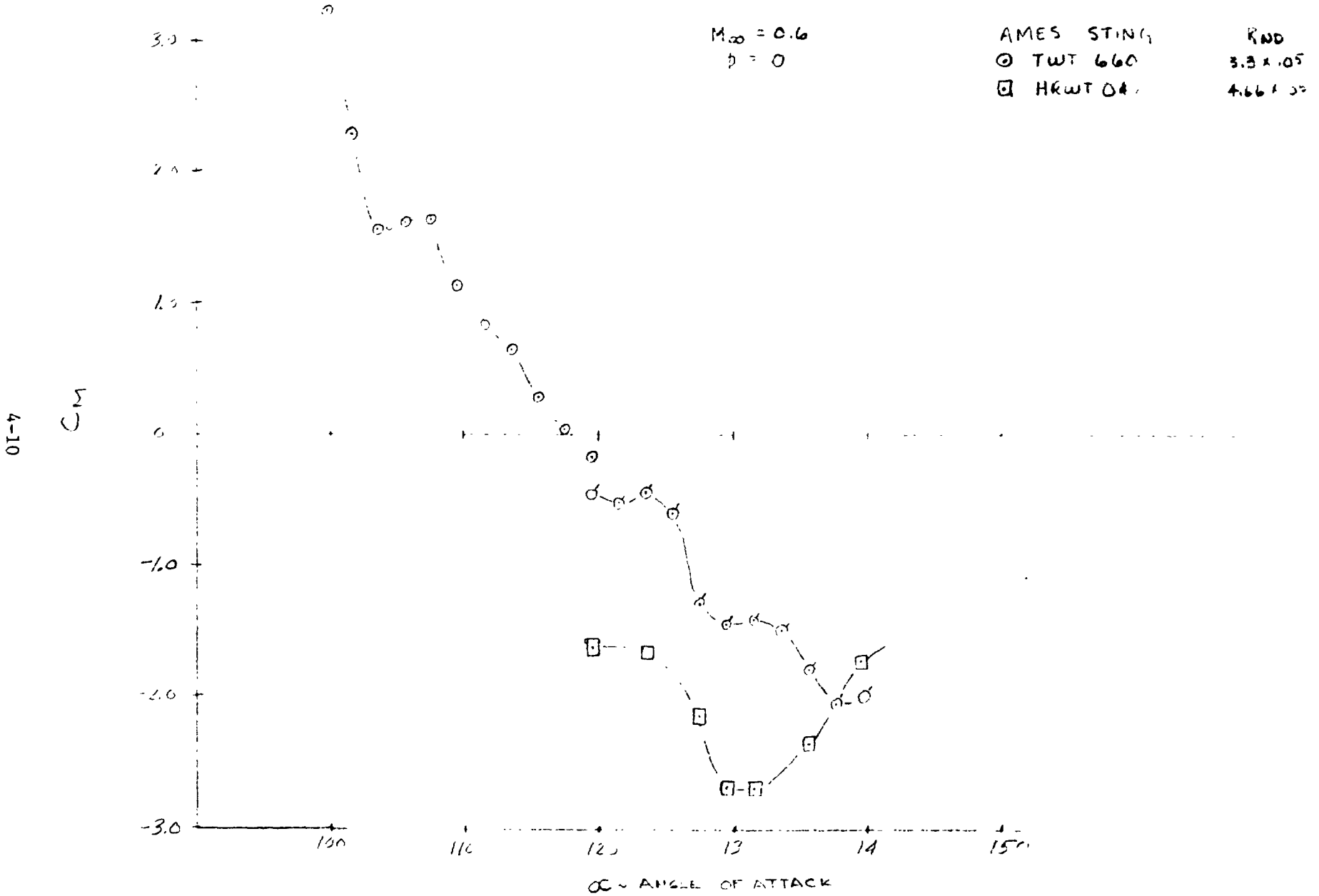

Figure 4-3. Pitching Moment Coefficient Versus α, TWT and HRWT, M_∞ = 0.6

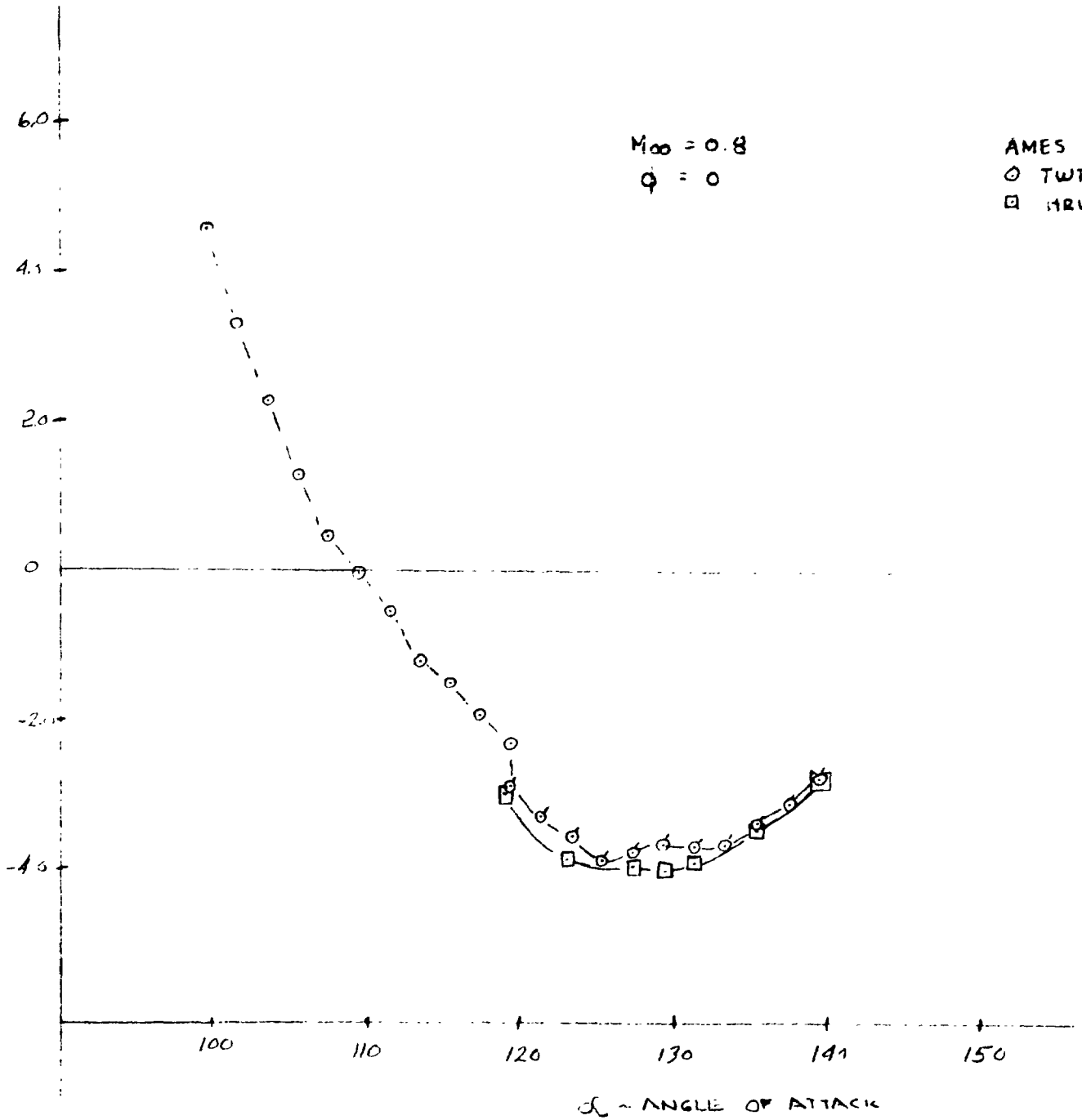

Figure 4-4. Pitching Moment Coefficient Versus α, TWT and HRWT, M_∞ = 0.8

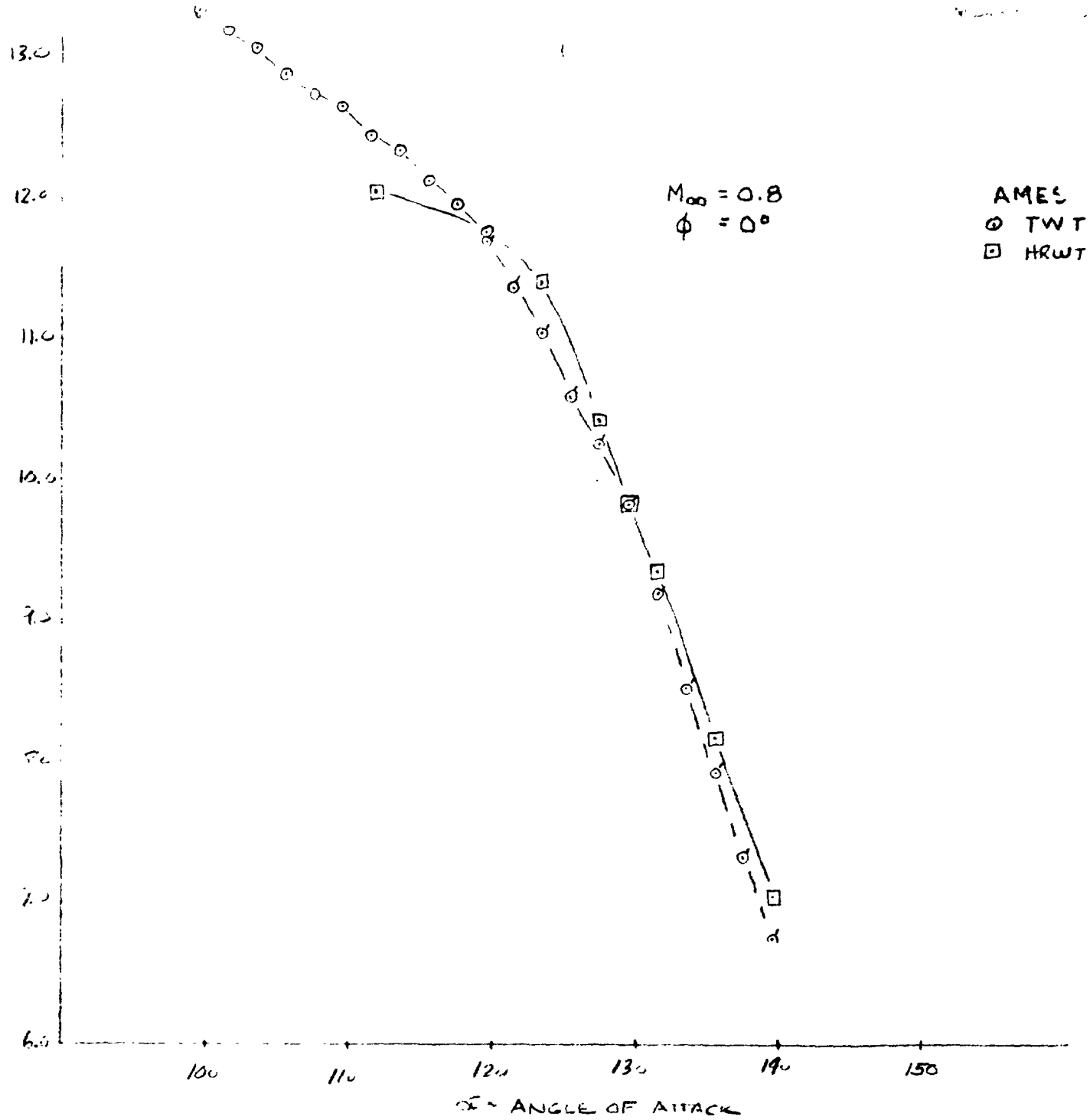

Figure 4-2. Normal Force Coefficient Versus α, TWT and HRWT, M_∞ = 0.8

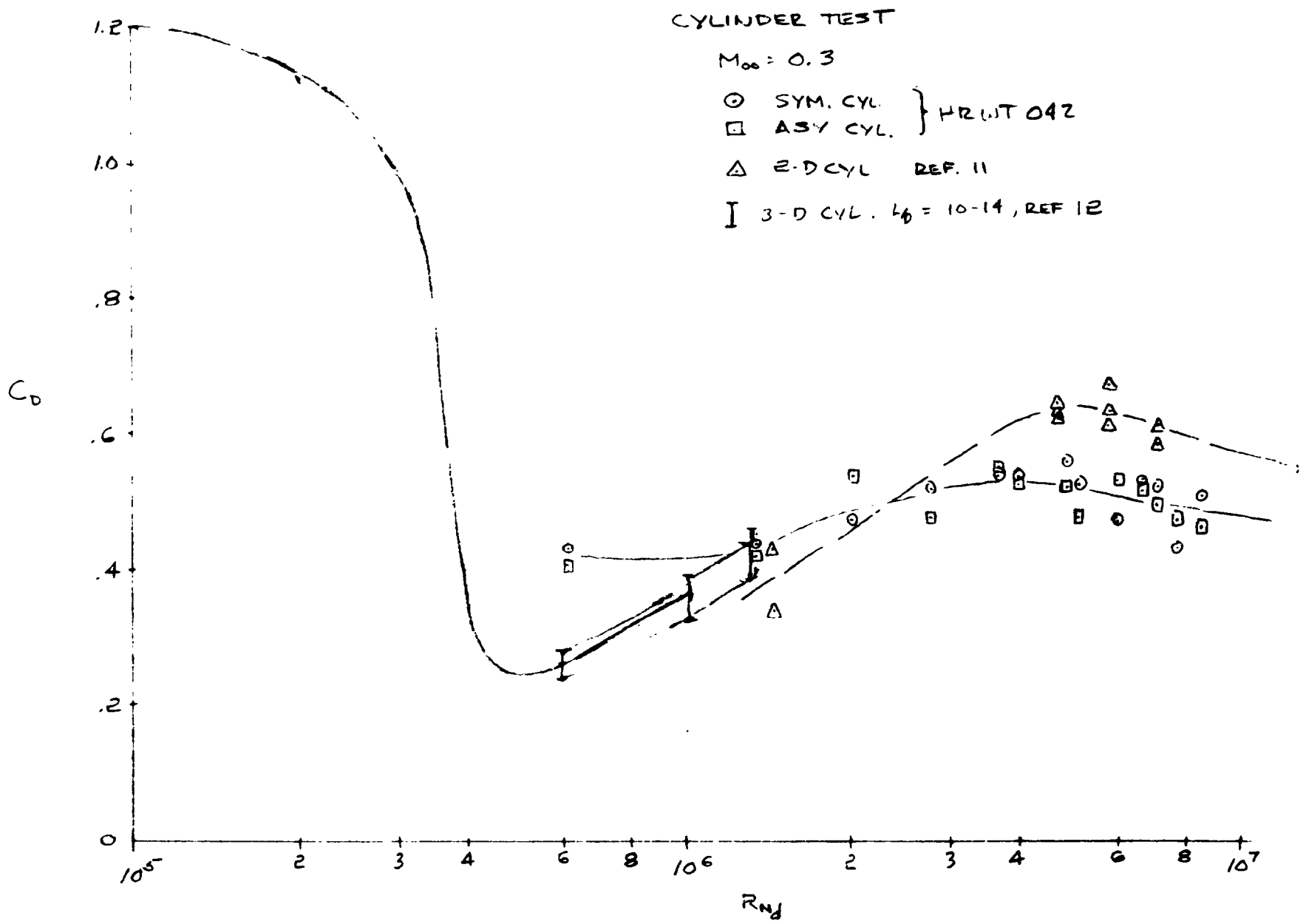

Figure 4-5. Crossflow Drag Coefficient Versus Reynolds Number, M_∞ = 0.3

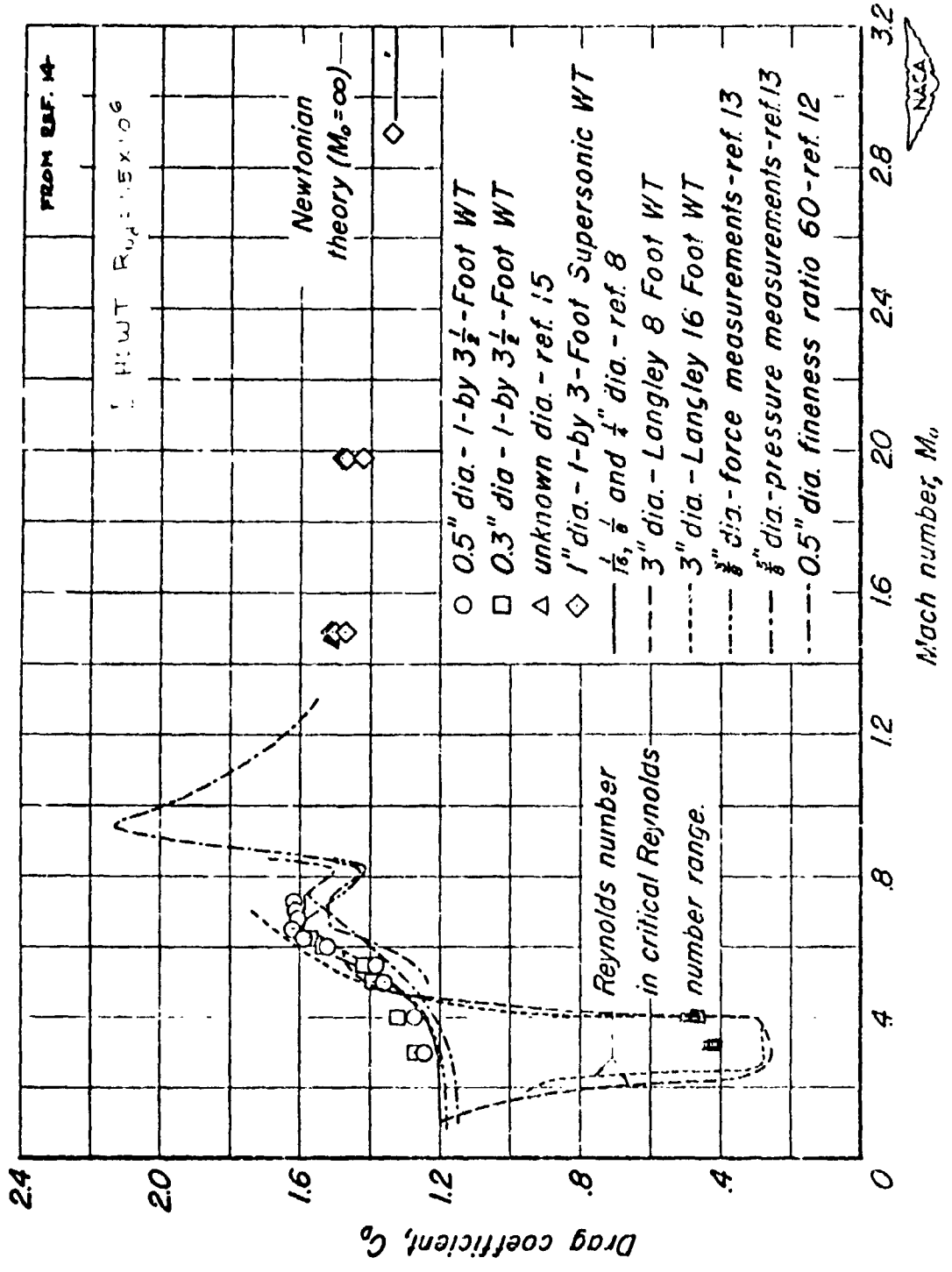

Figure 4-6. Crossflow Drag Coefficient Versus Mach Number

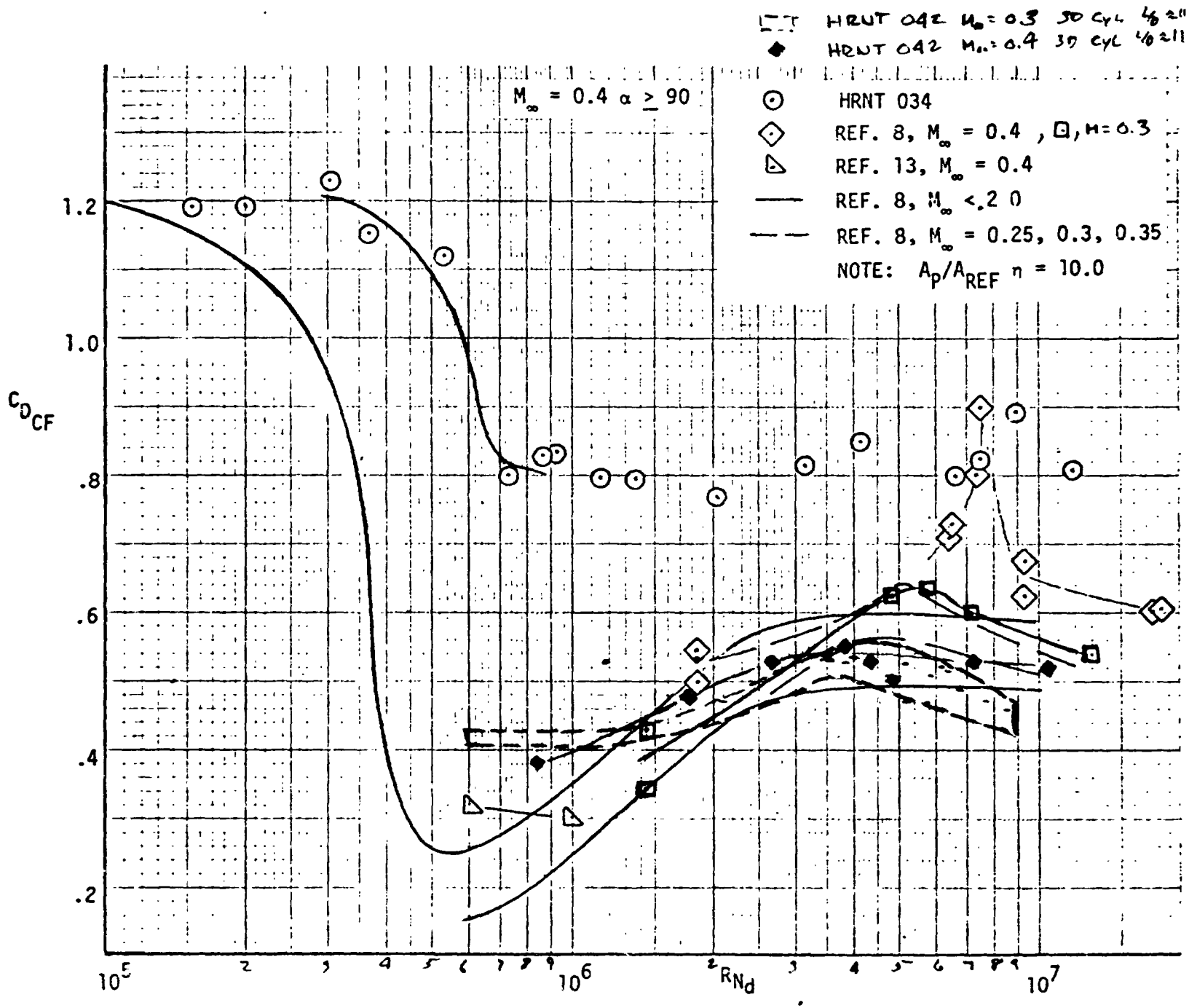

Figure 4-7. Crossflow Drag Coefficient Versus Reynolds Number, M_∞ = 0.4

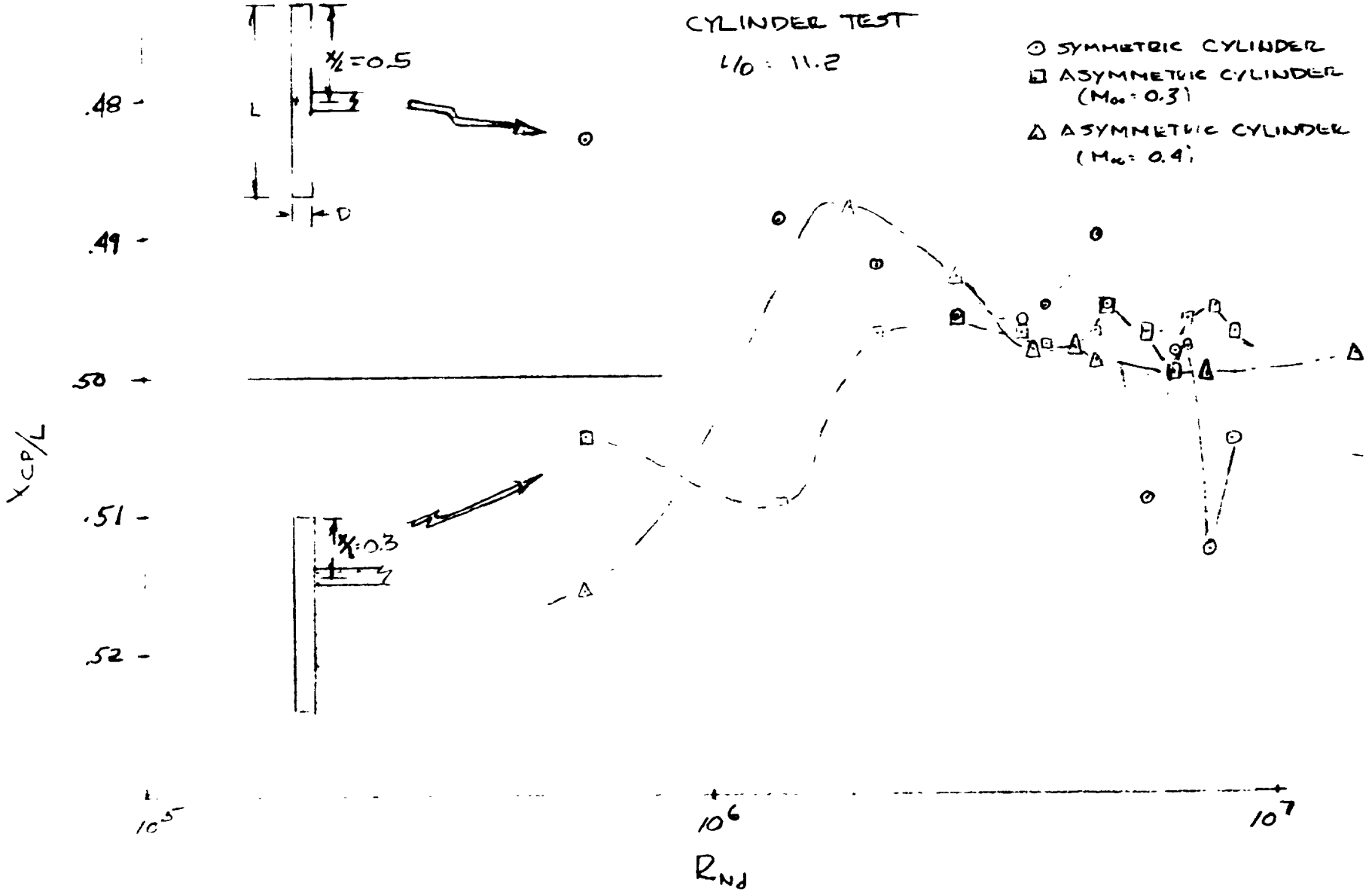

Figure 4-8. Cylinder Center of Pressure Versus Reynolds Number

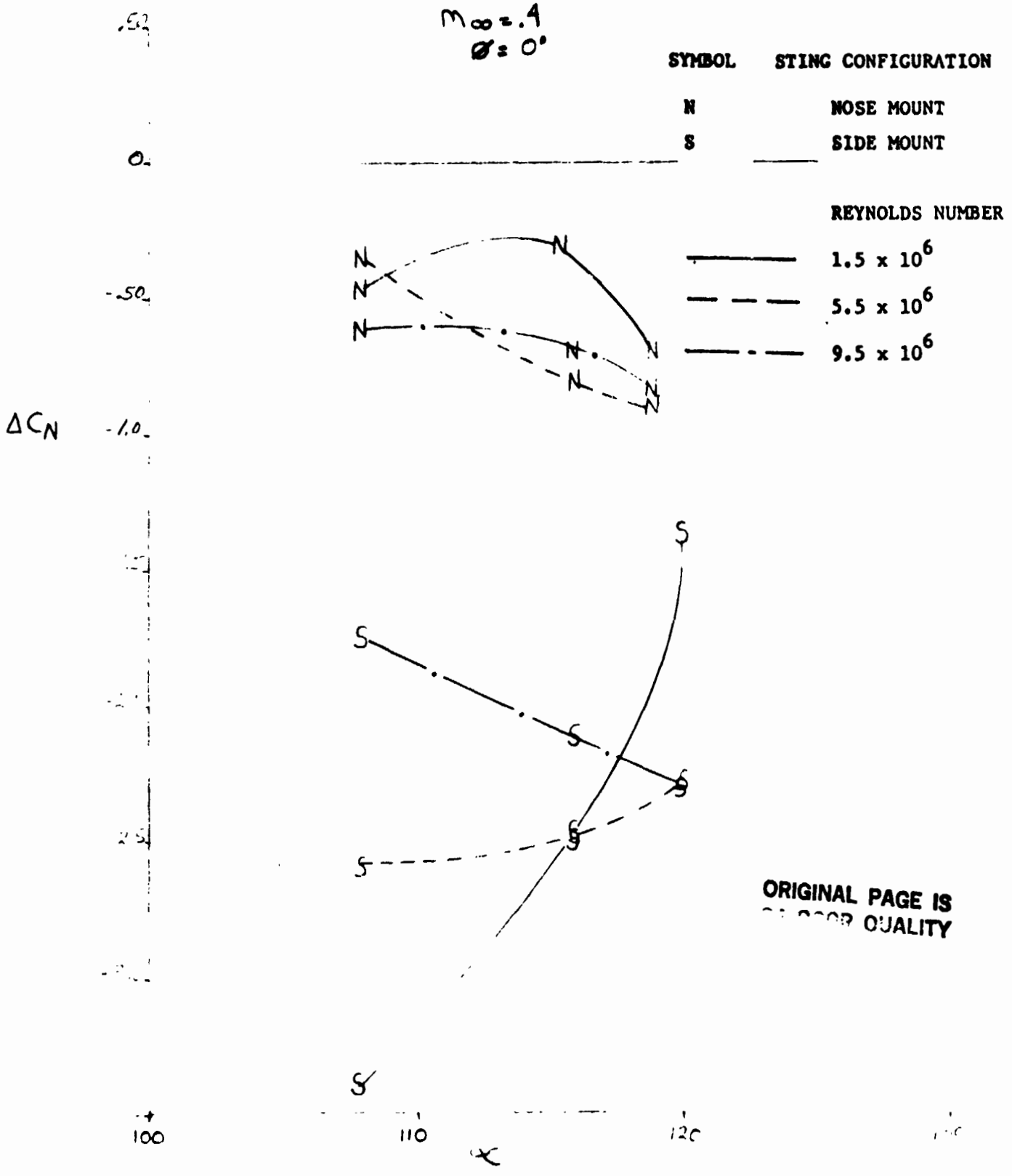

Figure 4-9. Normal Force Sting Interference, HRWT, M_∞ = 0.4, ϕ = 0°

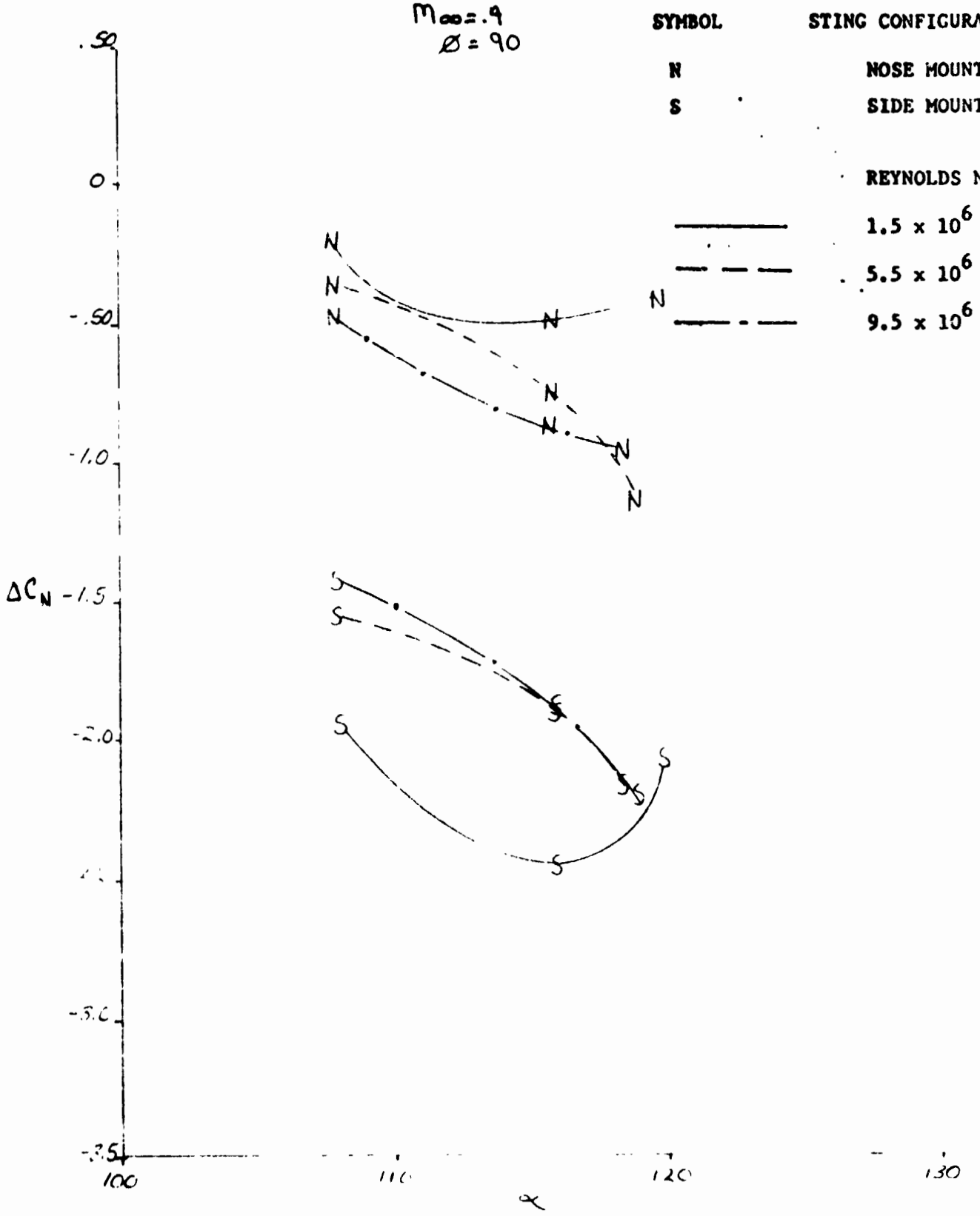

Figure 4-10. Normal Force Sting Interference, HRWT, $M_\infty = 0.4$, $\phi = 90°$

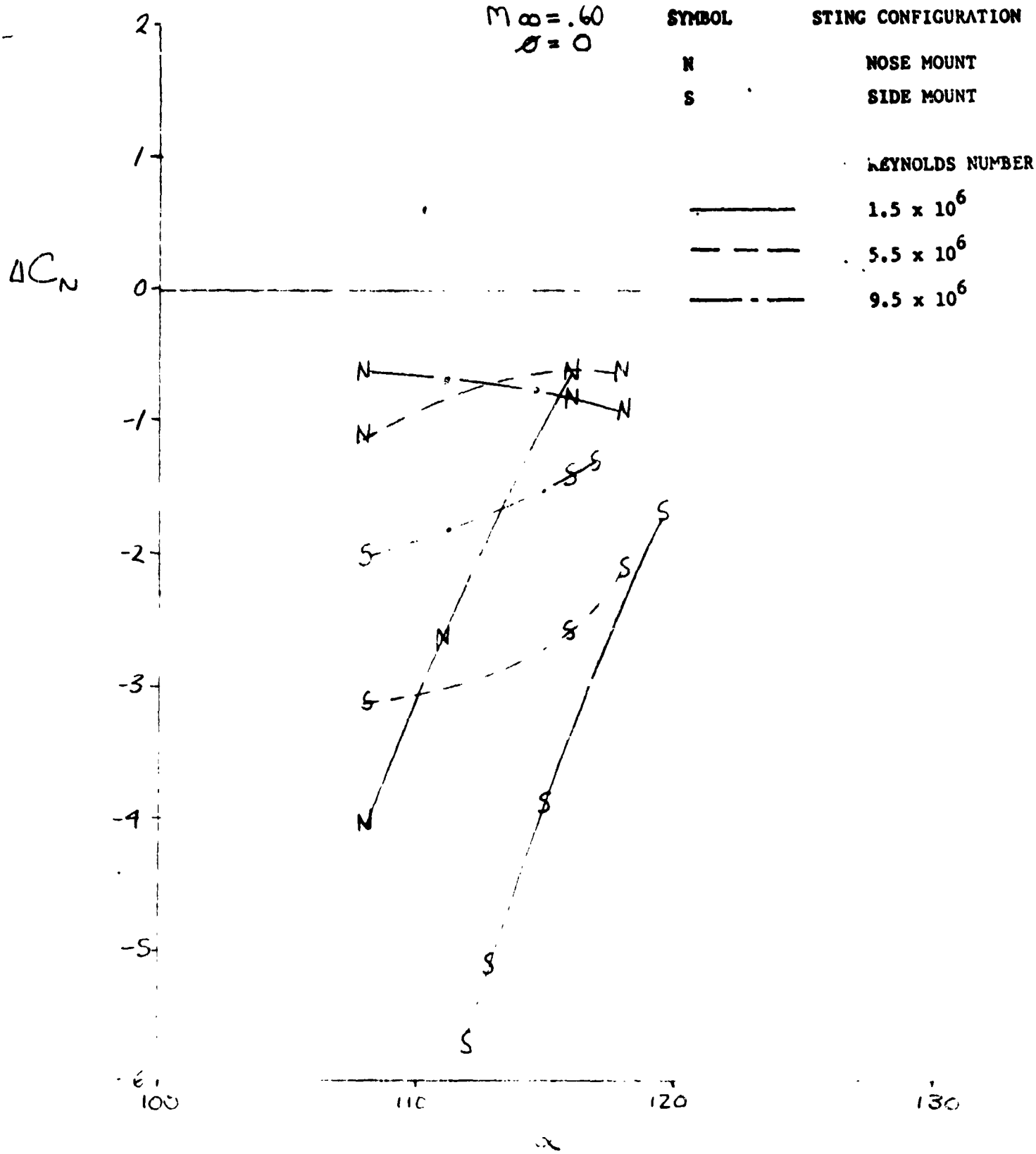

Figure 4-11. Normal Force Sting Interference, HRWT, $M_\infty = 0.6$, $\phi = 0°$

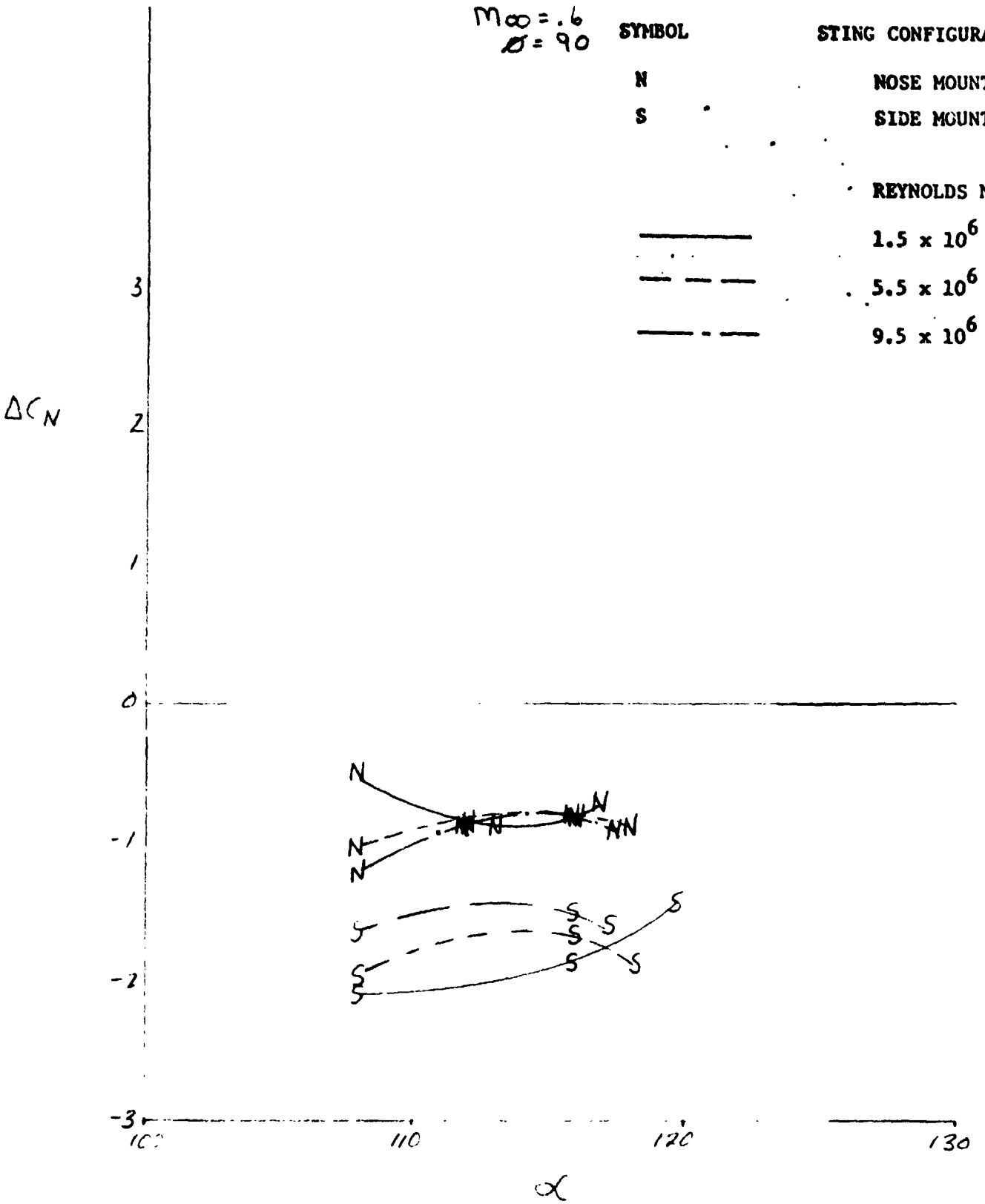

Figure 4-12. Normal Force Sting Interference, HRWT, $M_\infty = 0.6$, $\phi = 90°$

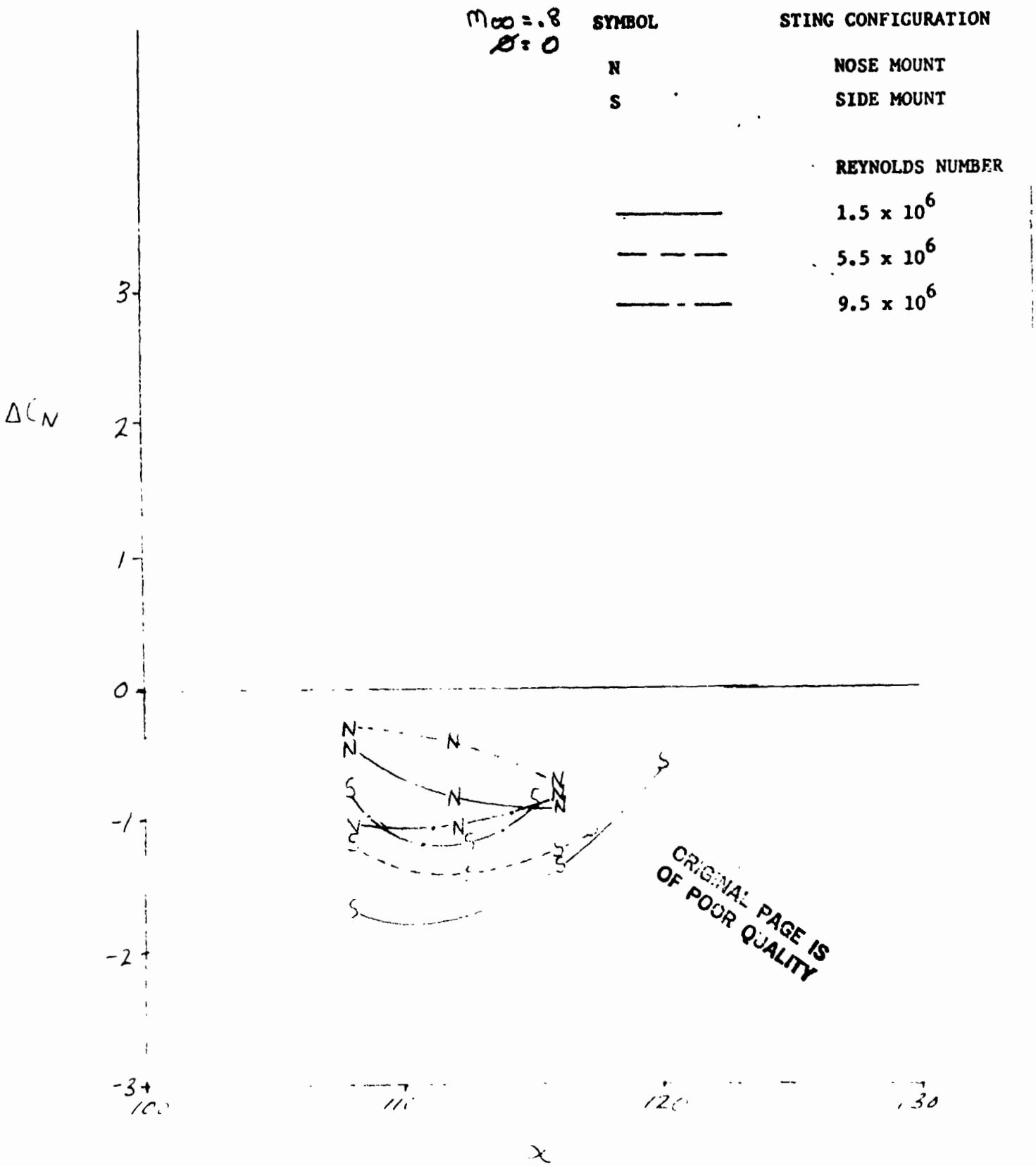

Figure 4-13. Normal Force Sting Interference, HRWT, $M_\infty = 0.8$, $\phi = 0°$

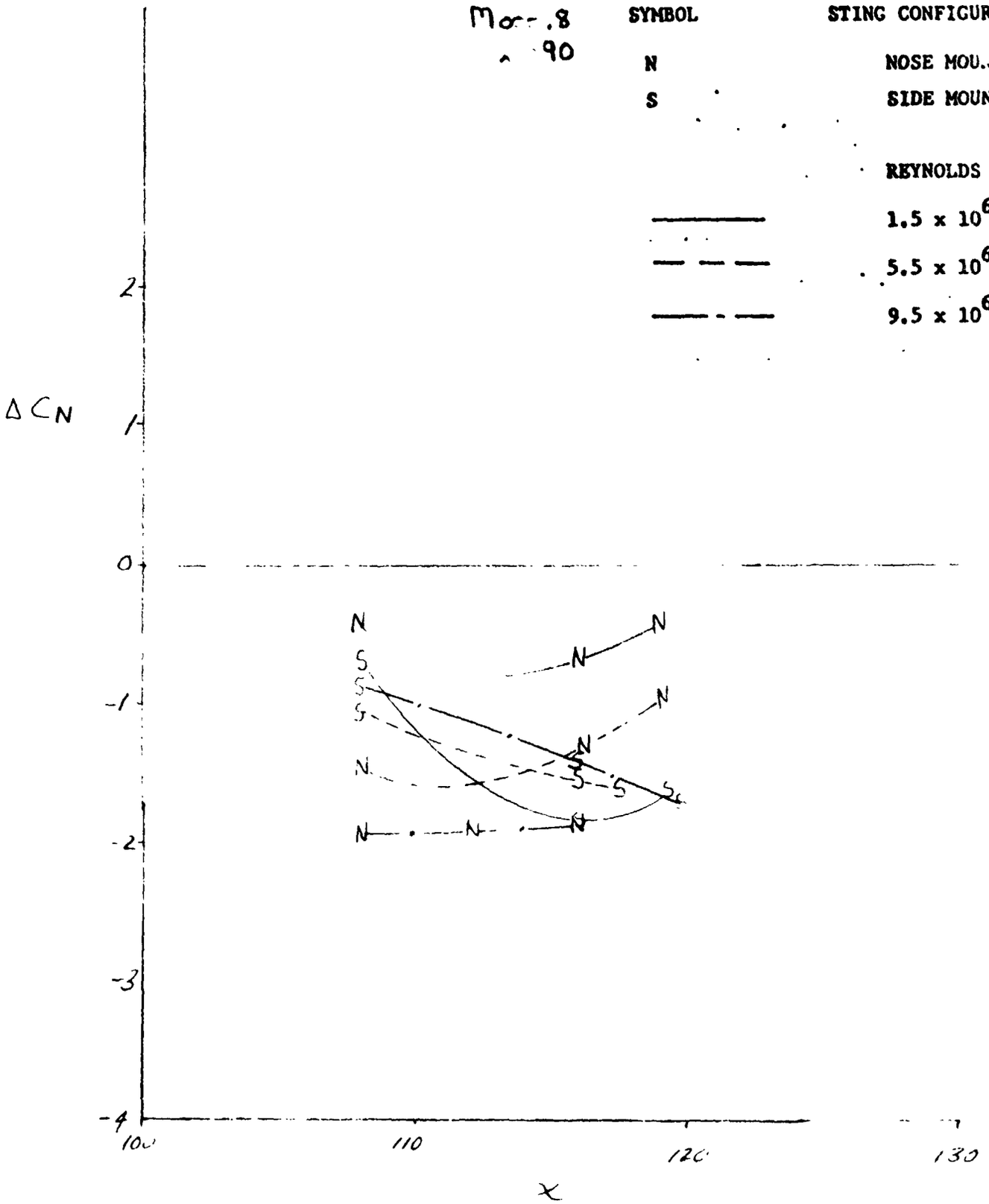

Figure 4-14. Normal Force Sting Interference, HRWT, $M_\infty = 0.8$, $\phi = 90°$

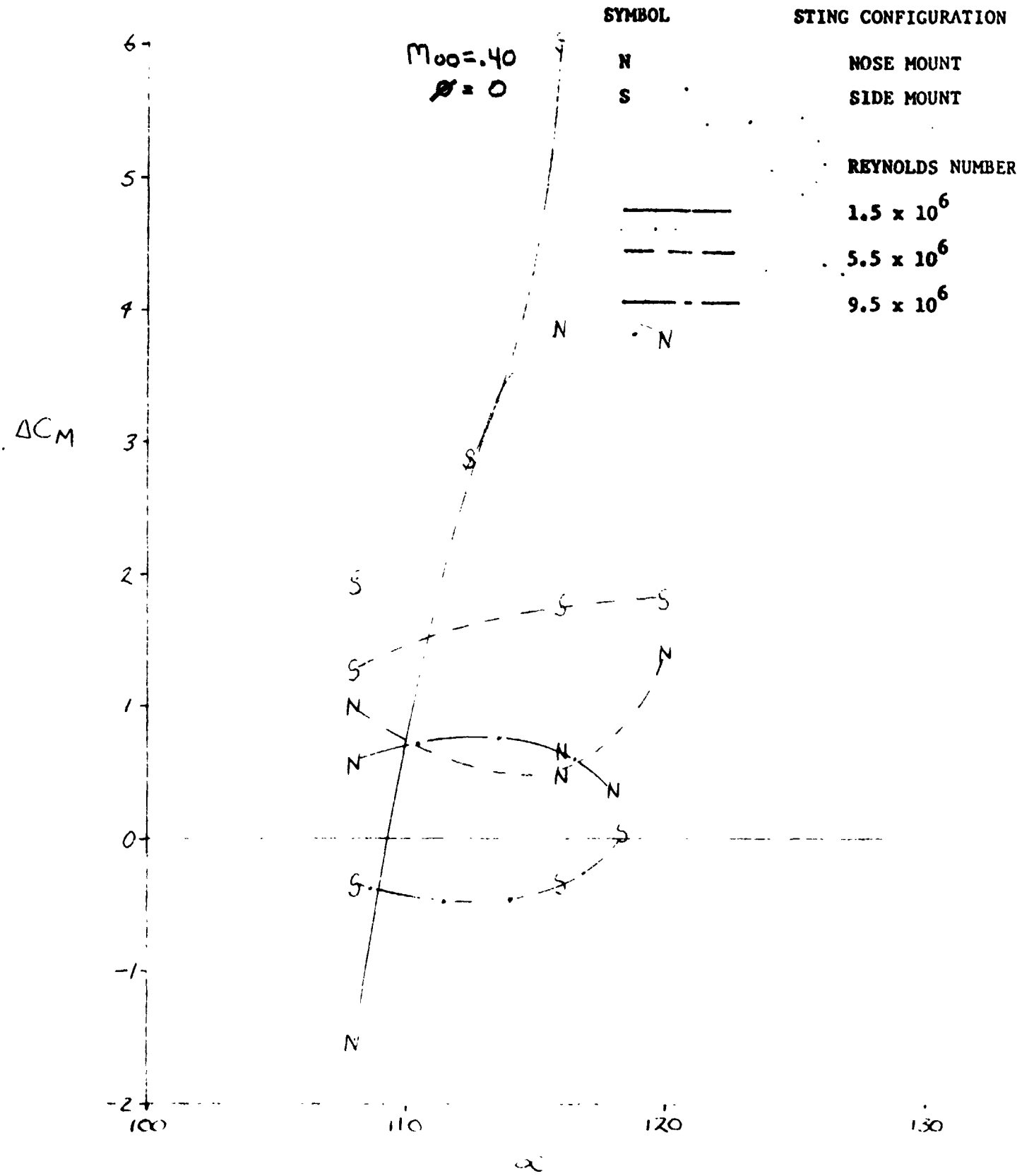

Figure 4-15. Pitching Moment Interference, HRWT, $M_\infty = 0.4$, $\phi = 0°$

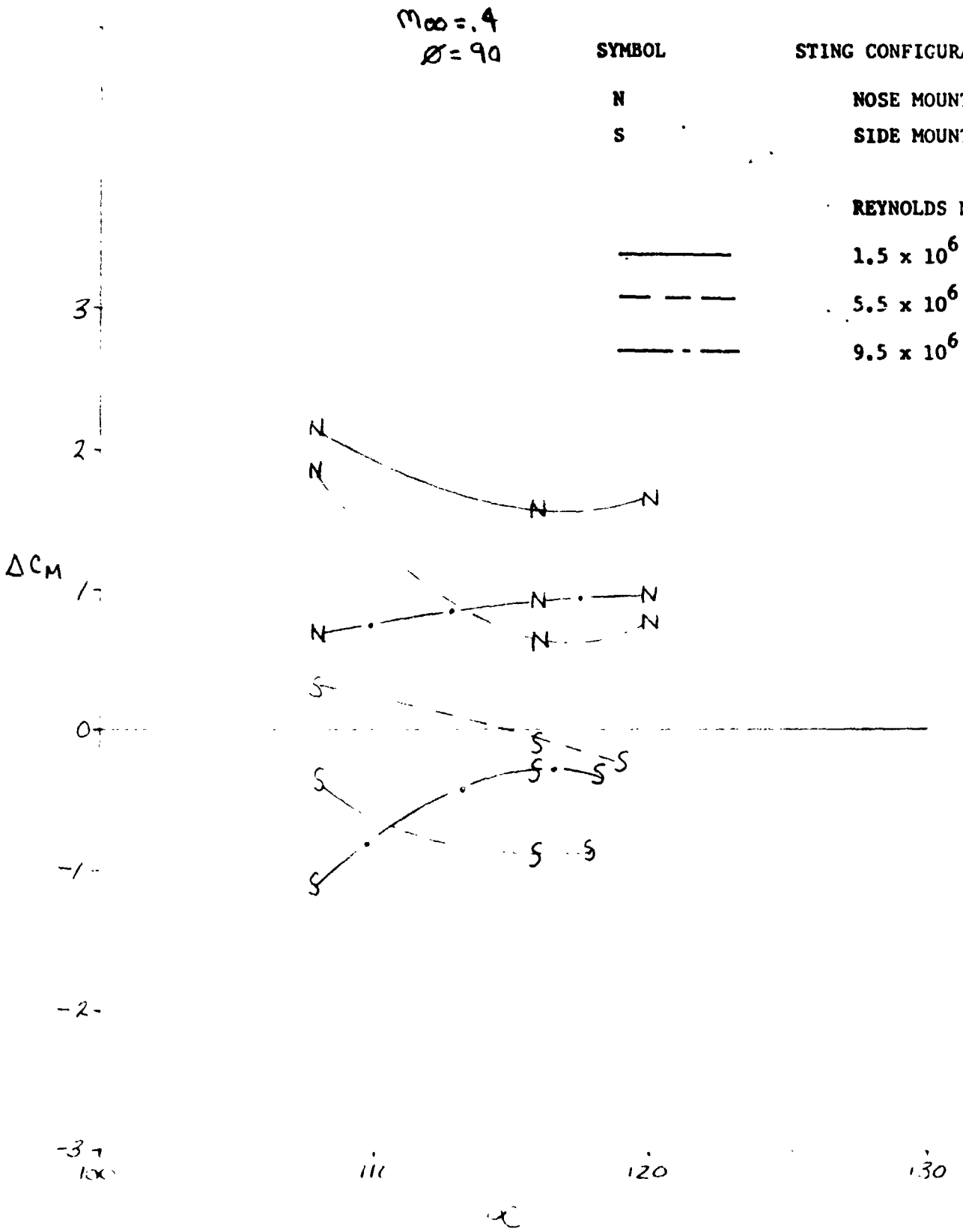

Figure 4-16. Pitching Moment Interference, HRWT, $M_\infty = 0.4$, $\phi = 90°$

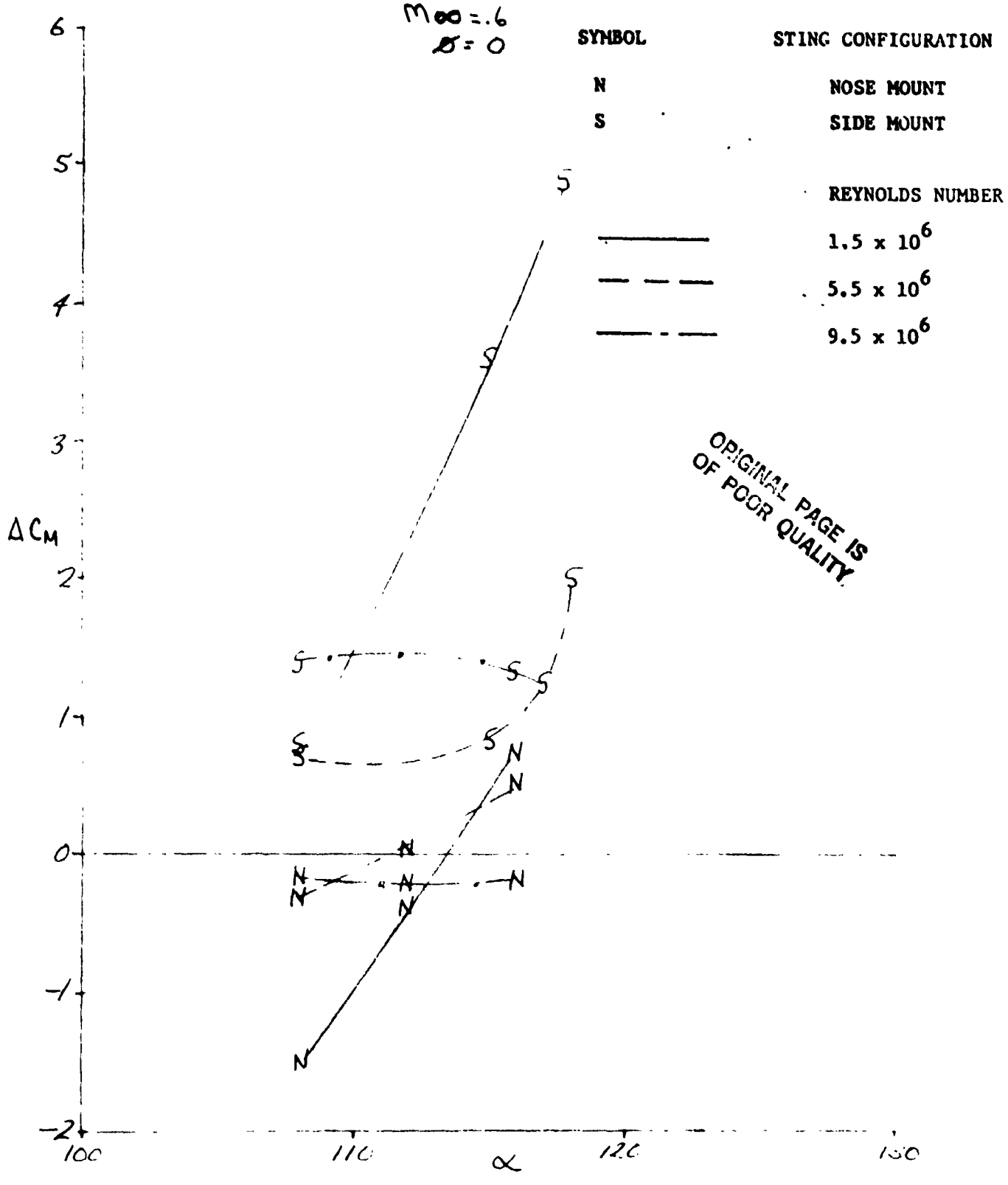

Figure 4-17. Pitching Moment Interference, HRWT, M_∞ = 0.6, ϕ = 0°

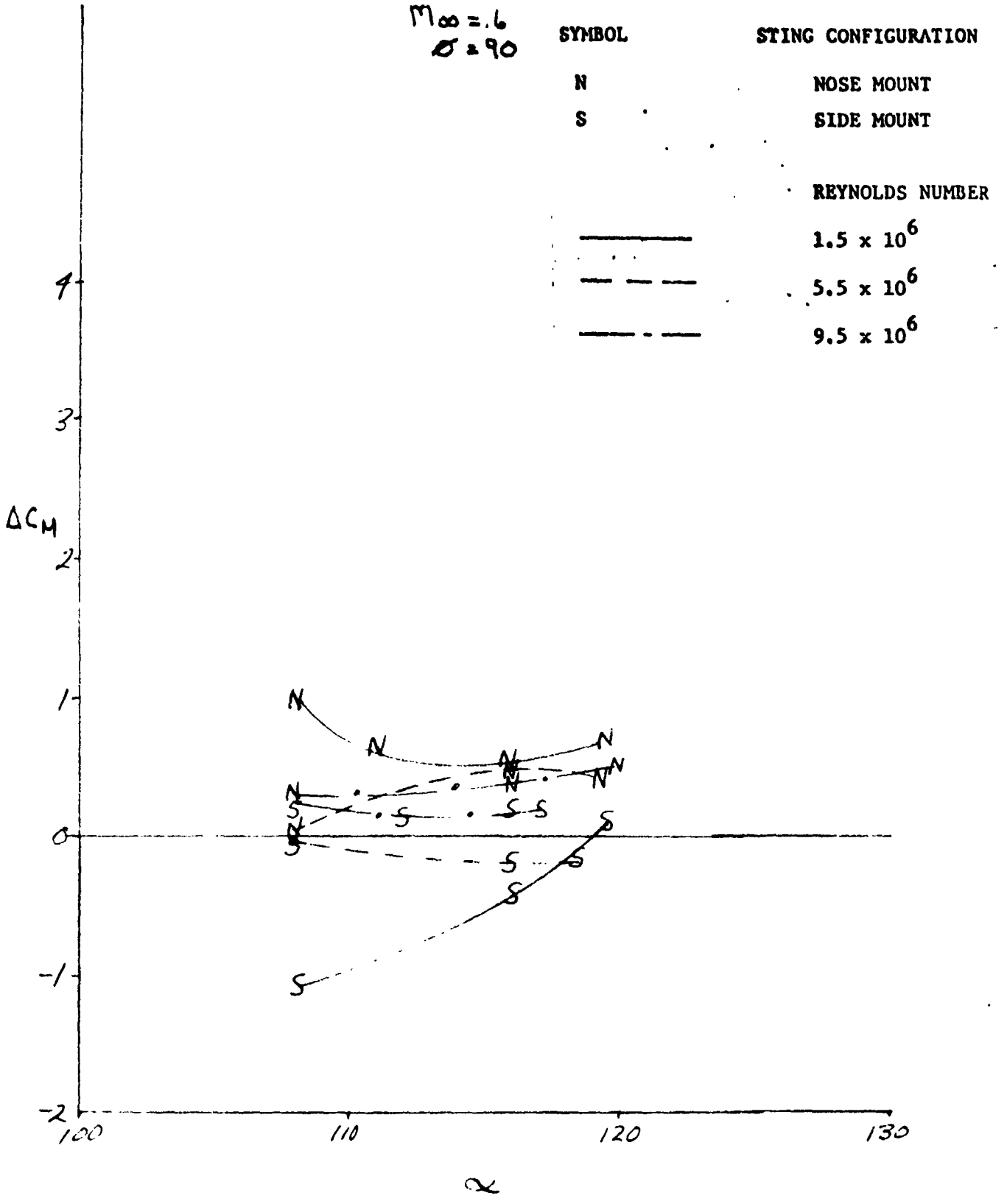

Figure 4-18. Pitching Moment Interference, HRWT, M_∞ = 0.6, ϕ = 90°

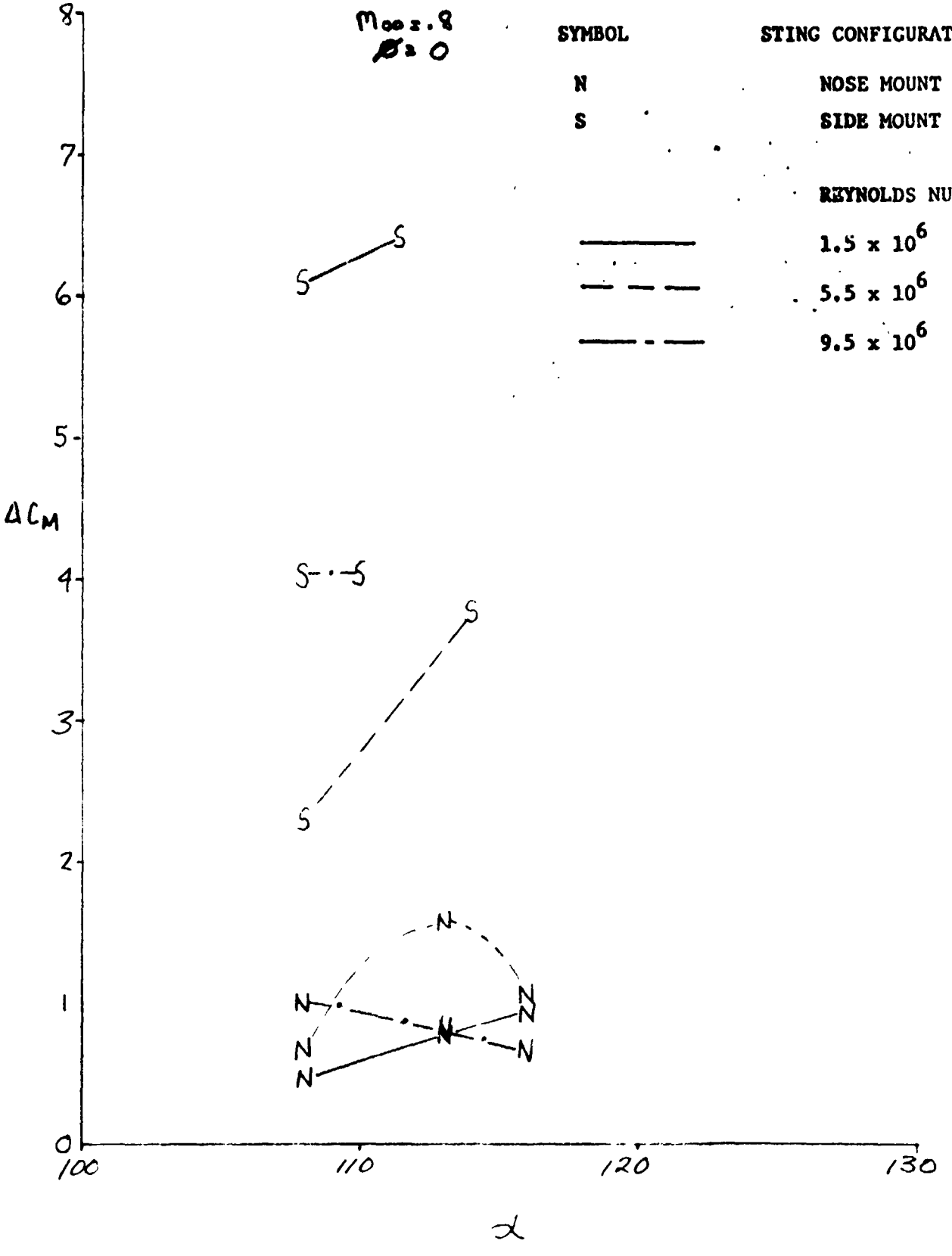

Figure 4-19. Pitching Moment Interference, HRWT, $M_\infty = 0.8$, $\phi = 0°$

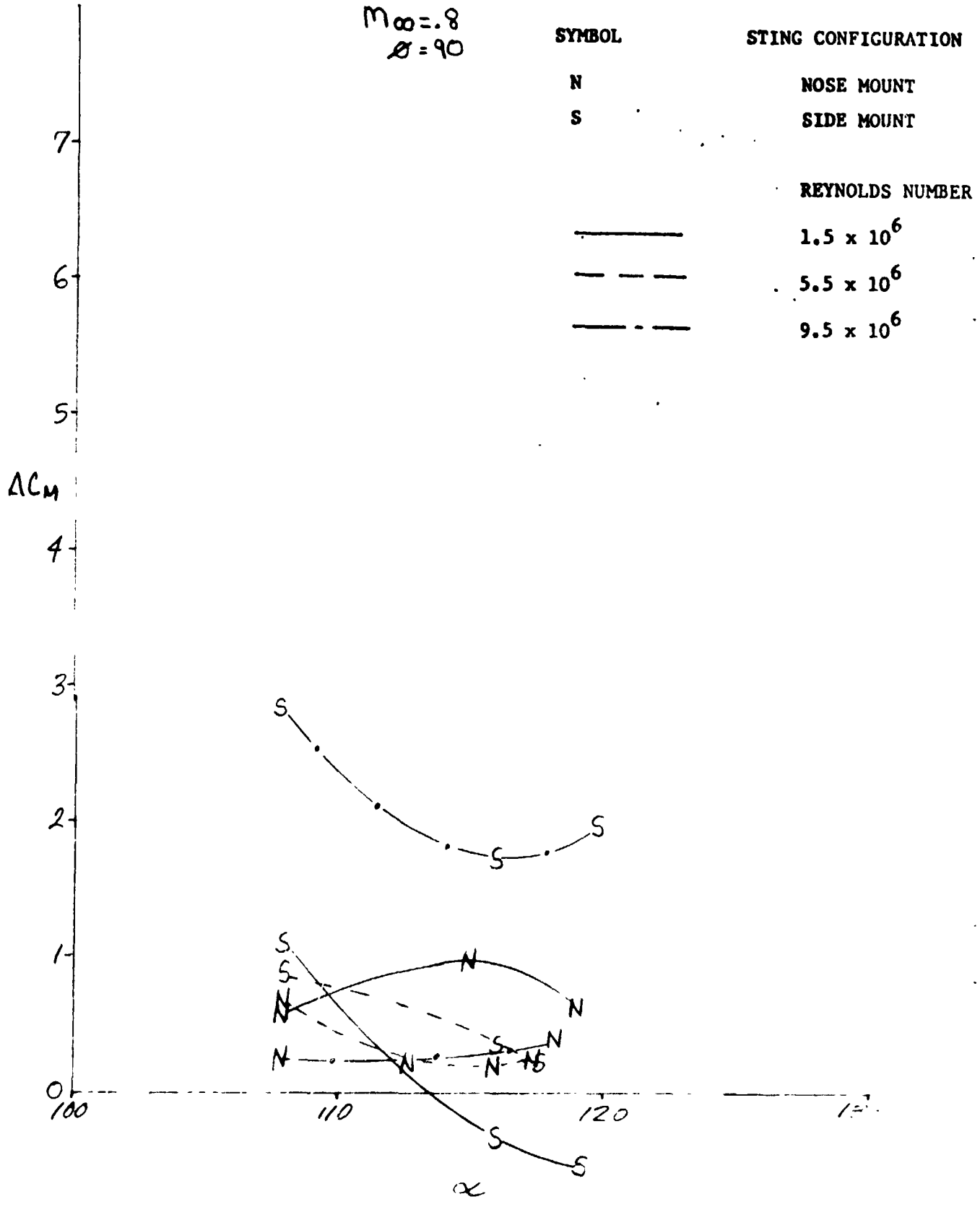

Figure 4-20. Pitching Moment Interference, HRWT, $M_\infty = 0.8$, $\phi = 90°$

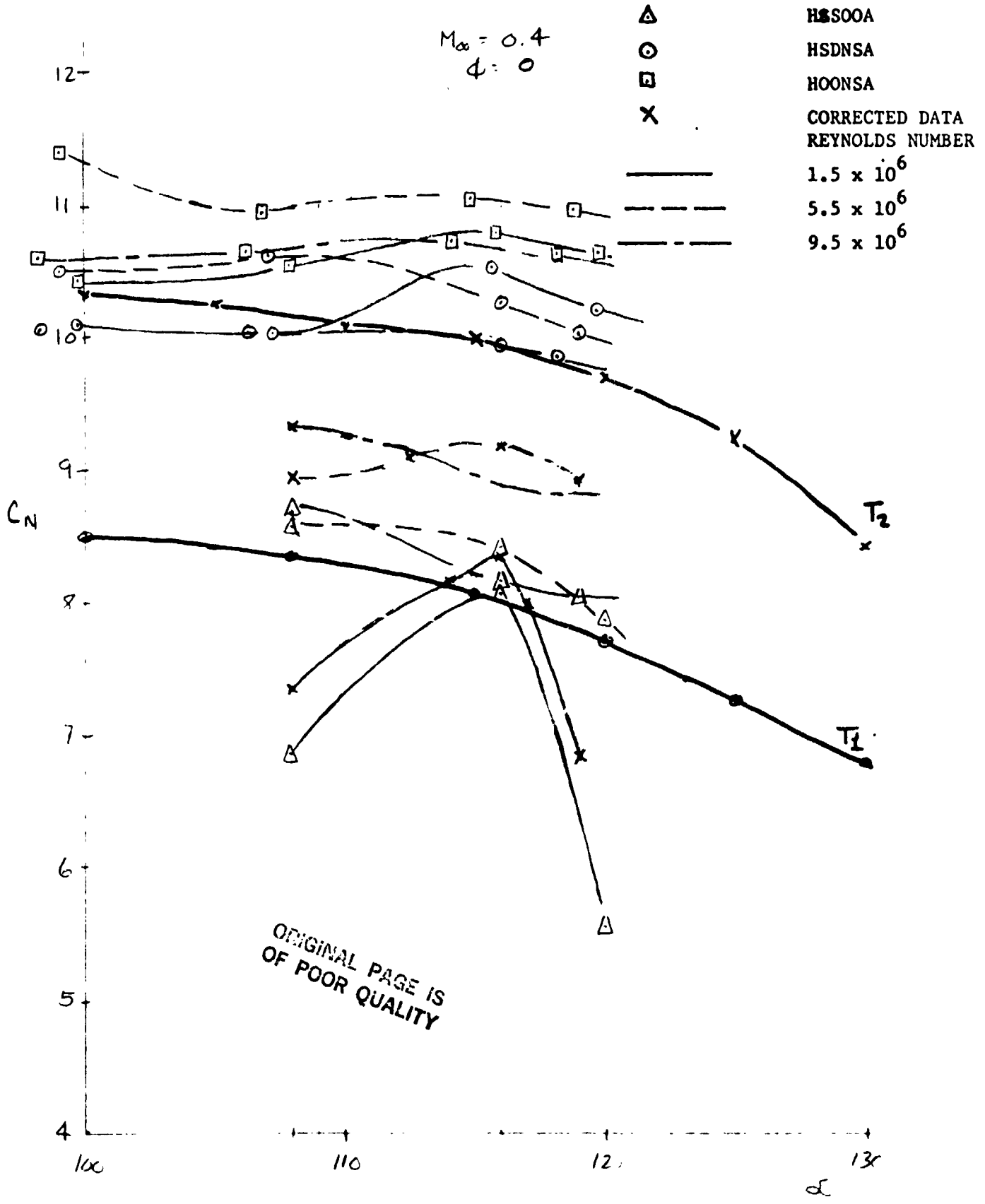

Figure 4-21. Normal Force Data, HRWT Side Mount, $M_\infty = 0.4$, $\phi = 0°$

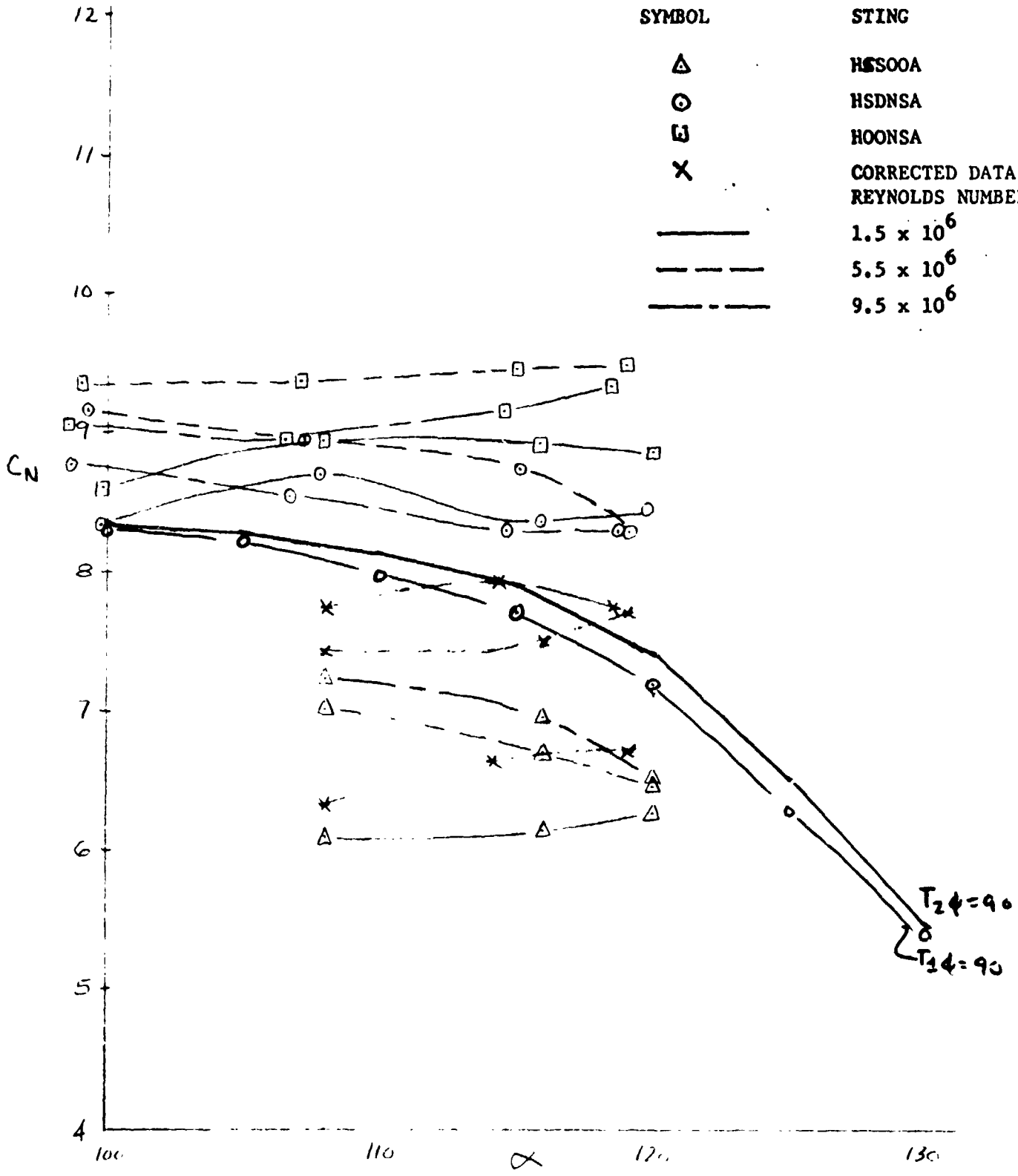

Figure 4-22. Normal Force Data, HRWT Side Mount, M_∞ = 0.4, ϕ = 90°

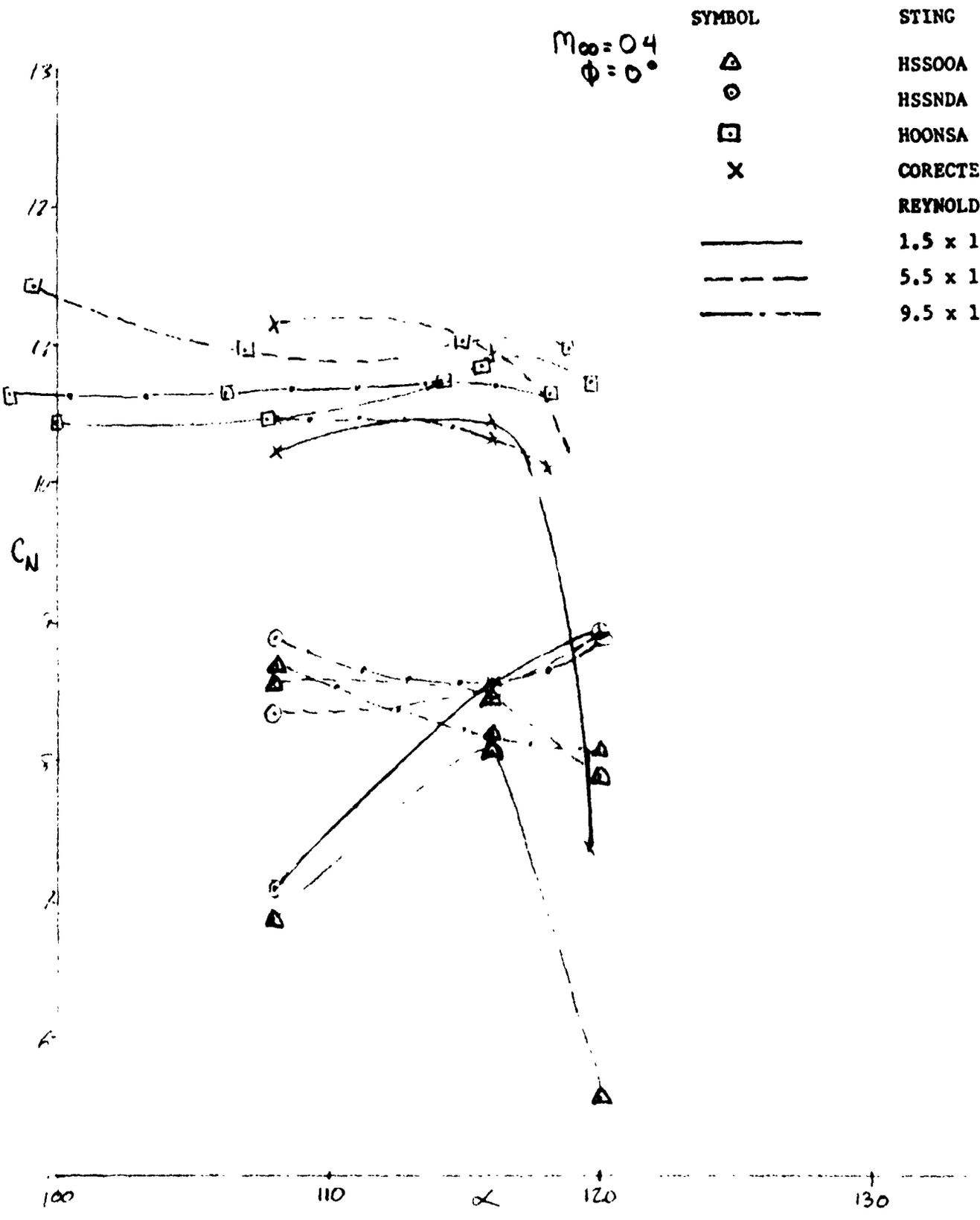

Figure 4-23. Normal Force Data, HRWT Nose Mount, M_∞ = 0.4, ϕ = 0°

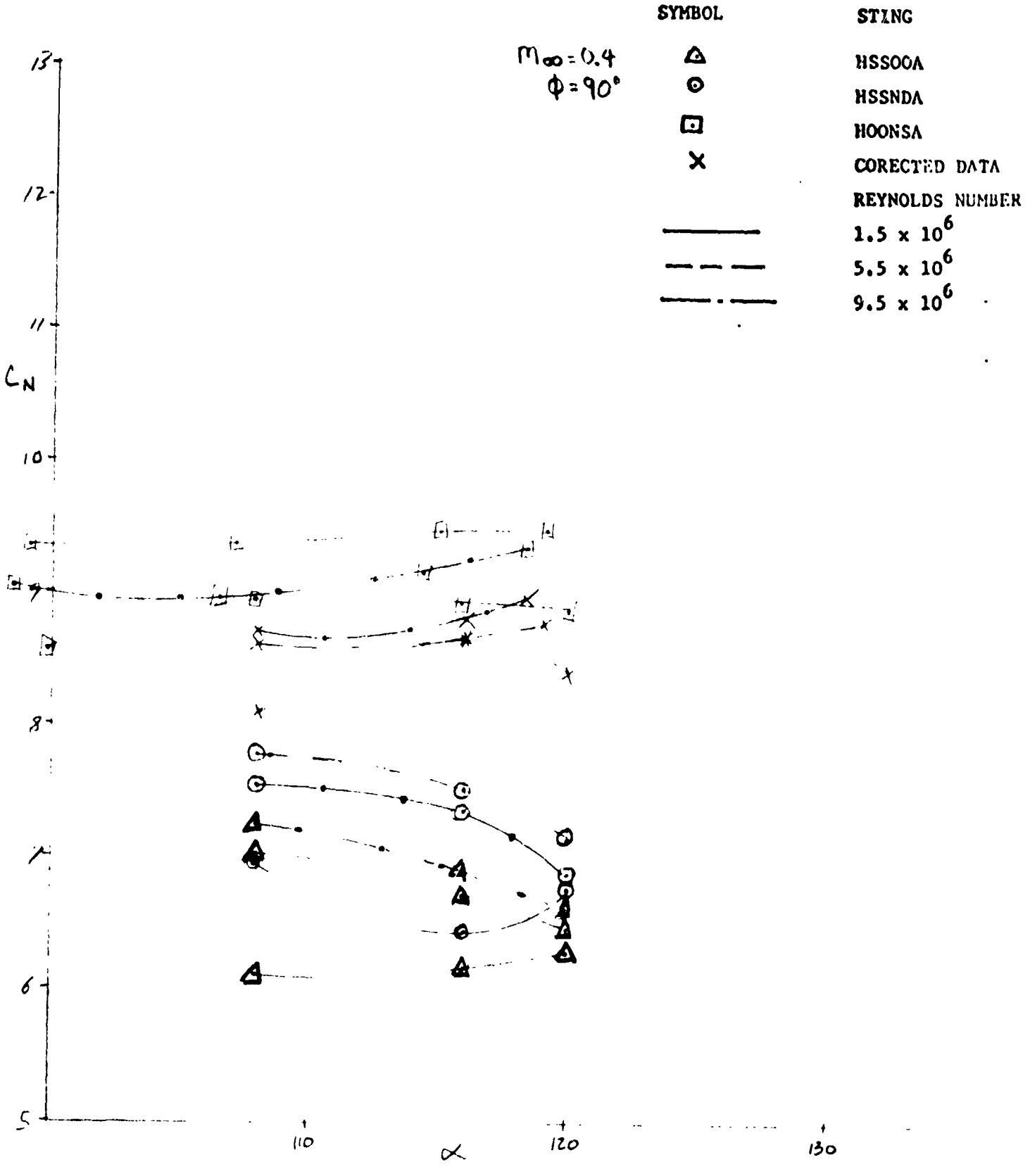

Figure 4-24. Normal Force Data, HRWT Nose Mount, M_∞ = 0.4, ϕ = 90°

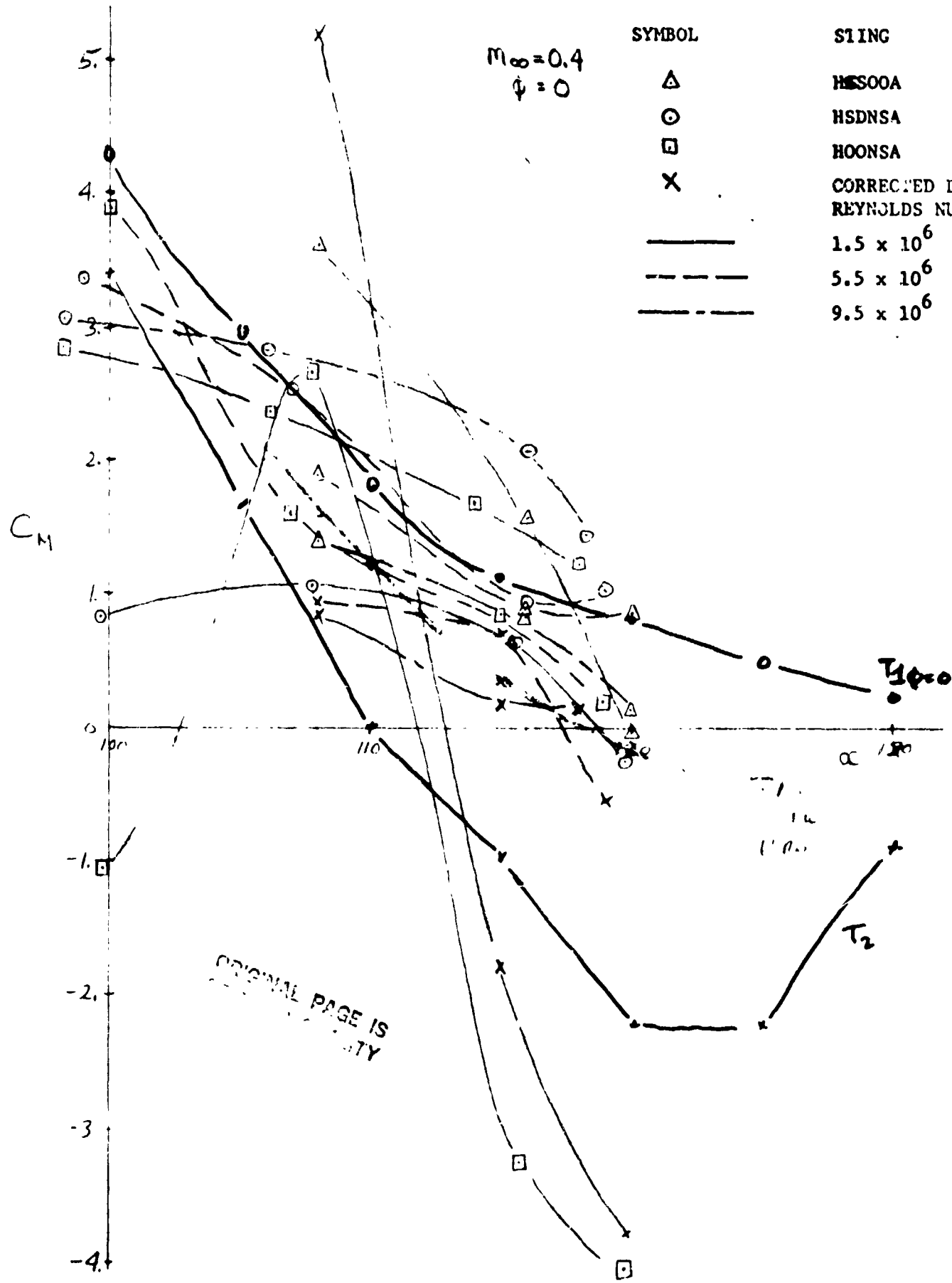

Figure 4-25. Pitching Moment Data, HRWT Side Mount, $M_\infty = 0.4$, $\phi = 0°$

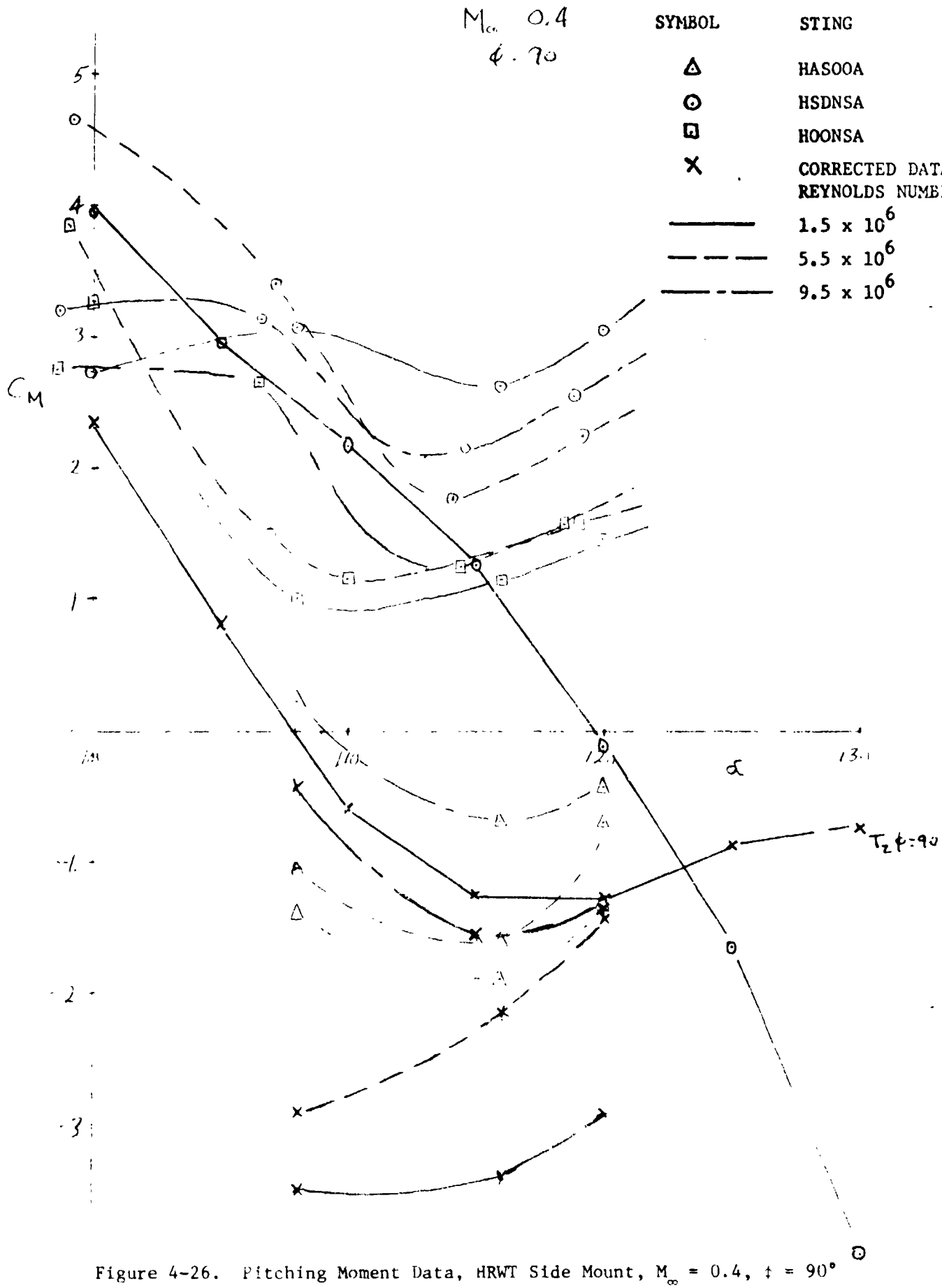

Figure 4-26. Pitching Moment Data, HRWT Side Mount, M_∞ = 0.4, ϕ = 90°

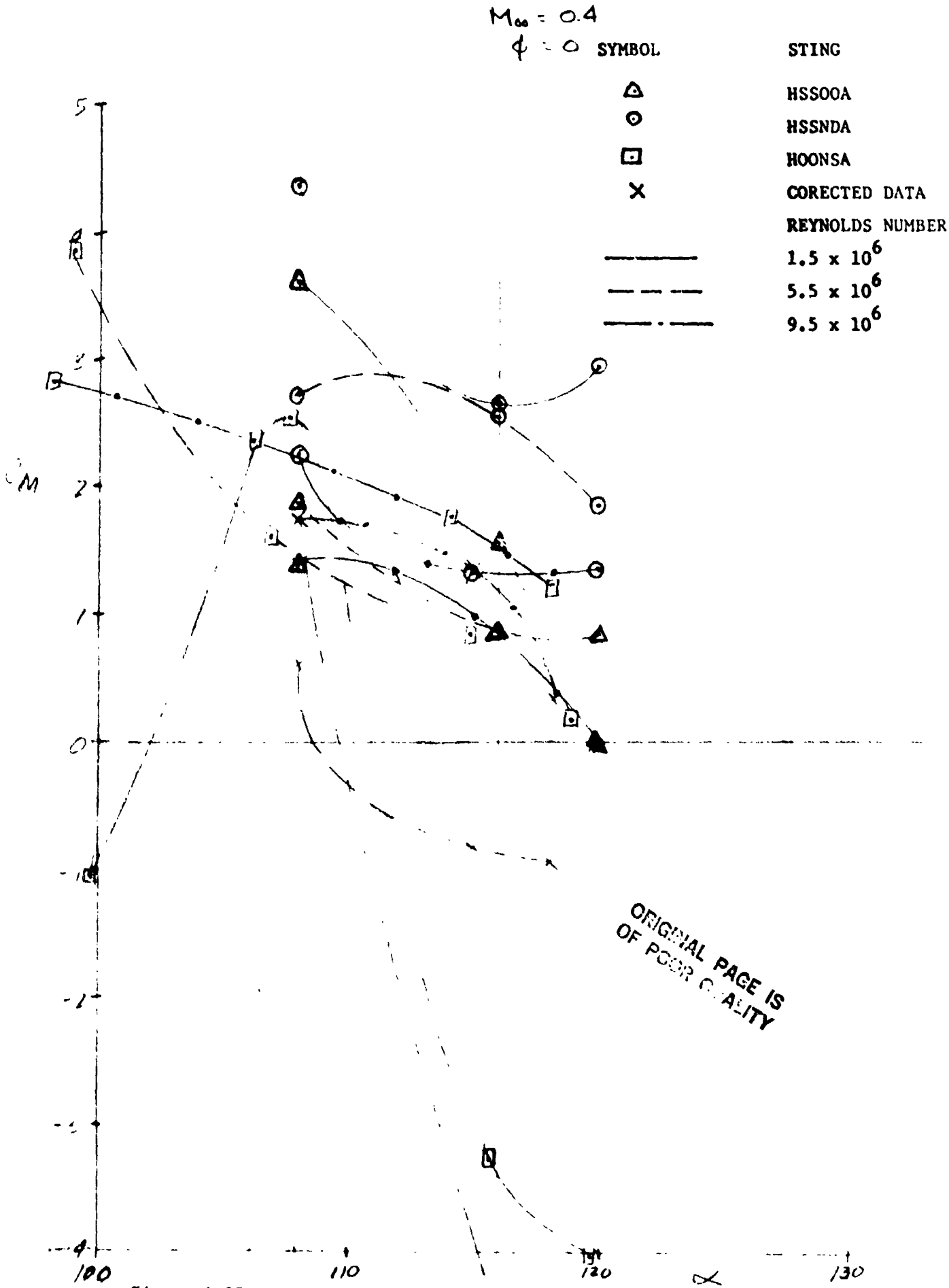

Figure 4-27. Pitching Moment Data, HRWT Nose Mount, $M_\infty = 0.4$, $\phi = 0°$

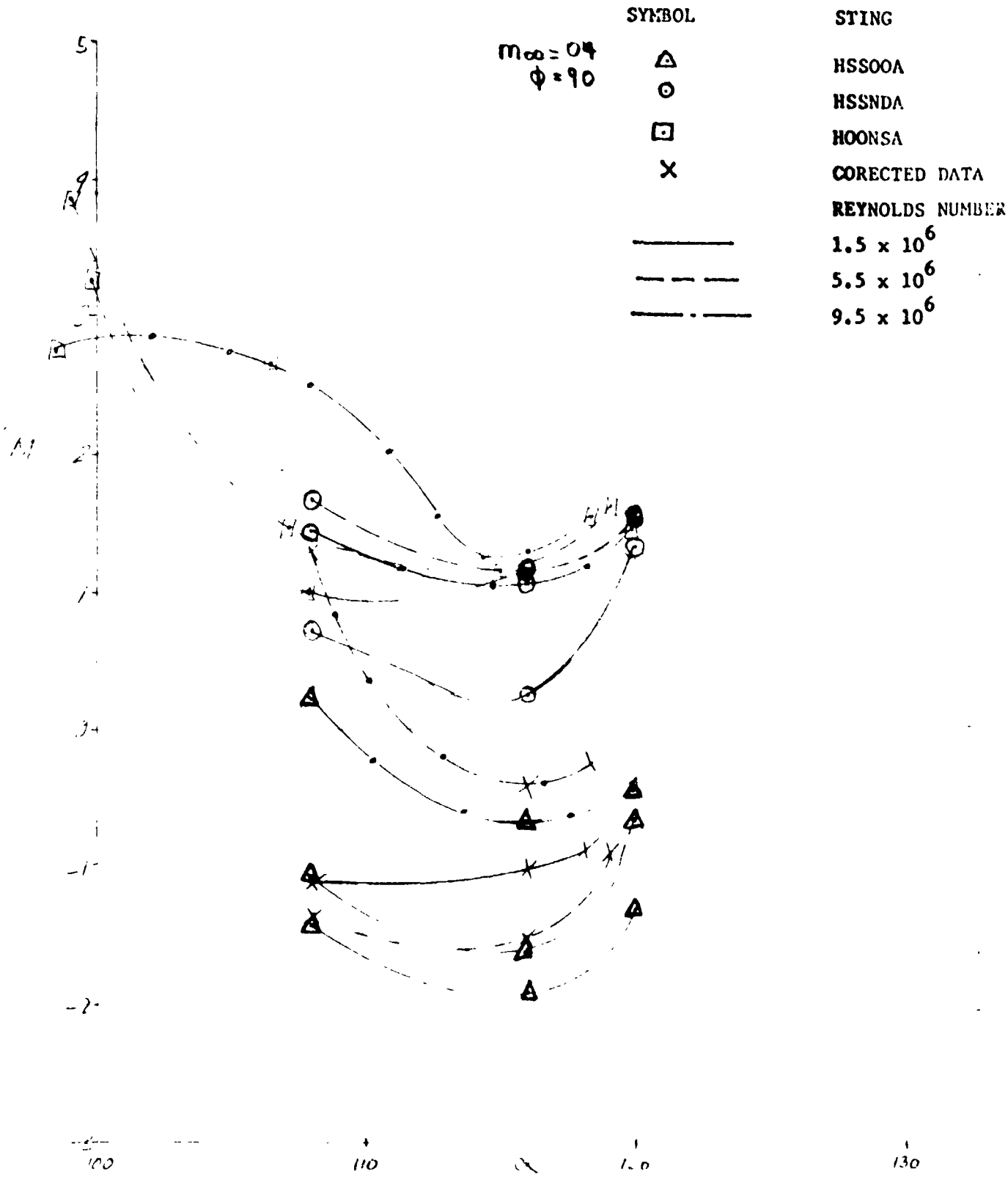

Figure 4-28. Pitching Moment Data, HRWT Nose Mount, $M_\infty = 0.4$, $\phi = 90°$

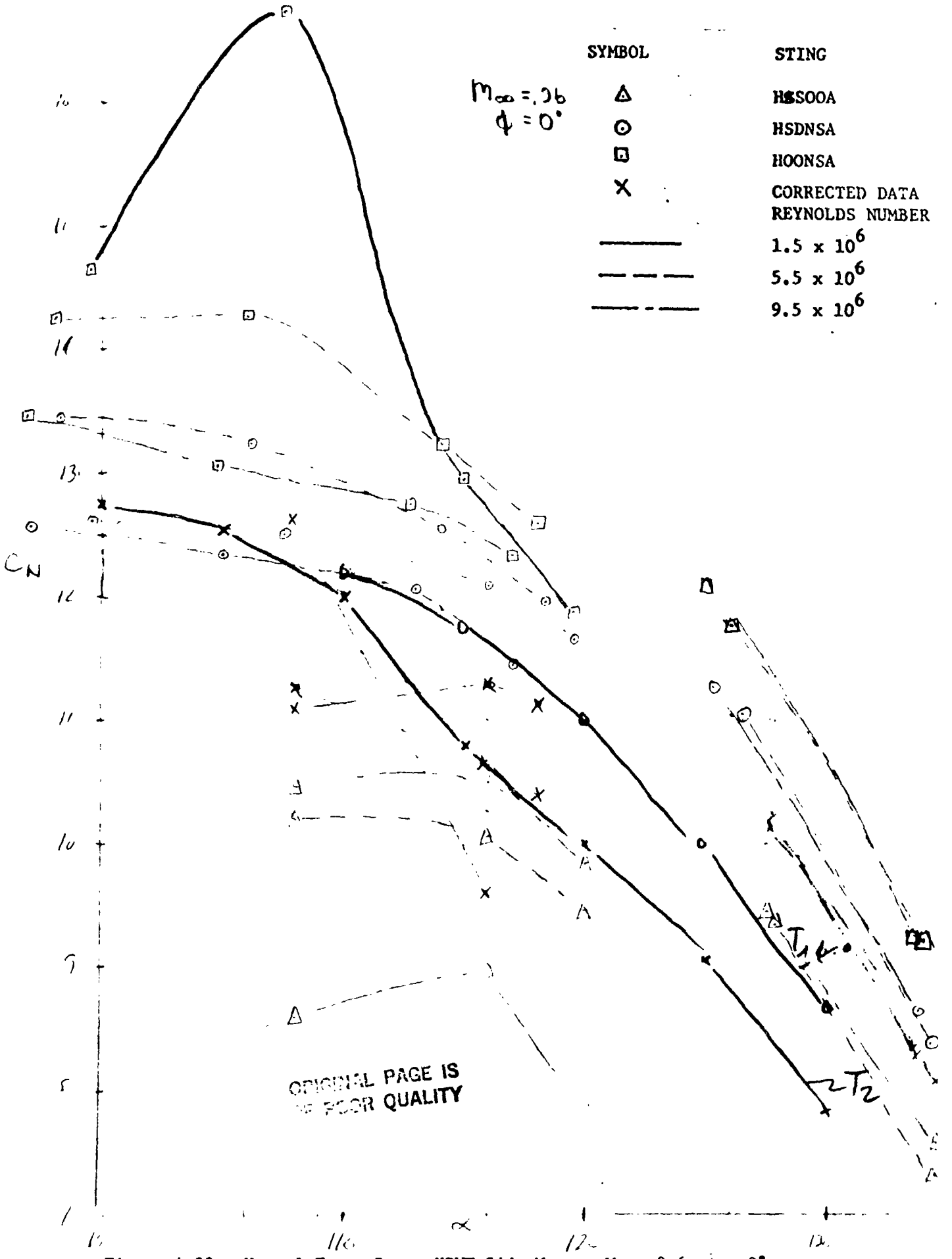

Figure 4-29. Normal Force Data, HRWT Side Mount, $M_\infty = 0.6$, $\phi = 0°$

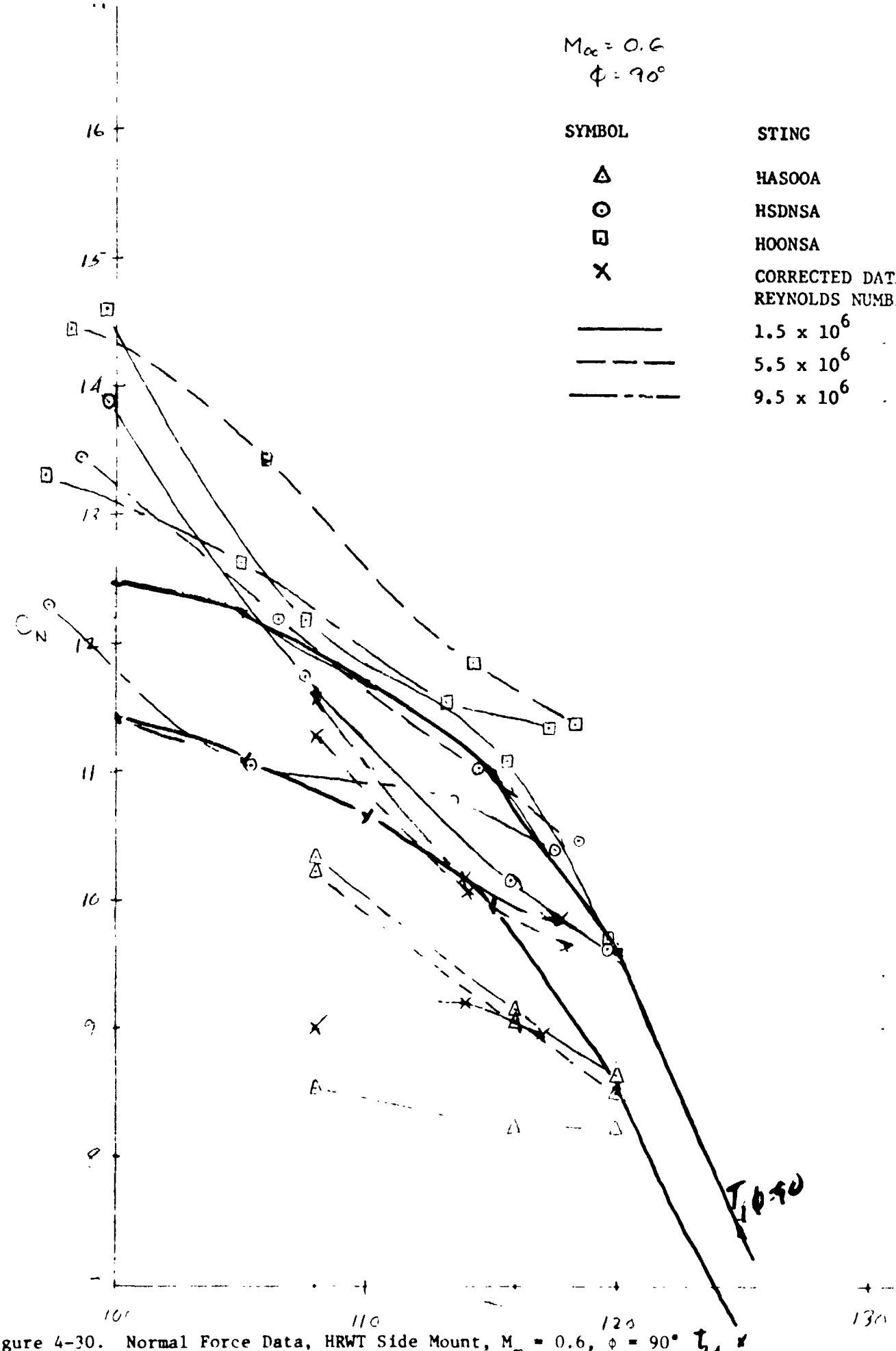

Figure 4-30. Normal Force Data, HRWT Side Mount, $M_\infty = 0.6$, $\phi = 90°$

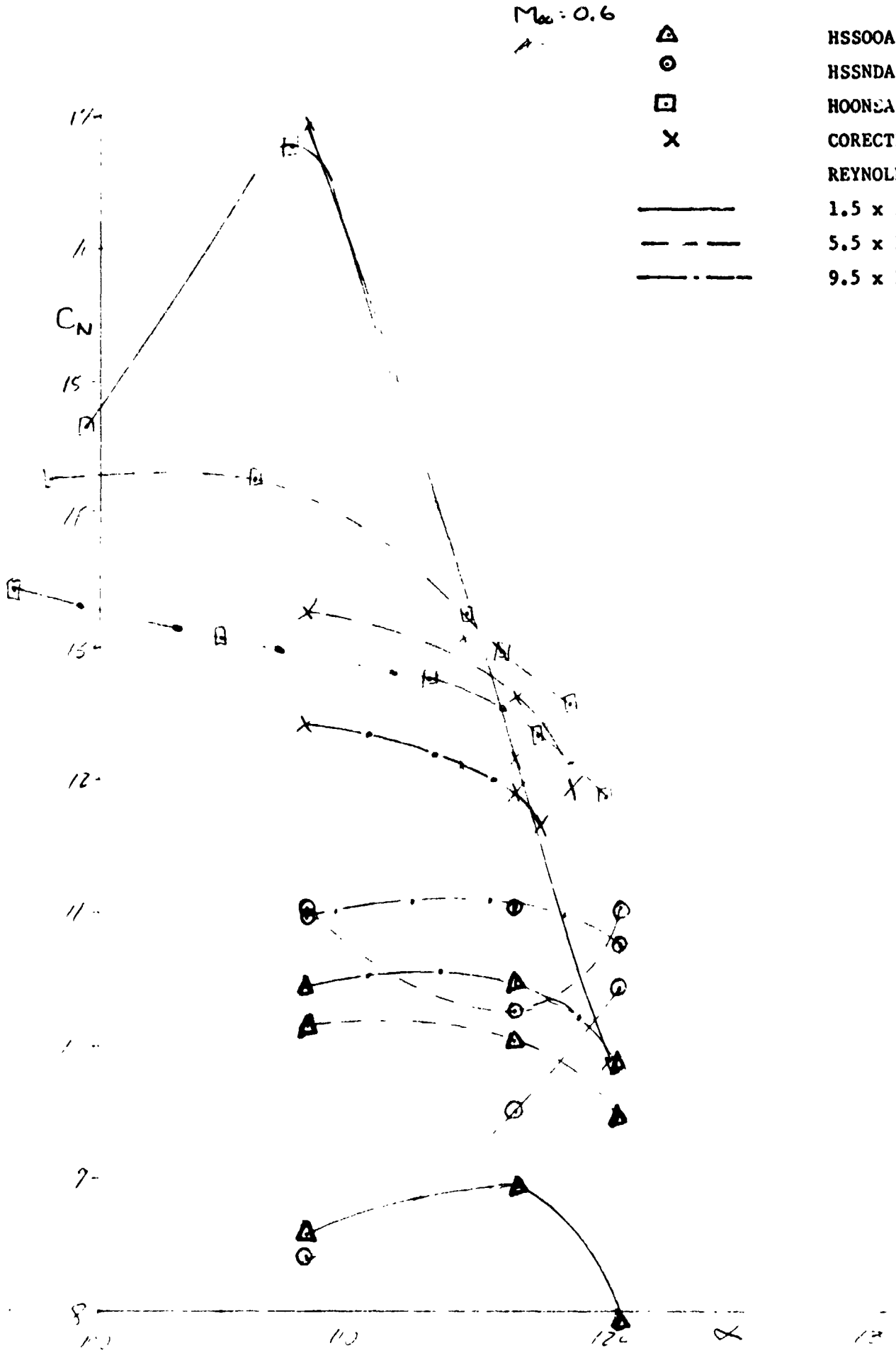

Figure 4-31. Normal Force Data, HRWT Nose Mount, $M_\infty = 0.6$, $\phi = 0°$

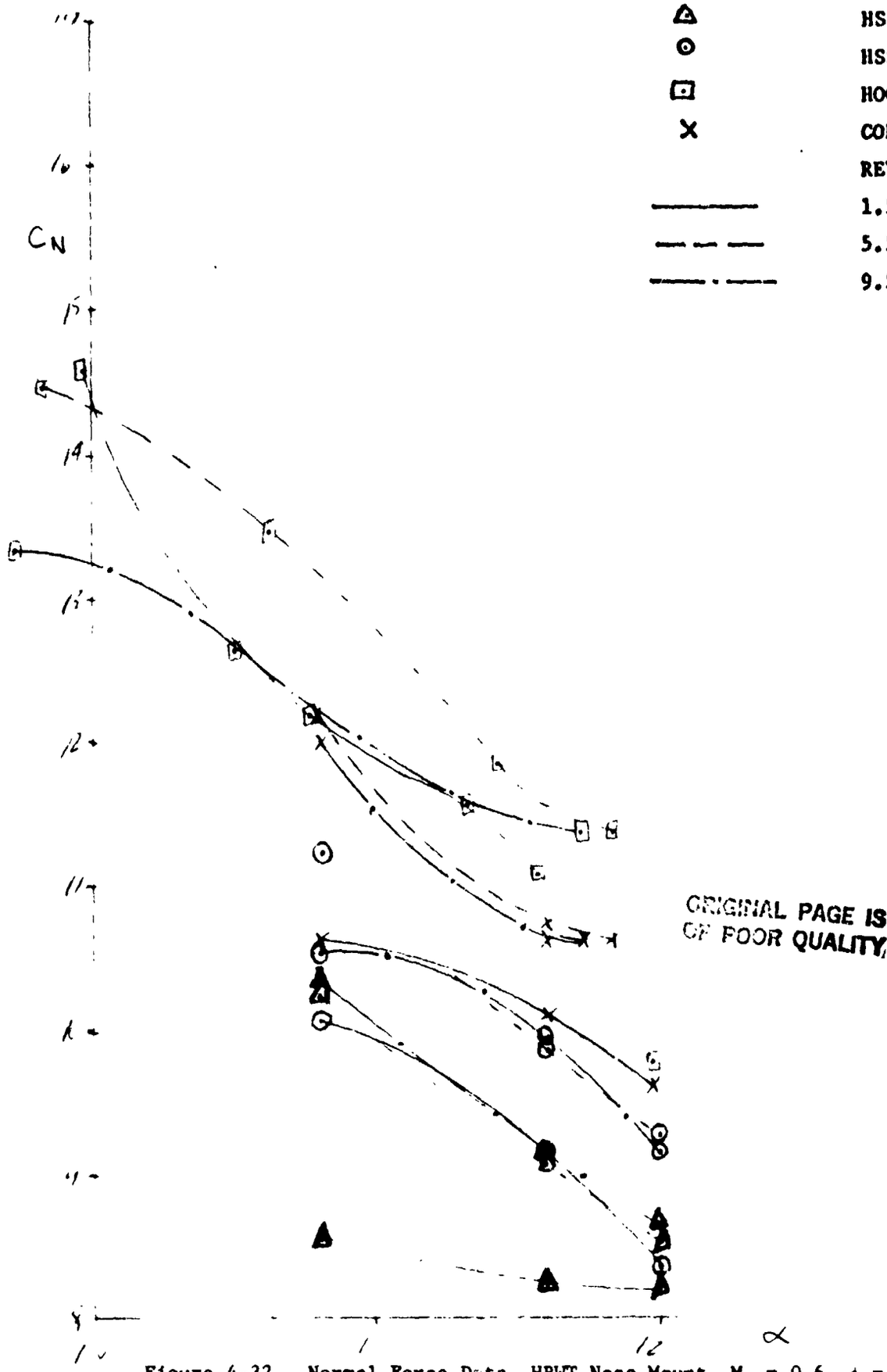

Figure 4-32. Normal Force Data, HRWT Nose Mount, $M_\infty = 0.6$, $\phi = 90°$

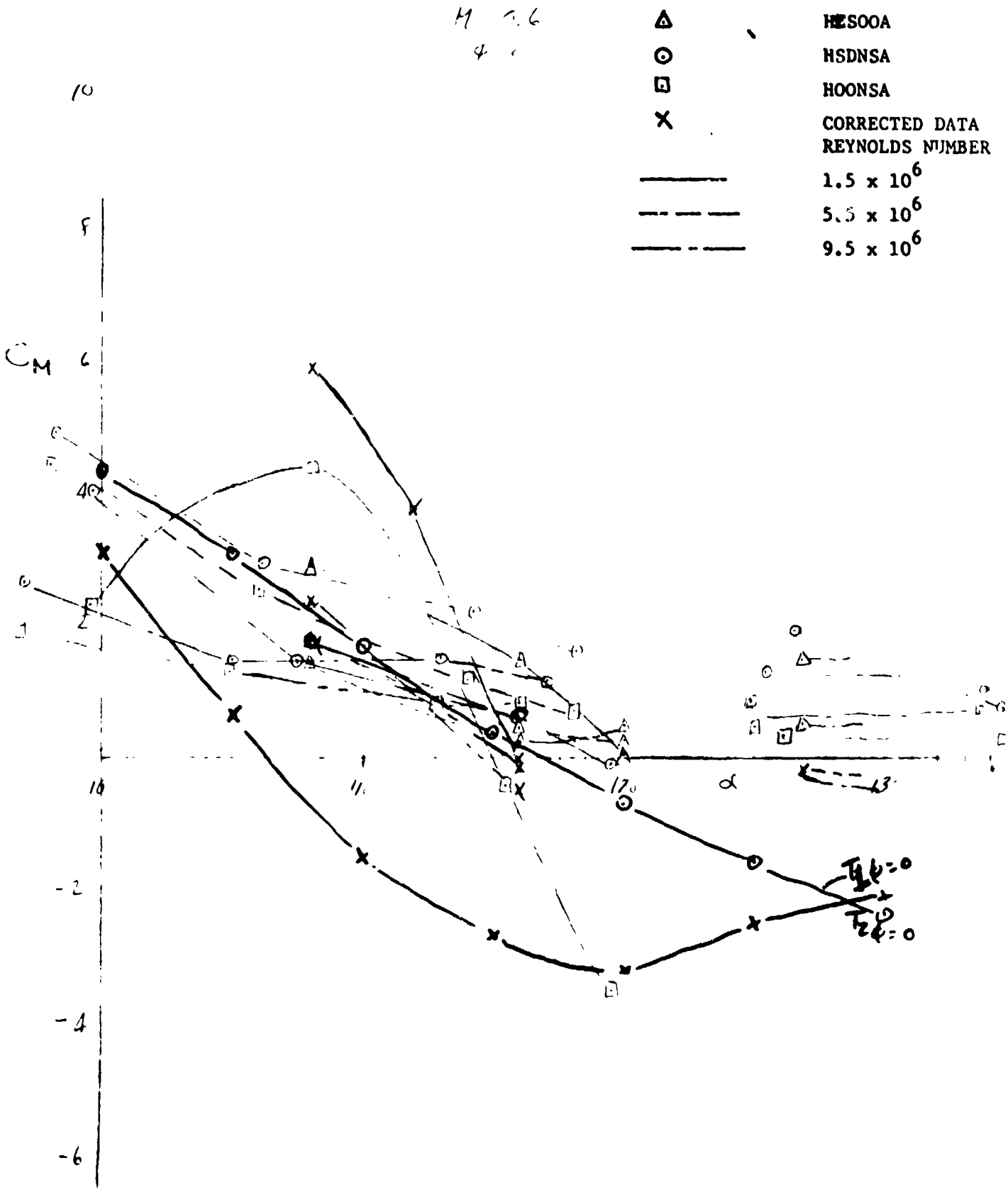

Figure 4-33. Pitching Moment Data, HRWT Side Mount, M_∞ = 0.6, ϕ = 0°

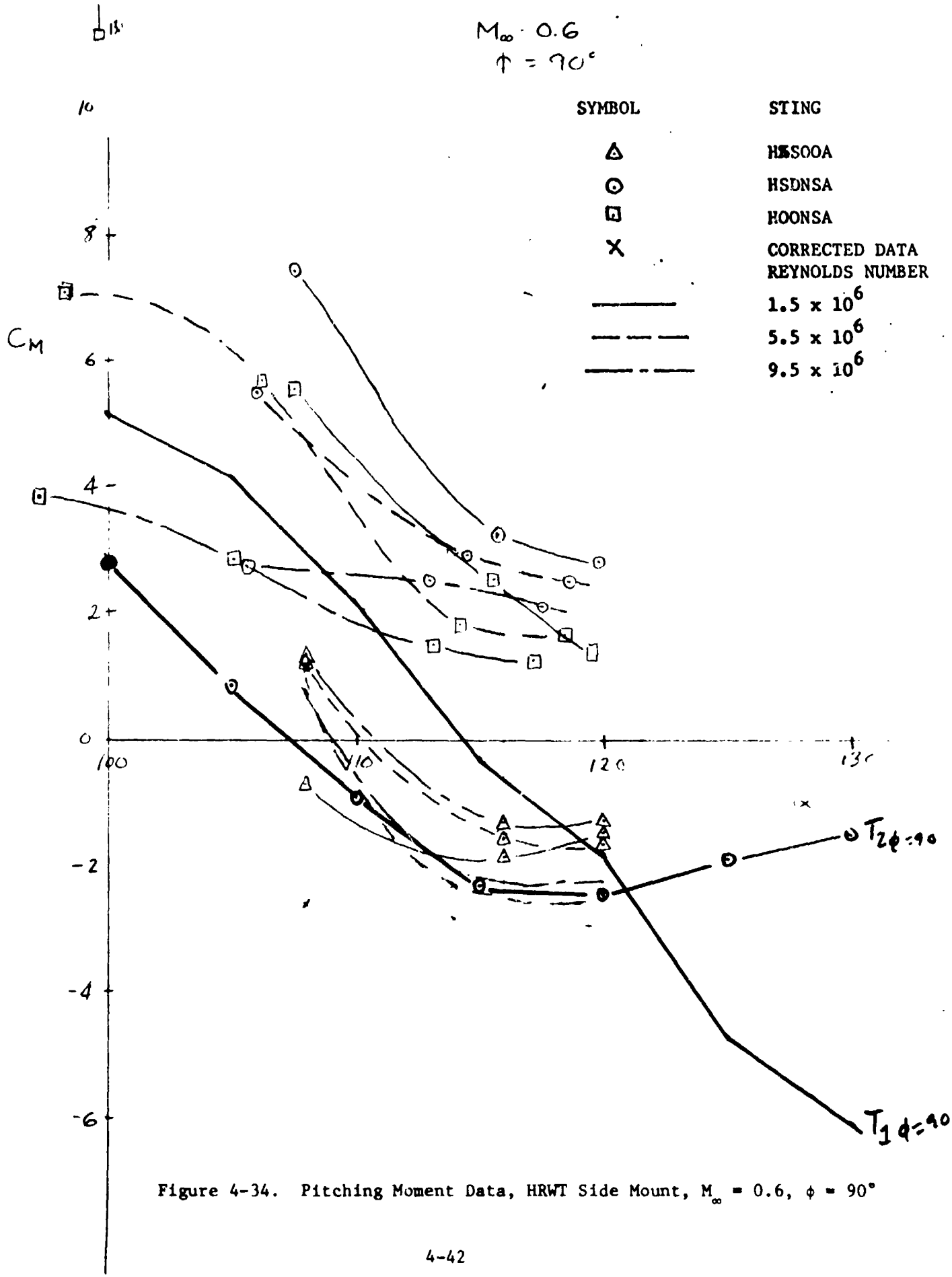

Figure 4-34. Pitching Moment Data, HRWT Side Mount, M_∞ = 0.6, ϕ = 90°

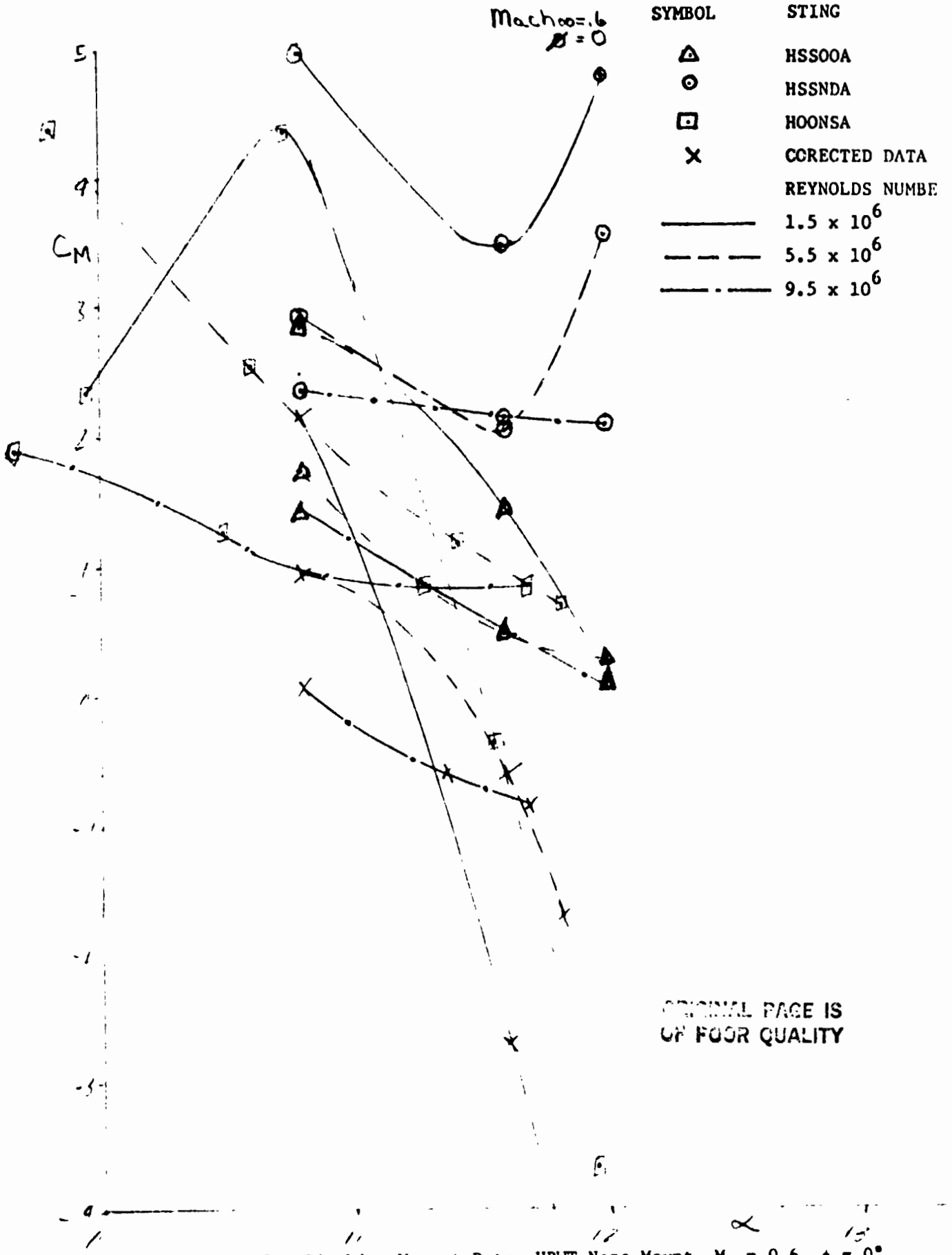

Figure 4-35. Pitching Moment Data, HRWT Nose Mount, $M_\infty = 0.6$, $\phi = 0°$

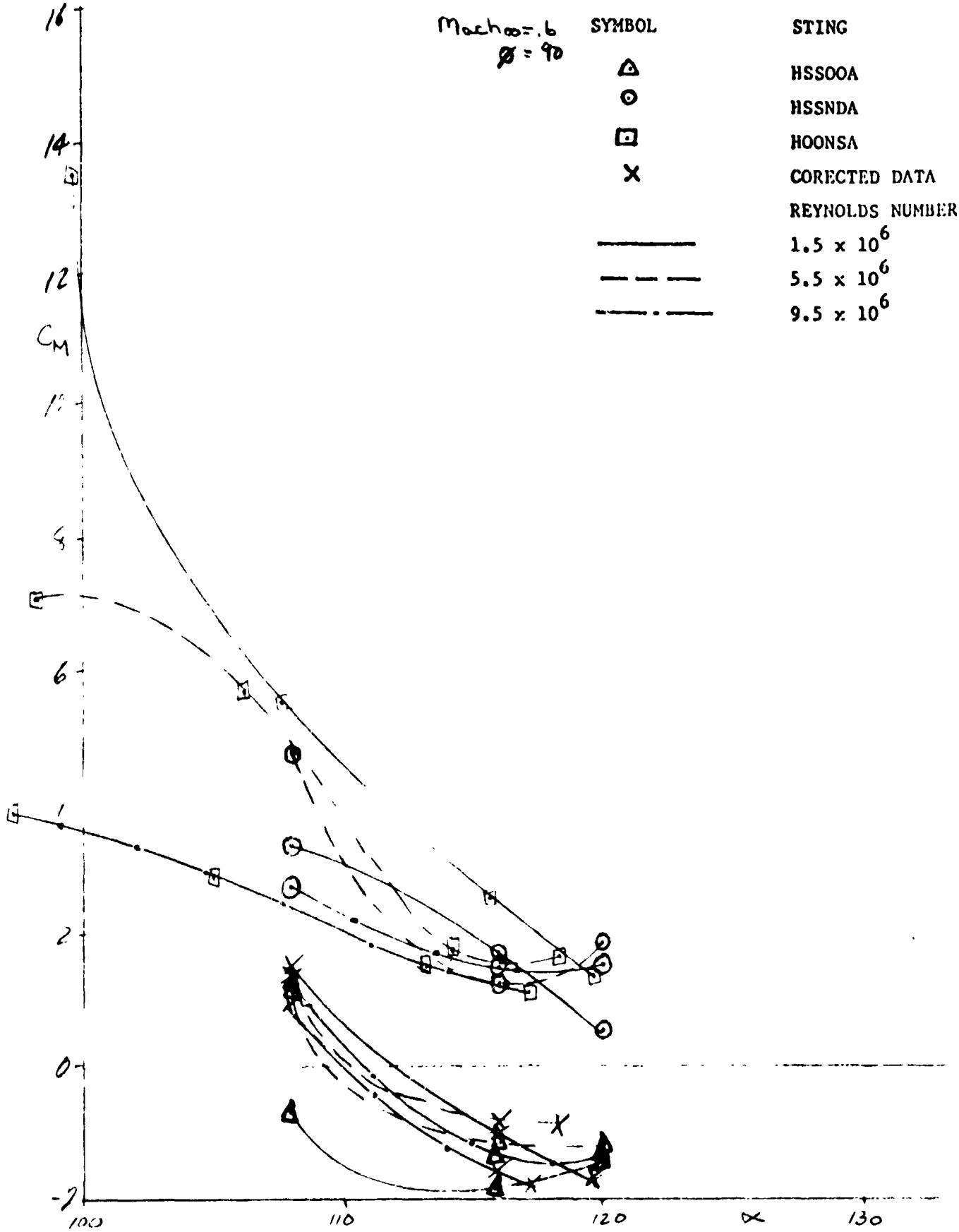

Figure 4-36. Pitching Moment Data, HRWT Nose Mount, M_∞ = 0.6, ϕ = 90°

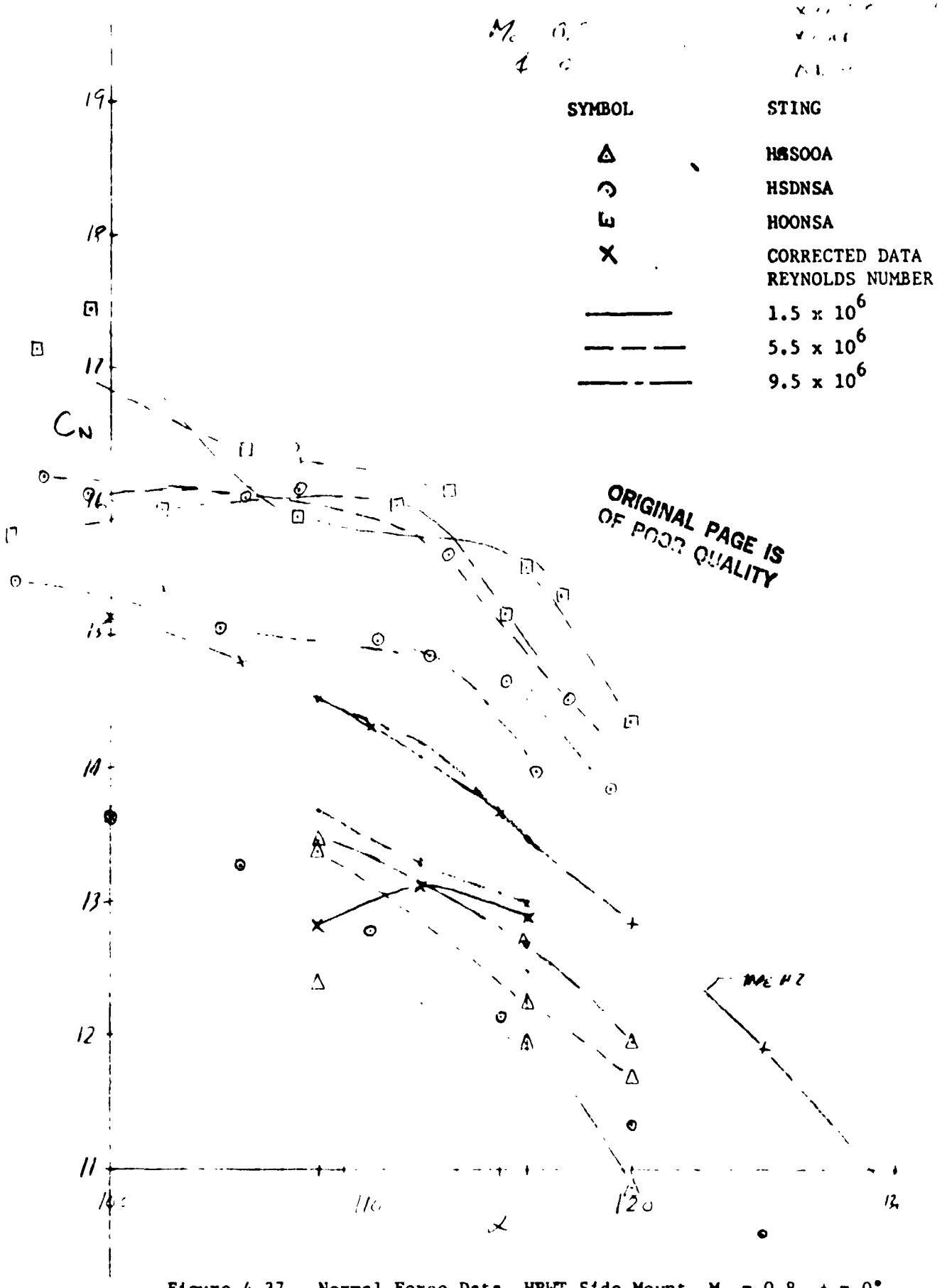

Figure 4-37. Normal Force Data, HRWT Side Mount, $M_\infty = 0.8$, $\phi = 0°$

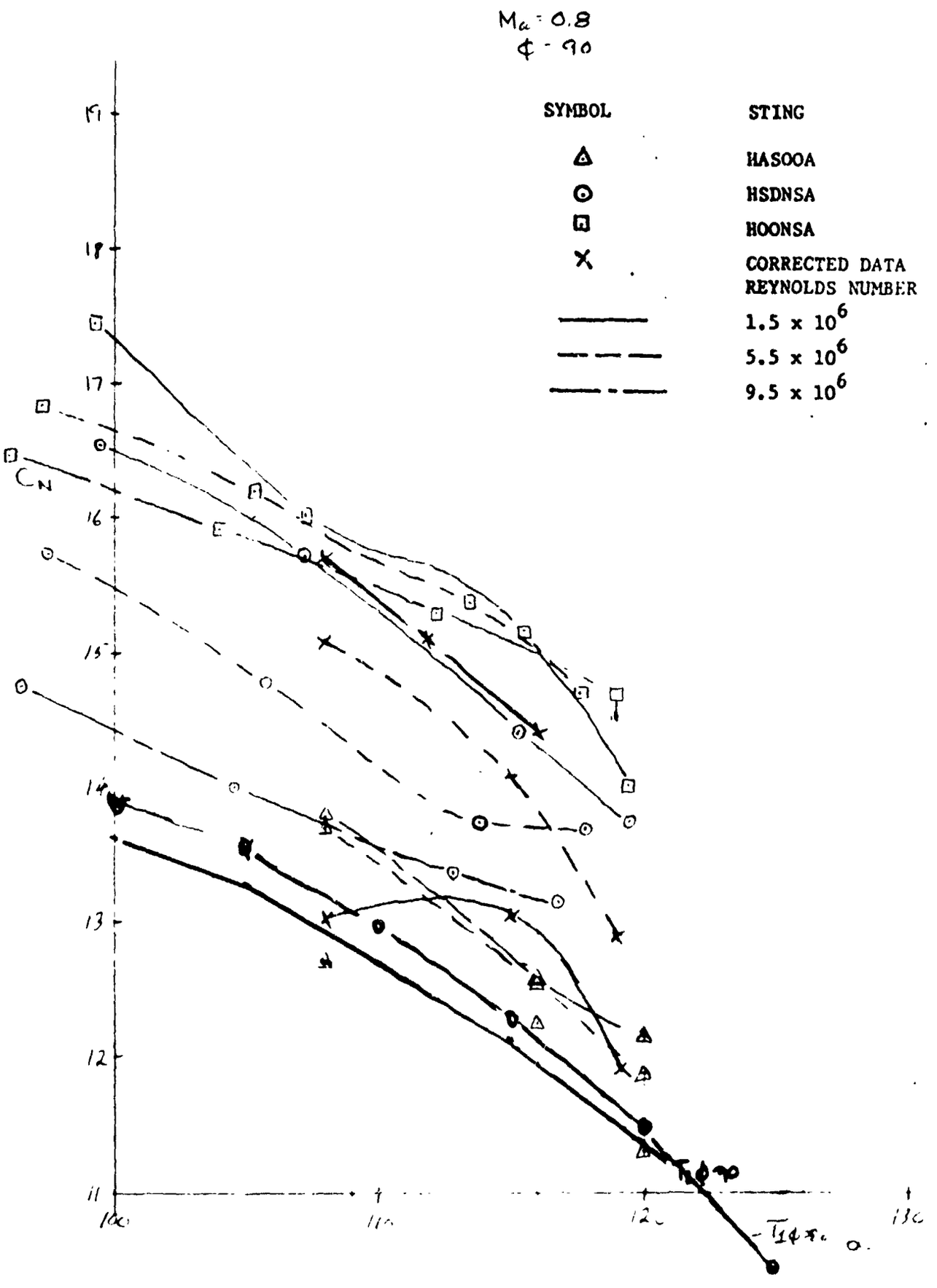

Figure 4-38. Normal Force Data, HRWT Side Mount, $M_\infty = 0.8$, $\phi = 90°$

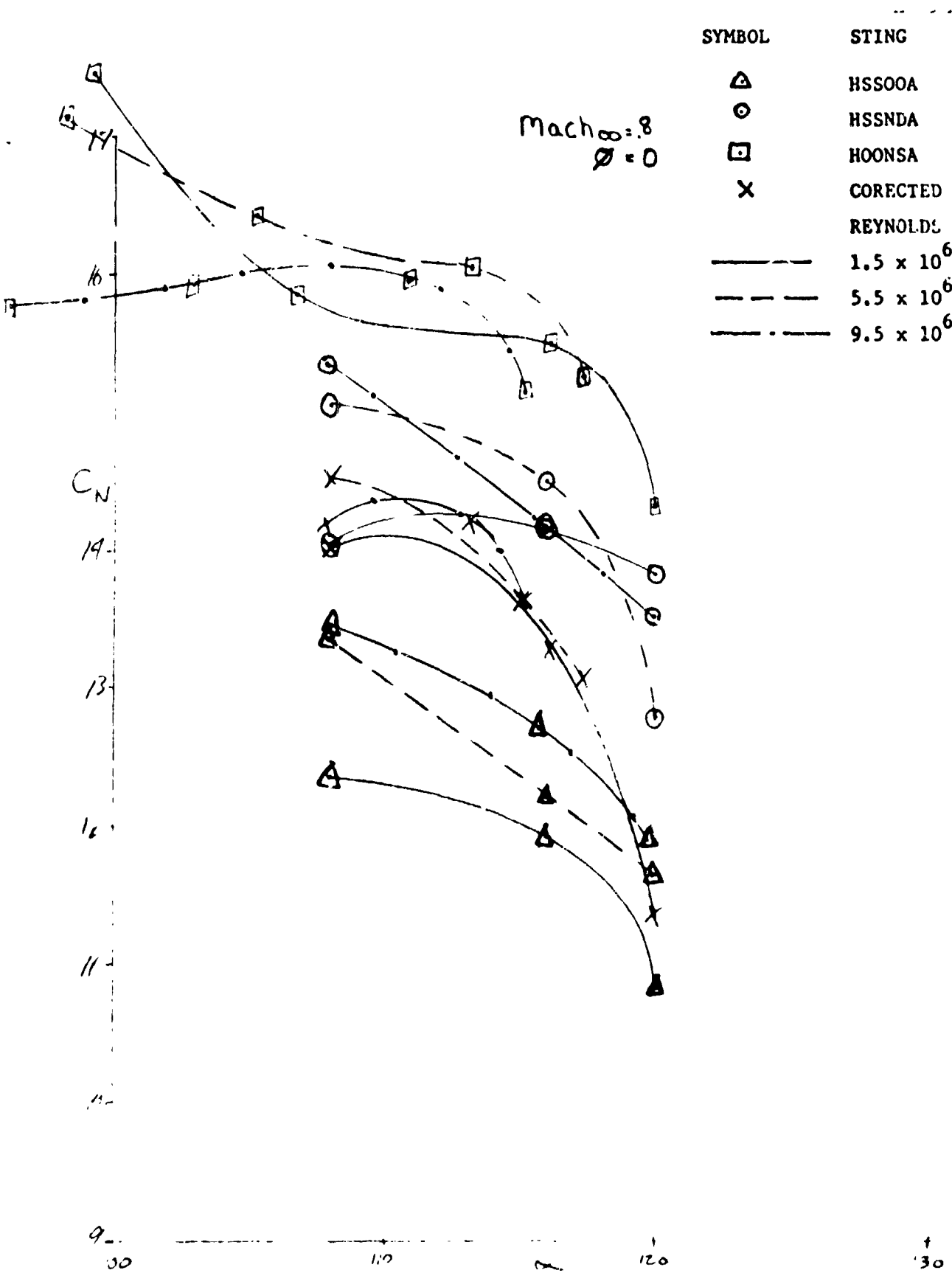

Figure 4-39. Normal Force Data, HRWT Nose Mount, $M_\infty = 0.8$, $\phi = 0°$

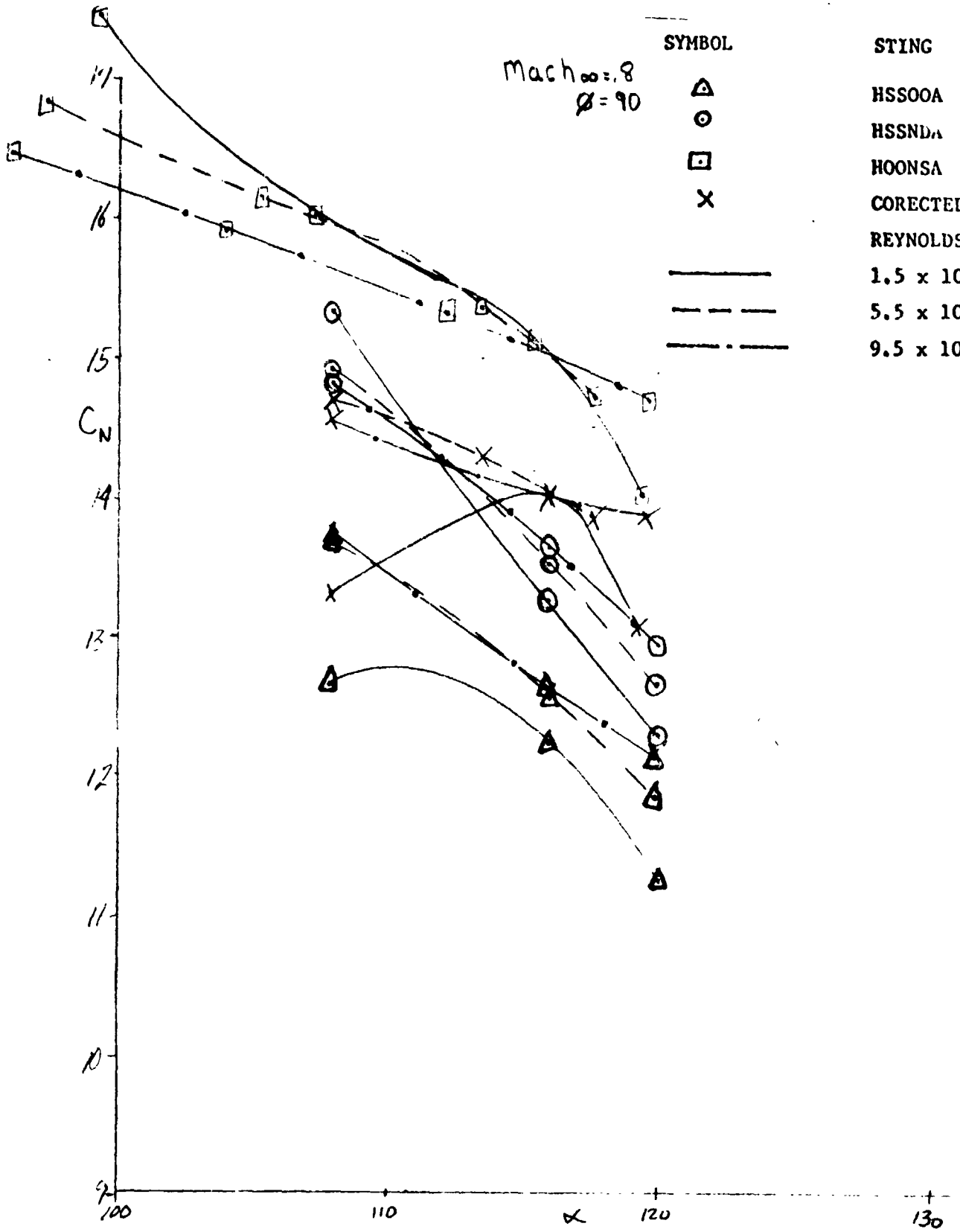

Figure 4-40. Normal Force Data, HRWT Nose Mount, $M_\infty = 0.8$, $\phi = 90°$

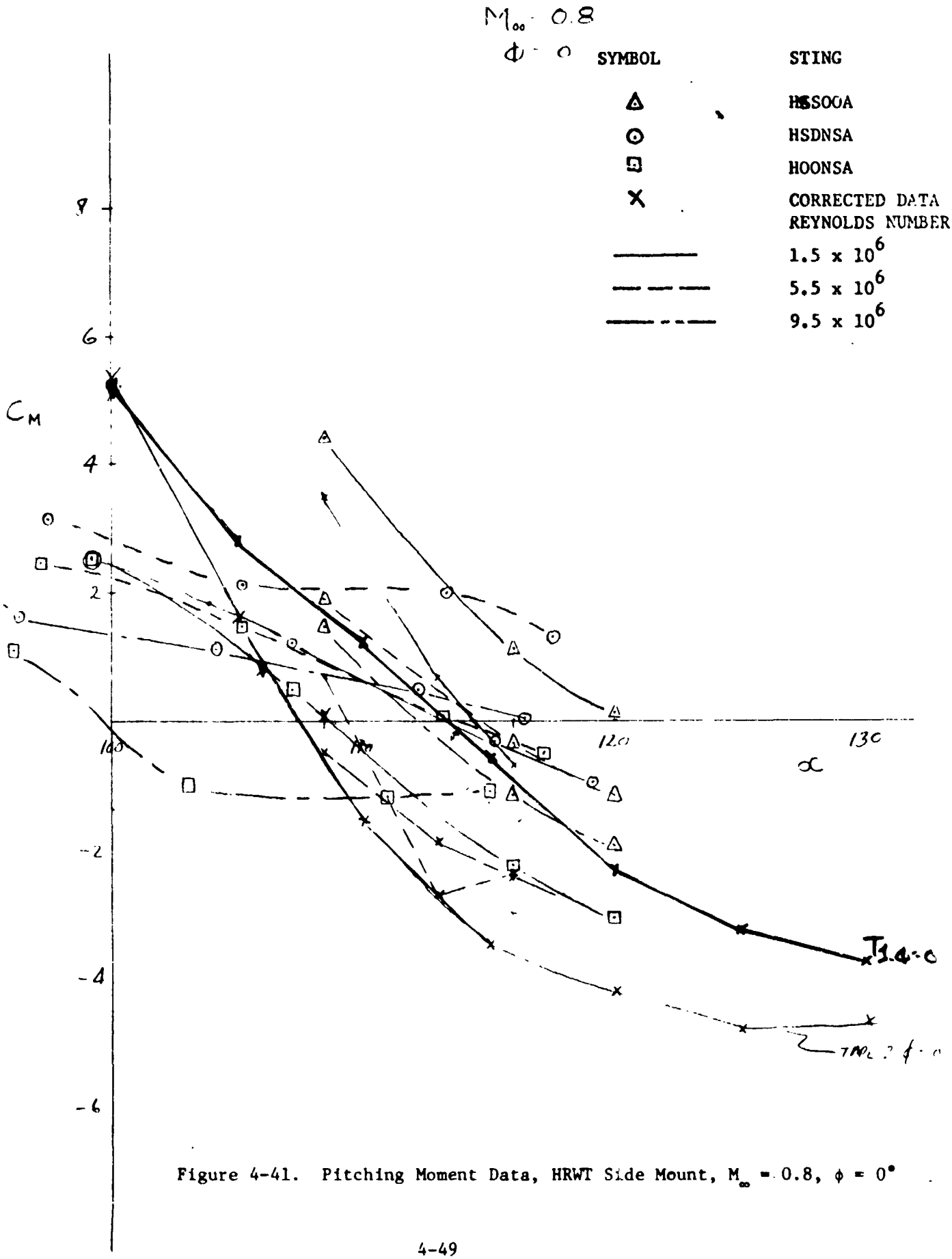

Figure 4-41. Pitching Moment Data, HRWT Side Mount, M_∞ = 0.8, ϕ = 0°

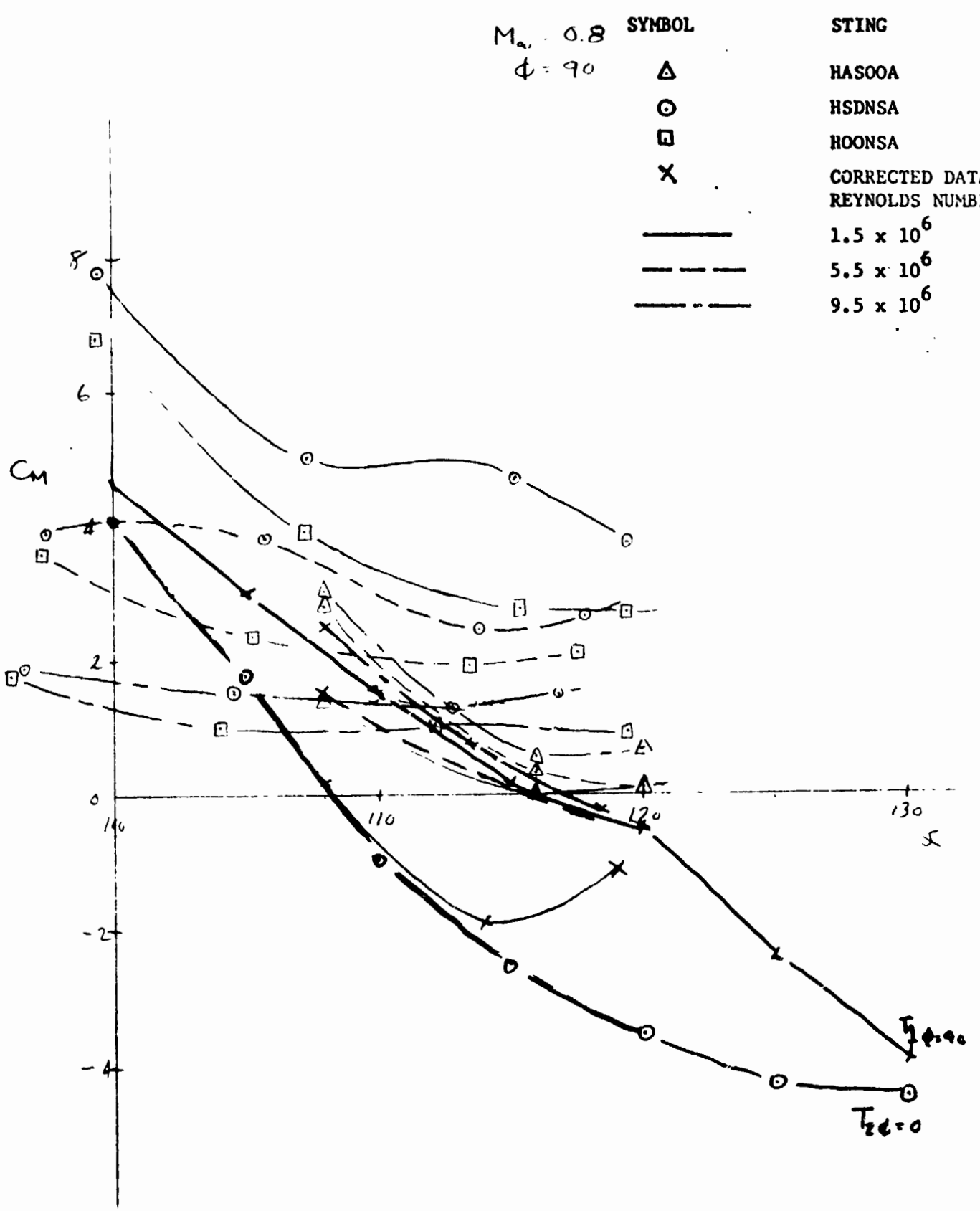

Figure 4-42. Pitching Moment Data, HRWT Side Mount, $M_\infty = 0.8$, $\phi = 90°$

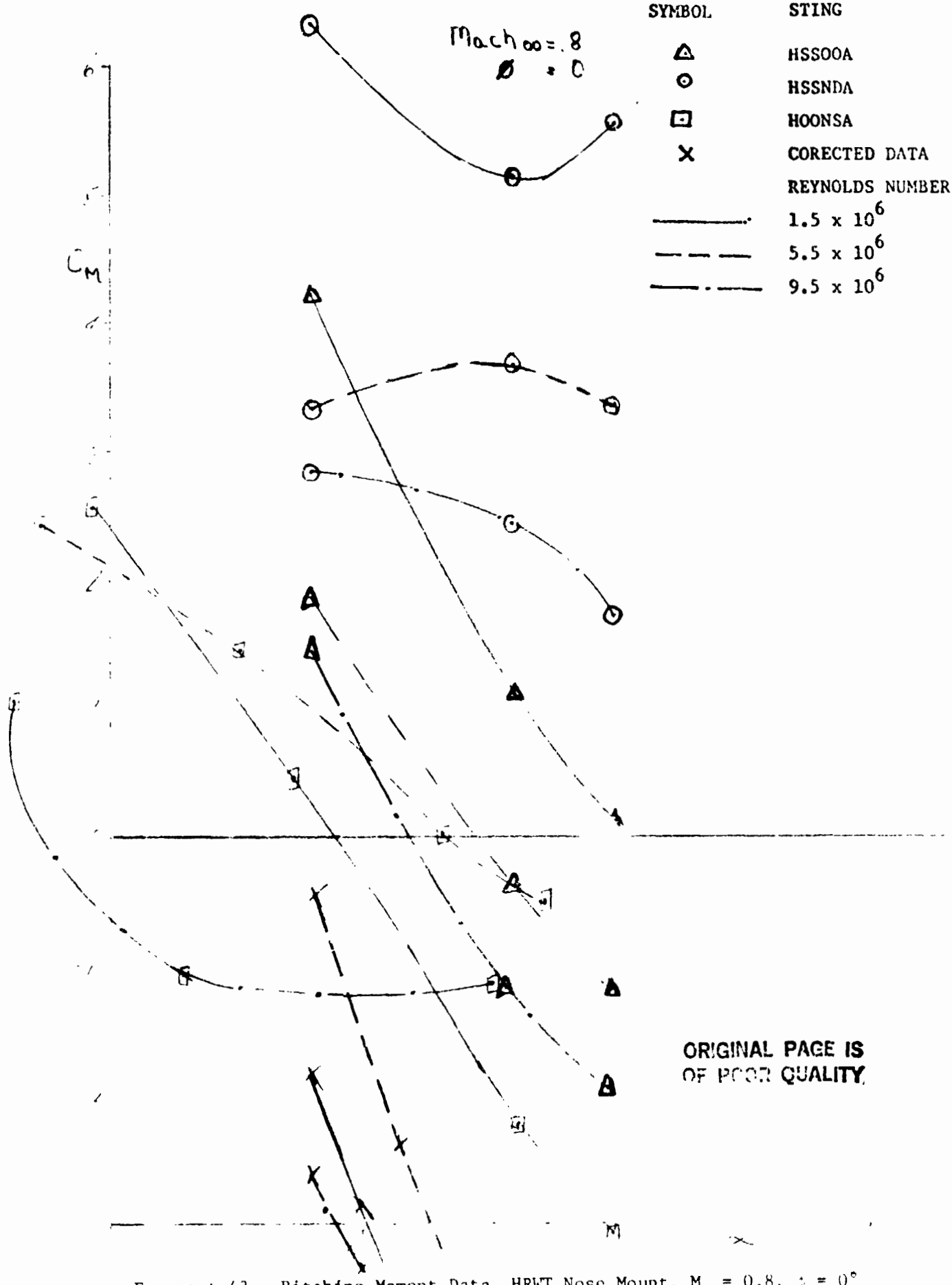

Figure 4-43. Pitching Moment Data, HRWT Nose Mount, M_∞ = 0.8, ϕ = 0°

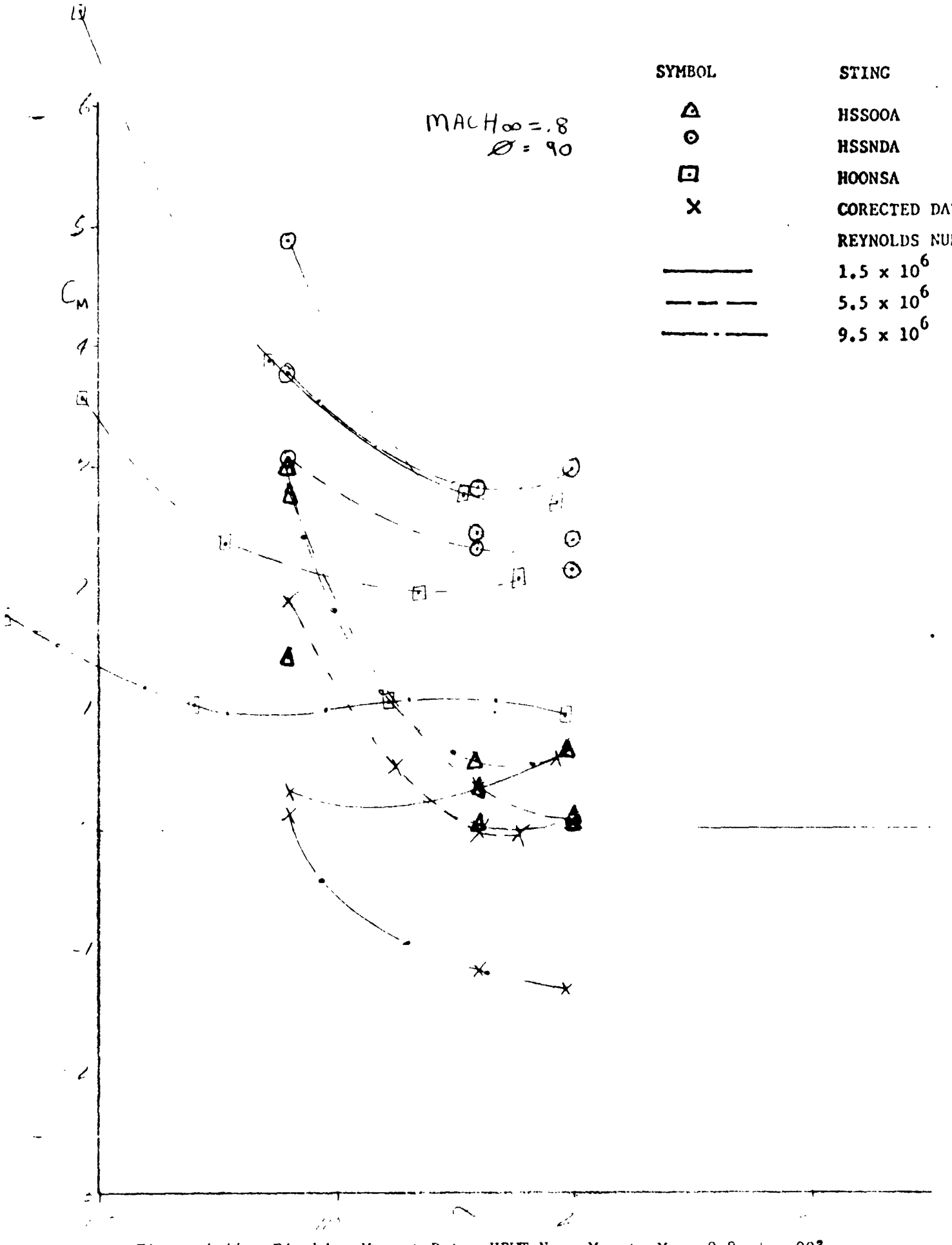

Figure 4-44. Pitching Moment Data, HRWT Nose Mount, M_c = 0.8, ϕ = 90°

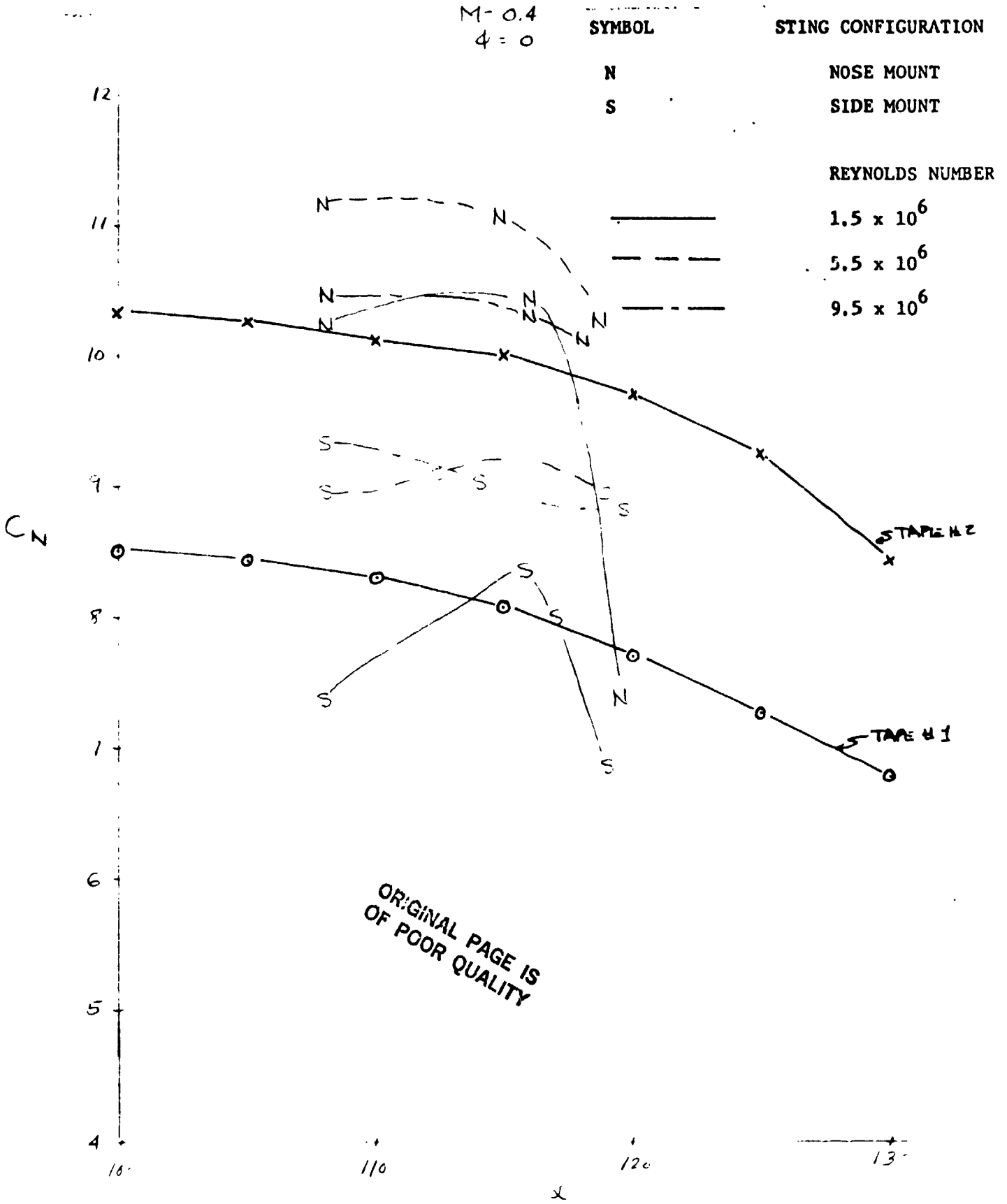

Figure 4-45. Summary Corrected Normal Force Data, HRWT, M_∞ = 0.4, ϕ = 0°

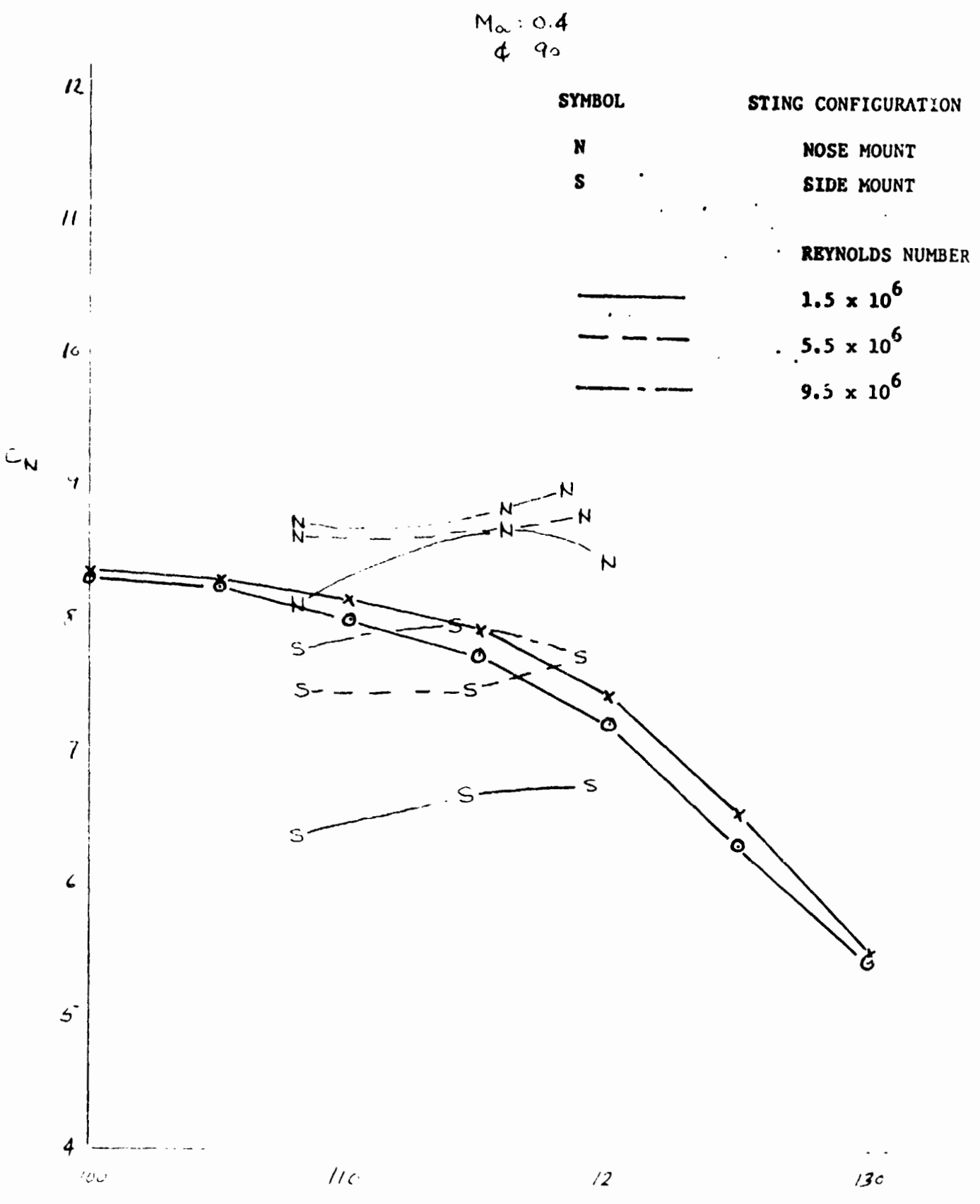

Figure 4-46. Summary Corrected Normal Force Data, HRWT, M_∞ = 0.4, ϕ = 90°

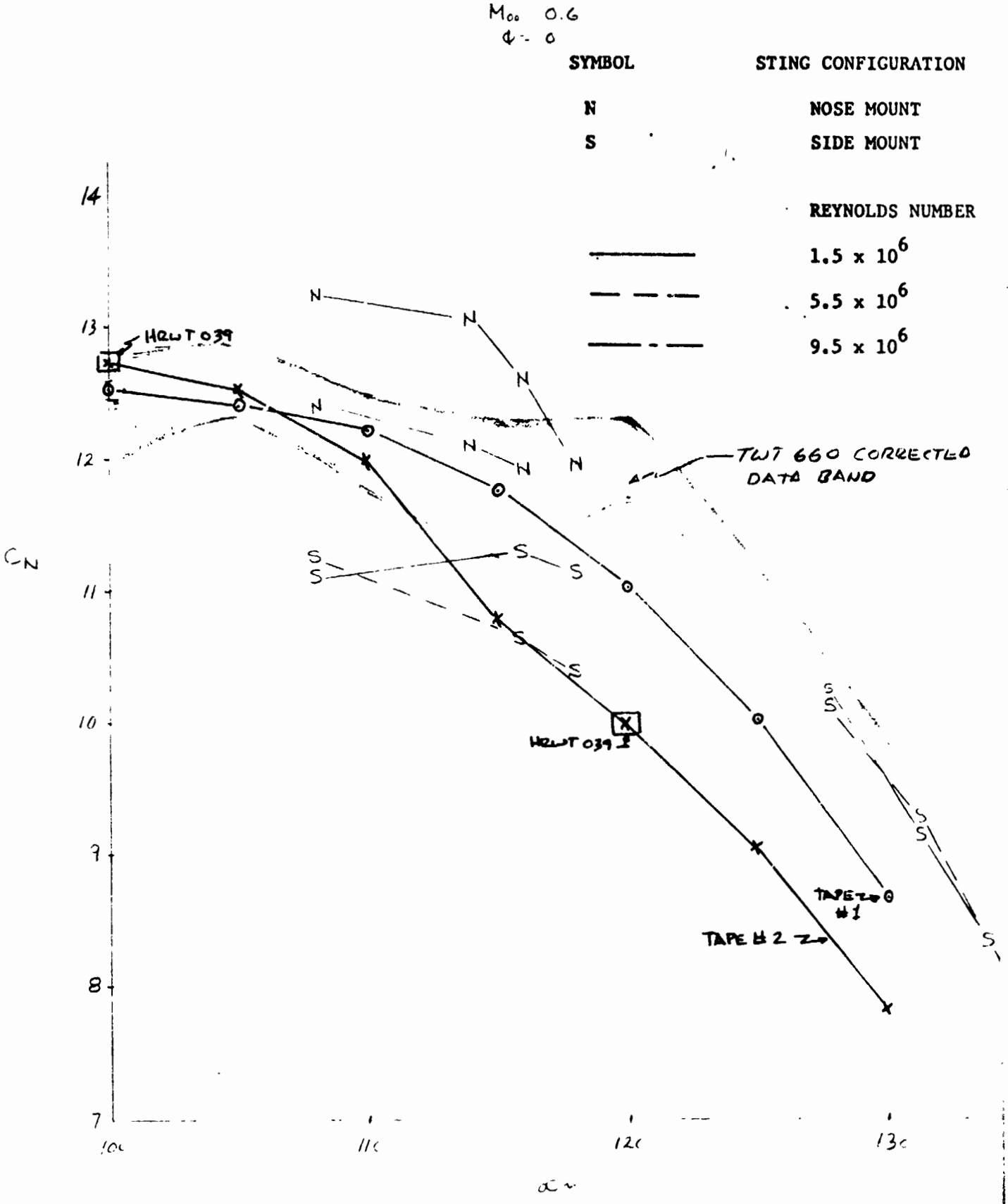

Figure 4-47. Summary Corrected Normal Force Data, HRWT, $M_\infty = 0.6$, $\phi = 0°$

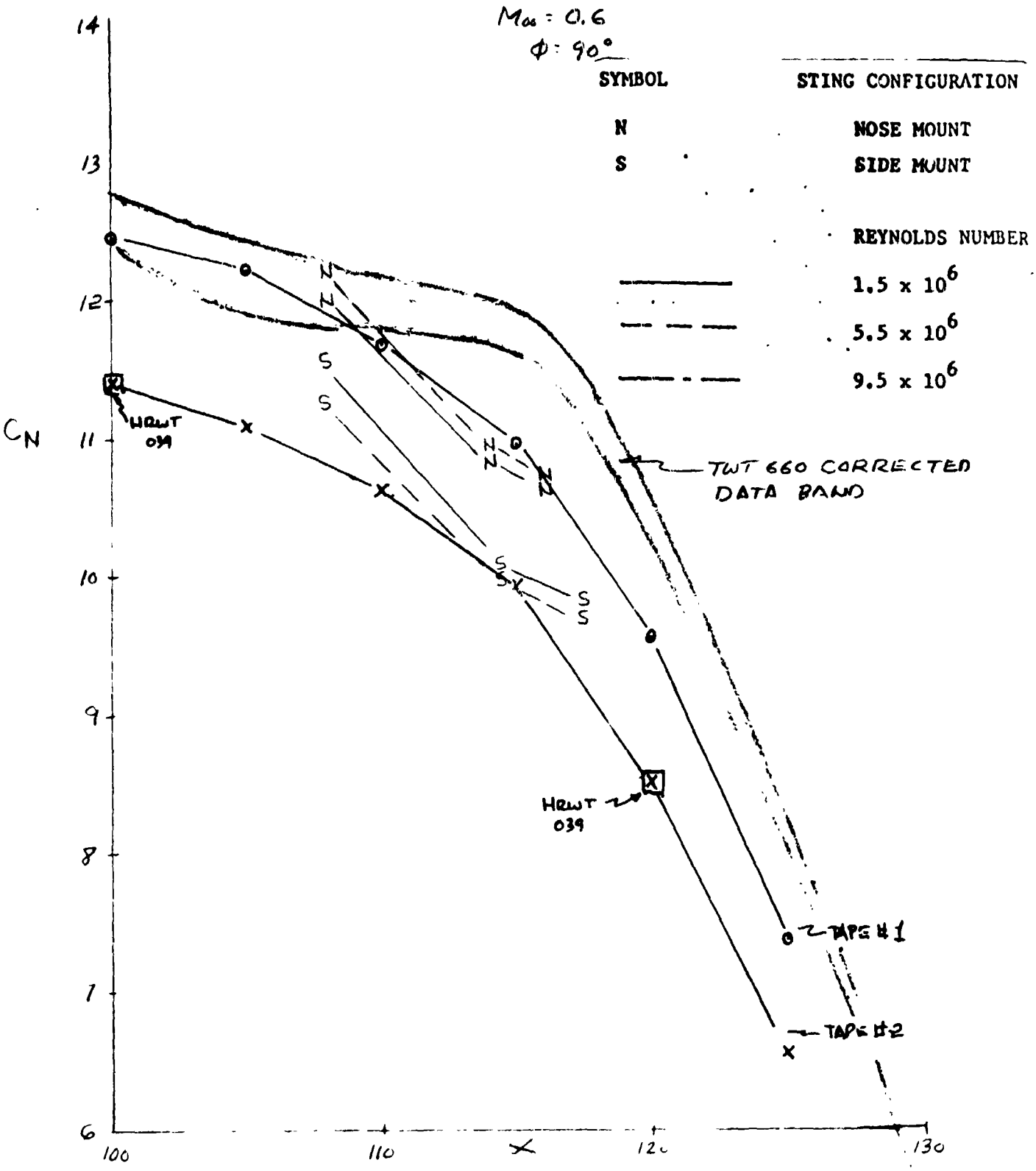

Figure 4-48. Summary Corrected Normal Force Data, HRWT, $M_\infty = 0.6$, $\phi = 90°$

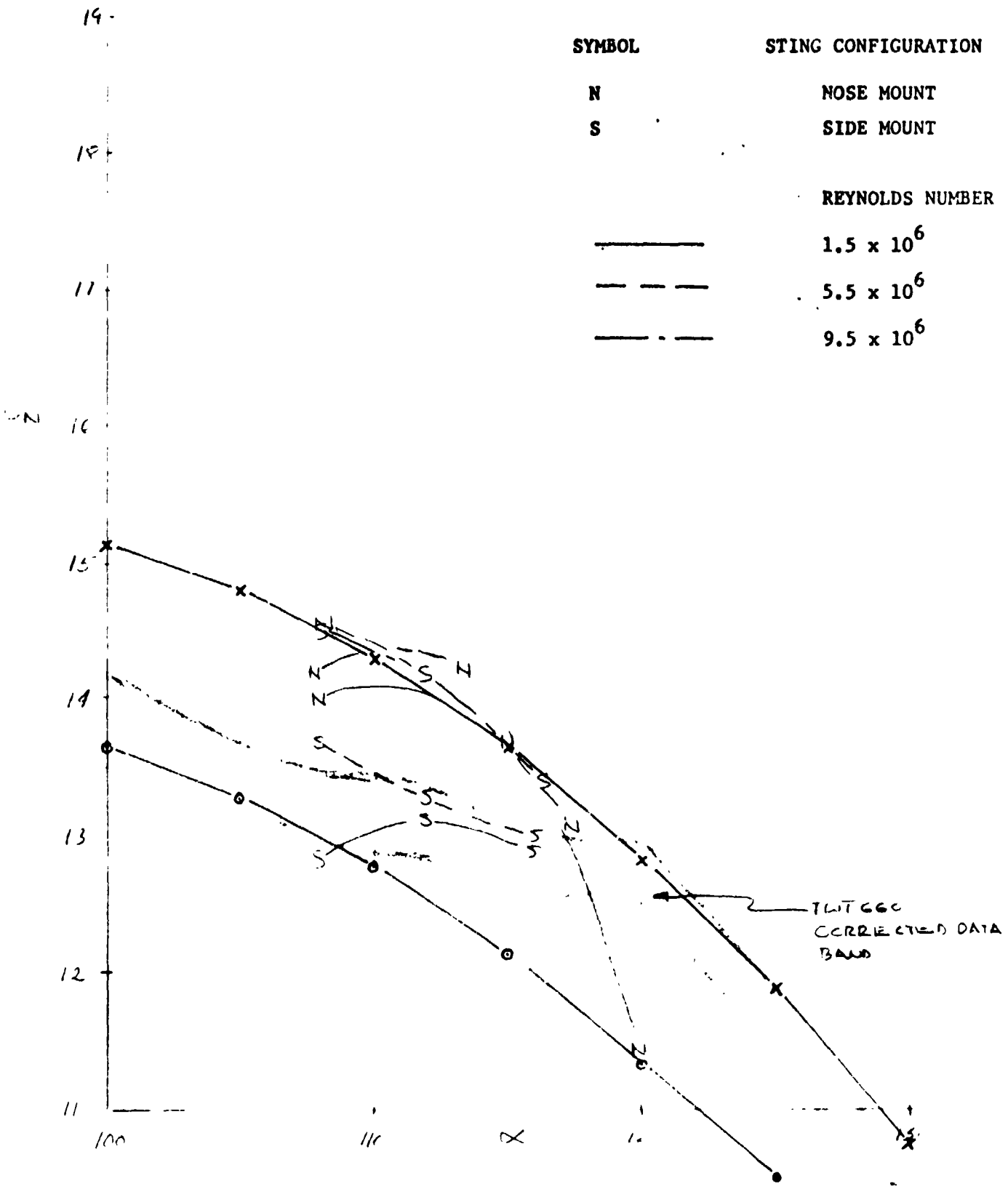

Figure 4-49. Summary Corrected Normal Force Data, HRWT, M_∞ = 0.8, ϕ = 0°

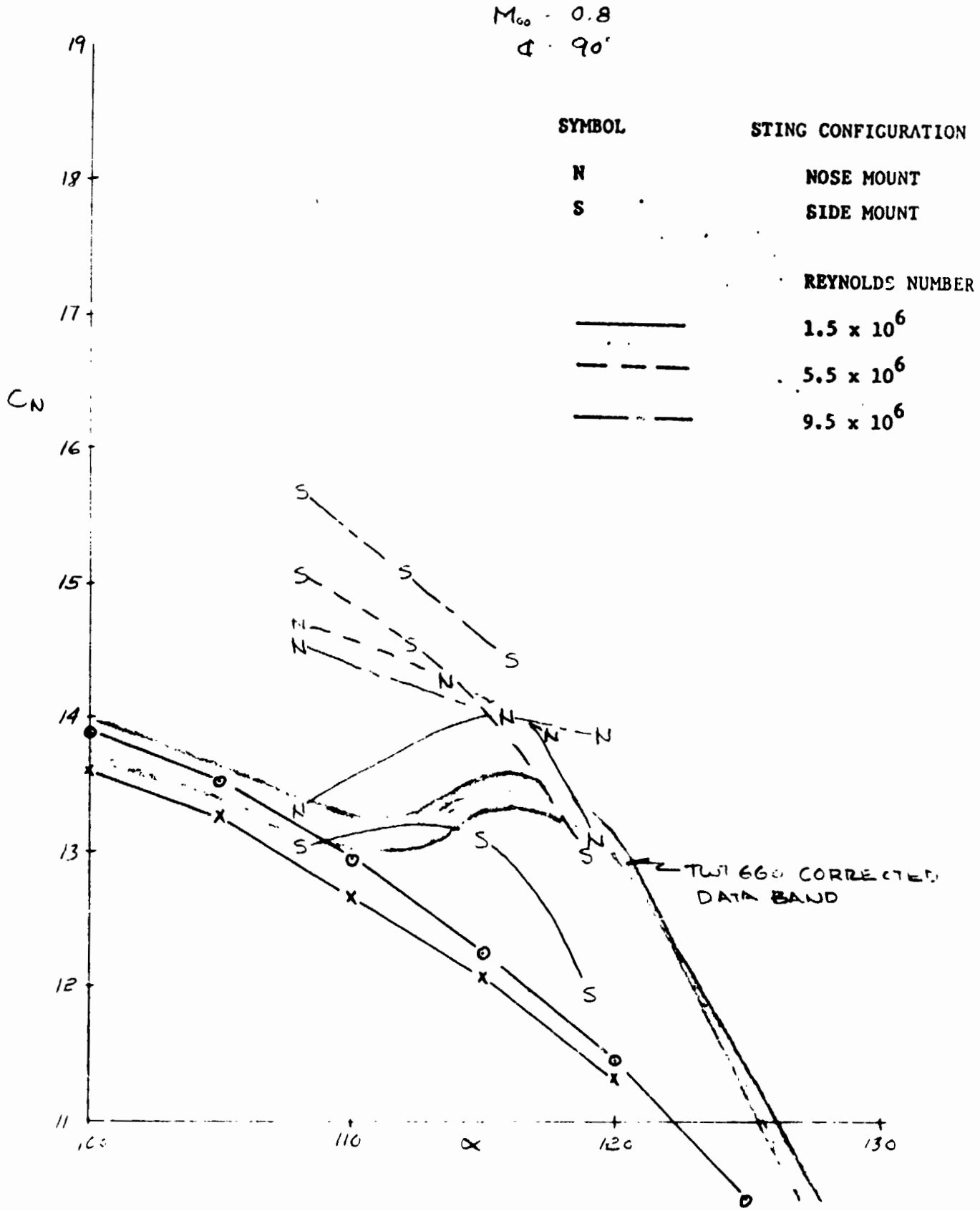

Figure 4-50. Summary Corrected Normal Force Data, HRWT, M_∞ = 0.8, ϕ = 90°

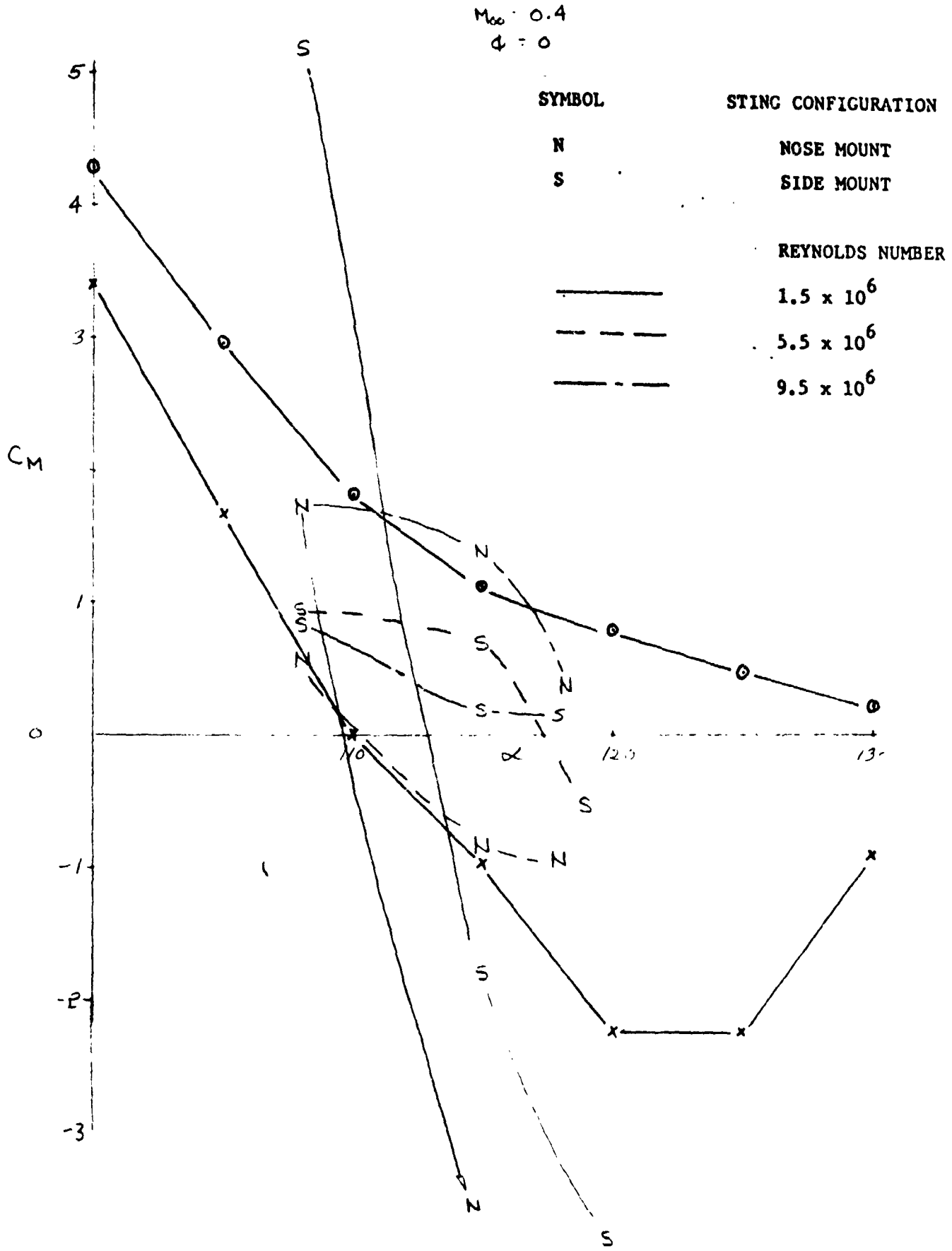

Figure 4-51. Summary Corrected Pitching Moment Data, HRWT, M_∞ = 0.4, ϕ = 0°

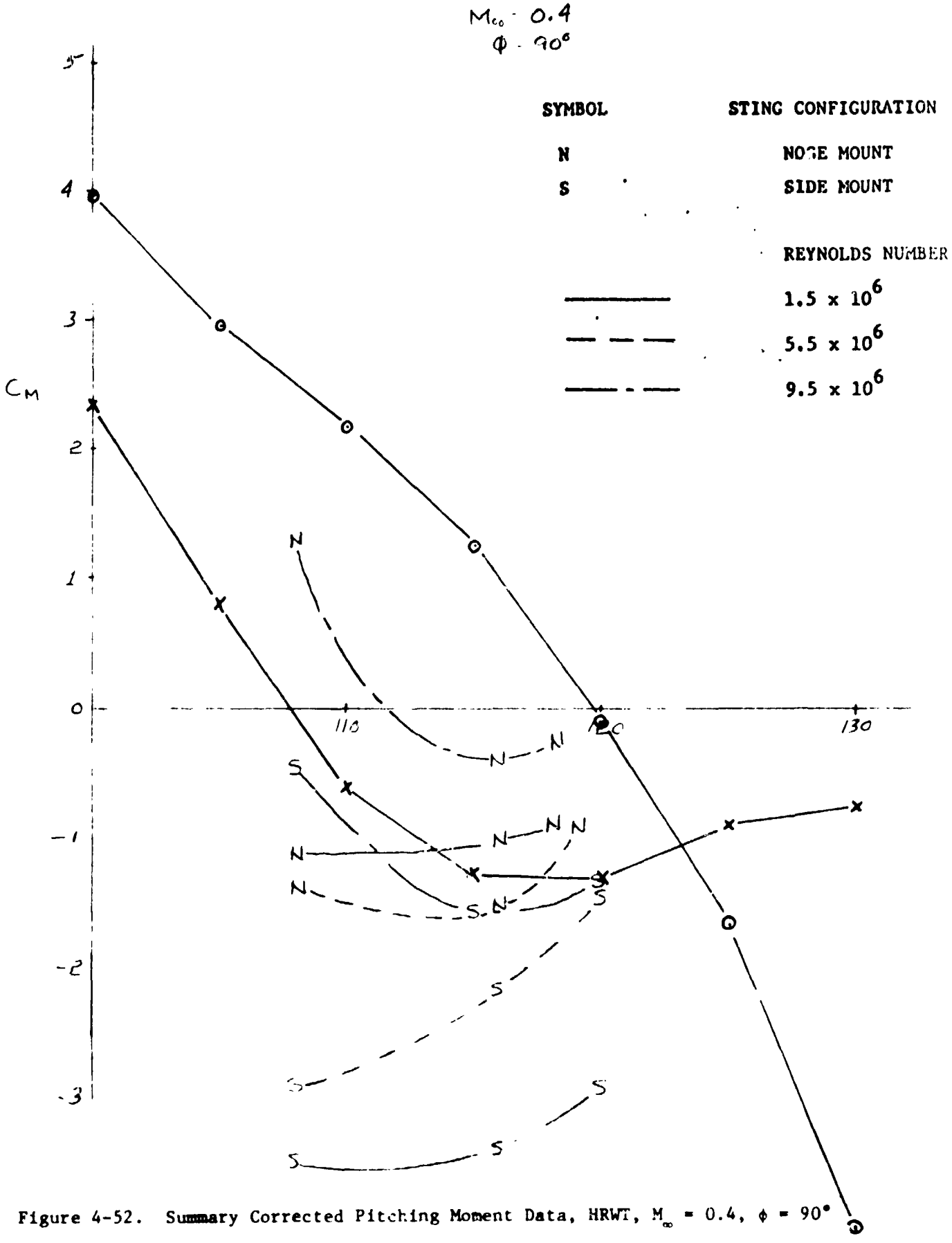

Figure 4-52. Summary Corrected Pitching Moment Data, HRWT, M_∞ = 0.4, ϕ = 90°

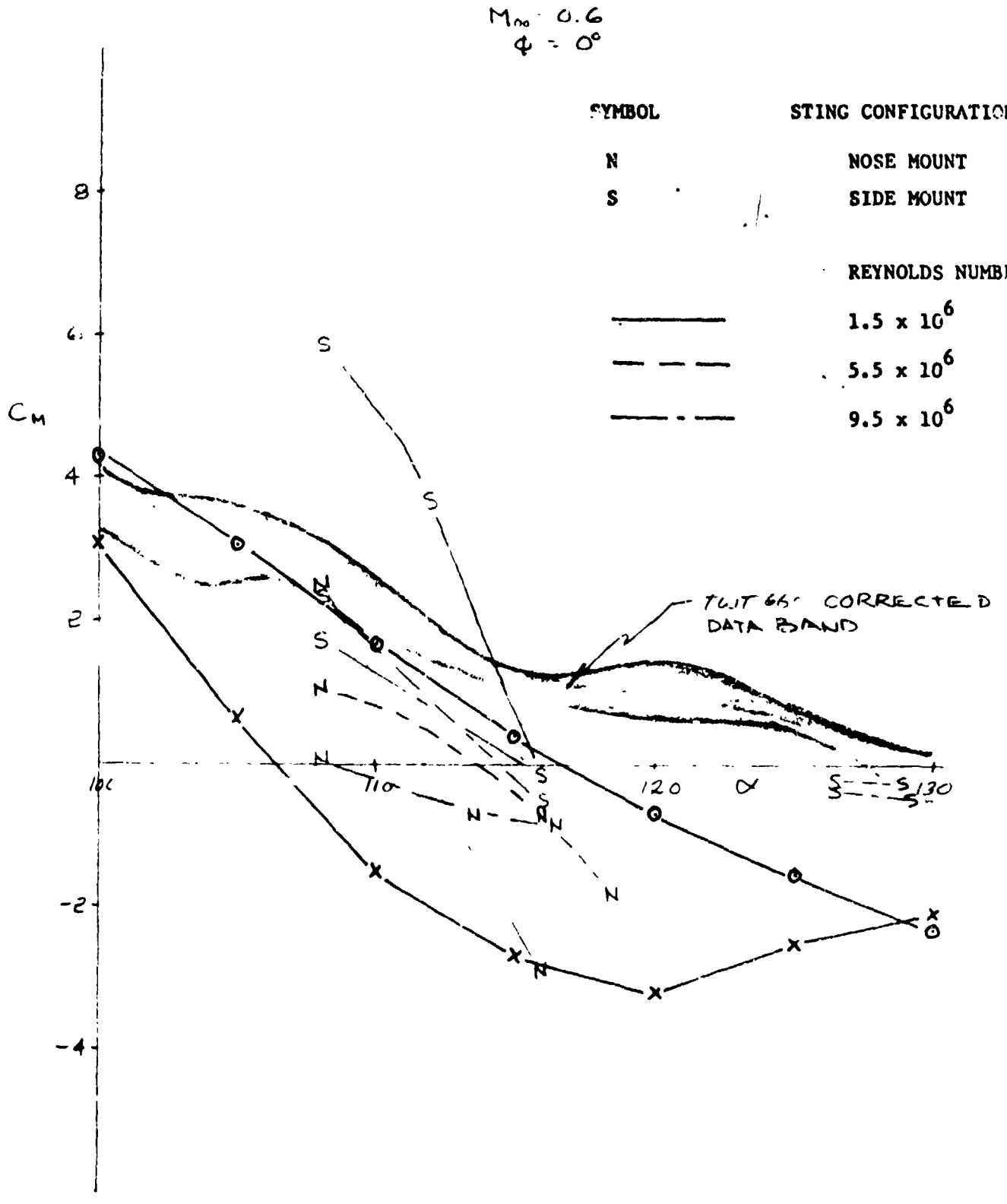

Figure 4-53. Summary Corrected Pitching Moment Data, HRWT, M_∞ = 0.6, ϕ = 0°

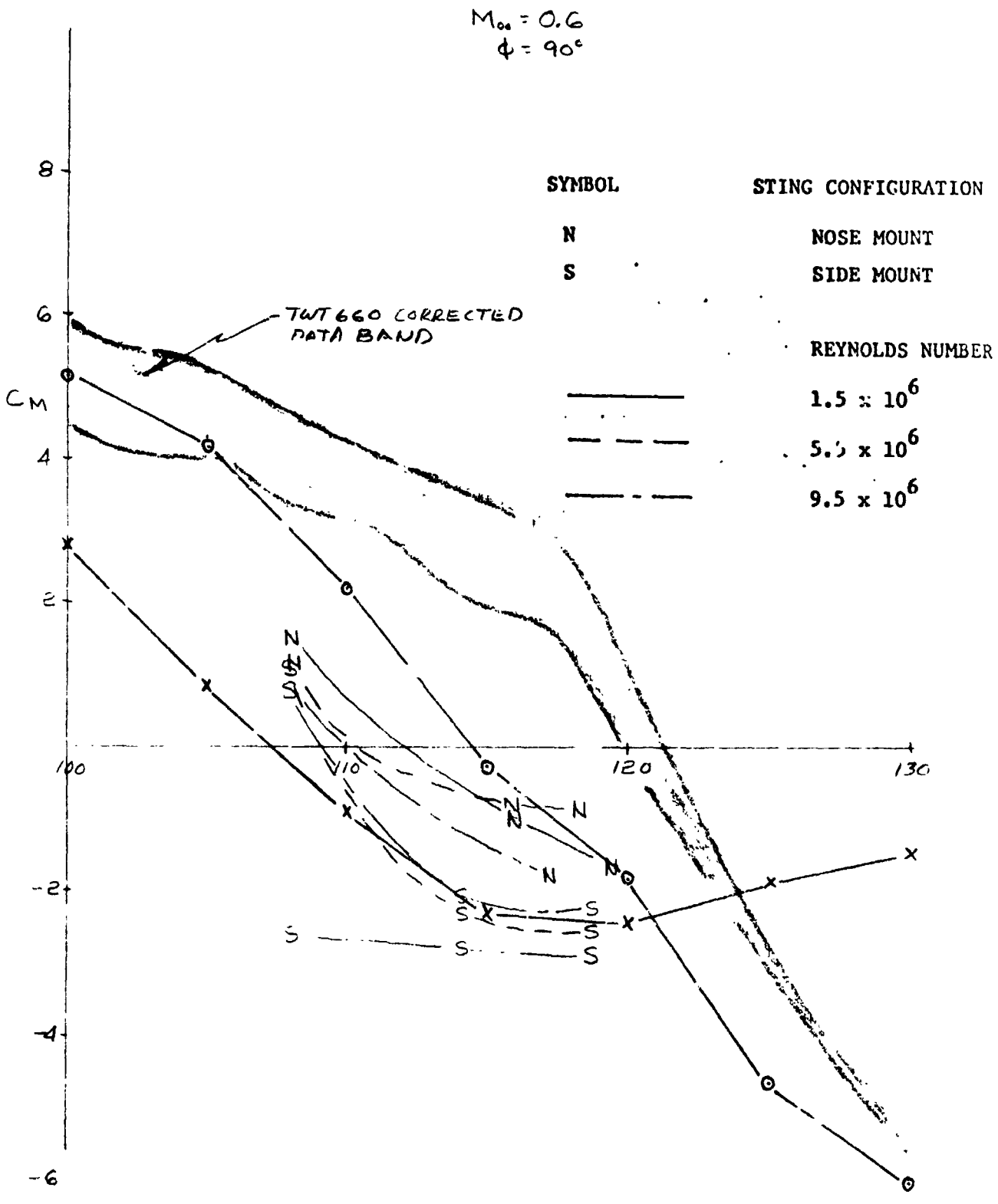

Figure 4-54. Summary Corrected Pitching Moment Data, HRWT, $M_\infty = 0.6$, $\phi = 90°$

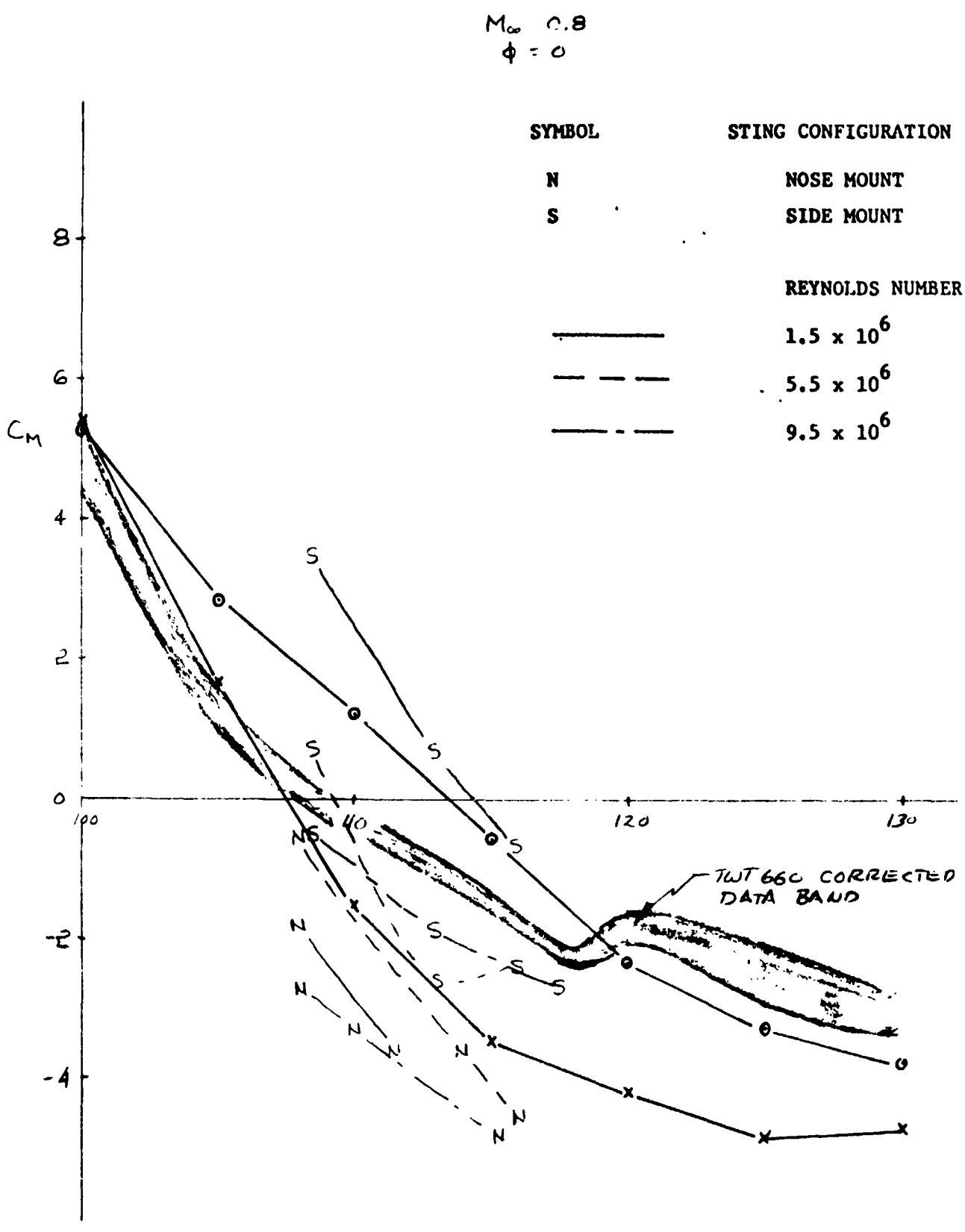

Figure 4-55. Summary Corrected Pitching Moment Data, HRWT, M_∞ = 0.8, ϕ = 0°

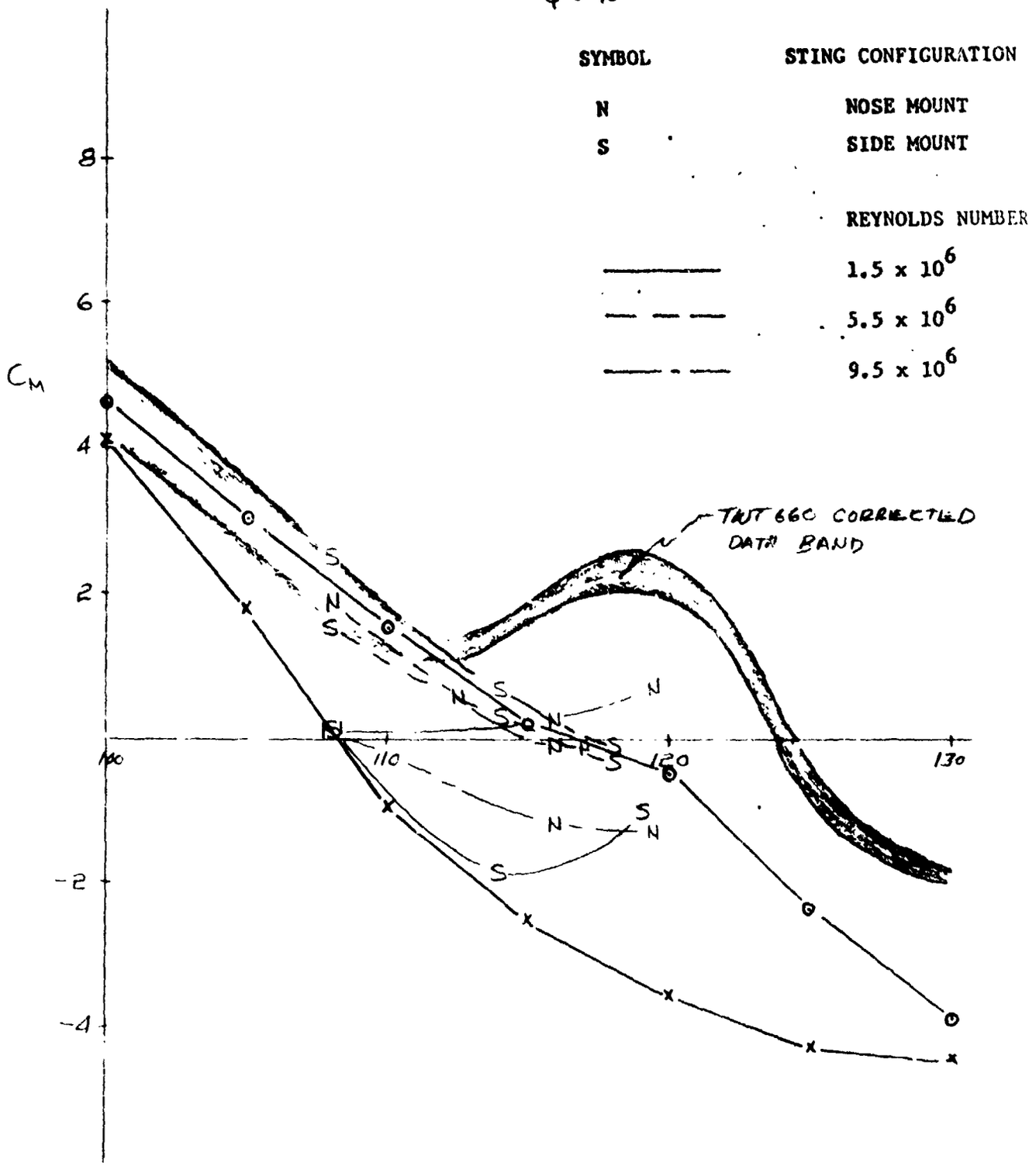

Figure 4-56. Summary Corrected Pitching Moment Data, HRWT, $M_\infty = 0.8$, $\phi = 90°$

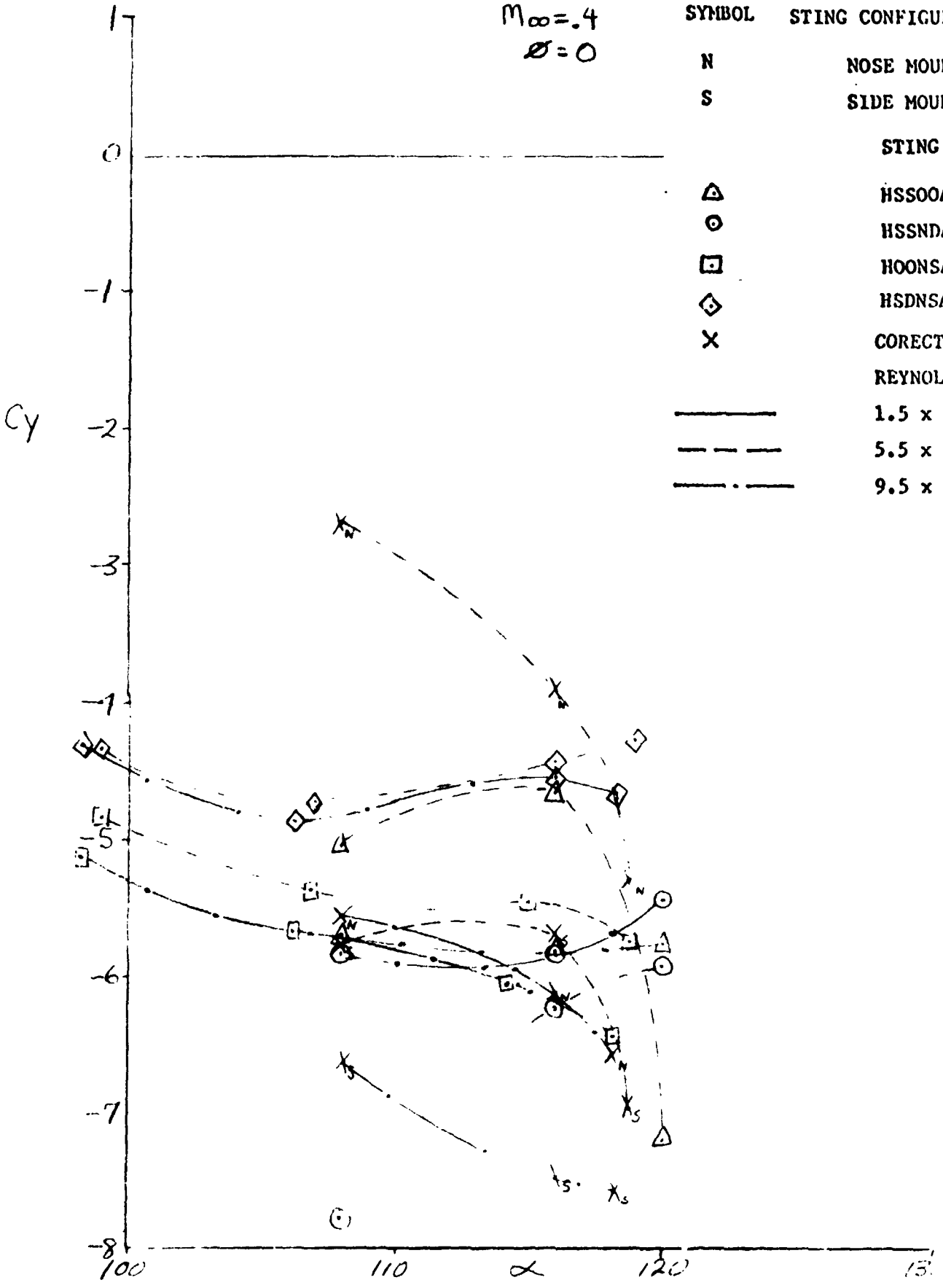

Figure 4-57. Side Force Data, HRWT M_∞ = 0.4, ϕ = 0

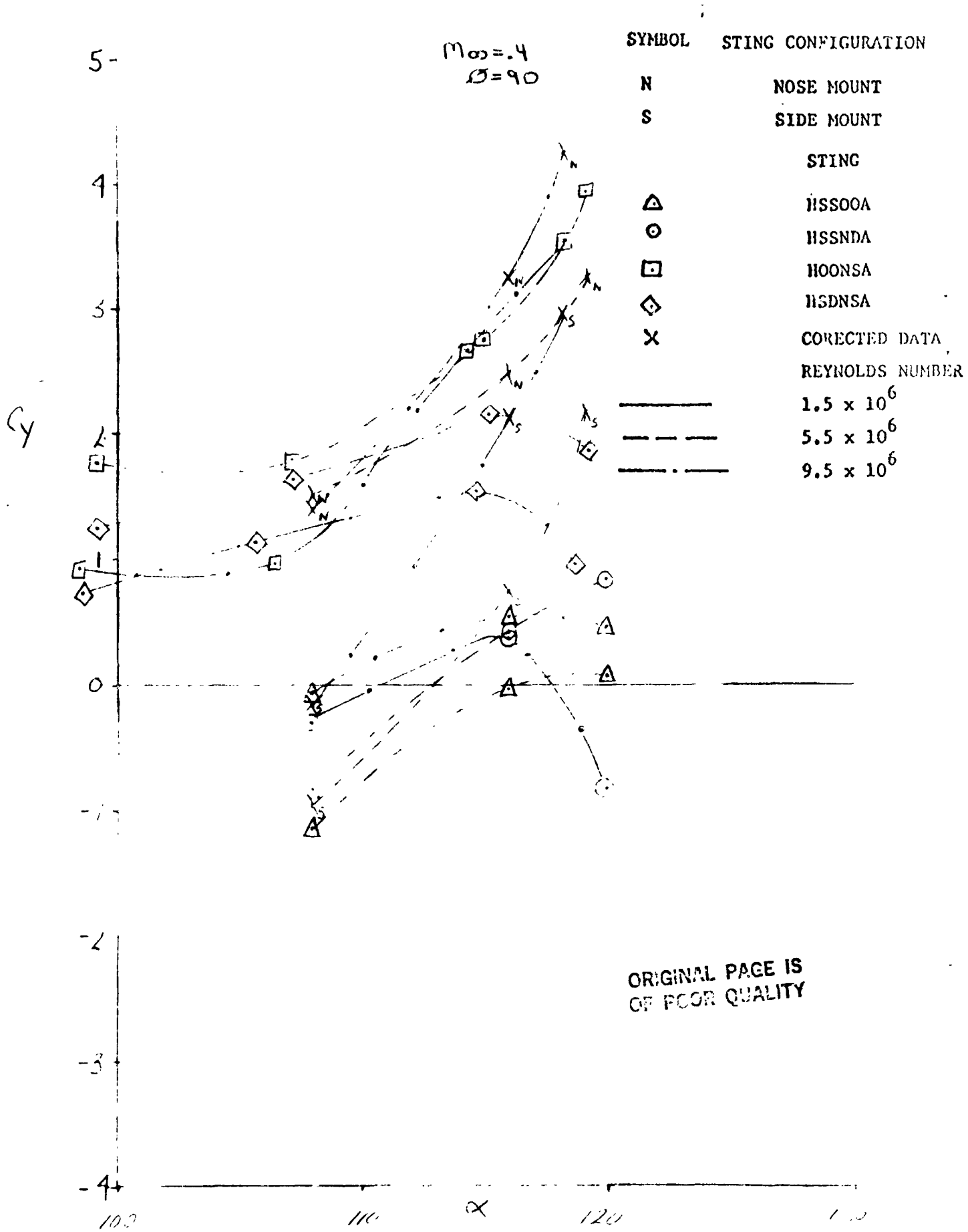

Figure 4-58. Side Force Data, HRWT M_∞ = 0.4, β = 90

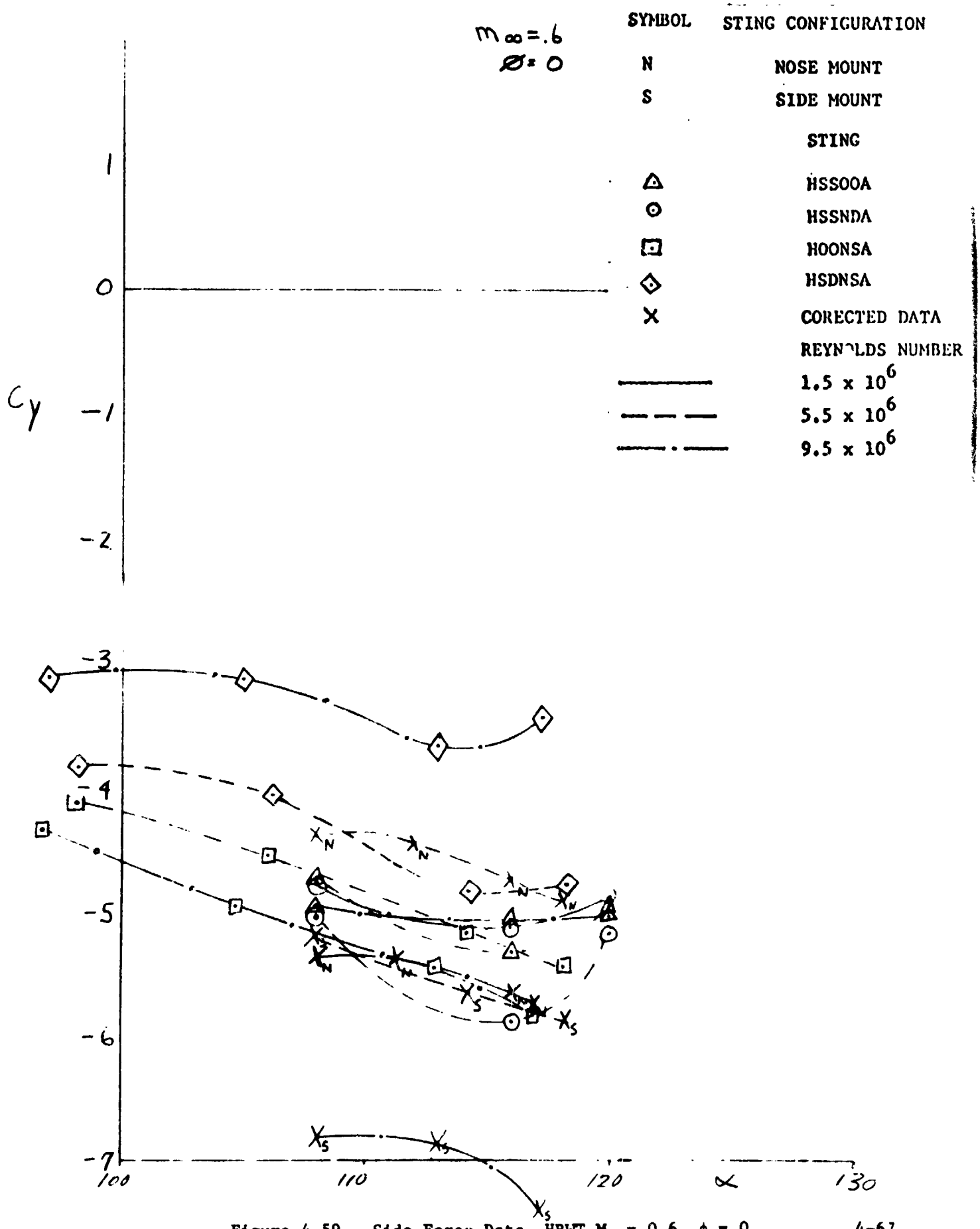

Figure 4-59. Side Force Data, HRWT M_∞ = 0.6, ϕ = 0

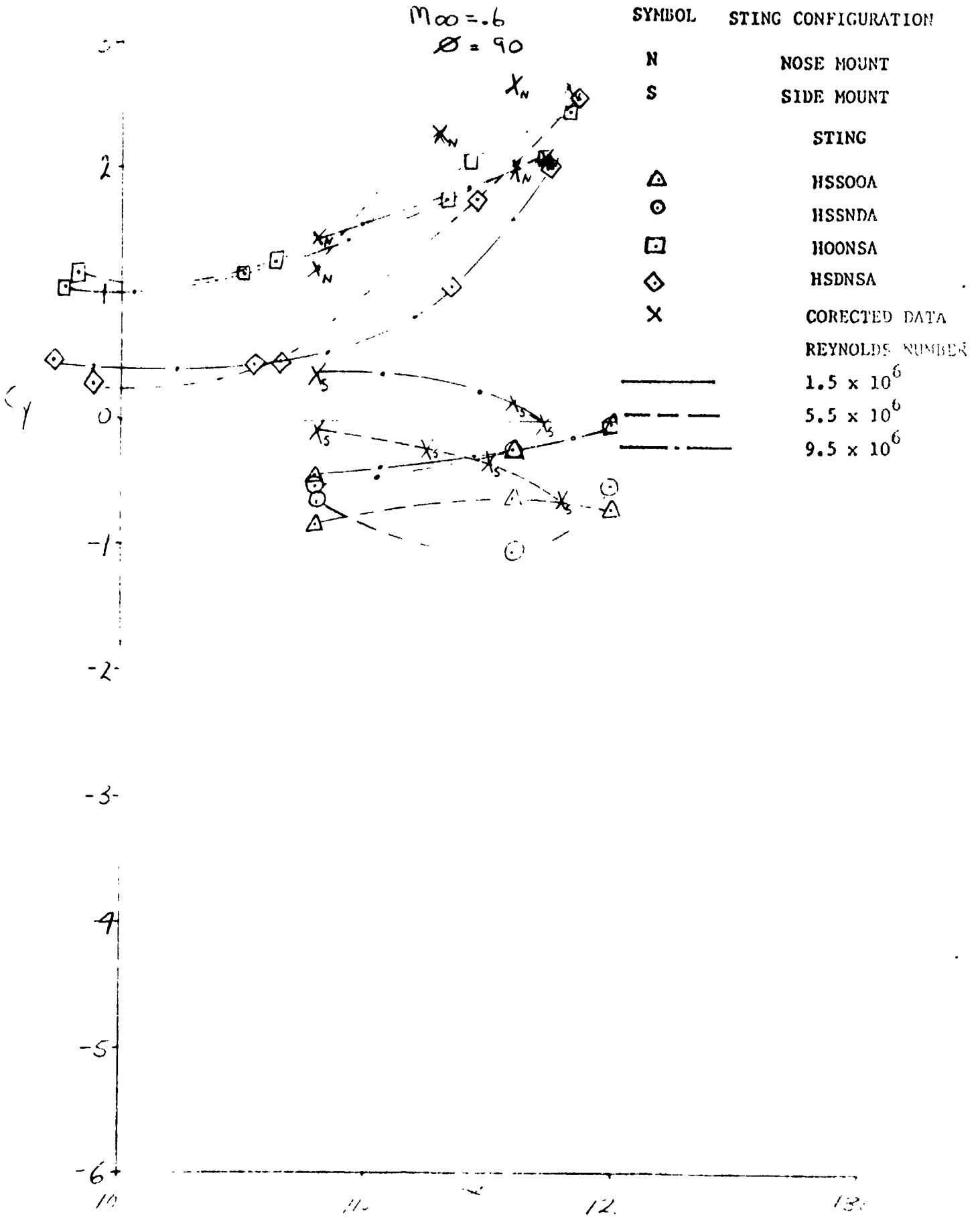

Figure 4-60. Side Force Data, HRWT M_∞ = 0.6, ϕ = 90

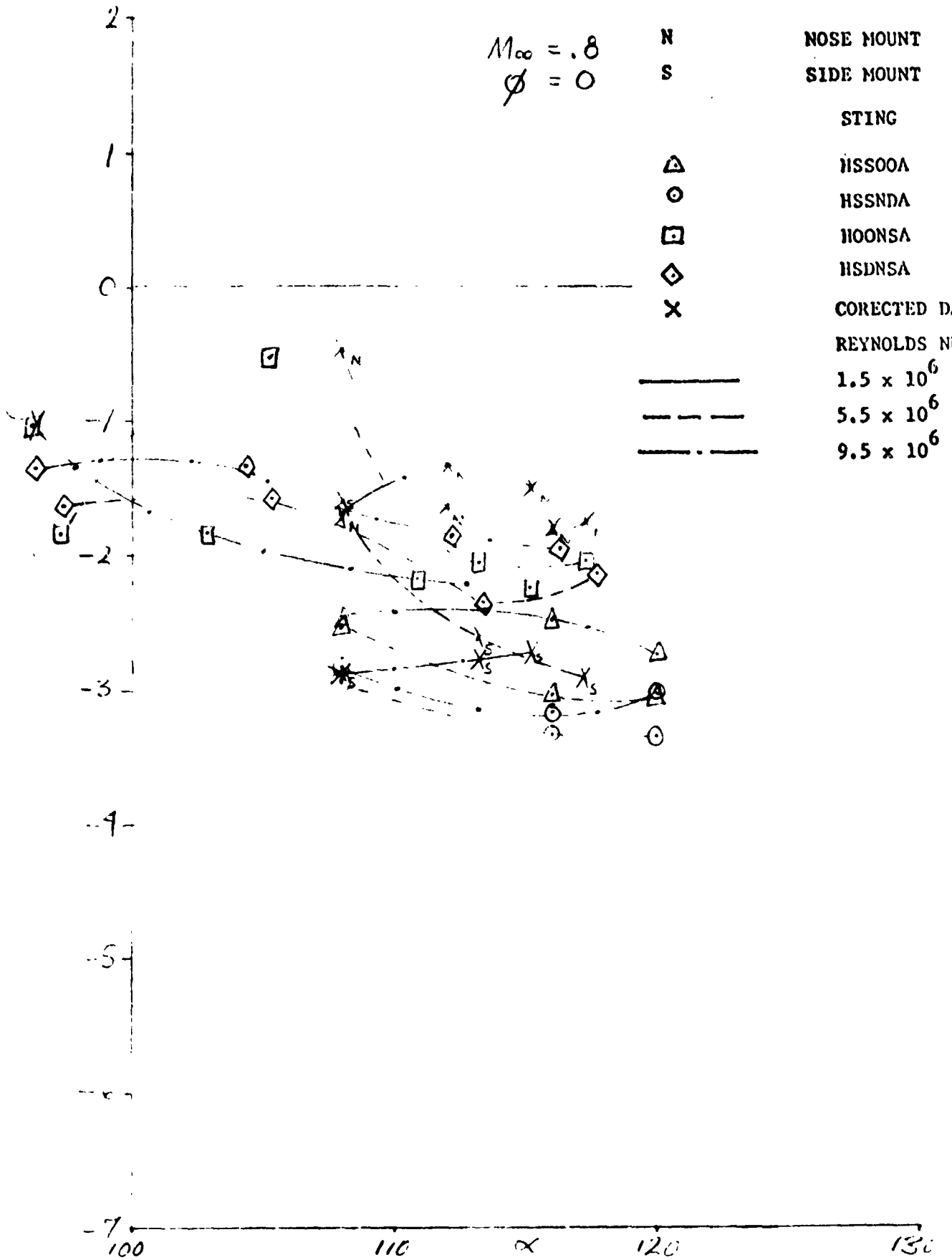

Figure 4-61. Side Force Data, HRWT M_∞ = 0.8, ϕ = 0

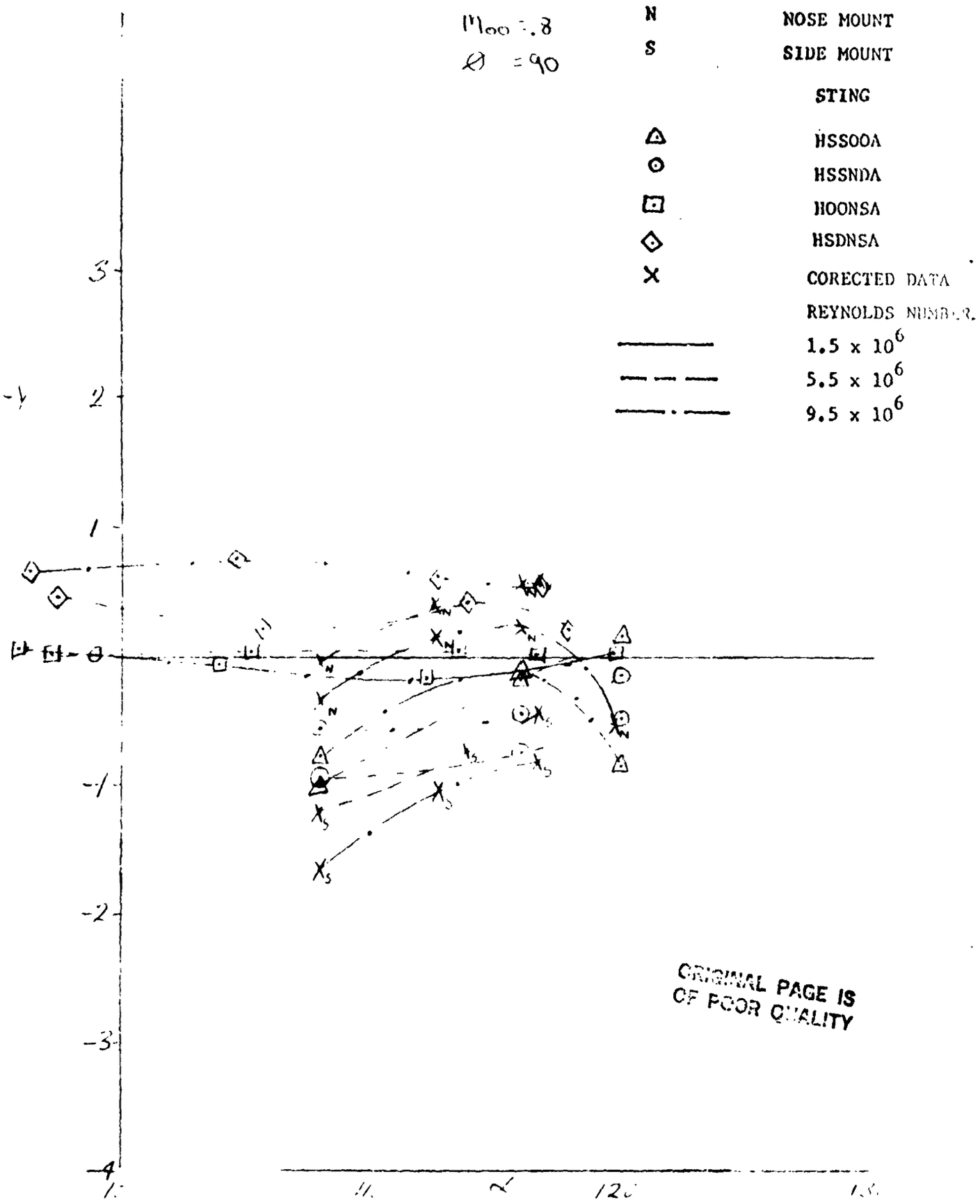

Figure 4-62. Side Force Data, HRWT $M_\infty = 0.8$, $\phi = 90$

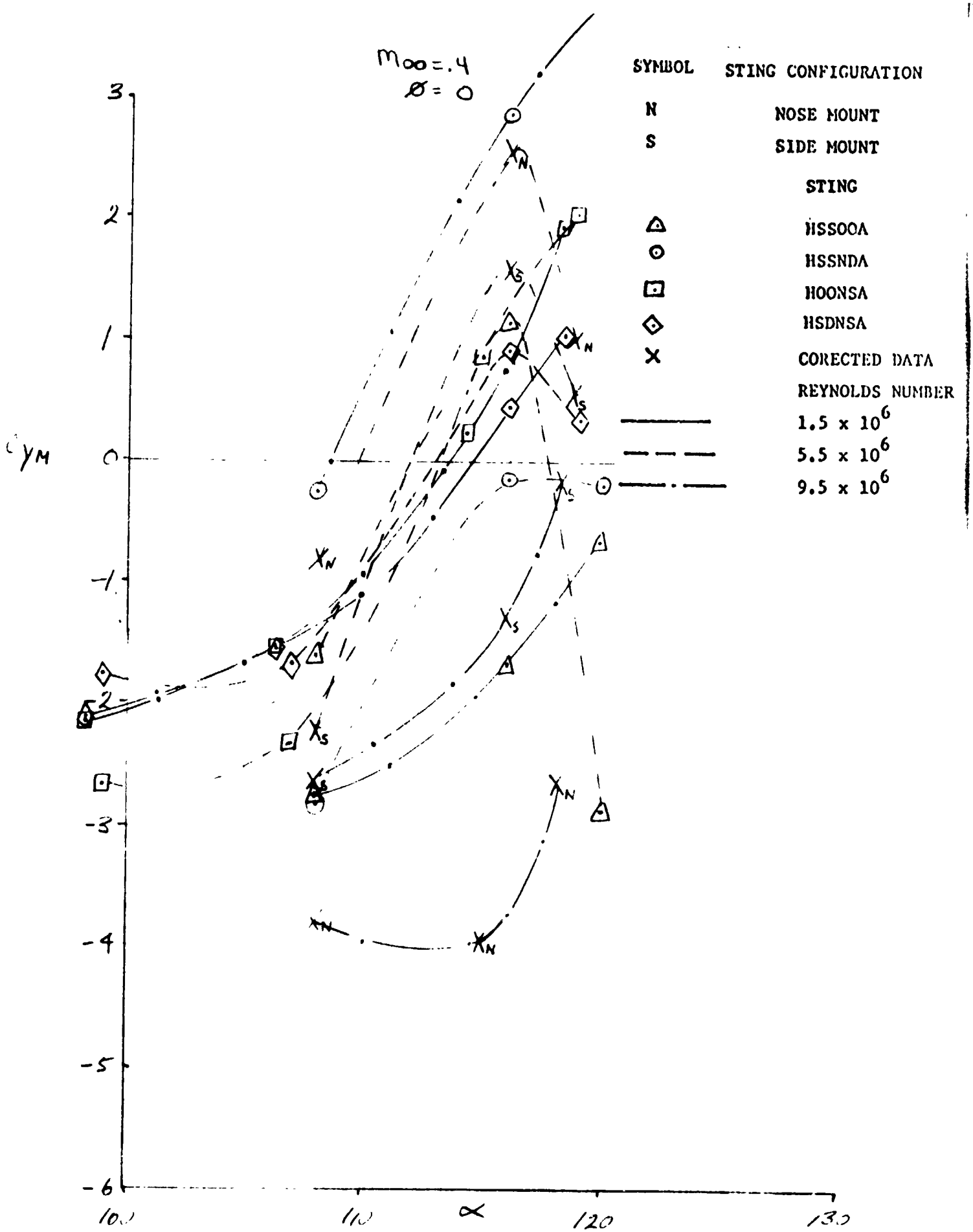

Figure 4-63. Yawing Moment Data, HRWT, $M_\infty = 0.4$, $\phi = 0$

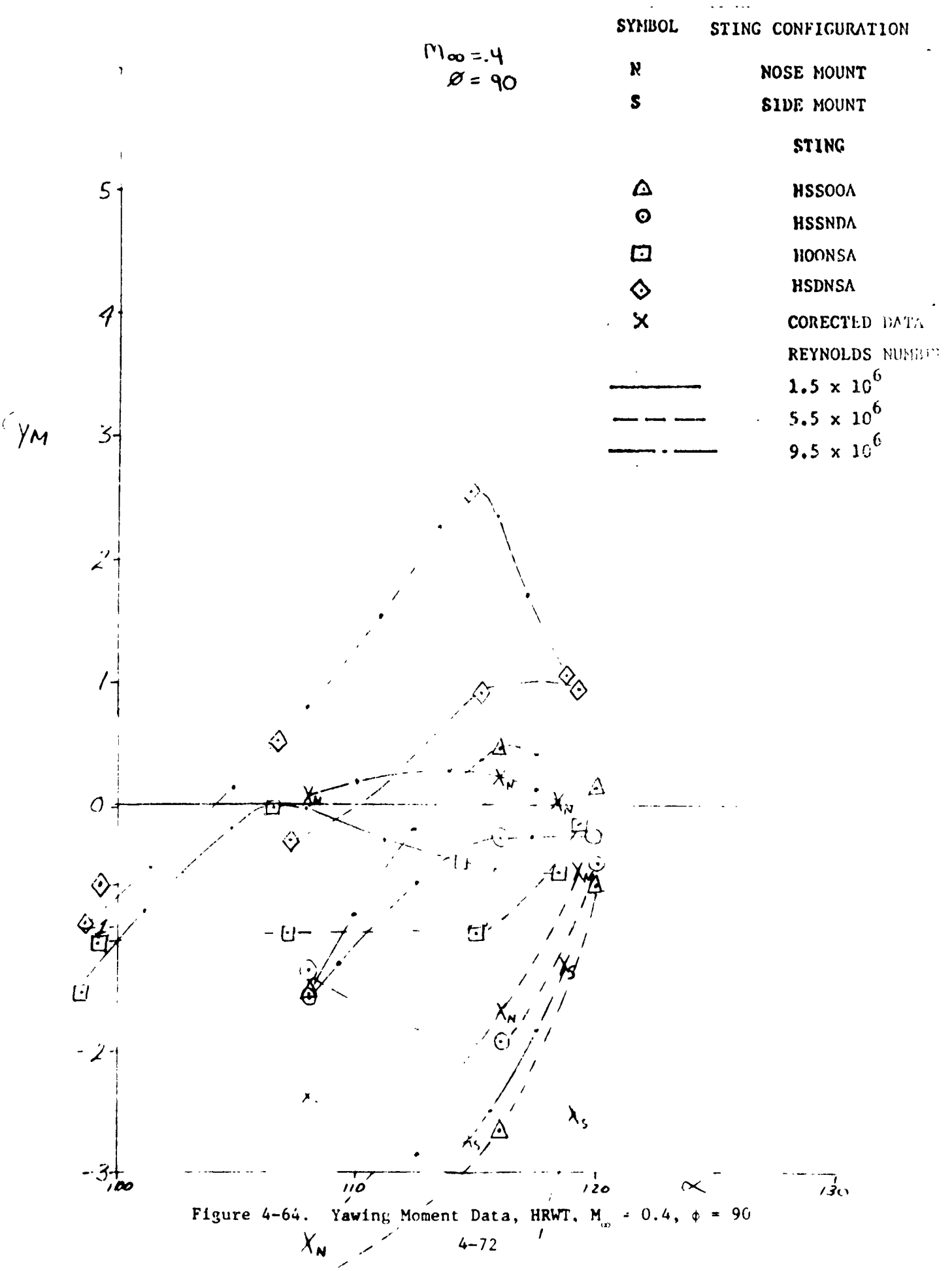

Figure 4-64. Yawing Moment Data, HRWT, M_∞ = 0.4, ϕ = 90

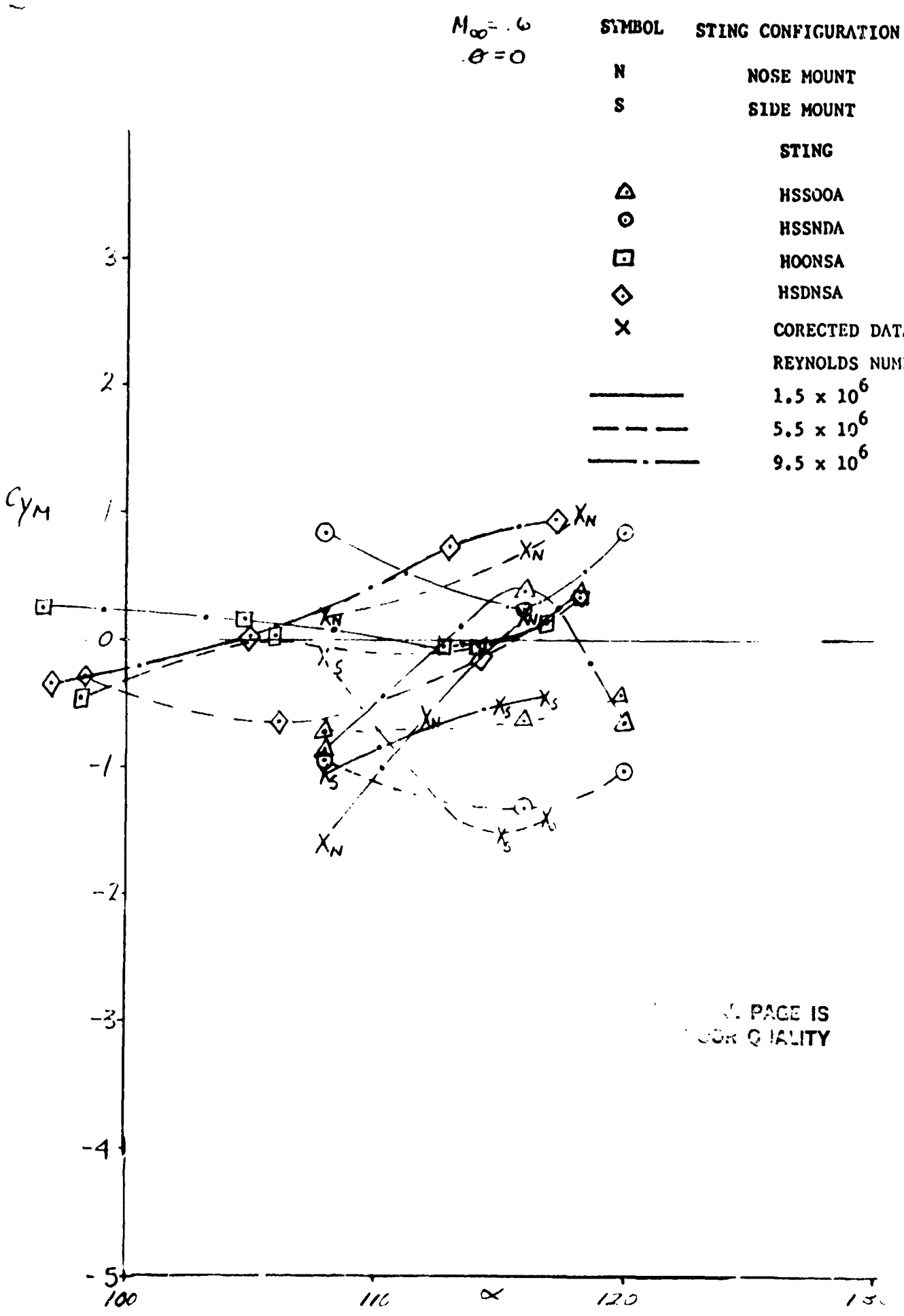

Figure 4-65. Yawing Moment Data, HRWT, $M_\infty = 0.6$, $\phi = 0$

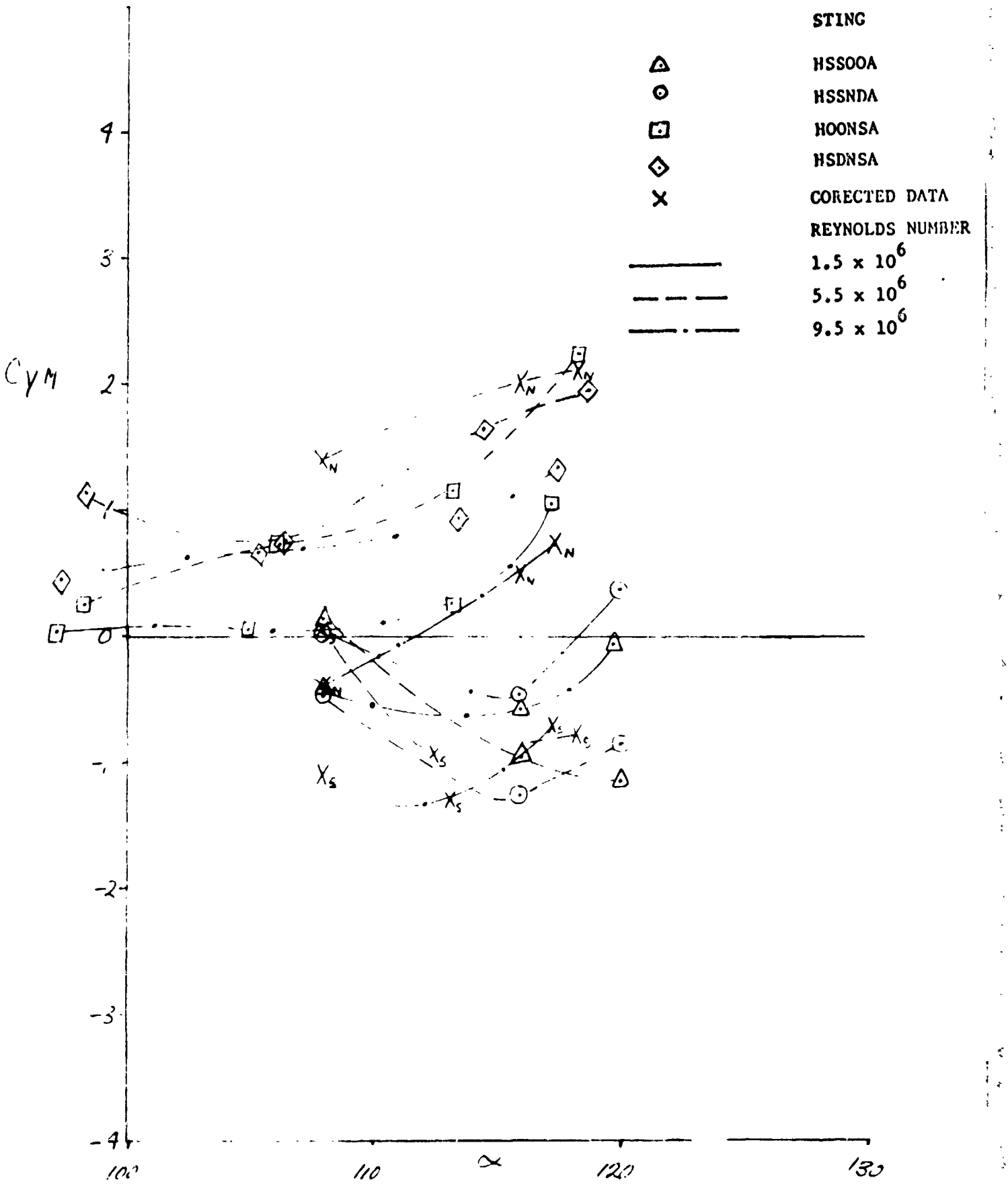

Figure 4-66. Yawing Moment Data, HRWT, M_∞ = 0.6, ϕ = 90

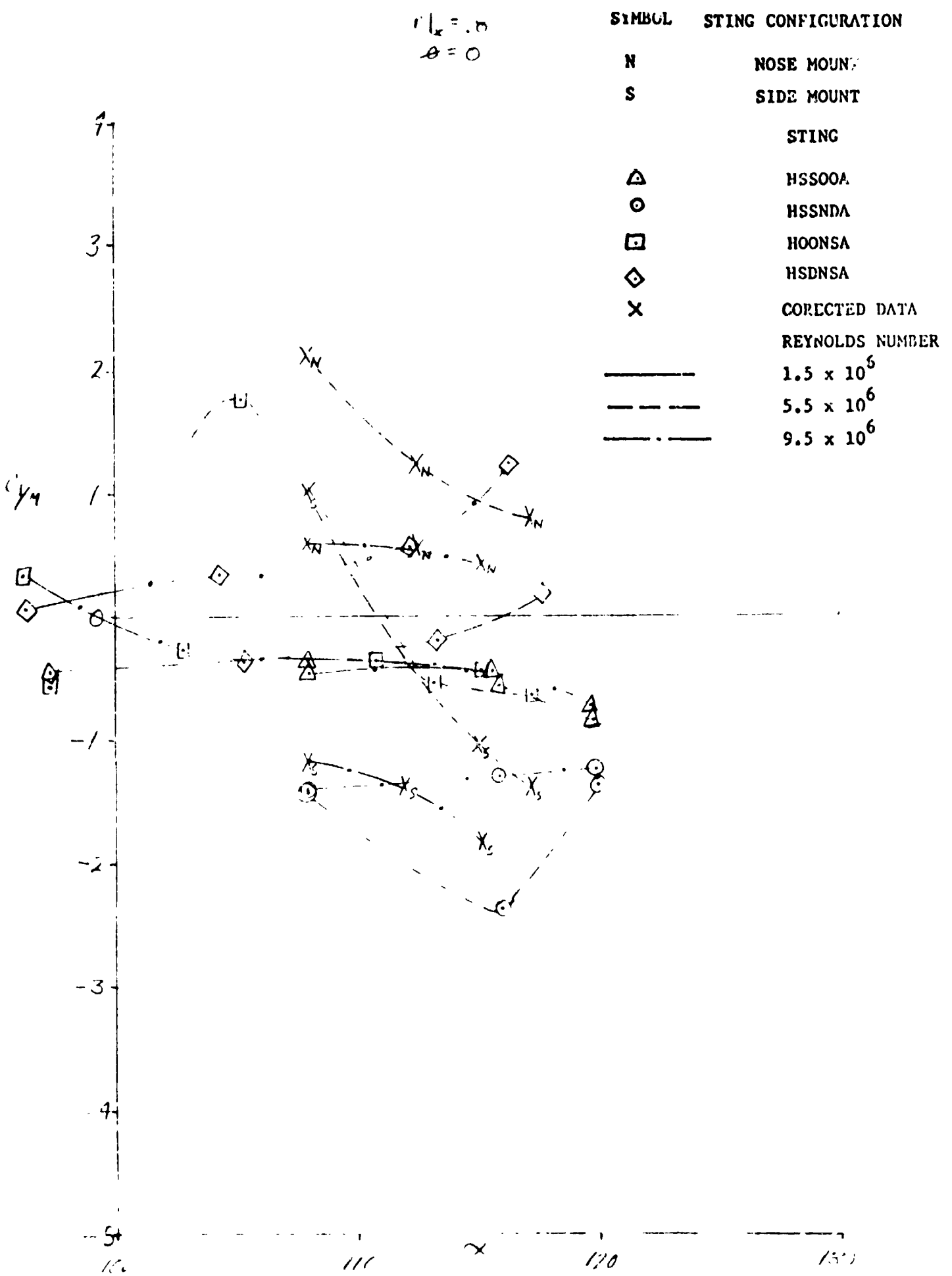

Figure 4-6 . Yawing Moment Data, HRWT, M_∞ = 0.8, ¢ = 0

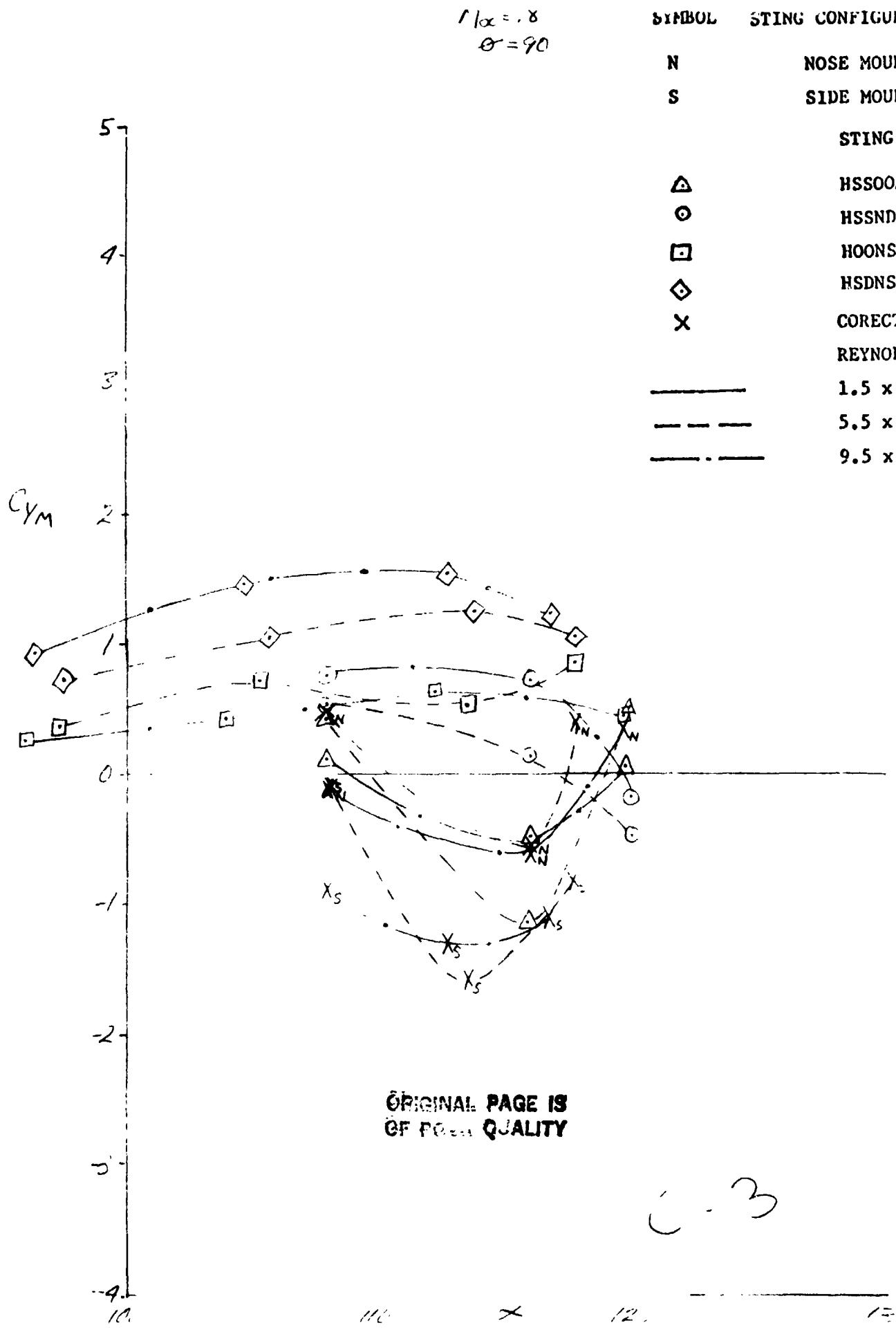

C-3

Figure 4-68. Yawing Moment Data, HRWT, M_∞ = 0.8, ϕ = 90

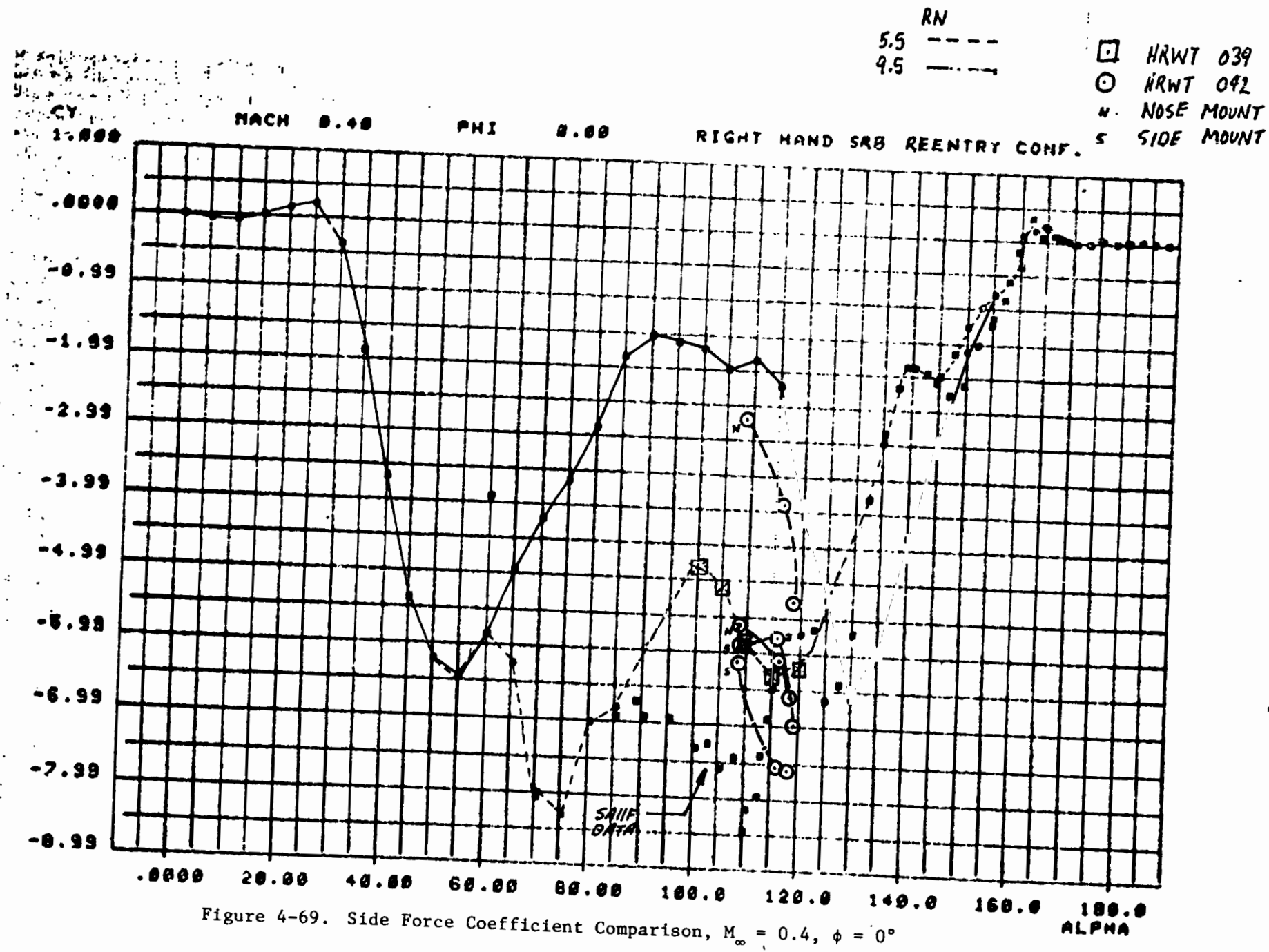

Figure 4-69. Side Force Coefficient Comparison, $M_\infty = 0.4$, $\phi = 0°$

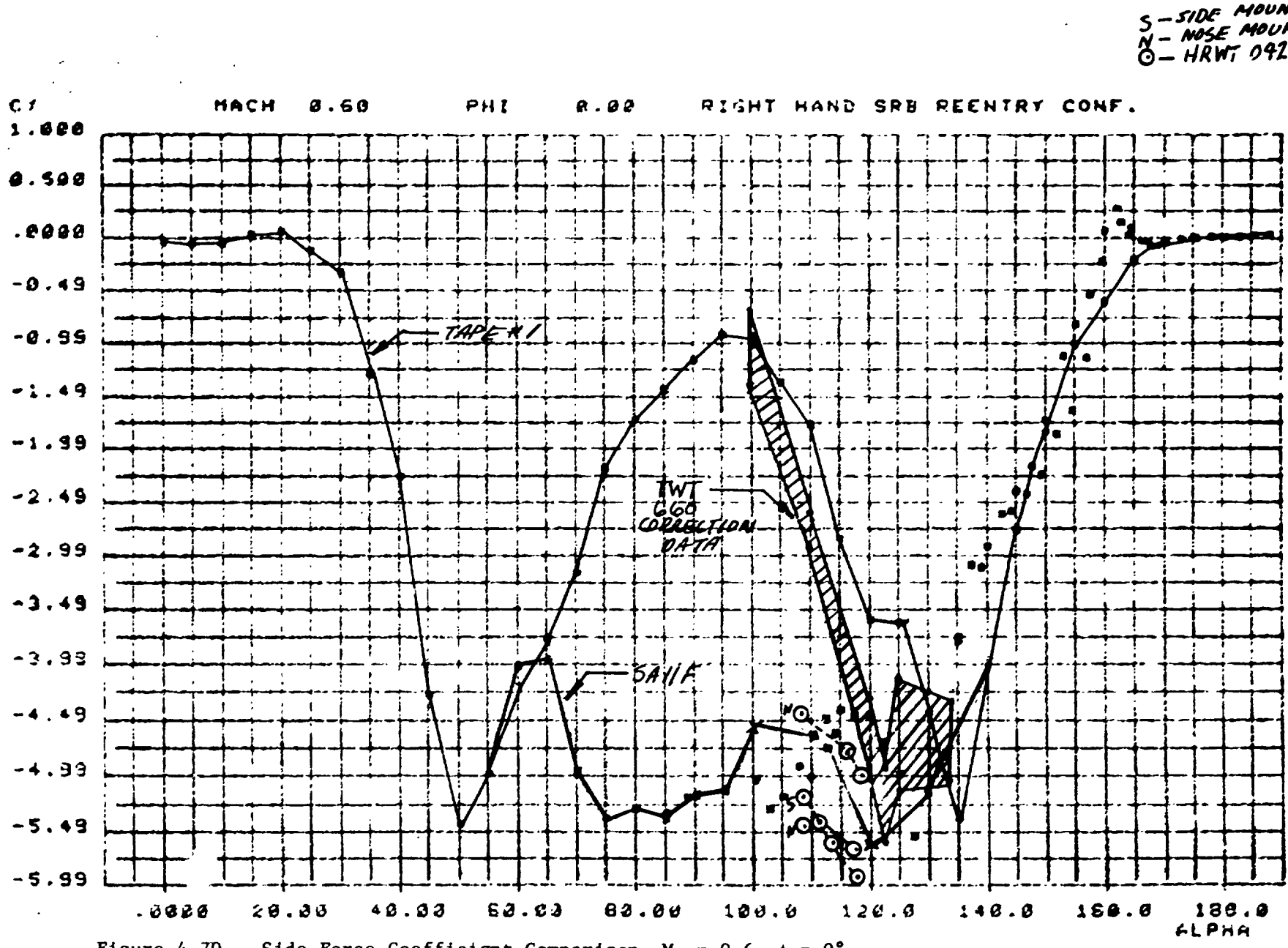

Figure 4-70. Side Force Coefficient Comparison, $M_\infty = 0.6$, $\phi = 0°$

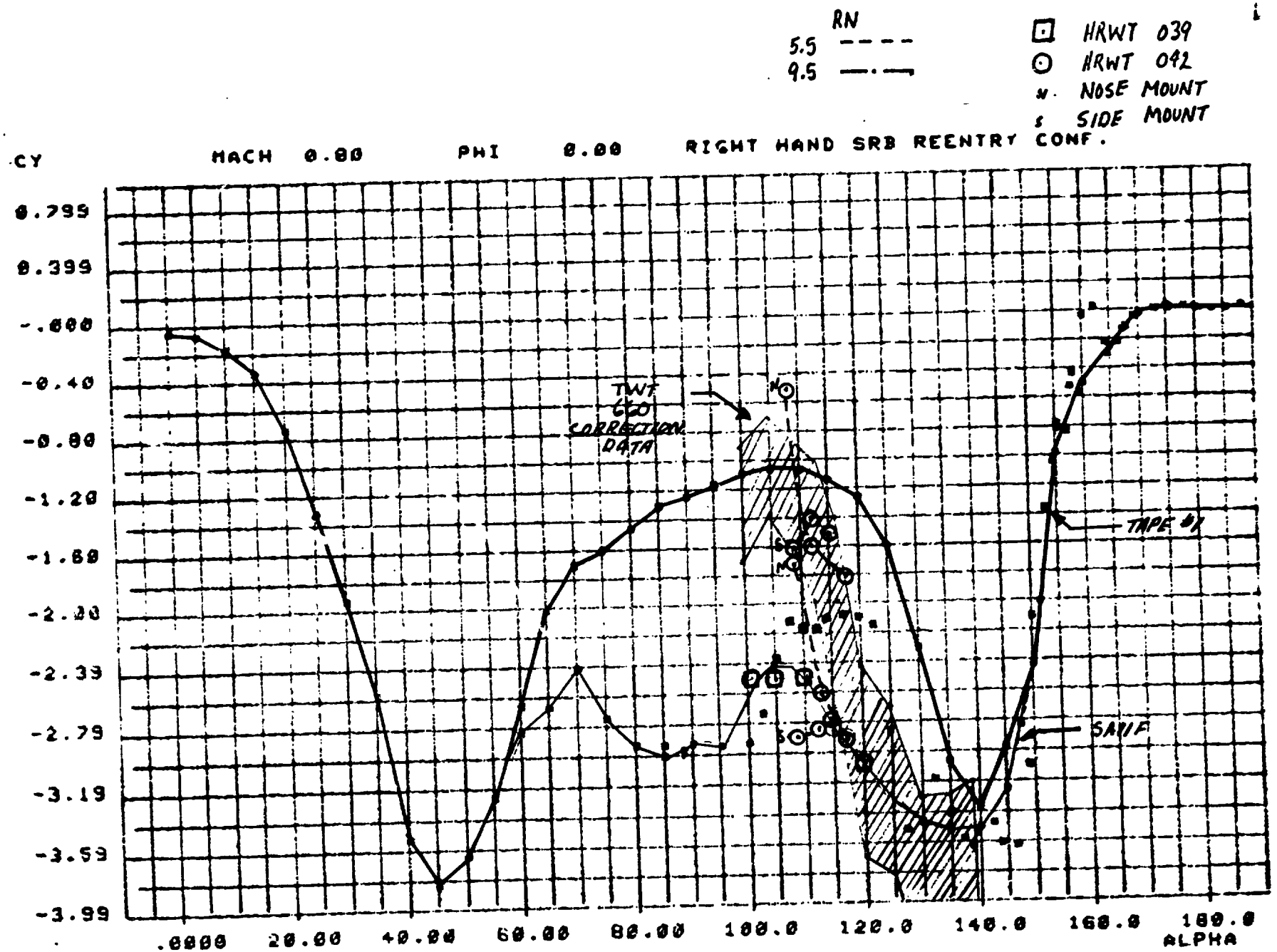

Figure 4-71. Side Force Coefficient Comparison, $M_\infty = 0.8$, $\phi = 0°$

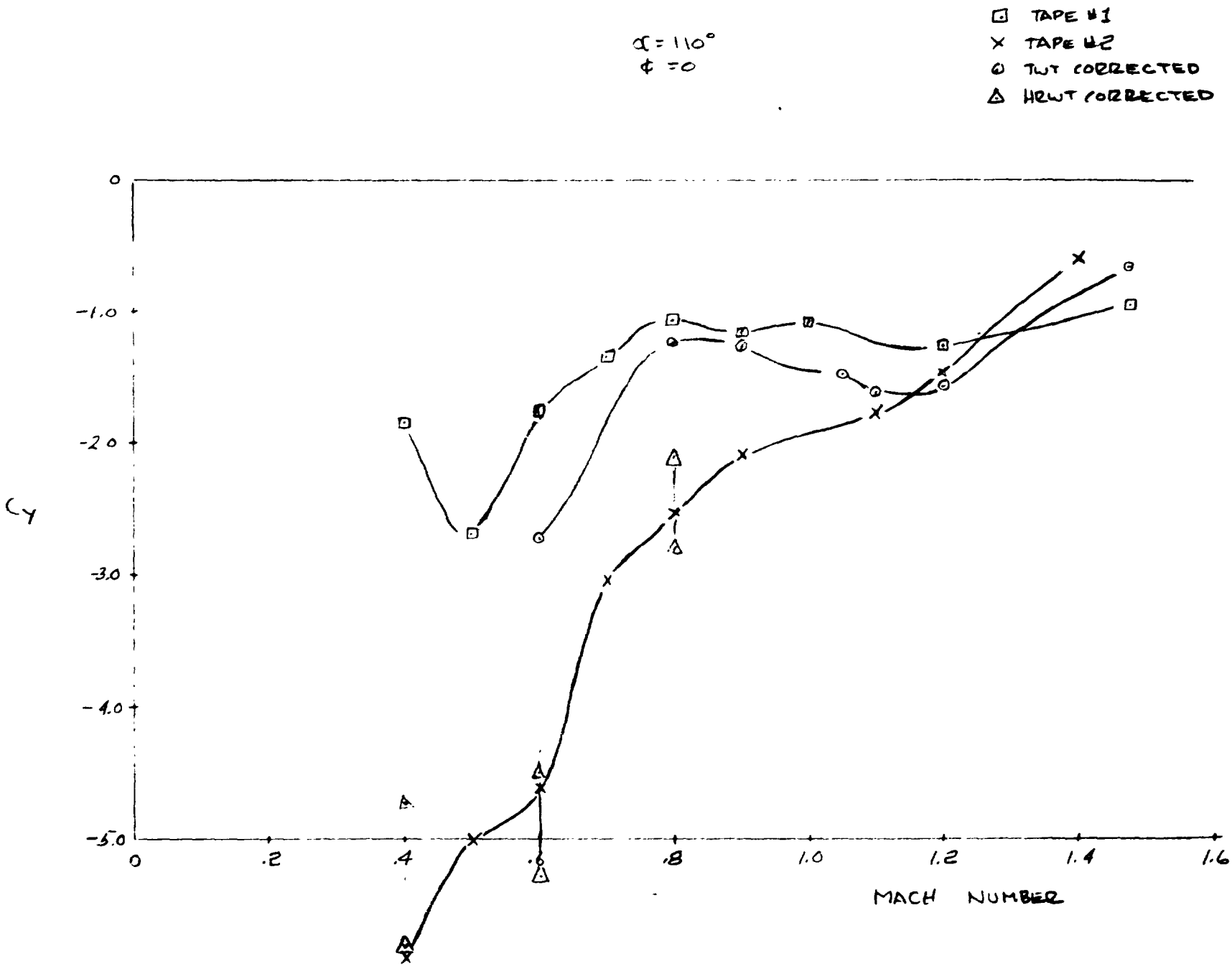

Figure 4-72. Side Force Coefficient Comparison Versus Mach Number

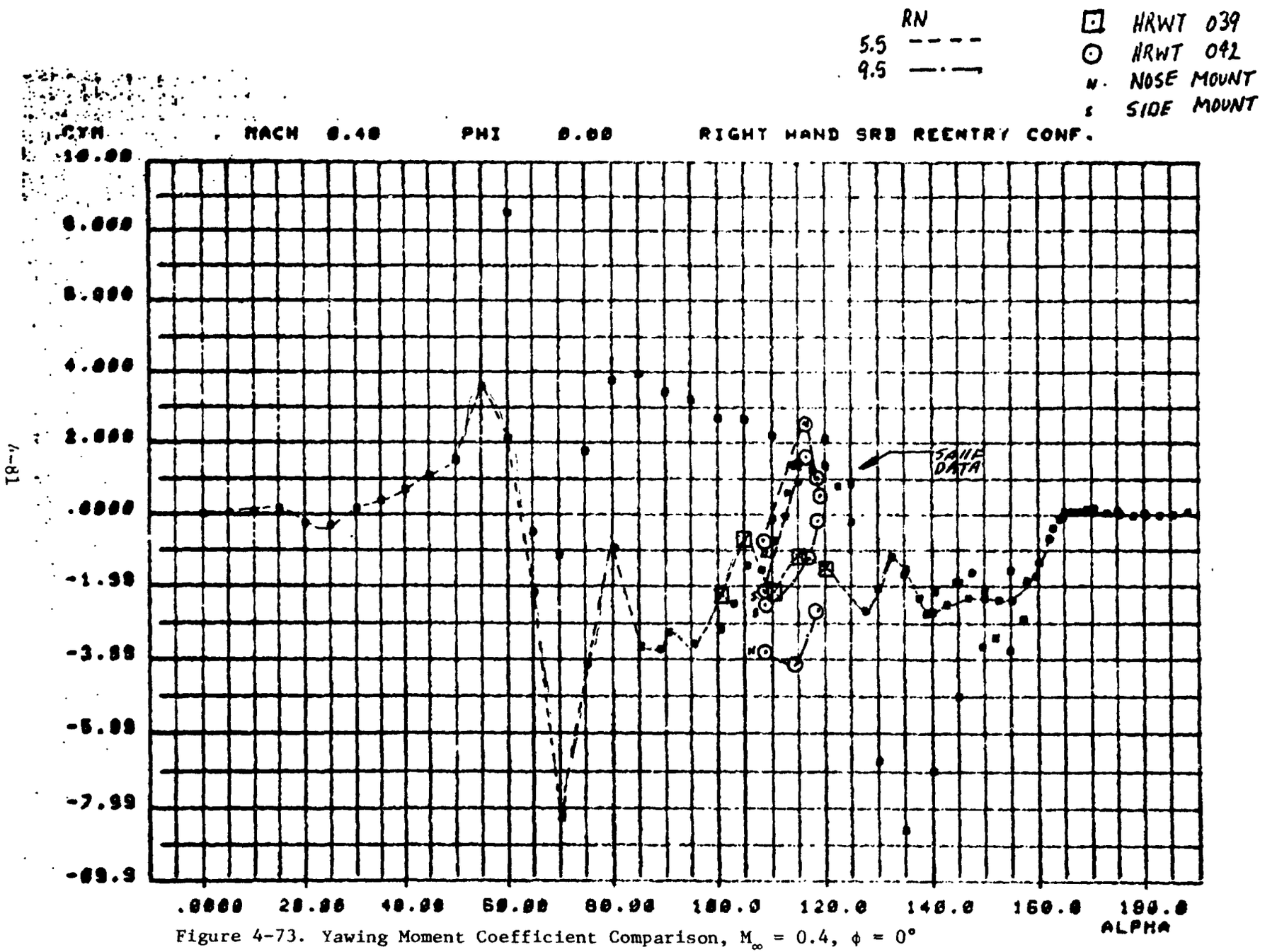

Figure 4-73. Yawing Moment Coefficient Comparison, $M_\infty = 0.4$, $\phi = 0°$

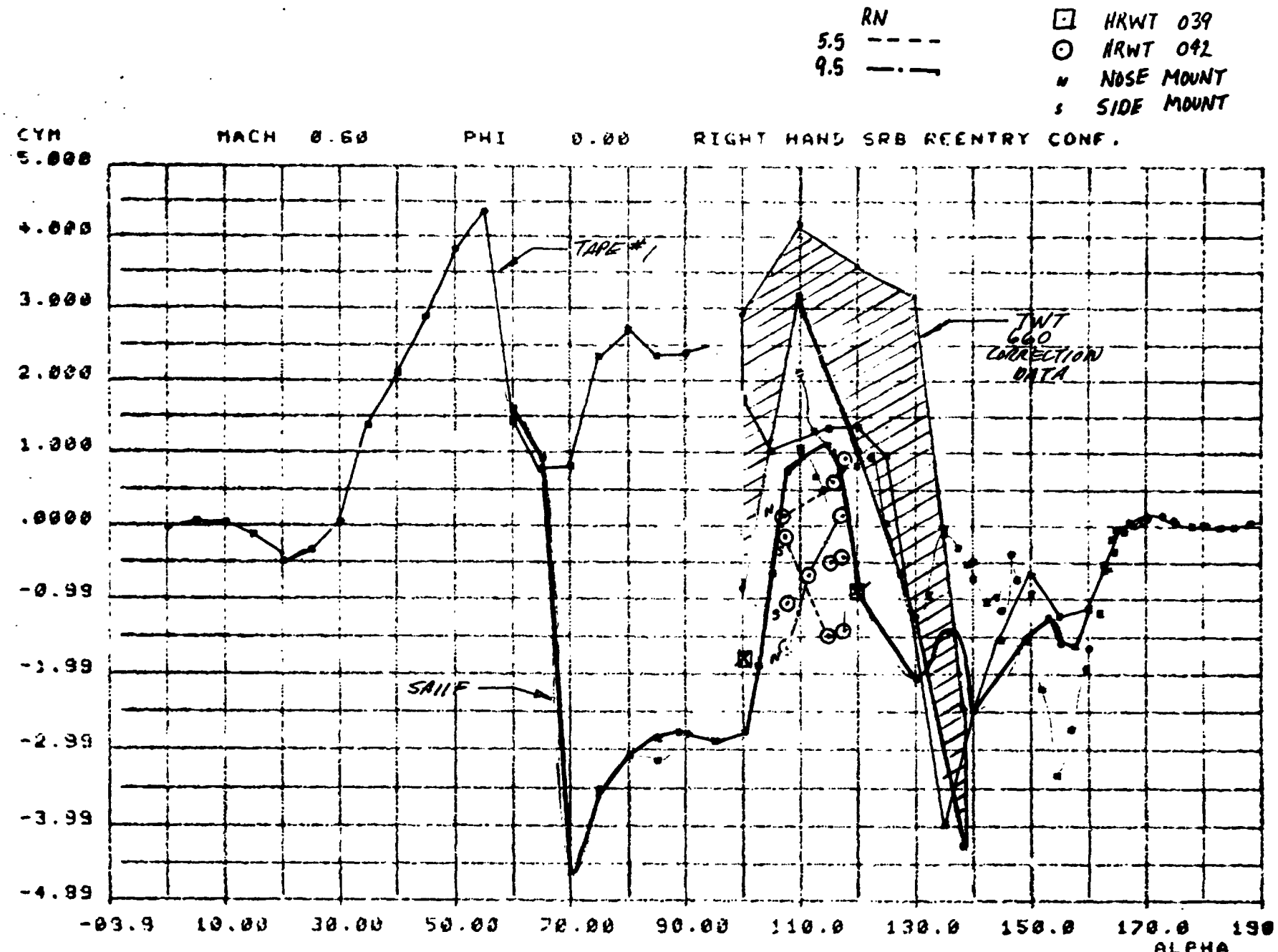

Figure 4-74. Yawing Moment Coefficient Comparison, $M_\infty = 0.6$, $\phi = 0°$

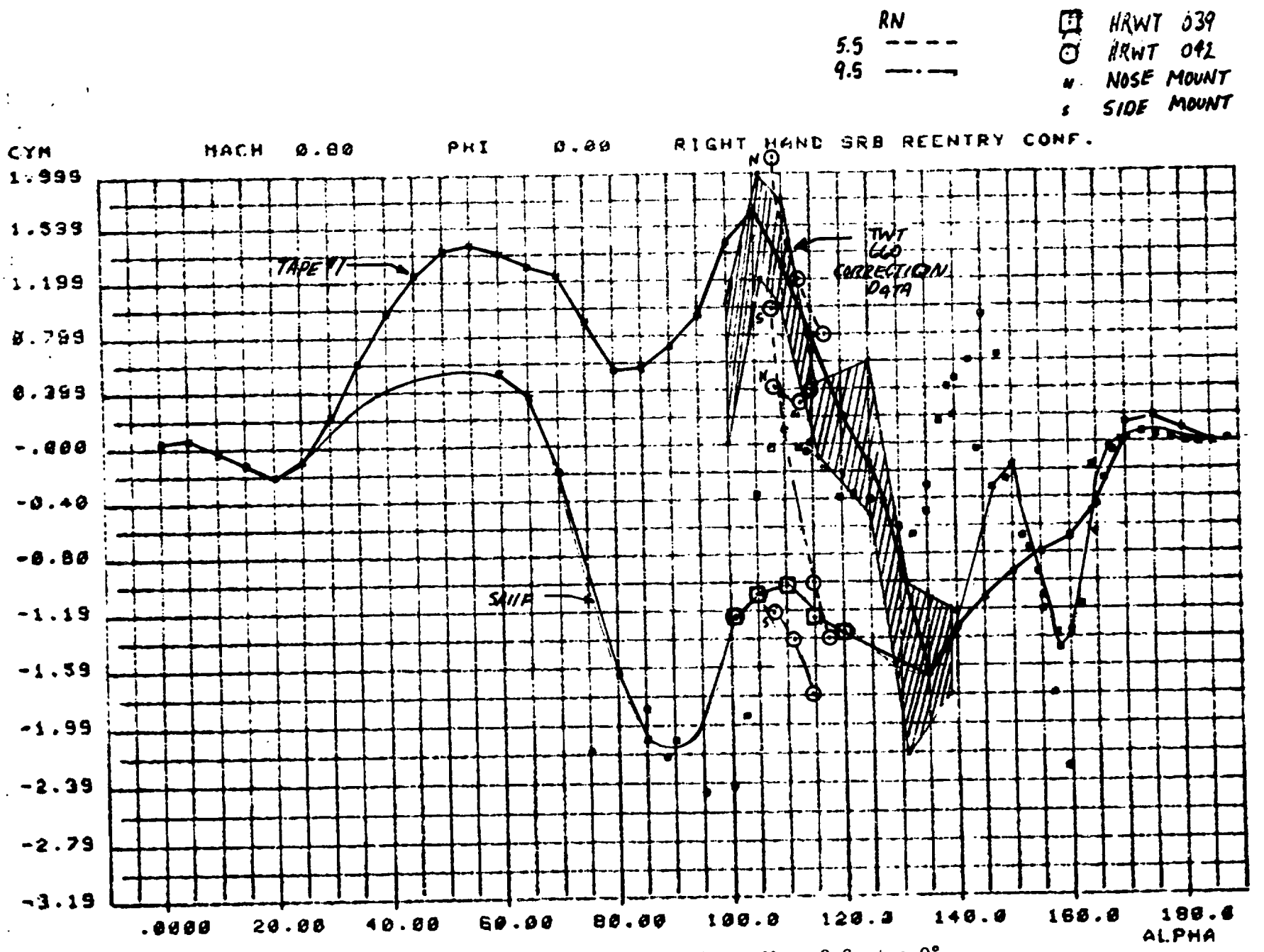

Figure 4-75. Yawing Moment Coefficient Comparison, $M_\infty = 0.8$, $\phi = 0°$

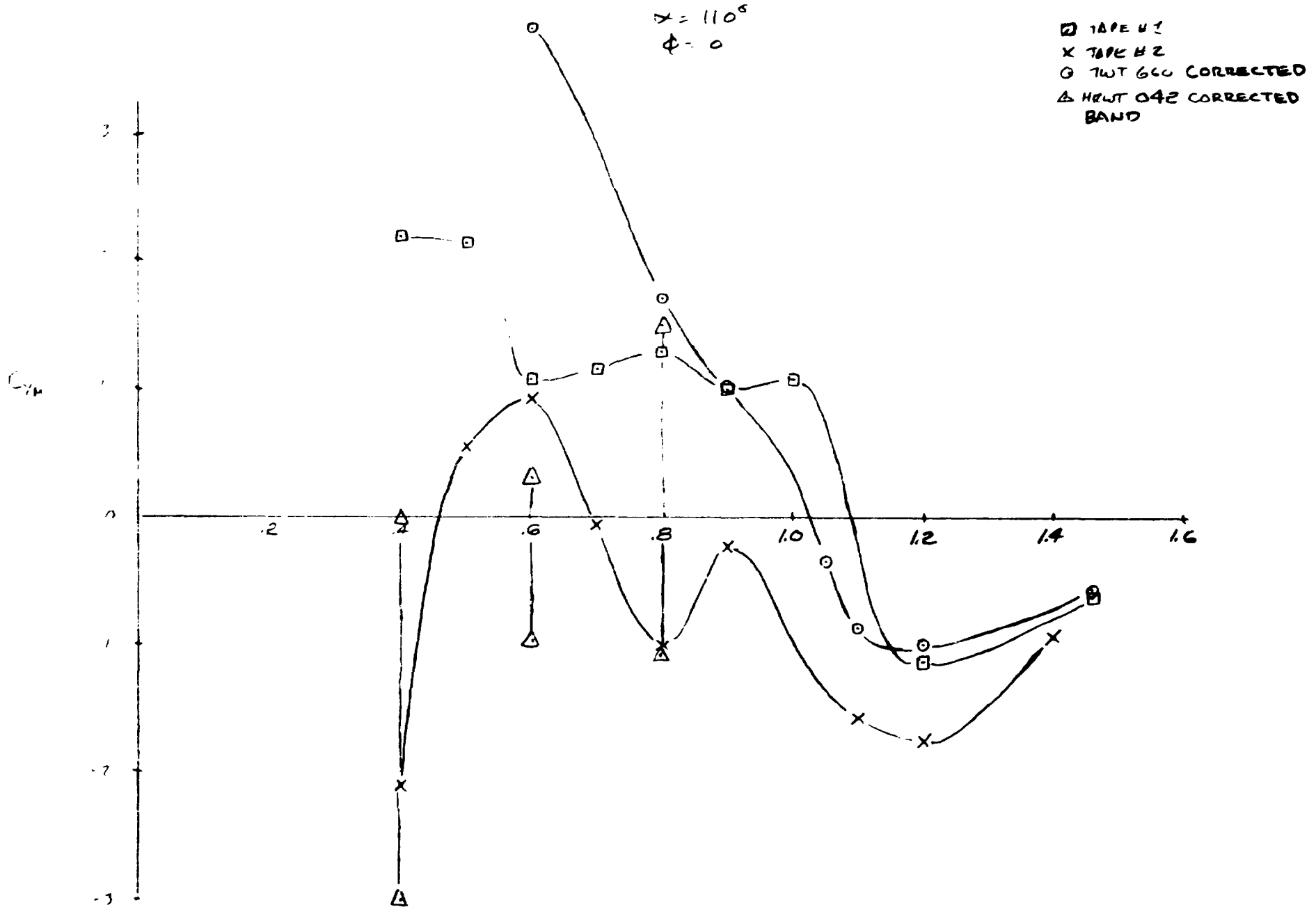

Figure 4-76. Yawing Moment Coefficient Comparison Versus Mach Number

Section V

STING INTERFERENCE CONCLUSIONS

The sting interference from the High Reynolds number test sting configuration was also determined in the TWT 660 test. This allowed an evaluation of the sting interference versus Reynolds number. Plots of the sting interference from this sting configuration versus Reynolds number are presented in Figures 5-1 through 5-3. The figures show that the sting interference is not a strong function of Reynolds number. The sting interference from the TWT 660 sting configurations is noted to be different from the HRWT sting interference. The normal force sting interference is generally less and the pitching moment sting interference has a different sign at Mach 0.6 and is smaller at Mach 0.8. The change in sign of the moment interference is due to the stings being located on different sides of the MRP. The MSFC and Ames side mounted stings are located forward of the MRP at 39 percent of the length (see Figures 2-6 and 2-14). The HRWT side mounted sting was located aft of the MRP at 68 percent of the body length. The MRP is at 59 percent of the body length.

The TWT 660 sting configurations are located forward of the MRP and thus the stings have a negative moment interference which moves the SRB X_{cp} aft. The high Reynolds number test sting configuration is located aft of the MRP and thus the sting interference has a positive value and moves the SRB X_{cp} forward. Comparison of the uncorrected center of pressure versus Reynolds number thus have shifts in the data as shown in Figure 5-4. The shift in the X_{cp} data versus Reynolds number is removed when both sets of data are corrected for sting interference as shown in the figure. The X_{cp} obtained with the forward sting configuration shifts aft and the X_{cp} obtained with the aft sting configuration shifts forward.

The relationship between the size of the various sting configurations and the level of sting interference is shown in Figure 5-5. Figure 5-5 shows that the level of sting interference is related to the size of the sting to the size of the cylinder. The figure shows that the Marshall sting has the lowest ratio of sting area to cylinder area and thus has the smallest sting interference.

The Ames sting configuration with an area 15 percent larger produce larger values of sting interference. The high Reynolds number type sting produced large value of sting interference for the majority of the test Mach numbers.

The following general conclusions are developed from the analysis of the sting interference data.

1. All side mounted stings reduced the airload on the SRB.
2. The airload reduction is proportional to the relative size of the sting and model.
3. The side mounted sting created less sting moment interference for angles of attack from 100 to 120 degrees.
4. The nose mounted sting created less sting moment interference for angles of attack greater than 120 degrees.

The analysis of the corrected data base from both the TWT 660 and HRWT wind tunnel tests was conducted to evaluate what changes were required to the existing SRB reentry aerodynamic data. The analysis of the TWT 660 results (Section III) at Mach 1.1, 1.2 and 1.46 identified major differences in the normal force and pitching moment characteristics that were significantly different from Tape #1 and Tape #2 characteristics. The corrected axial force characteristics were not appreciably changed. The lateral-directional characteristics were also not significantly influenced. The analysis of the high Reynolds number data (Section4) identified corrected pitching moment data trends at Mach numbers of 0.4, 0.6, and 0.8 that were also different from either SRB data tapes. The lateral-directional characteristics at these Mach numbers were not sufficiently defined as being different from the Tape #2 values to warrant changes. The corrected TWT 660 longitudinal data at Mach 0.9 was compared to the data Tape #2 results using the 039 Reynolds number trends. This comparison is presented in Figures 5-6 through 5-11. These figures show that the Tape #2 data adequately represent the corrected data considering the influence of Reynolds number. Thus the normal force coefficient required changing at Mach 1.1, 1.2, and 1.46 and the pitching moment coefficient required changing at essentially all Mach numbers covered by the test program except Mach 0.9.

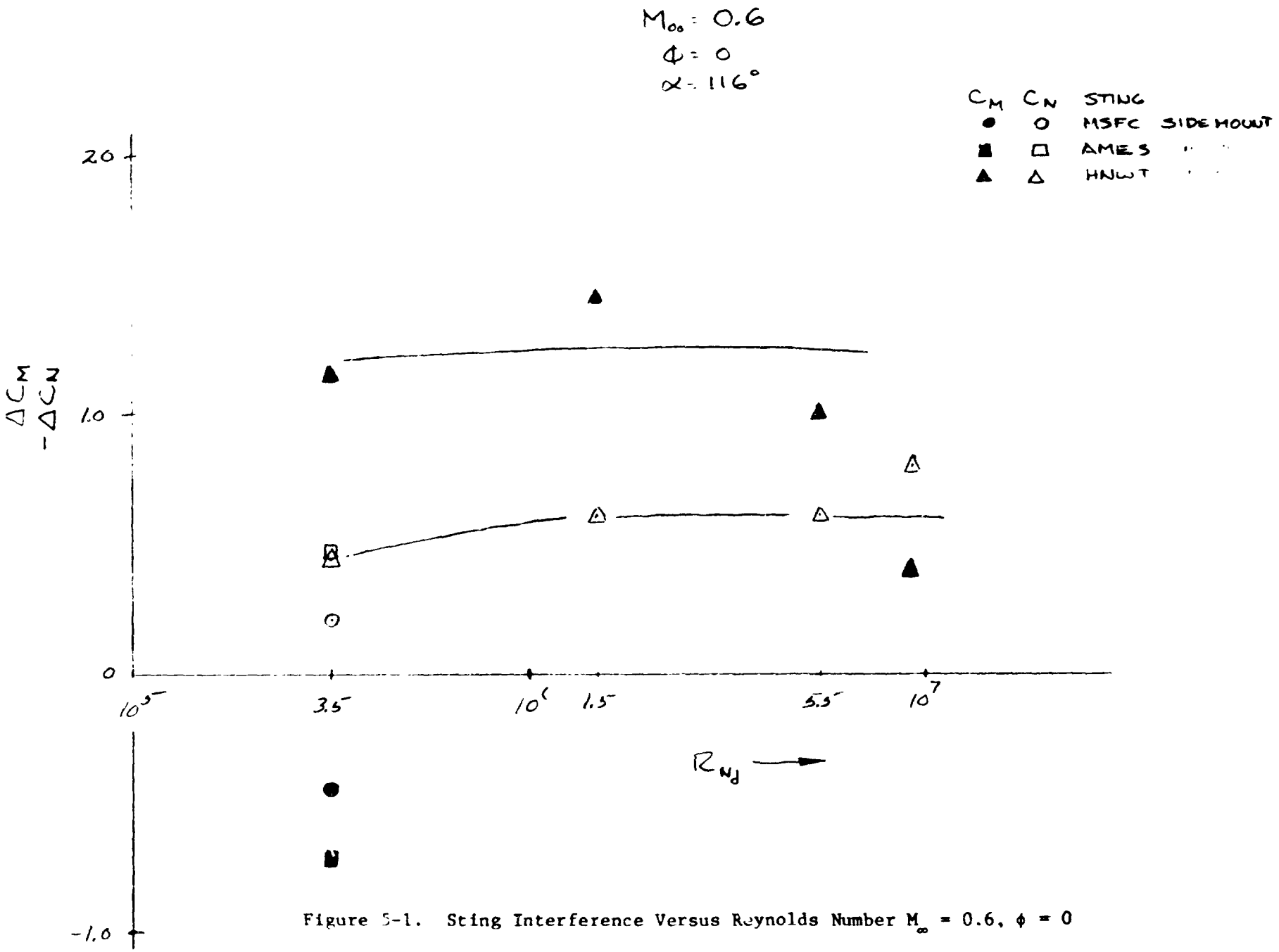

Figure 5-1. Sting Interference Versus Reynolds Number $M_\infty = 0.6$, $\phi = 0$

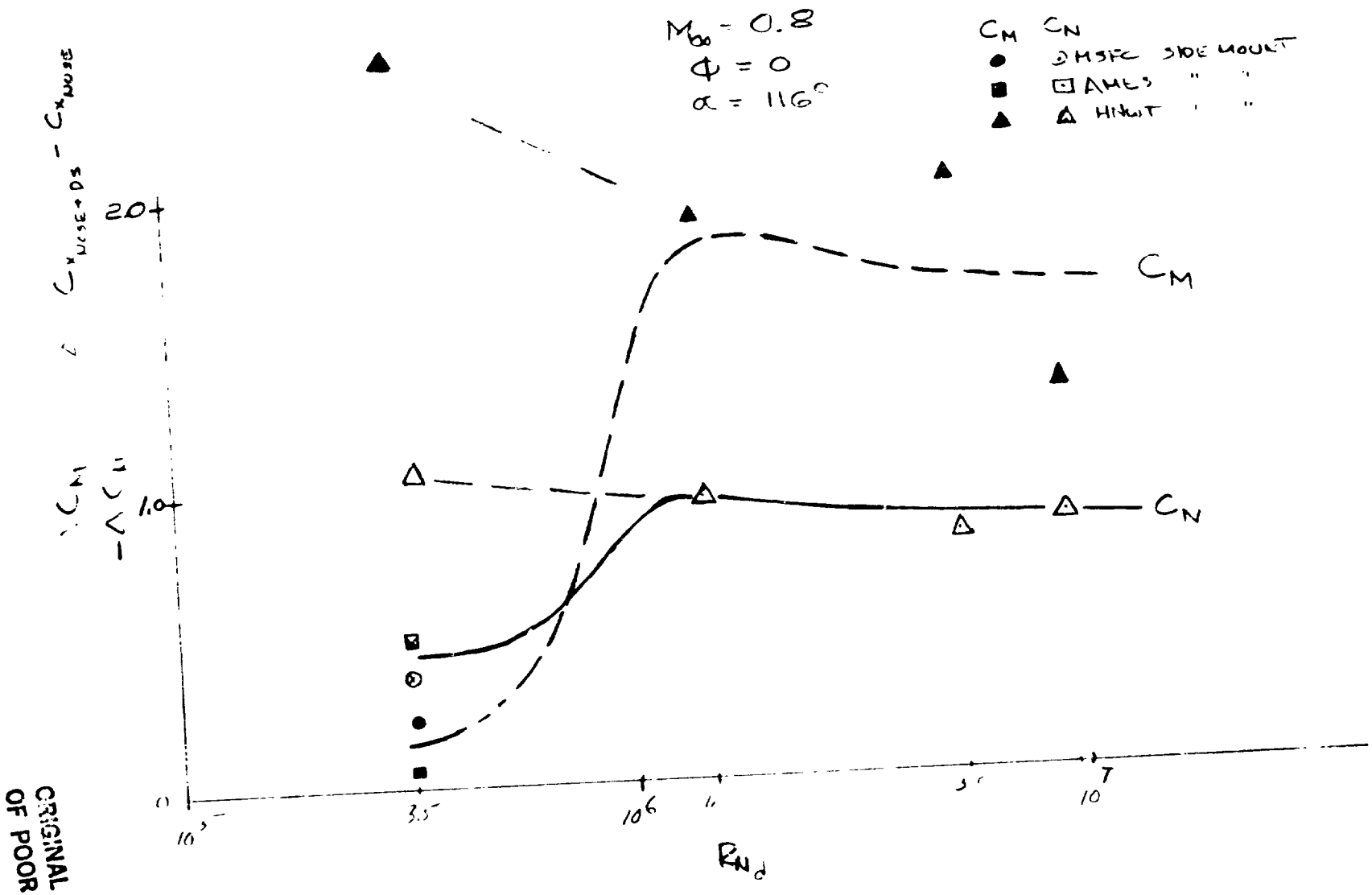

Figure 5-2. Sting Interference Versus Reynolds Number $M_\infty = 0.8$, $\phi = 0$

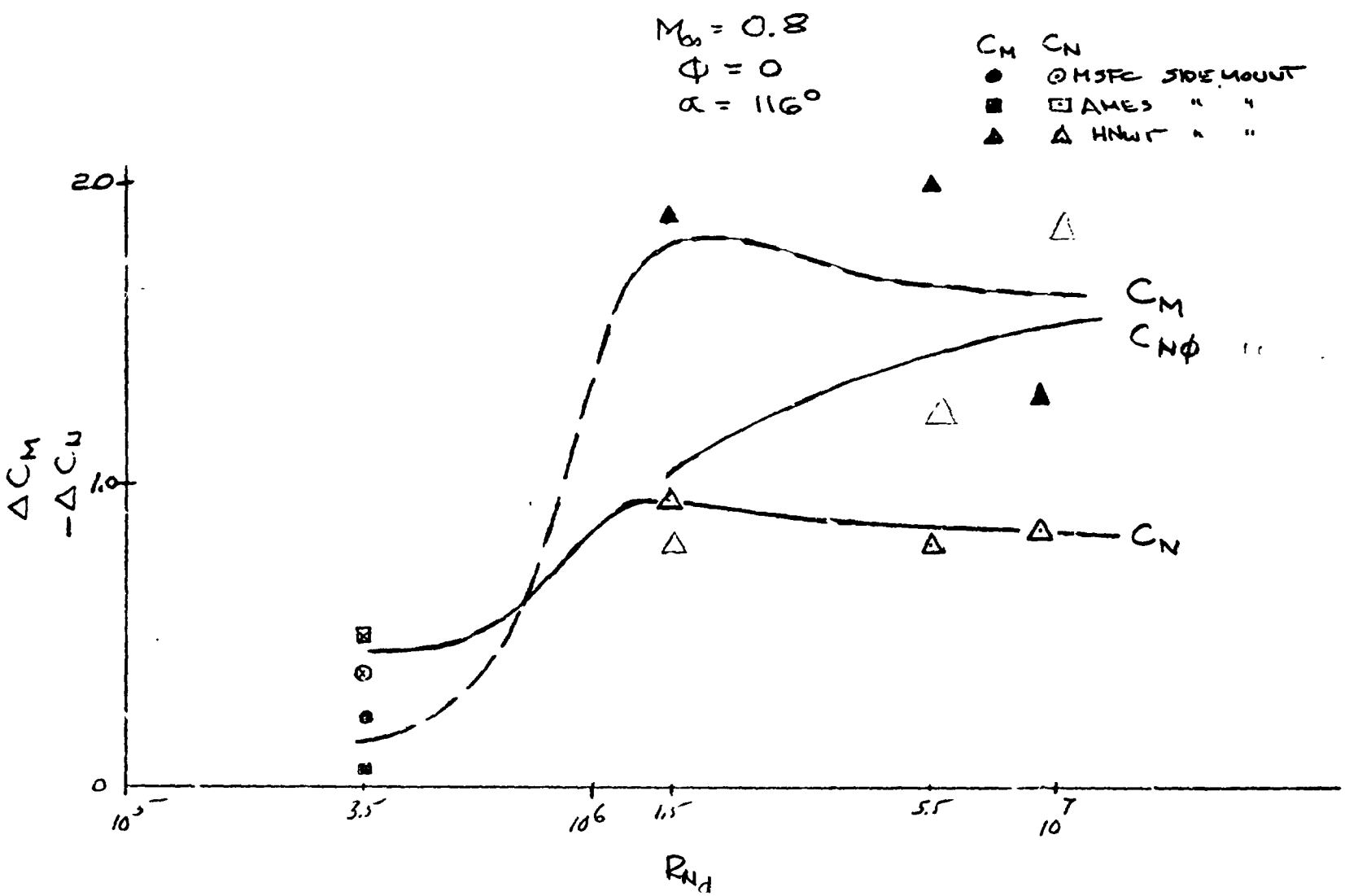

Figure 5-3. Sting Interference Versus Reynolds Number $M_\infty = 0.8$, $\phi = 90$

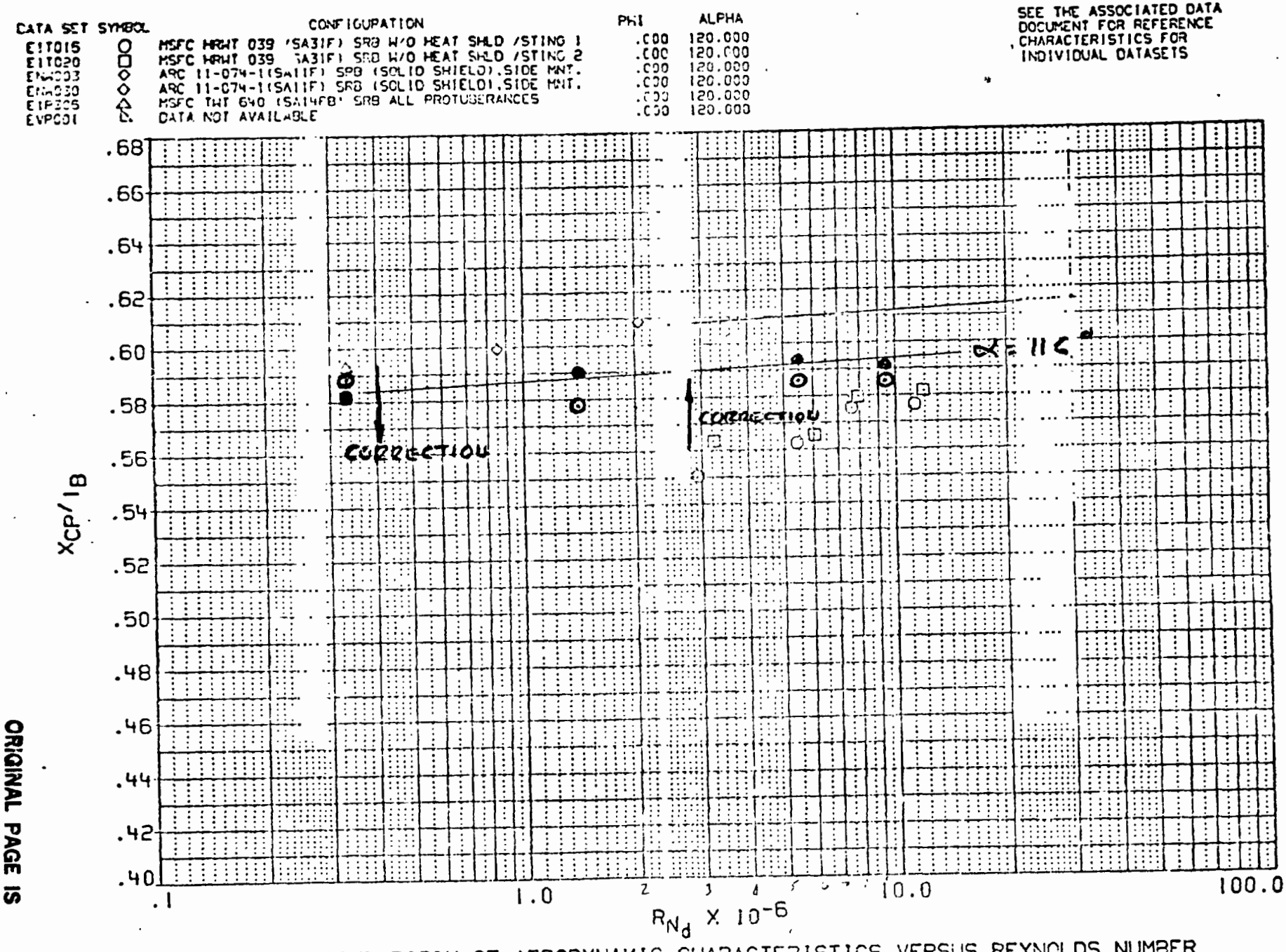

COMPARISON OF AERODYNAMIC CHARACTERISTICS VERSUS REYNOLDS NUMBER

(C)MACH = .60

Figure 5-4. Center of Pressure Versus Reynolds Number

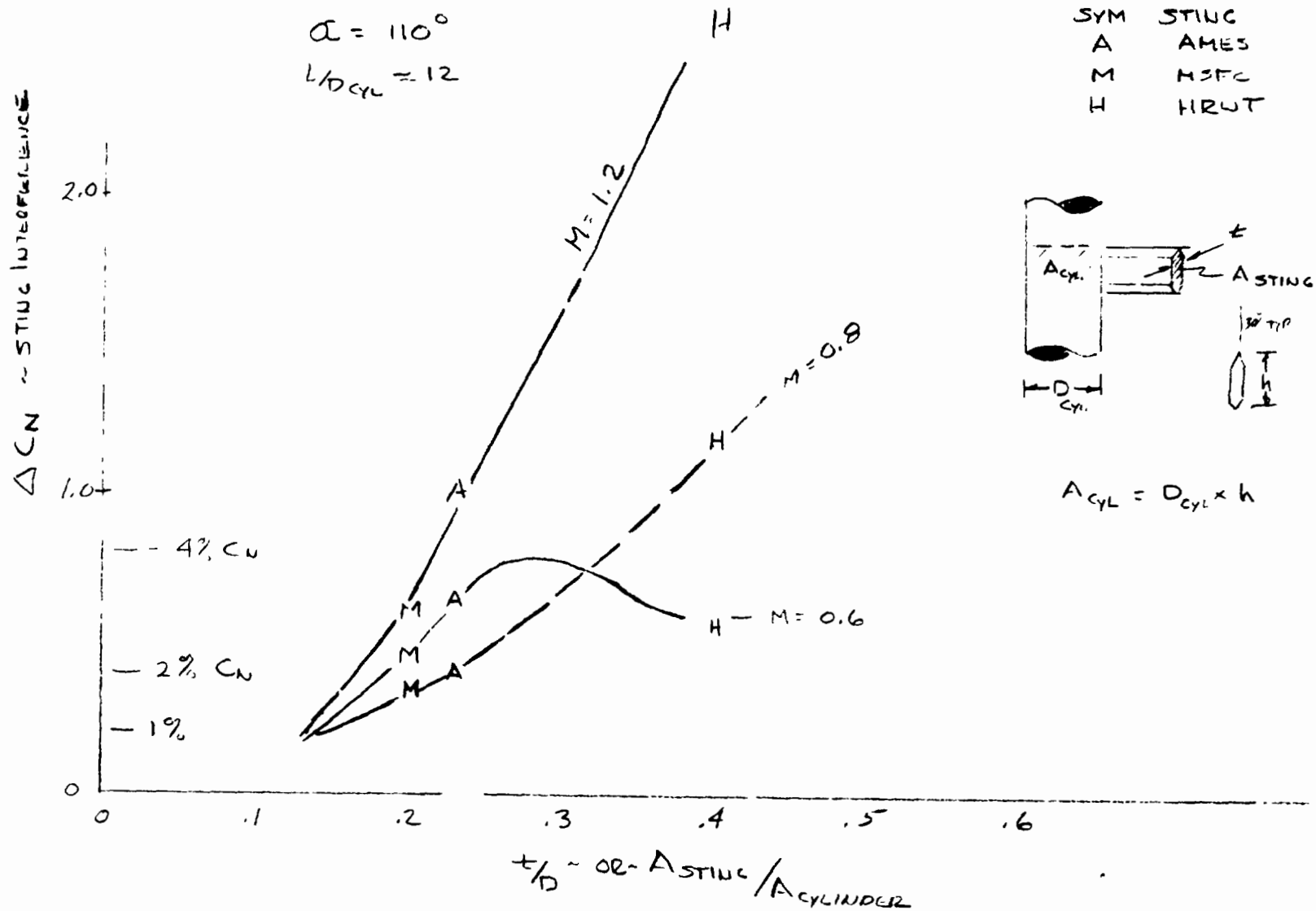

Figure 5-5. Sting Interference Versus Sting Area Ratio

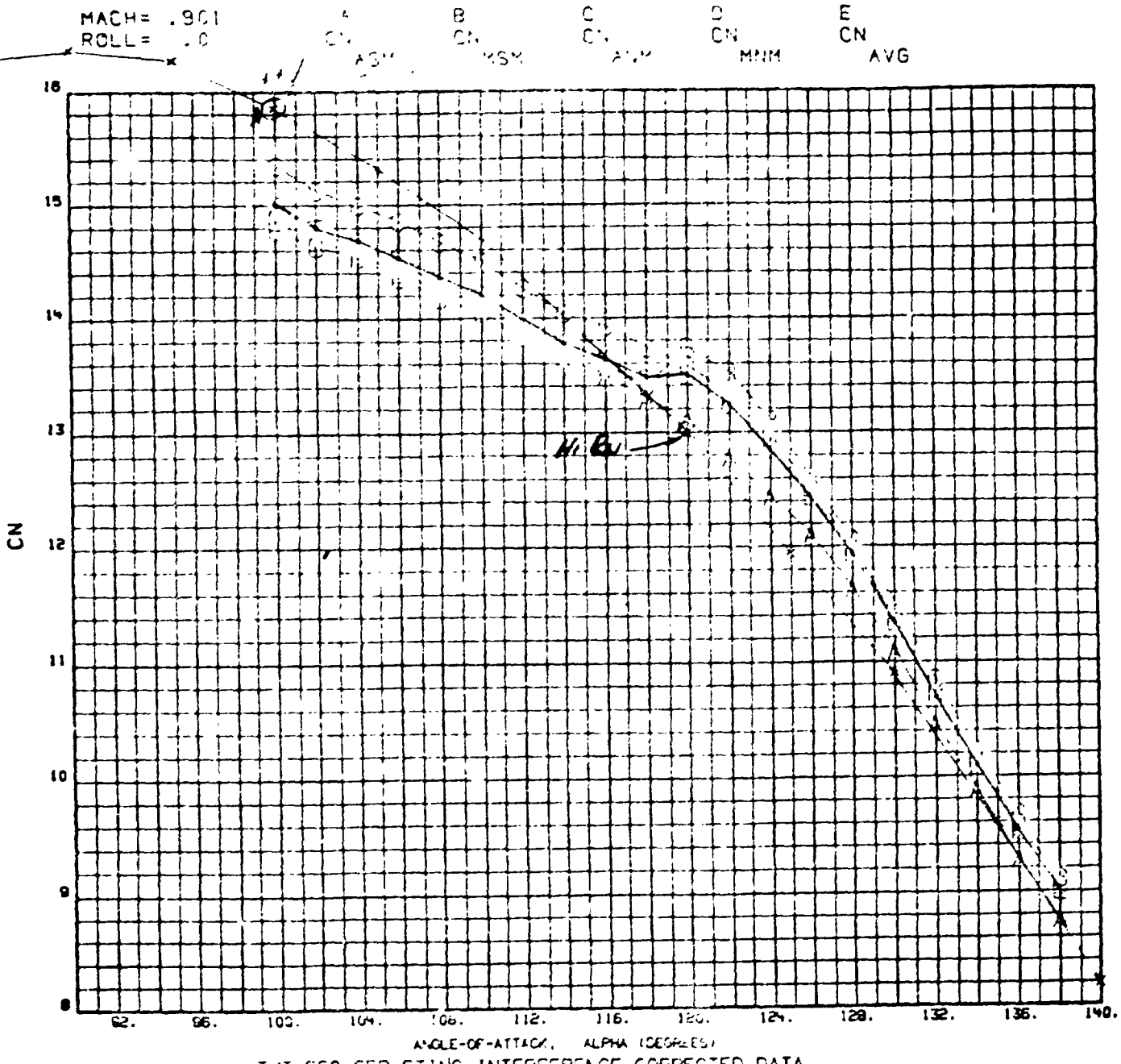

Figure 5-6. Normal Force Coefficient Versus α, $M_\infty = 0.9$, $\phi = 0$

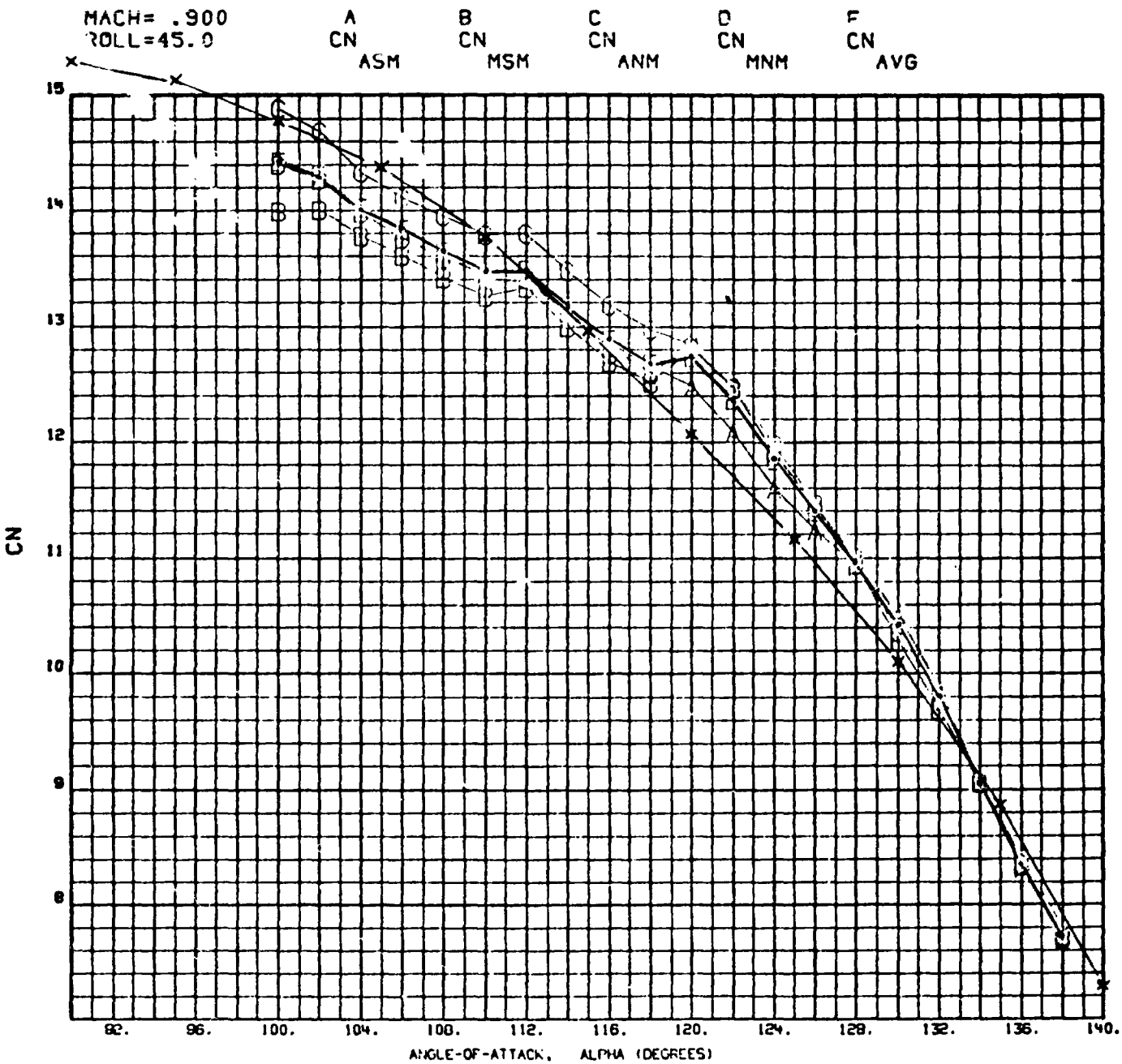

Figure 5-7. Normal Force Coefficient Versus α, $M_\infty = 0.9$, $\phi = 45$

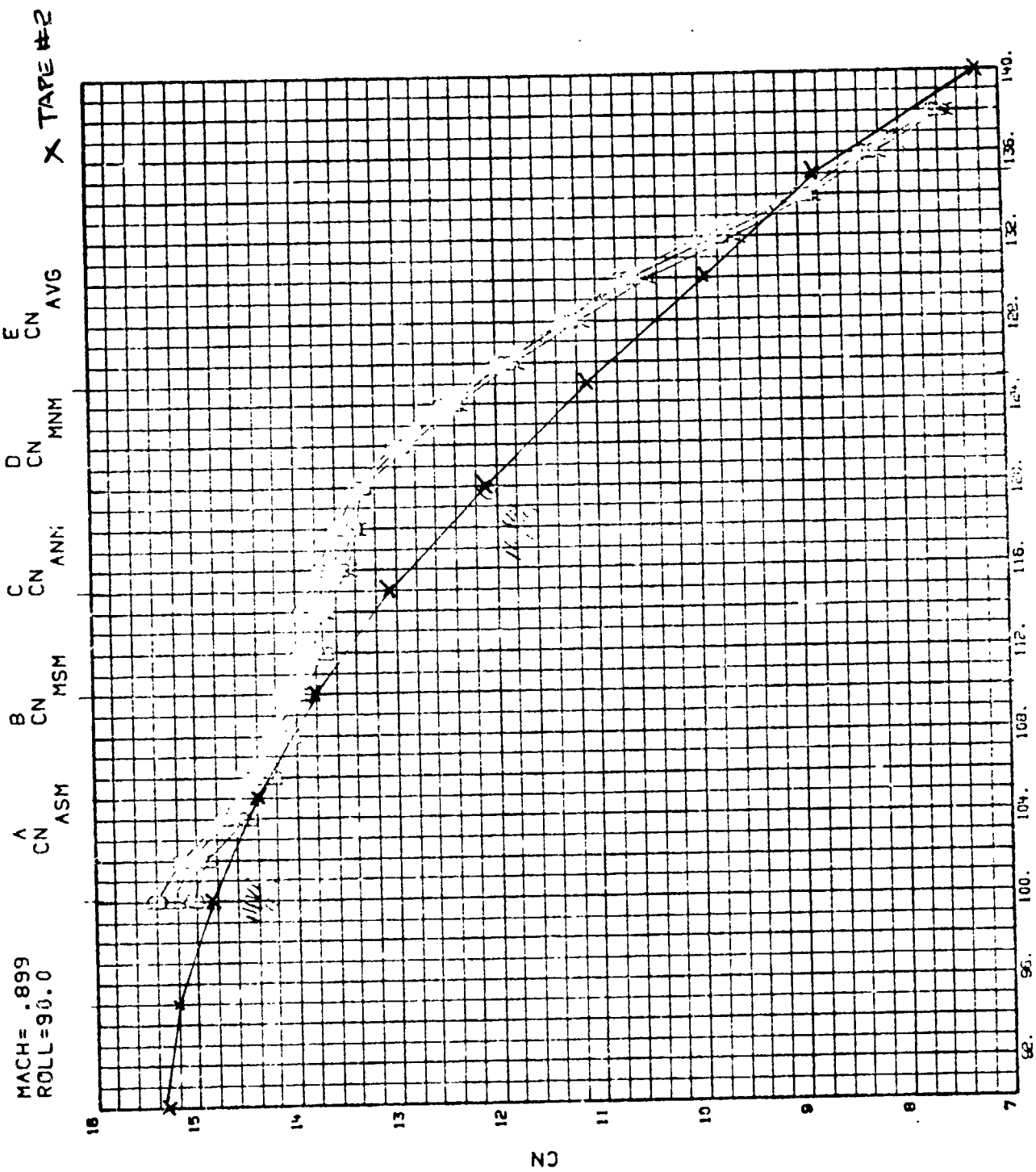

Figure 5-8. Normal Force Coefficient Versus α, $M_\infty = 0.9$, $\phi = 90$

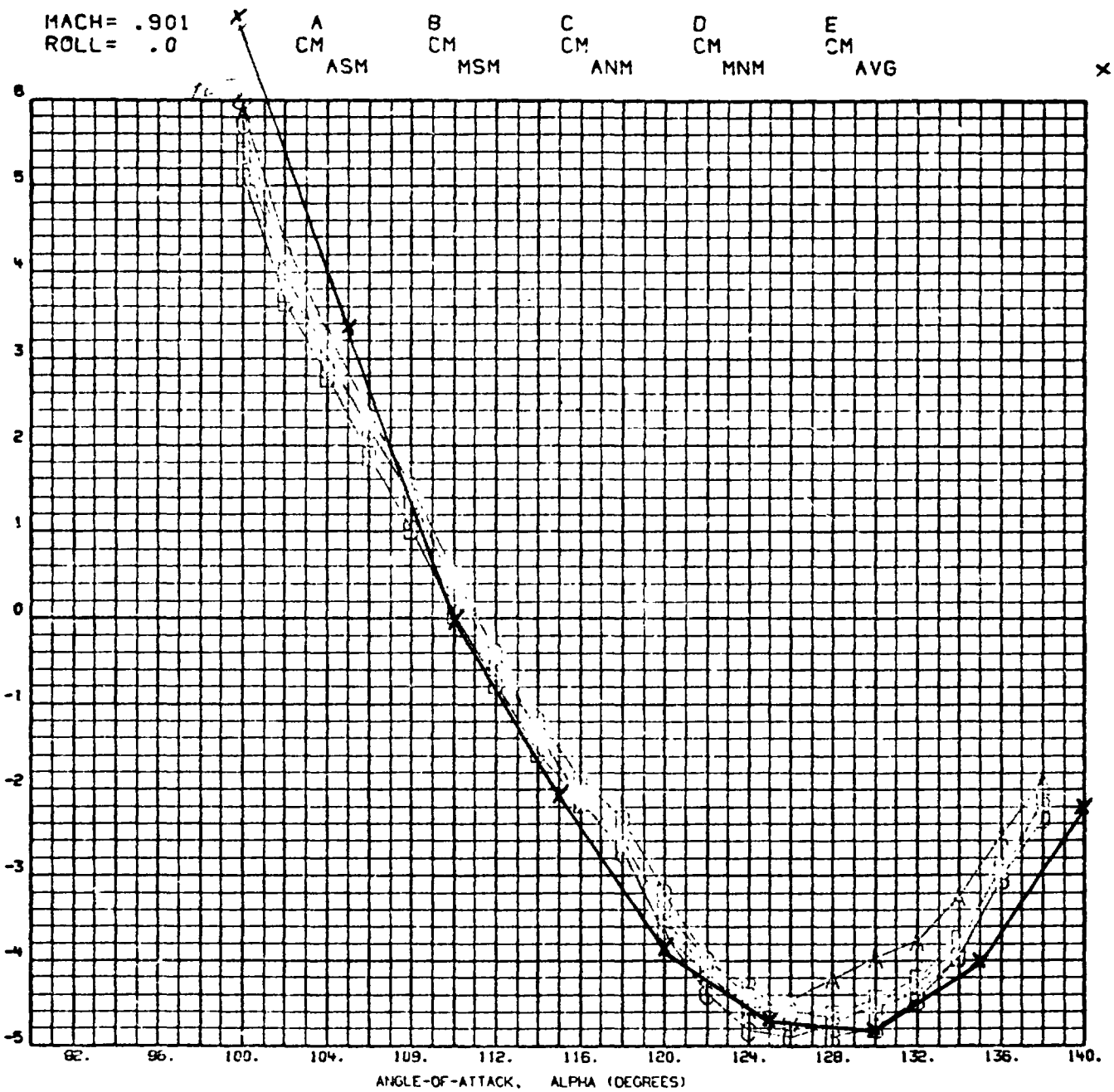

Figure 5-9. Pitching Moment Coefficient Versus α, $M_\infty = 0.9$, $\phi = 0$

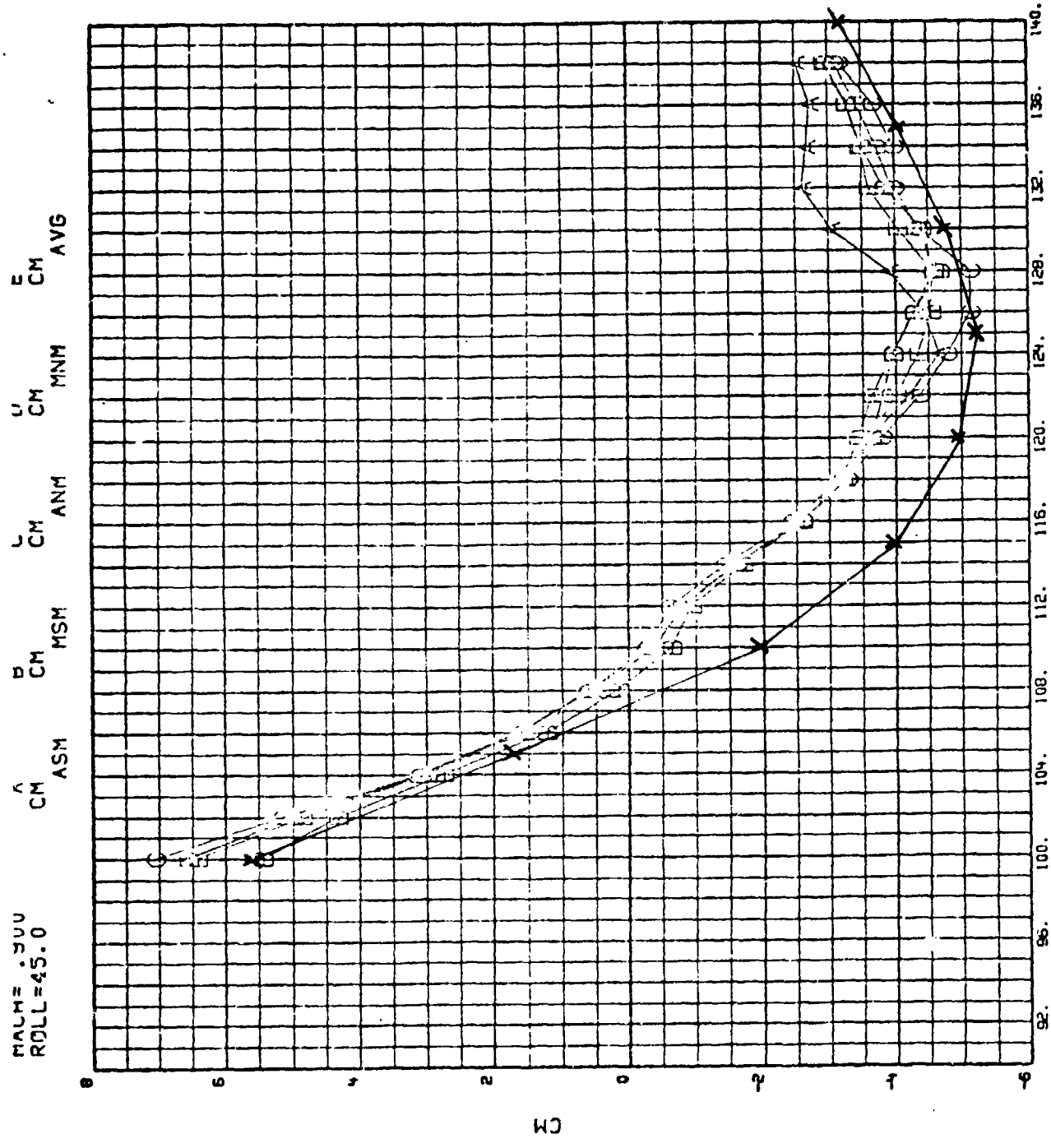

TWT-660 SRB STING INTERFERENCE CORRECTED DATA

Figure 5-10. Pitching Moment Coefficient Versus α, $M_\infty = 0.9$, $\phi = 45$

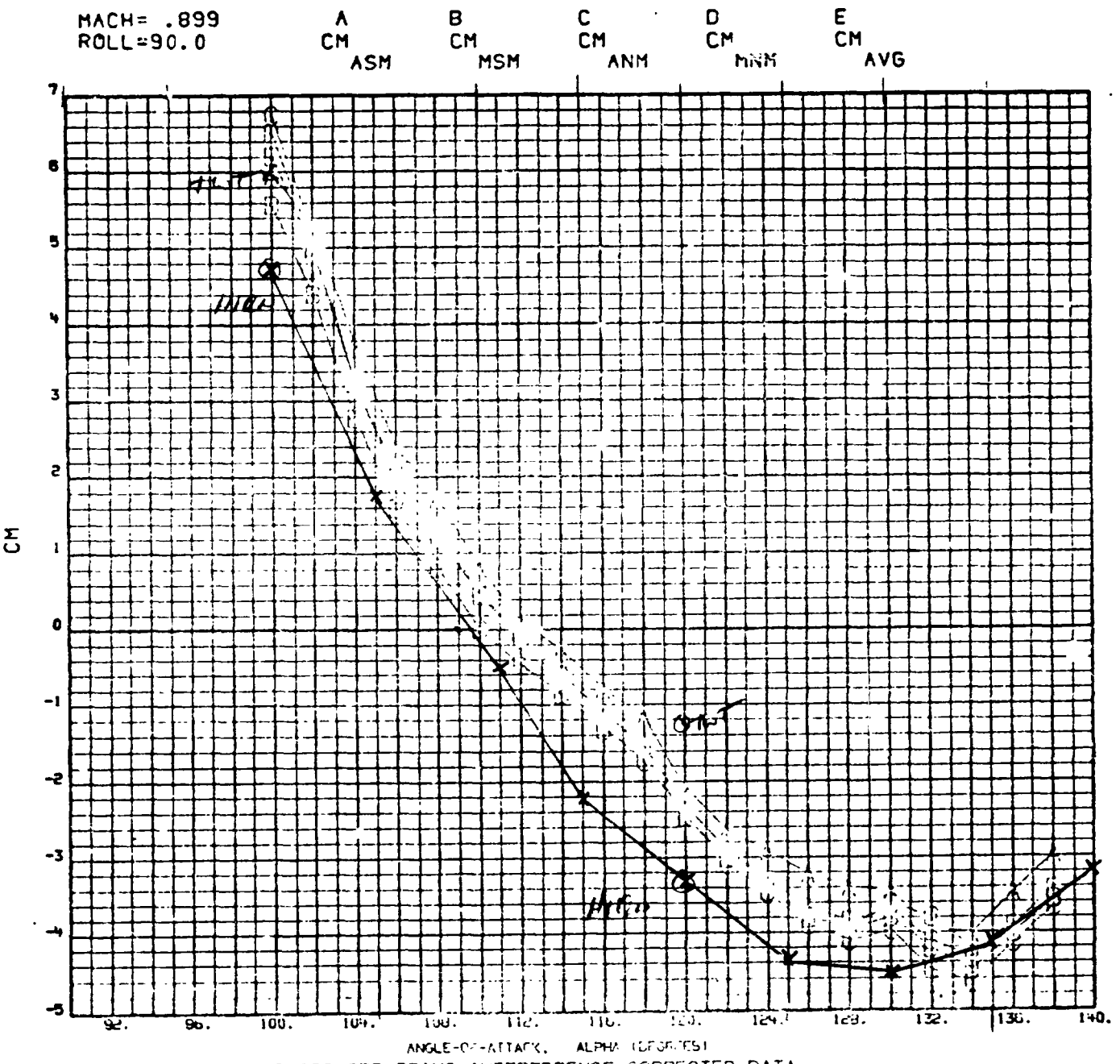

Figure 5-11. Pitching Moment Coefficient Versus α, $M_\infty = 0.9$, $\phi = 90$

Section VI

SRB AERODYNAMIC MATH MODEL

A new math model of the right SRB reentry aerodynamic characteristics was developed. The new math model is based on the results from the test TWT 660 and HRWT test 042. The math model was developed by evaluating the differences between the data from both tests corrected for sting interference and the math model known as DATA TAPE #2. There are currently two basic SRB reentry aerodynamic data tapes. The wind tunnel test programs used to develop each tape is shown in Table 2-2. Data Tape #2 has a much improved lateral directional math model. Since the sting interference tests showed little if any change in the laterial directional data Tape 2 was used as the basis for modification. The primary emphasis in modification concentrated on the normal force and pitching moment coefficients. These two coefficients had the largest changes due to sting interference. Two techniques were used to develop the new math model, transonic data that has little Reynolds number influence was modified using the TWT 660 data corrected for sting interference. The subsonic data that is influenced by Reynolds number was modified using a procedure that incorporated sting interference corrected data from both test programs (TWT 660 and HRWT 042). Both procedures are described below.

TRANSONIC DATA MODIFICATION (M_∞ = 1.1, 1.2, 1.40)

The data correction required to data Tape #2 at Mach number of 1.1, 1.2, and 1.46 were developed by comparing plots of the data Tape #2 coefficient with the corrected data from TWT 660 and data Tape #1. An example of this comparison is presented in Figures 3-17 and 3-27. The figures show that the band of corrected data is sufficiently removed from the TAPE 2 data (SA11F) to require modification. Several techniques were evaluated in modifying the data. The initial technique consisted of applying the Ames correction to the SA11F data. This technique produced the curves shown in Figures 3-18 and 3-20. The resultant curves required extensive fairing to smooth. This is probably due to the differences between the Ames data and the data obtained in the 14-inch tunnel with the Ames sting configuration. These figures show that the basic data is

different and thus the sting interference from the stings are different, which causes data fairing problems when using the TWT 660 Ames configuration sting interference data to correct the SA11F data. Comparison of the two sets of data indicate the SA11F Ames sting configuration has larger sting interference than the TWT 660 Ames sting configuration. This may be due to the added bulk hardware at the knuckle joint of the SA11F test (see Figures 2-14 and 2-38). This hardware was not simulated in the TWT 660 test. The increase in normal force from the TWT 660 test indicates a reduction in sting interference. An additional indication of the extent of the sting interference in the SA11F test is the shape of the normal force curve. The dips in the curve indicate a substantial amount of sting interference that varies significantly with angle of attack. An indication of the potential variation of the sting interference from the Ames type of sting configuration is evident in Figures 3-4. It is noted in the figure that the sting interference of the Ames sting configuration varies by a factor of over 2.0 over the angle of attack range investigated.

The procedure that was used was to smooth the average of all 4 sets of corrected sting interference data and then fair the new curve into the Tape 2 data over the angle of attack range from 70 to 180 degrees. The extent of the fairing generally required less than this range of angle of attack. This type of fairing was used because the band of corrected data from the four sting configurations was generally small compared to the difference between the Tape #2 data and the corrected data. An additional problem was that the corrected data did not form a smooth curve, indicating that all the sting interference had not been removed or that mutual sting interference existed at certain attitudes. This is evident by the data presented in Figure 3-35.

SUBSONIC DATA MODIFICATION

The aerodynamic data on SRB data Tape #2 for Mach numbers of 0.4, 0.5, 0.6, 0.7, 0.8, and 0.9 were evaluated for potential changes due to the sting interference data base. Potential sting interference corrections were available from the TWT 660 test program at Mach numbers of 0.6 and 0.8. Potential sting interference corrections from the HRWT 042 test program at Mach 0.4, 0.6, and 0.8 were available. These data were assembled and compared with test data

from TWT test 640, SA11F, and HRWT 039 to evaluate specific Mach and Reynolds number trends. Section IV showed that the corrected HRWT 042 data is significantly different from the TWT 660 data. Thus the HRWT data has to be used to evaluate the corrected data trends. Specific trends with Reynolds number were difficult to evaluate due to differences between the corrected nose mount and side mount data. The procedure that was used was to use the average of the corrected High Reynolds number data.

Summary plots of the corrected normal force coefficient data are presented in Figures 4-45 through 4-50. The analysis of the corrected data compared to the data Tape #2 showed that differences of a magnitude to warrant changes did not exist. Thus no corrections were made to the normal force coefficient data.

Summary plots of the corrected pitching moment coefficient data are presented in Figures 4-51 through 4-56. The analysis of these data showed that significant differences existed between the corrected data and data Tape #1 and #2. The corrected pitching moment coefficient curves are presented in Figures 6-1 through 6-6. The pitching moment coefficient at Mach 0.4, 0.6, and 0.8 was corrected to the average of the HRWT 042 data trends as shown in the figures. The figures show that the corrected trim angle of attack is generally closer to Tape #1 values than Tape #2.

Corrections to the Tape #2 pitching moment at roll angles other than zero and 90 degrees were developed by evaluating the pitching moment coefficient and corrections versus roll angle for Tape #1 and the corrected data from test HRWT 042. This produced a set of preliminary pitching moment corrections for evaluation at selected angles of attack. These data were used as a basis to evaluate preliminary pitching moment curves and values of α_{TRIM}. The resultant values of α_{TRIM} versus Mach number was then used to evaluate the potential values of α_{TRIM} at the two Mach numbers where there was not sting interference data (M = 0.5 and 0.7). These data were then converted to an effective delta in pitching moment coefficient which was applied to the Tape #2 data. This provided a basis for correcting the Tape #2 pitching moment coefficient at Mach 0.5 and 0.7. The net correction to Tape #2 represents approximately 75% of the difference between Tape #1 and Tape #2.

A comparison of the resultant values of α_{TRIM} versus Mach number is presented in Figures 6-7 through 6-14. Also presented on the figures are values of α_{TRIM} from Tape #1 and Tape #2.

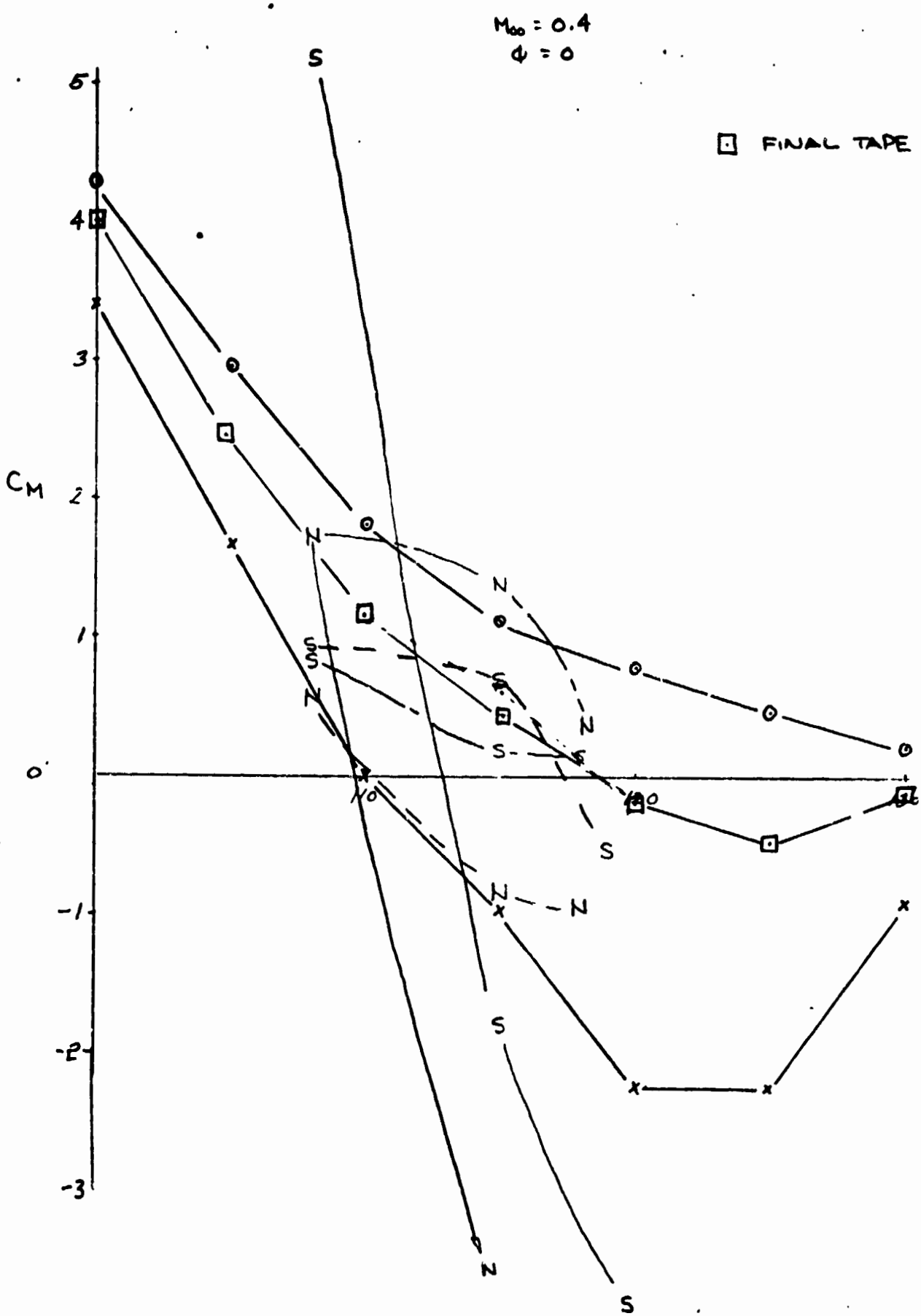

Figure 6-1. Corrected Pitching Moment Coefficient, $M_\infty = 0.4$, $\phi = 0$

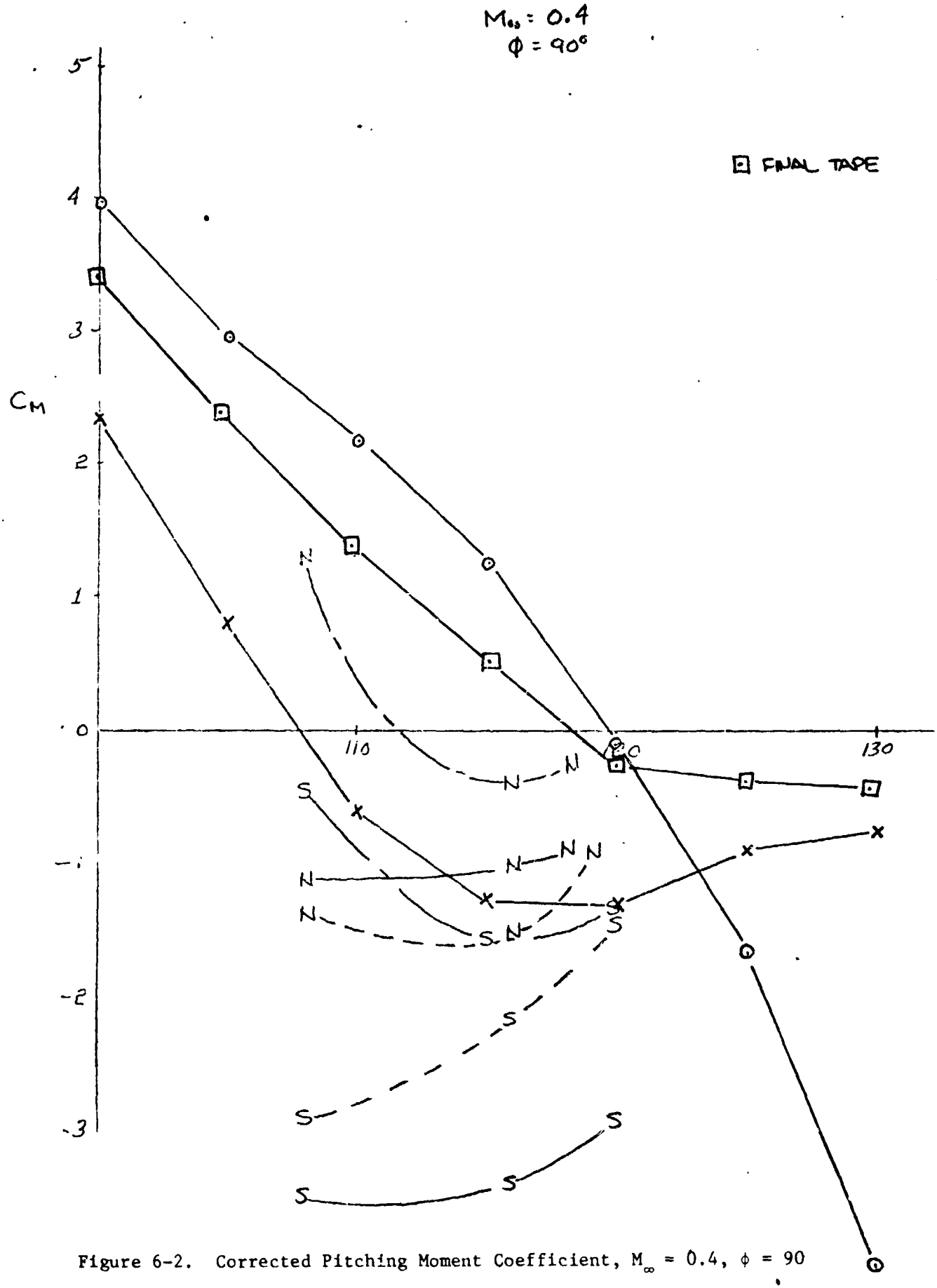

Figure 6-2. Corrected Pitching Moment Coefficient, $M_\infty = 0.4$, $\phi = 90$

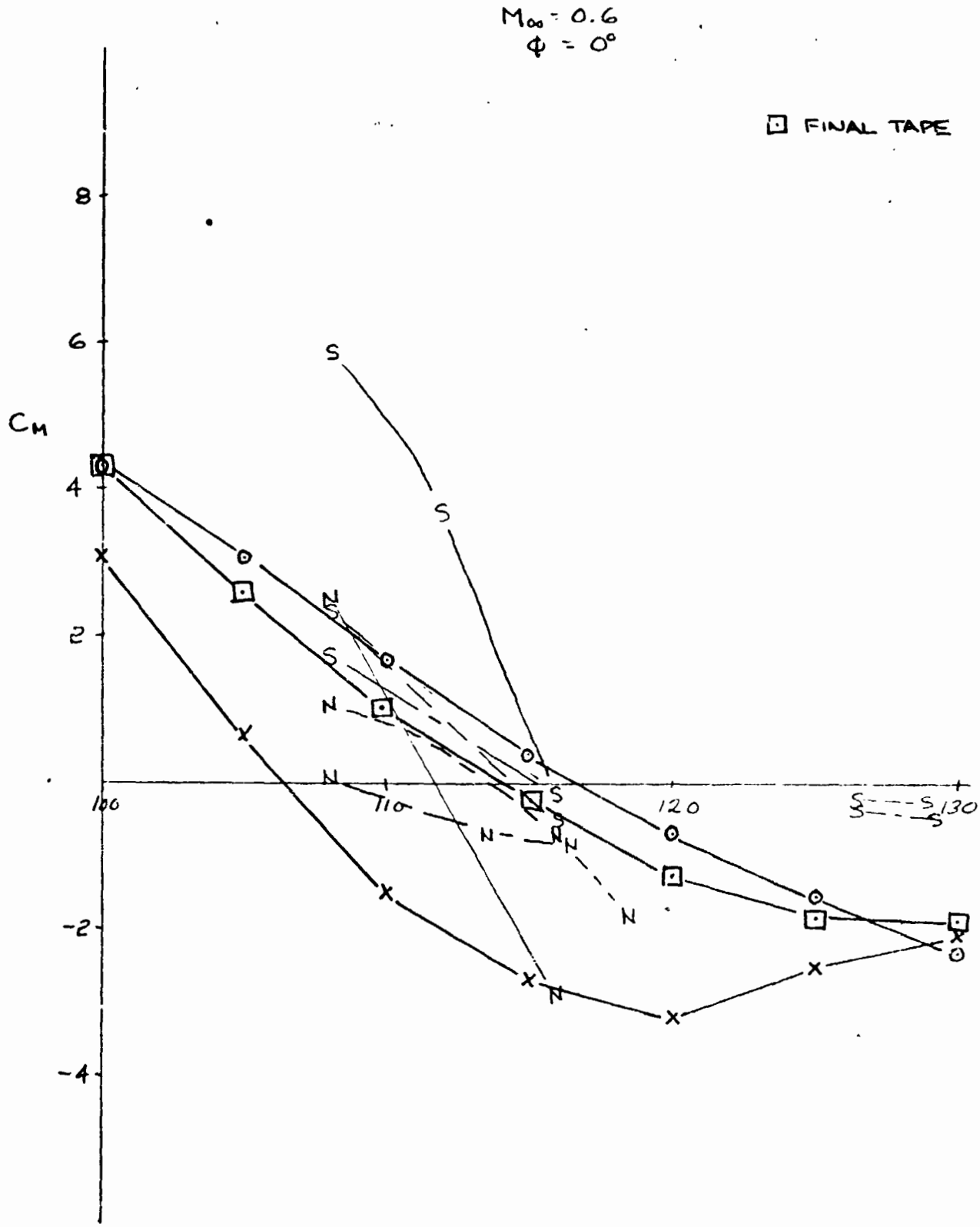

Figure 6-3. Corrected Pitching Moment Coefficient, $M_\infty = 0.6$, $\phi = 0$

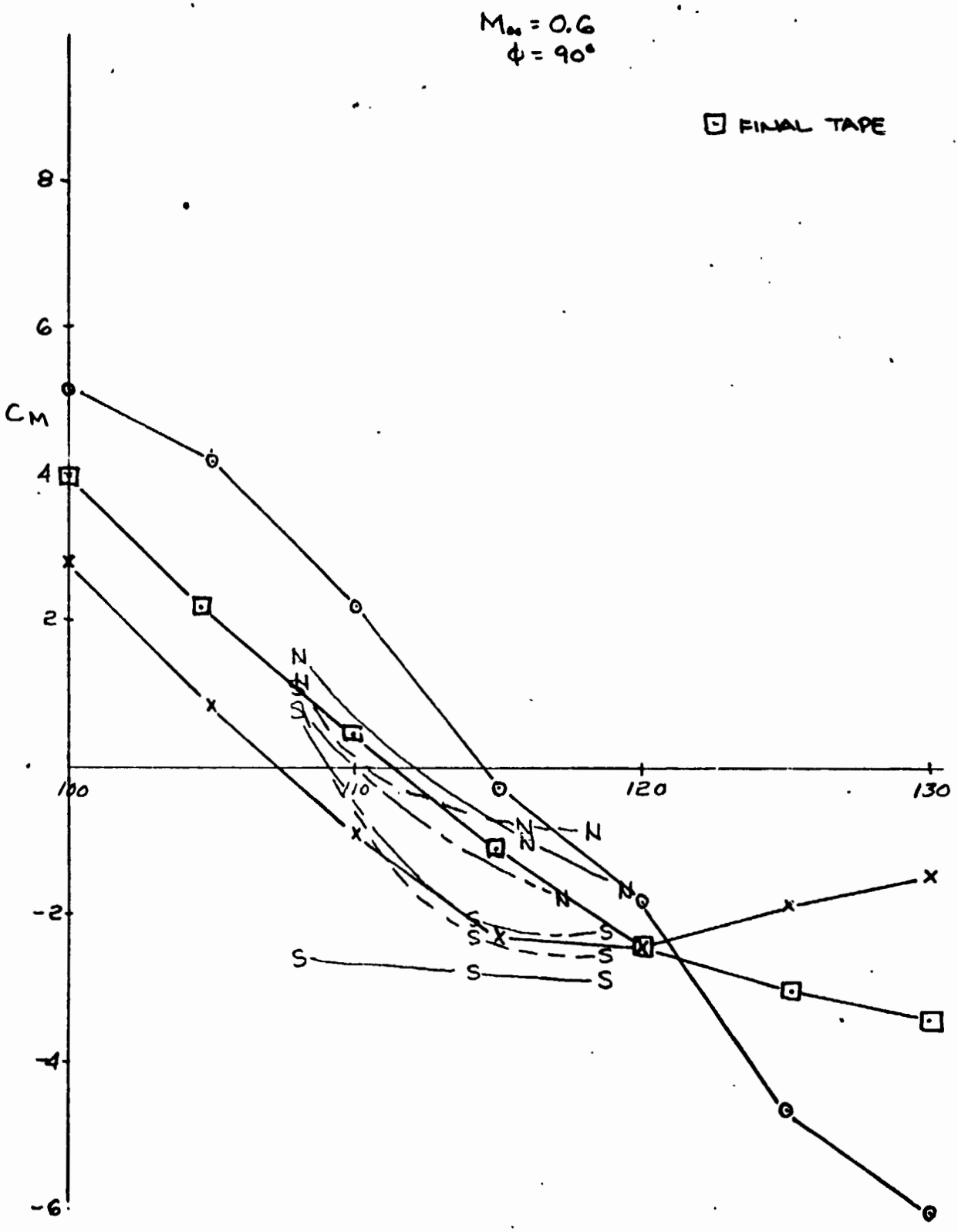

Figure 6-4. Corrected Pitching Moment Coefficient, $M_\infty = 0.6$, $\phi = 90$

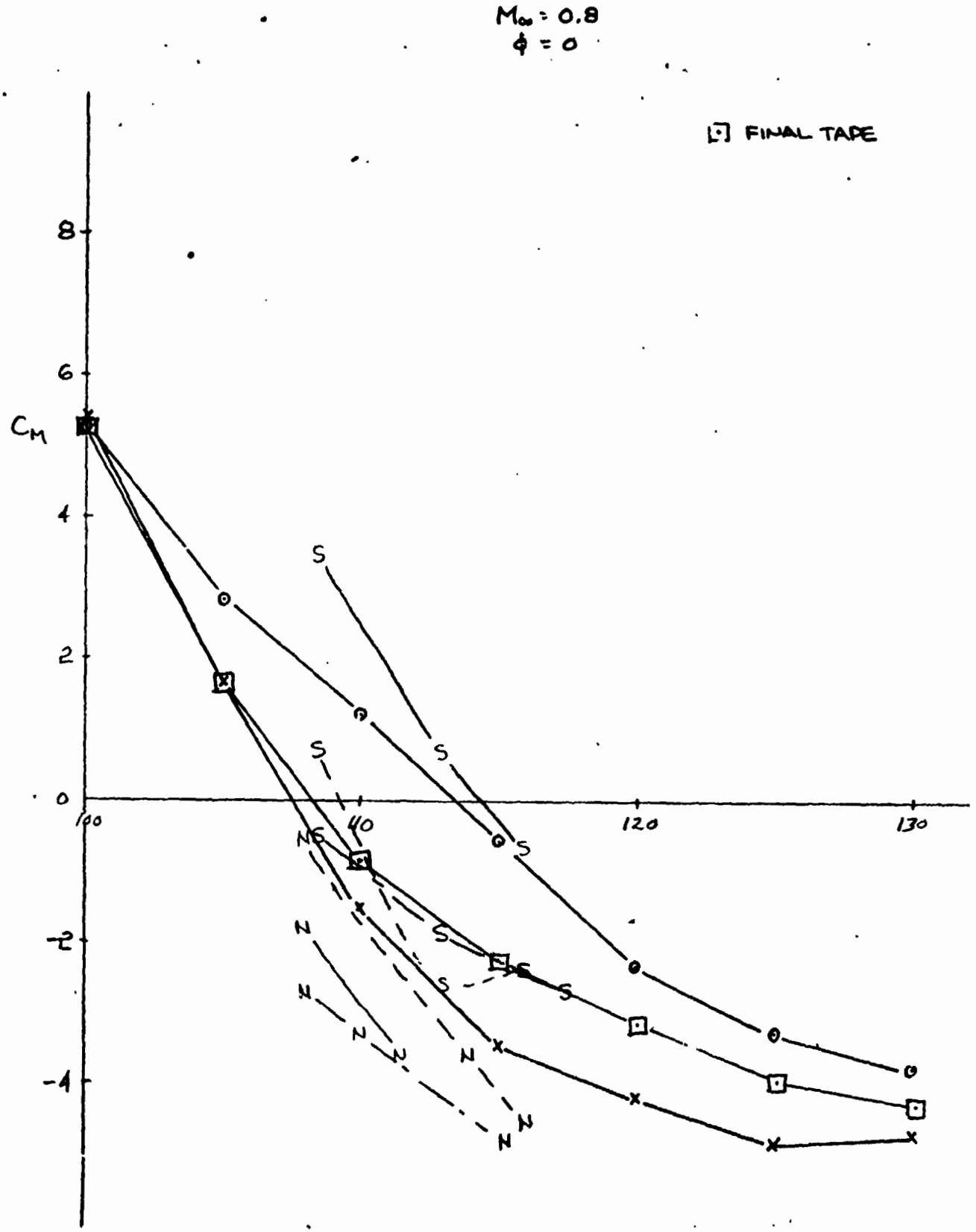

Figure 6-5. Corrected Pitching Moment Coefficient, $M_\infty = 0.8$, $\phi = 0$

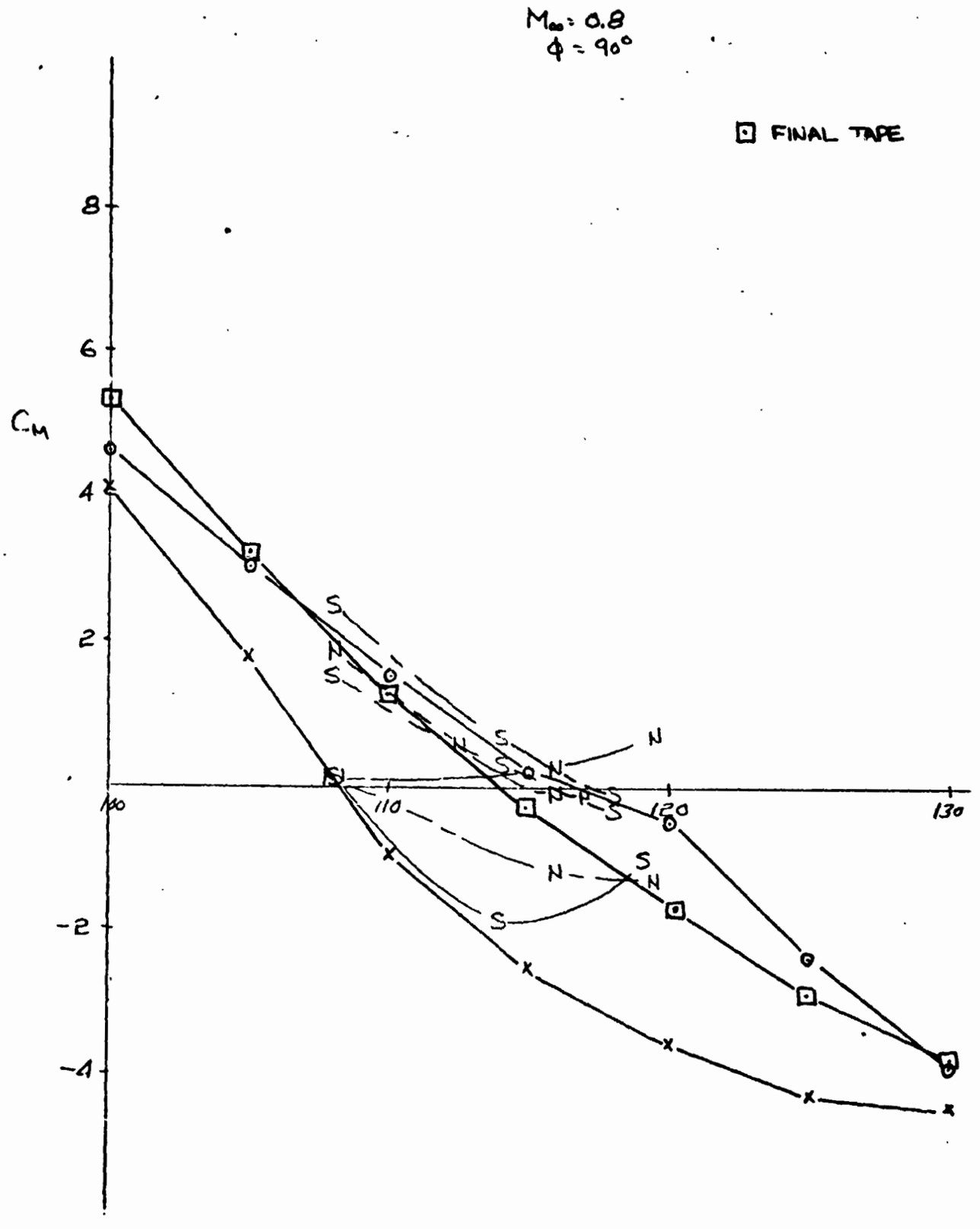

Figure 6-6. Corrected Pitching Moment Coefficient, $M_\infty = 0.8$, $\phi = 90$

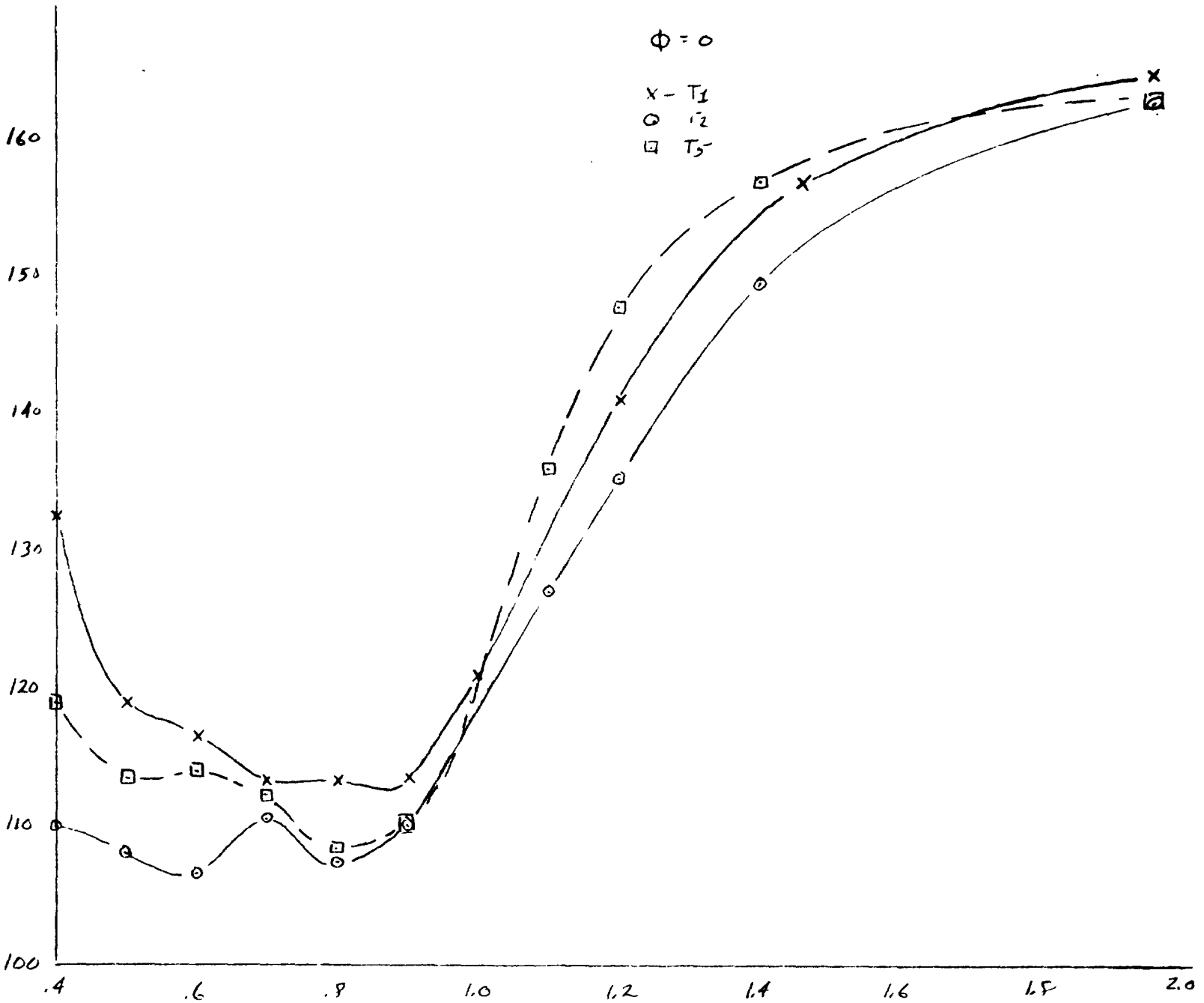

Figure 6-7. Corrected Trim Angle of Attack, ϕ = 0

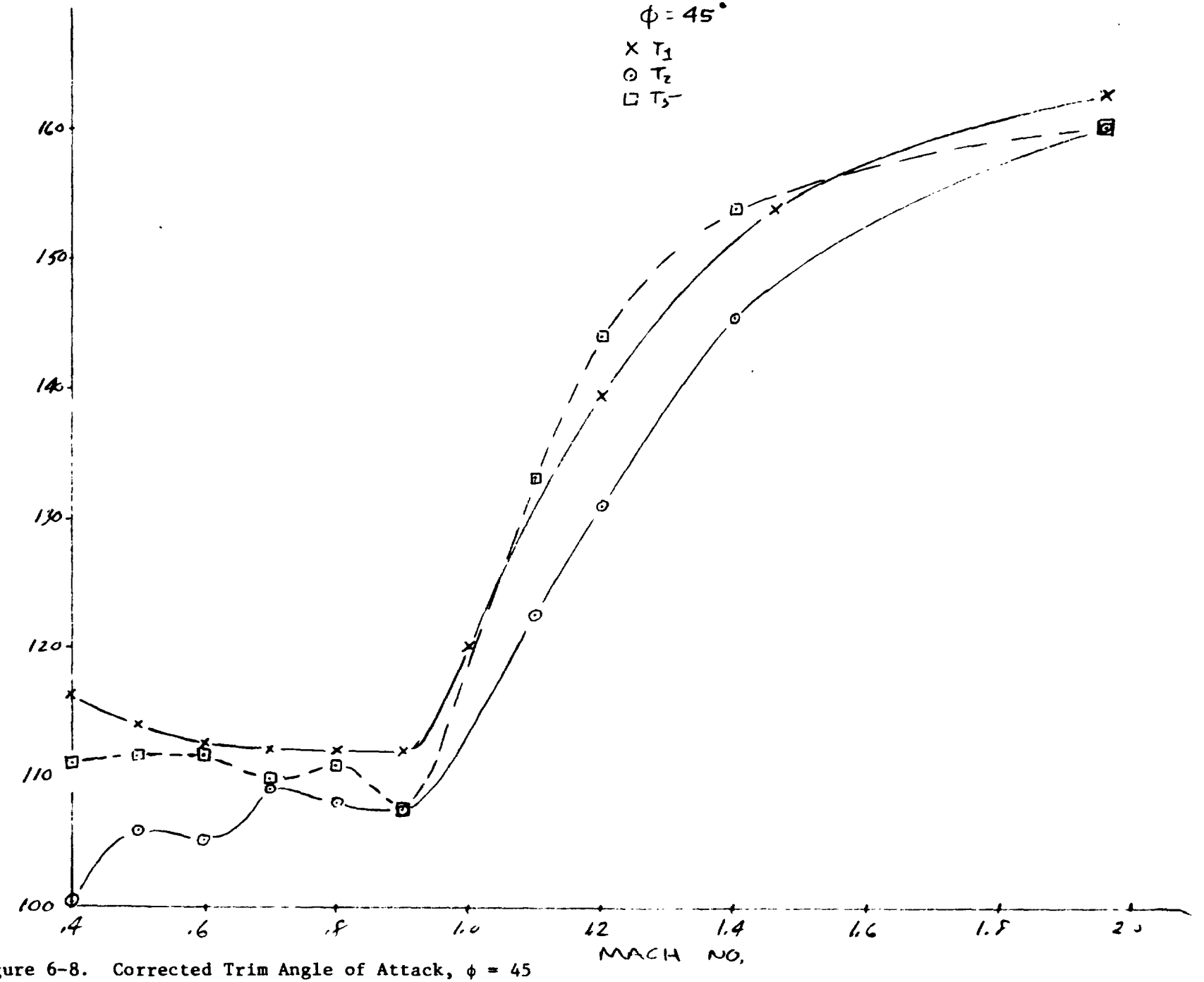

Figure 6-8. Corrected Trim Angle of Attack, ϕ = 45

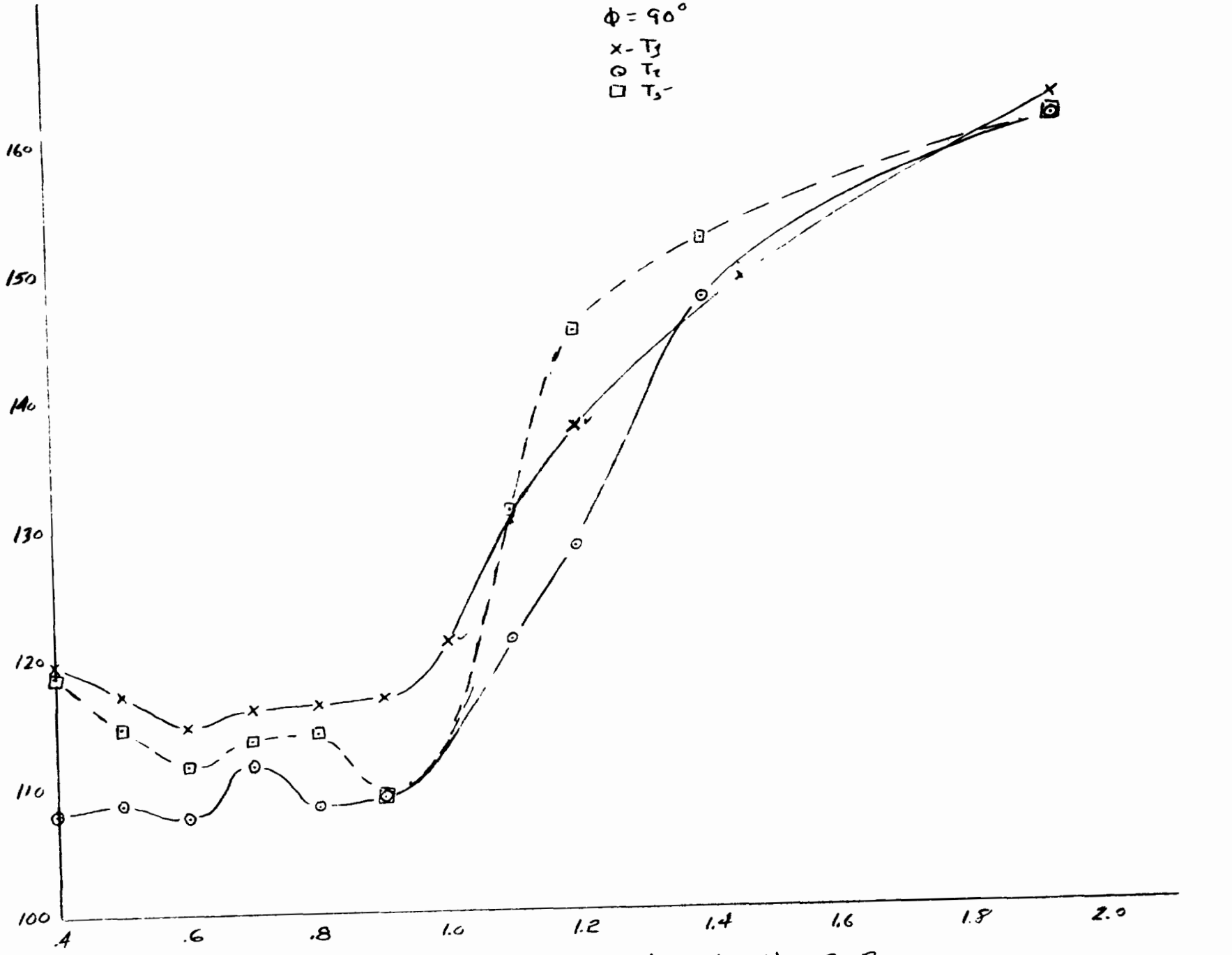

Figure 6-9. Corrected Trim Angle of Attack, ϕ = 90

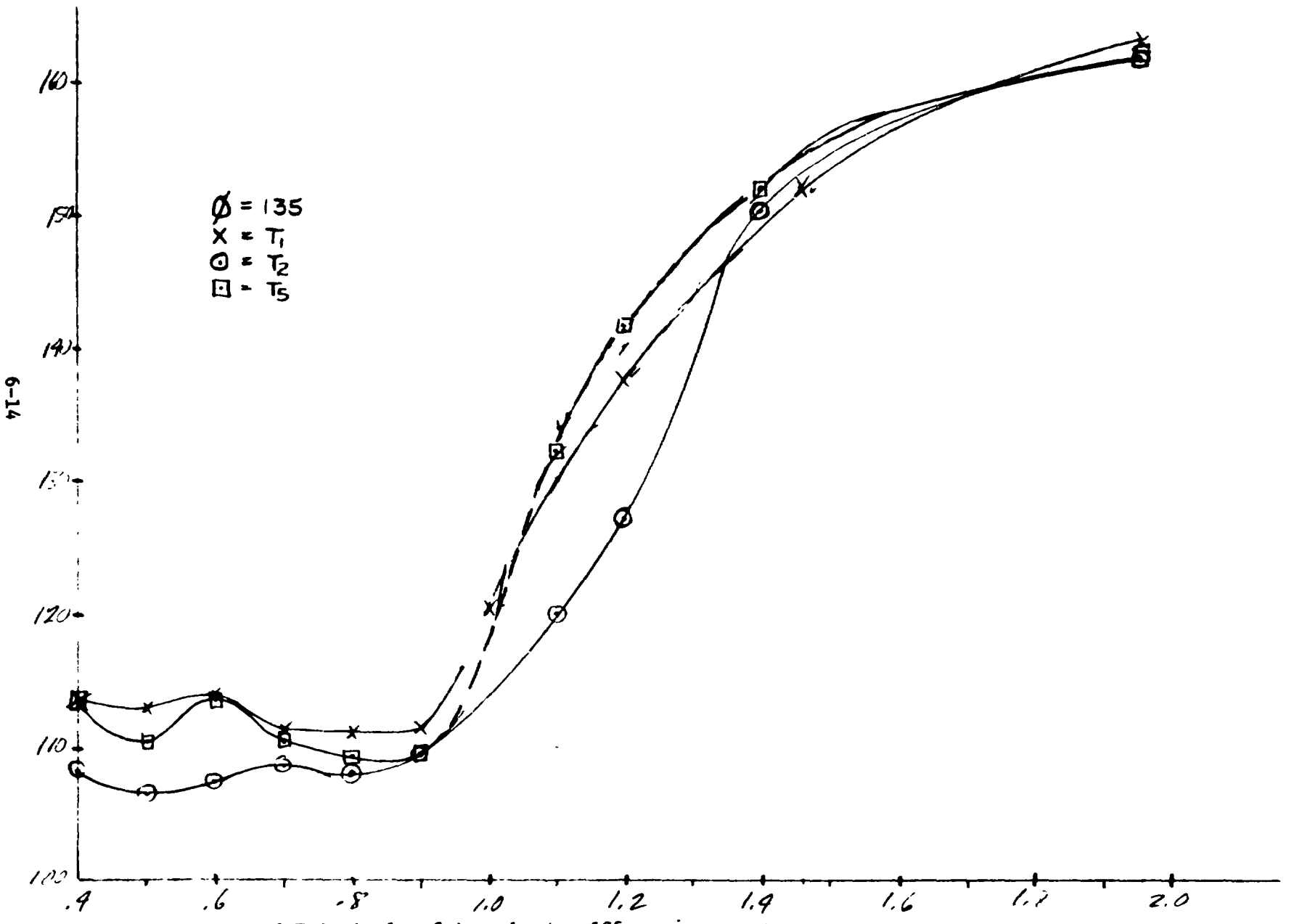

Figure 6-10. Corrected Trim Angle of Attack, ϕ = 135

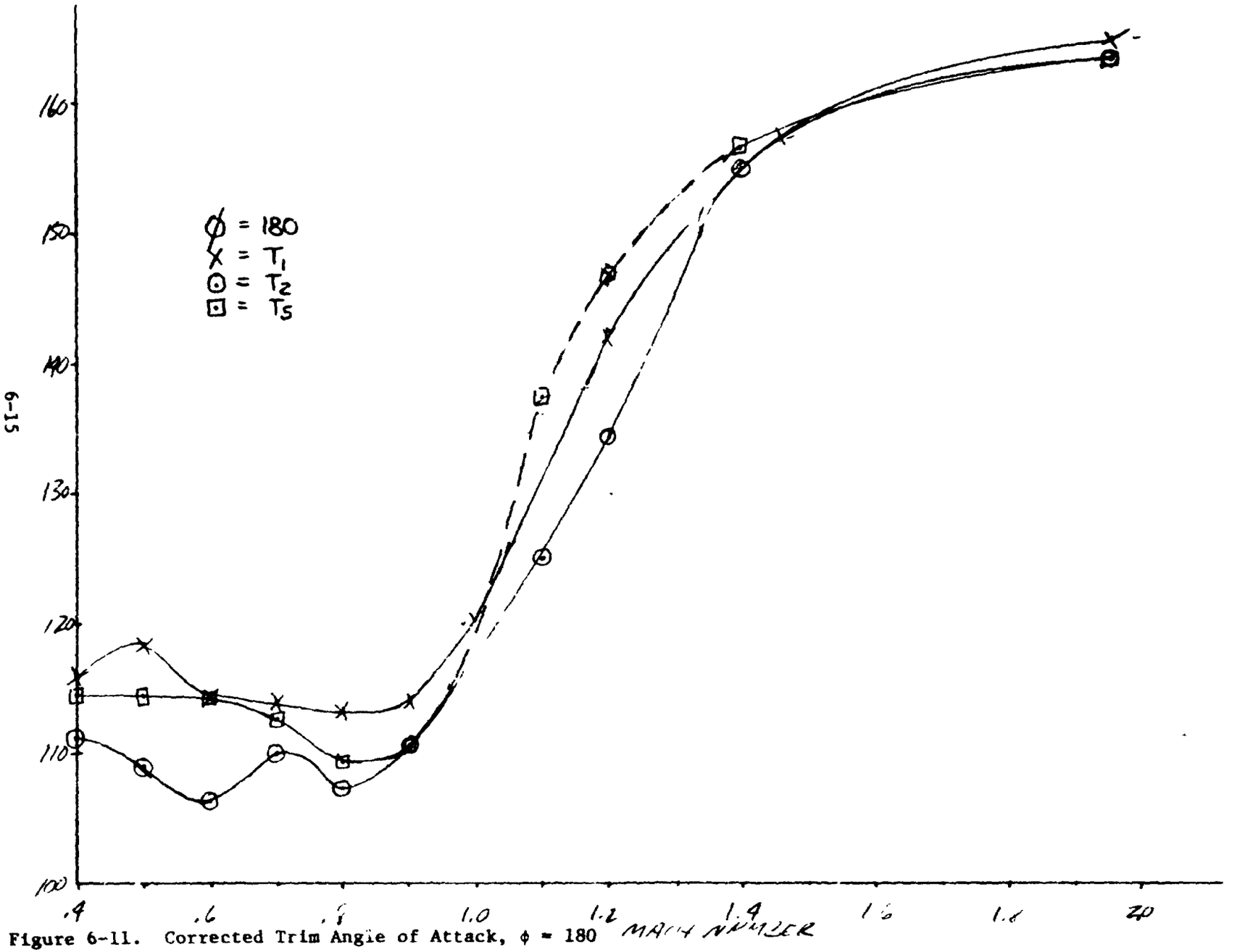

Figure 6-11. Corrected Trim Angle of Attack, ϕ = 180

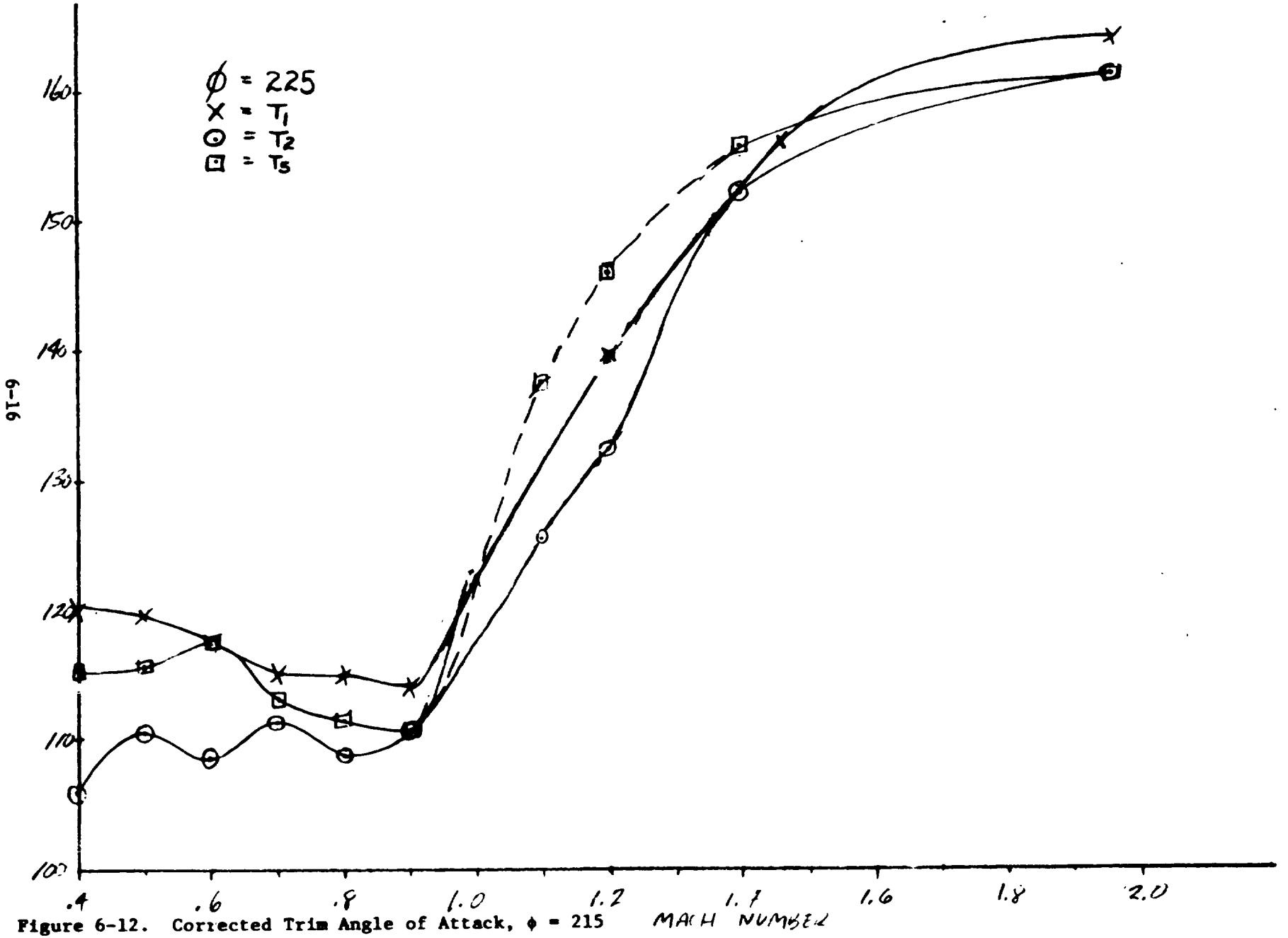

Figure 6-12. Corrected Trim Angle of Attack, ϕ = 215

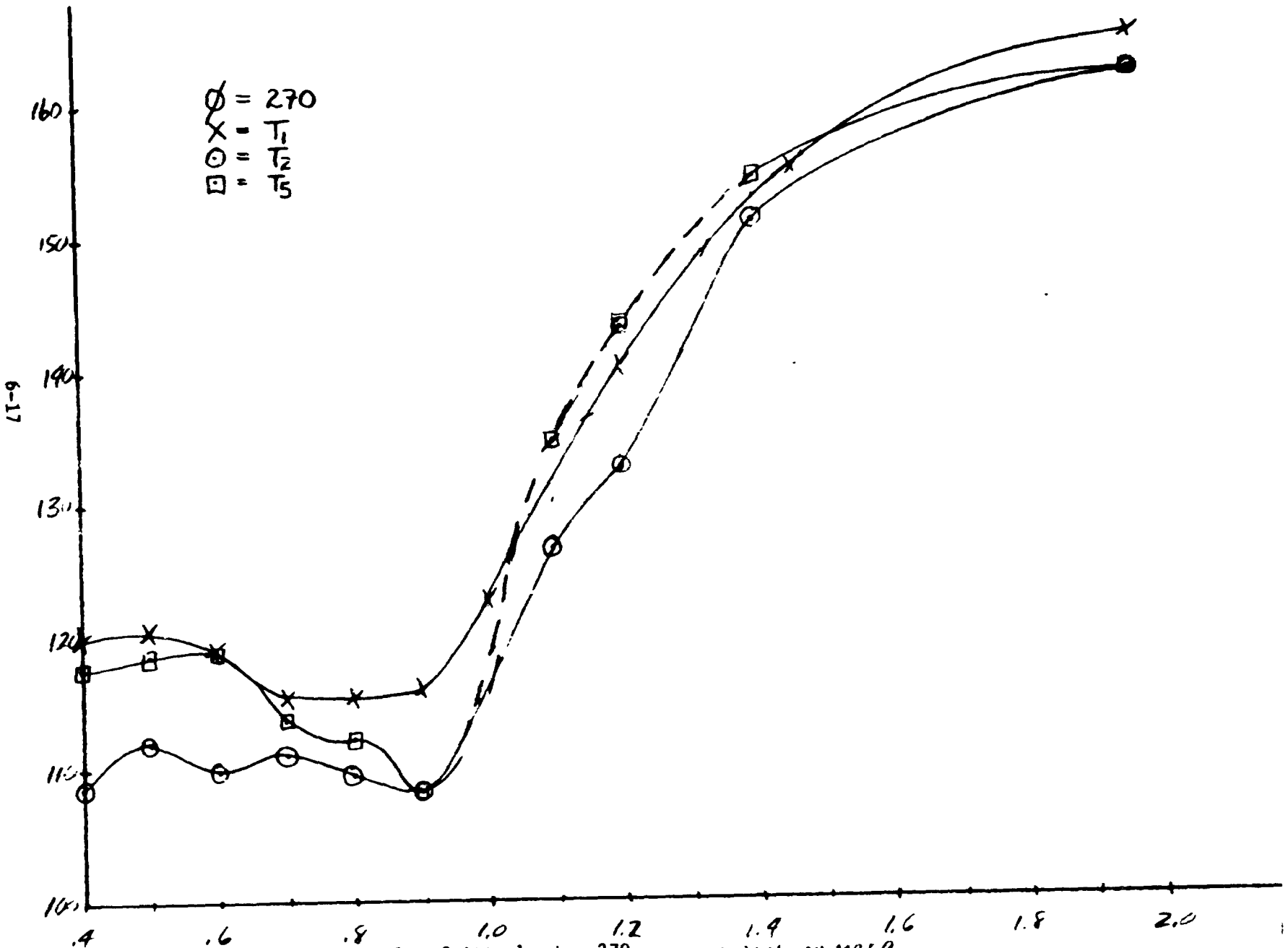

Figure 6-13. Corrected Trim Angle of Attack, ϕ = 270

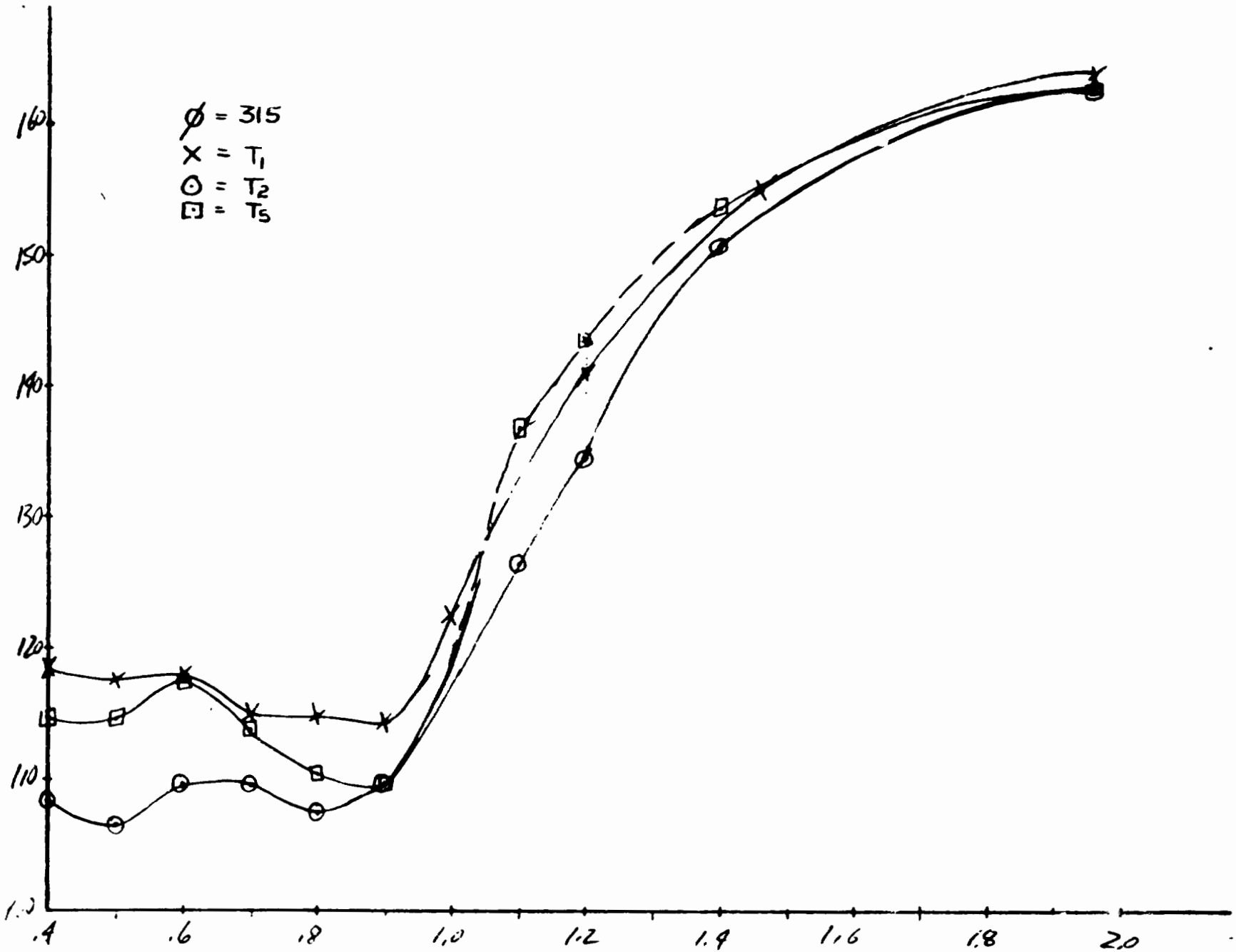

Figure 6-14. Corrected Trim Angle of Attack, ϕ = 315

Section VII

CONCLUSIONS

The analysis of the sting interference data from tests TWT 660 and HRWT 042 identified the following general influence of the sting.

1. The side mount sting almost always reduces the normal force coefficient of the model.
2. The amount of reduction depends on the relative size of the sting to the model.
3. The pitching moment sting interference depends on the size and location of the sting.
4. The SRB pitching moment side mount sting interference was smaller than the nose mount sting interference for angles of attack from 100 degrees to 120 degrees.
5. The SRB nose mount sting interference was smaller for angles of attack from 120 to 140 degrees.
6. The Ames side mount sting configuration had higher sting interference than the MSFC side mount sting configuration.
7. The corrected normal force and pitching moment wind tunnel data was significantly different from the SRB aero data Tape #1 and Tape #2 for Mach numbers of 1.1, 1.2, and 1.46.
8. The corrected pitching moment at all subsonic Mach numbers was different from either data Tape #1 or #2.
9. A new SRB aerodynamic math model was developed incorporating new normal force and pitching moment data commensurate with conclusions #7 and #8.

Section VIII

REFERENCES

1. Andrews, C. D., "Results of an Independent Assessment of SRB Reentry Aerodynamics," MSFC Memo ED32-78-28, June 5, 1978.

2. Ramsey P. E. and Hengle, J. E., "Pretest Information for a SRB Sting Interference Study in the MSFC 14-inch TWT," MSFC Memo ED32-78-28, September 1979.

3. Hengle, J. E., "Pretest Information for an SRB Sting Interference Study in the MSFC High Reynolds Number Wind Tunnel (HRWT)," MSFC Memo ED32-81-3, January 19, 1981.

4. Streby, G. D., "Static Stability Characteristics of a 0.00548 Scale Model of a Right Hand 146 Inch Diameter Solid Rocket Booster Reentry Configuration Tested in the NASA-MSFC 14 x 14 Inch Trisonic Wind Tunnel," NSI M-9224-77-9, 1 March 1977.

5. Quinn, R. W., "Aerodynamic Static Stability Characteristics of a 0.00548-Scale Model of the Space Shuttle 146 Inch Diameter Solid Rocket Booster Reentry Configuration at High Angles of Attack," AEDC-DR-76-50, 9 June 1976.

6. Braddock, W. F. and Streby, G. D., "A Static Stability, Pressure and Nozzle Gimbal Moment Wind Tunnel Test of the Space Shuttle SRB at Reentry Attitudes," NSI M-9230-75-479, 17 November 1975.

7. Braddock, W. F., "Addendum to the SA11F Pretest Report (NSI M-9230-75-479)," NSI M-9230-76-13, 12 March 1976.

8. Winkler, G. W., "MSFC HRWT 034, Data Listing," NSI Memo M-9230-75-455, dated September 1975.

9. Winkler, G. W., "An Aerodynamic Static Stability Wind Tunnel Test of a 0.00856 Scale Model of the Space Shuttle 146 Inch Diameter Solid Rocket Booster Reentry Configuration in the NASA/MSFC High Reynolds Number Wind Tunnel," NSI M-9224A-77-8, 1 March 1977.

10. "Aerodynamic Roll Characteristics of a 0.00548 Scale 146 Inch Solid Rocket Booster Reentry Configuration (MSFC Model No. 486) Over a Portion of the Reentry Flight Regime in the NASA/MSFC 14 Inch Trisonic Wind Tunnel (SA21F)," Chrysler DMS-DR2345, June 1977.

11. Jones, G. W., Jr., Cincotta, J., and Walker, W., "Aerodynamic Forces on a Stationary and Oscillating Circular Cylinder at High Reynolds Numbers," NASA TR R-300, Feb. 1969.

12. McKinney, L. W., "Effects of Fineness Ratio and Reynolds Number on the Low-Speed Crosswind Drag Characteristics of Circular and Modified-Square Cylinders," NASA TND-540, October 1960.

13. James, W. D., Paris, S. W., and Malcolm, G. H., "Study of Viscous Cross-flow Effects on Circular Cylinders at High Reynolds Numbers," AIAA Journal, Vol. 18, No. 9, 1980, pp. 1066-1072.

14. Yowen, F. E. and Perhim, E. W., "Drag of Circular Cylinders for a Wide Range of Reynolds Numbers and Mach Numbers," NACA TN-2960, June 1953.